INFORMATION TO USERS

This manuscript has been reproduced from the microfilm master. UMI films the text directly from the original or copy submitted. Thus, some thesis and dissertation copies are in typewriter face, while others may be from any type of computer printer.

The quality of this reproduction is dependent upon the quality of the copy submitted. Broken or indistinct print, colored or poor quality illustrations and photographs, print bleedthrough, substandard margins, and improper alignment can adversely affect reproduction.

In the unlikely event that the author did not send UMI a complete manuscript and there are missing pages, these will be noted. Also, if unauthorized copyright material had to be removed, a note will indicate the deletion.

Oversize materials (e.g., maps, drawings, charts) are reproduced by sectioning the original, beginning at the upper left-hand corner and continuing from left to right in equal sections with small overlaps.

Photographs included in the original manuscript have been reproduced xerographically in this copy. Higher quality 6" x 9" black and white photographic prints are available for any photographs or illustrations appearing in this copy for an additional charge. Contact UMI directly to order.

ProQuest Information and Learning
300 North Zeeb Road, Ann Arbor, MI 48106-1346 USA
800-521-0600

UMI®

Reproduced with permission of the copyright owner. Further reproduction prohibited without permission.

Graduate School Form 9
(Revised 7/94)

PURDUE UNIVERSITY
GRADUATE SCHOOL
Thesis Acceptance

This is to certify that the thesis prepared

By Sergio Adrian Leonardi

Entitled Partially-Premixed Combustion in Porous Radiant Burners

Complies with University regulations and meets the standards of the Graduate School for originality and quality

For the degree of Doctor of Philosophy

Signed by the final examining committee:

R Viskanta, chair

Steven Frankel

L. H. Tsou

Approved by: E Dan Hirleman / Anil Bajaj 7/19/00
Department Head Date
School of Mechanical Engineering

This thesis ☑ is no longer confidential ☐ is not to be regarded as confidential. R Viskanta
Major Professor

Format Approved by:

or Anil Bajaj
Chair, Final Examining Committee Thesis Format Adviser

10 Dec 01

PARTIALLY-PREMIXED COMBUSTION IN POROUS RADIANT BURNERS

A Thesis

Submitted to the Faculty

of

Purdue University

by

Sergio Adrián Leonardi

In Partial Fulfillment of the

Requirements for the Degree

of

Doctor of Philosophy

August 2000

UMI Number: 3055515

UMI®

UMI Microform 3055515

ProQuest Information and Learning Company
300 North Zeeb Road
P.O. Box 1346
Ann Arbor, MI 48106-1346

To Tauna,
my loving wife,
and Paul,
my beautiful son.

ACKNOWLEDGMENTS

I would like to thank my mentor and major professor. Dr. Raymond Viskanta. whose counsel, guidance and encouragement made this endeavor possible. It was an honor to work under his supervision. Without his untiring and creative effort. patience and willingness to share his time and knowledge. I would not have been able to finish this thesis.

I am also overflowing with gratitude toward my co-advisor, Prof. Jay Gore. whose insight and support helped to successfully complete this project. The influence of an individual of his stature on a budding researcher is immeasurable. His energetic approach to both the experimental and numerical aspects were invaluable.

I am also grateful to Prof. Thomas Downar and Prof. Michael Plesniak for their advice and help. In addition, I must express my sincere thankfulness to them for accepting to serve on my advisory committee, and Prof. Steven Frankel and Prof. Lefteri Tsoukalas for joining the examining committee.

I am truly indebted to Dr. Prem Singh for his guidance and help with the instrumentation in the laboratory and for sharing his experience on the operation of the radiant burners. My deep appreciation goes to all the staff and graduate students in the School of Mechanical Engineering, but especially Marcus Bianchi and Andrei Fedorov for their friendship.

A special note of thanks goes to the students who guided me when I was just starting to work on porous media (Xiaoyong Fu) and on numerical predictions of flames using detailed chemistry (Jongmook Lim). Dr. Marc Rumminger's assistance with the modifications of PREMIX equations was greatly valued as well as those of Prof. Makihito Nishioka, of Tsukuba University, Japan, who provided advice regarding changes in the gridding routine.

I would like to convey my appreciation to Bob Willis for his help in designing and fabricating the burner housing, as well as for his counsel on what not to do in machining; Max Coffman, for building the burner prototype; Ron Evans, for his help with the computers; Dr. Matthew Krane, for helping with the microscope and the photographs of the flame support materials; the staff at PUCC (Purdue University Computer Center), for providing access and support of the RISC 6000 cluster; and Mark Senn, for helping with the final thesis format.

The completion of this work would not have been possible without the aid of several people who supplied samples and/or property data of porous materials: Dr. Ozzie Missoum (Acotech Corporation), Dr. Truett Sweeting (Hi-Tech Ceramics), and Robert LeClaire and Margaret Vogel-Martin (3M Ceramic Fiber Products).

This work was supported in part by the Gas Research Institute through a subcontract from S. S. Energy Environmental International, Inc. Useful discussions with Mr. Shyam Singh were appreciated.

Finally, I would like to thank, from the bottom of my heart, the love, encouragement and unconditional support of my dear wife Tauna, who still found the time and energy to proofread the manuscript while working on her Ph.D. thesis and taking care of our baby son.

TABLE OF CONTENTS

Page

LIST OF TABLES ix

LIST OF FIGURES xi

NOMENCLATURE xvi

ABSTRACT xx

1 INTRODUCTION 1

1.1 Background 1

1.2 Description of Different Types of Radiant Burners 5

1.3 Literature Review 9

1.3.1 Early Work on Porous Inert Radiant Burners 9

1.3.2 Recent Studies on Porous Inert Radiant Burners 15

1.3.3 Catalytic Radiant Burners/Heaters 20

1.3.4 Partially-Premixed Flames 25

1.4 Objectives and Scope of Study 32

1.4.1 Motivation 32

1.4.2 Specific Objectives 33

2 EXPERIMENTS 35

2.1 Introduction 35

2.2 Burner Selection 35

2.3 Experimental Arrangement 48

2.4 Description of Global Measurements 50

2.4.1 Radiant Flux 51

2.4.2 Combined Radiation and Convection 54

2.4.3 Burner Surface Spectral Intensity 55

Page

2.4.4 Exhaust Gas Temperature and Spectral Intensity 57
2.4.5 Pollutant Emissions 60
2.4.6 Burner Temperature 62
2.5 Experimental Data 64
2.5.1 Partially-Premixed Commercial Catalytic Burner 64
2.5.2 Prototype Fiber Burners 64
2.5.2.1 Radiation Efficiency for the Prototype Burners . . . 64
2.5.2.2 Combined Efficiency for the Prototype Burners . . . 67
2.5.2.3 Surface Temperature for the Prototype Burners . . . 69
2.5.2.4 Temperature of the Exhaust Gases 71
2.5.2.5 Pollutant Emissions 73
3 MATHEMATICAL MODELING OF A POROUS RADIANT BURNER . 80
3.1 Introduction 80
3.2 Mathematical Description 81
3.2.1 Assumptions 81
3.2.2 Model Equations 84
3.2.3 Radiative Transfer 85
3.2.4 Boundary Conditions 88
3.3 Volumetric Heat Transfer Coefficient 90
3.4 PREMIX Chemical Mechanism Description 90
3.5 Computer Program Modifications 91
3.6 PREMIX Solution Strategy 93
3.7 Code Validation 96
4 COMPARISON OF MODEL PREDICTIONS WITH EXPERIMENTAL DATA 101
4.1 Introduction 101
4.2 Characteristics of Porous Matrix 101
4.2.1 Volumetric Heat Transfer Coefficient 102

Page
4.2.2 Radiation Properties 104
4.3 Comparison of Model Predictions with Data 107
4.3.1 Temperature of the Exhaust Gases 107
4.3.2 Solid Surface Temperature 112
4.3.3 Radiation Efficiency 112
4.3.4 NO Emissions 120
4.3.5 CO Emissions 120
4.3.6 Unburned Hydrocarbons Emissions 124
4.4 Discussion of the Comparison 124
5 PARAMETRIC STUDY 133
5.1 Choice of Baseline Parameters 133
5.2 Influence of the Volumetric Heat Transfer Coefficient 149
5.3 Influence of the Equivalence Ratio 164
5.4 Influence of the Firing Rate 172
5.5 Influence of the Downstream O_2 Concentration 176
5.6 Influence of the Surface Emittance 181
5.7 Influence of the Solid Thermal Conductivity 184
5.8 Influence of the Extinction Coefficient 187
5.9 Influence of the Scattering Coefficient (Albedo) 190
5.10 Influence of the Fuel Composition 192
5.11 Summary 197
6 CONCLUSIONS AND RECOMMENDATIONS 199
6.1 Conclusions 199
6.2 Recommendations for Future Work 202
LIST OF REFERENCES 206
APPENDICES 220
Appendix A: Experimental Uncertainty Estimation 220
Appendix B: Volumetric Heat Transfer Coefficient of Fiber Mats 222

Page

B.1 Introduction 222

B.2 Mathematical Description and Theory for Data Reduction . . 223

B.3 Measurements and Data Reduction 226

B.4 Correlations 230

B.5 Shortcomings for Some Materials 230

Appendix C: Specific Heat Determination 234

C.1 Nextel 312 Specific Heat Results 234

C.2 Fecralloy Specific Heat Results 234

Appendix D: Radiation Thermometer Calibrations 237

Appendix E: GRI-Mech 2.11 Chemical Mechanism for CH_4 Combustion . . 239

E.1 Involved Elements and Species 239

E.2 Chemical Reactions 239

Appendix F: Modified PREMIX Input File 249

Appendix G: Description of PREMIX Solution Algorithm (TWPNT) . . . 252

VITA 254

LIST OF TABLES

Table Page

2.1 Thermophysical properties of fibrous materials 50

2.2 Nextel fiber composition (wt. %) 51

2.3 Fecralloy fiber composition (wt. %) 52

2.4 Radiometer specifications 53

2.5 Heat flux meter specifications 54

3.1 Discrete ordinates for the one-dimensional S_N approximation. 88

4.1 Local values of volumetric heat transfer coefficient 104

4.2 Natural gas composition (vol. %) 131

5.1 Base case parameters for sample calculations 135

5.2 Model burner radiation efficiency for different values of the volumetric heat transfer coefficient 163

5.3 Model burner radiation efficiency for different equivalence ratios 166

5.4 Model burner radiation efficiency for different equivalence ratios (rich flames up to $\Phi = 1.4$) 171

5.5 Model burner radiation efficiency for different firing rates 174

5.6 Model burner radiation efficiency for different concentrations of O_2 at the downstream boundary 181

5.7 Model burner radiation efficiency for different values of the matrix surface emittance 182

5.8 Model burner radiation efficiency for different thermal conductivities of the solid matrix 185

5.9 Model burner radiation efficiency for different values of the extinction coefficient 189

5.10 Model burner radiation efficiency for different values of the scattering coefficient 190

Table Page

5.11 Unburned hydrocarbon emissions increase for the model burner using natural gas instead of methane as fuel 196

5.12 Model burner radiation efficiency for different fuels 196

5.13 Summary of the effects of the different problem parameters on burner performance characteristics 198

Appendix Table

A.1 Error propagation for radiation efficiency 221

LIST OF FIGURES

Figure — Page

1.1 Schematic of two types of radiant porous burners: embedded flame and surface flame. 6

1.2 Schematic of two types of radiant burners: direct-fired and indirect-fired. 7

1.3 Schematic of two types of direct-fired radiant porous burners: ported and impingement. 8

2.1 Schematic of the prototype radiant gas burner and its main components 36

2.2 Fecralloy NIT200S prototype burner; $\Phi = 1.0$, firing rate of 70 $\frac{kW}{m^2}$ 38

2.3 Nextel 312 prototype burner; $\Phi = 0.8$, firing rate of 60 $\frac{kW}{m^2}$ 38

2.4 Fecralloy NIT200S prototype burner with a Nextel 312 diffusion layer; $\Phi = 1.0$, firing rate of 70 $\frac{kW}{m^2}$ 39

2.5 Flow distribution results based on FLUENT when a fuel jet enters a rectangular inlet plenum 41

2.6 Flow distribution results based on FLUENT when a fuel jet enters a diffuser-based burner inlet plenum 41

2.7 Schematic of a diffuser-based burner inlet plenum 43

2.8 Rear view of the diffuser-based housing for the prototype burner 44

2.9 Single-layer Fecralloy NIT200S prototype burner; $\Phi = 0.9$, firing rate of 300 $\frac{kW}{m^2}$ 45

2.10 Double-layer Fecralloy NIT200S prototype burner; $\Phi = 1.0$, firing rate of 270 $\frac{kW}{m^2}$ 46

2.11 Single-layer Fecralloy NIT200S prototype burner; $\Phi = 1.1$, firing rate of 170 $\frac{kW}{m^2}$ 47

2.12 Schematic of the experimental arrangement for burner operation 49

2.13 Schematic of the heater and radiometer orientation 55

2.14 Schematic of the heater and calorimeter orientation 56

2.15 Schematic of the spectral intensity measurement apparatus 58

Figure Page

2.16 Schematic of the "fast infrared array spectrometer" (FIAS) experimental arrangement 61

2.17 Schematic of the pollutant emission analysis apparatus 63

2.18 Effect of partially premixing fuel and air on a diffusion-type catalytic burner: dependence on the firing rate 65

2.19 Radiation efficiency for Fecralloy burner: dependence on the firing rate . 68

2.20 Combined efficiency for Fecralloy burner: dependence on the firing rate . 70

2.21 Surface temperature for Fecralloy burner: dependence on the firing rate . 72

2.22 Typical emission spectrum for the burner exhaust gases 74

2.23 Exhaust gases temperature for Fecralloy burner: dependence on the firing rate 75

2.24 Carbon monoxide emissions for Fecralloy burner: dependence on the firing rate 77

2.25 Nitrous oxide emissions for Fecralloy burner: dependence on the firing rate 78

2.26 Unburned hydrocarbon emissions for Fecralloy burner: dependence on the firing rate 79

3.1 Schematic of a one-dimensional porous burner and the relevant heat transfer modes 82

3.2 Diagram of PREMIX modifications 94

3.3 Flow chart for PREMIX and its modifications 95

3.4 Local energy budget (gas phase) inside a radiant burner 99

3.5 Local energy budget (solid phase) inside a radiant burner 100

4.1 Metal fiber pad structures: knitted and sintered Fecralloy 107

4.2 Comparison (prediction vs. data) of the exit gas temperature, $\Phi = 1.1$. 109

4.3 Comparison (prediction vs. data) of the exit gas temperature, $\Phi = 1.0$. 110

4.4 Comparison (prediction vs. data) of the exit gas temperature, $\Phi = 0.9$. 111

4.5 Comparison (prediction vs. data) of the surface temperature, $\Phi = 1.1$ . . 113

4.6 Comparison (prediction vs. data) of the surface temperature, $\Phi = 1.0$ . . 114

4.7 Comparison (prediction vs. data) of the surface temperature, $\Phi = 0.9$ . . 115

Figure Page

4.8 Comparison (prediction vs. data) of radiation efficiencies, $\Phi = 1.1$ 117

4.9 Comparison (prediction vs. data) of radiation efficiencies, $\Phi = 1.0$ 118

4.10 Comparison (prediction vs. data) of radiation efficiencies, $\Phi = 0.9$ 119

4.11 Comparison (prediction vs. data) of NO emissions, $\Phi = 1.1$ 121

4.12 Comparison (prediction vs. data) of NO emissions, $\Phi = 1.0$ 122

4.13 Comparison (prediction vs. data) of NO emissions, $\Phi = 0.9$ 123

4.14 Comparison (prediction vs. data) of CO emissions, $\Phi = 1.1$ 125

4.15 Comparison (prediction vs. data) of CO emissions, $\Phi = 1.0$ 126

4.16 Comparison (prediction vs. data) of CO emissions, $\Phi = 0.9$ 127

4.17 Comparison (prediction vs. data) of UBH emissions, $\Phi = 1.1$ 128

4.18 Comparison (prediction vs. data) of UBH emissions, $\Phi = 1.0$ 129

4.19 Comparison (prediction vs. data) of UBH emissions, $\Phi = 0.9$ 130

5.1 Temperature distribution inside model burner 137

5.2 Temperature difference distribution inside model burner 138

5.3 Gas velocity distribution inside model burner 140

5.4 Gas density distribution inside model burner 141

5.5 Selected (major) species distributions inside model burner 143

5.6 Selected (minor) species distributions inside model burner 144

5.7 Selected species (relevant to NO mechanisms) distributions inside model burner 147

5.8 Selected species (relevant to NO mechanisms) distributions inside model burner, in terms of a progress variable 148

5.9 Temperature distribution inside model burner for three different values of the volumetric heat transfer coefficient 150

5.10 Major species distribution inside model burner for three different values of the volumetric heat transfer coefficient 151

5.11 Minor species distribution inside model burner for three different values of the volumetric heat transfer coefficient 152

5.12 Major species distribution inside model burner for three different values of the volumetric heat transfer coefficient, in terms of the progress variable 155

Figure Page

5.13 Minor species distribution inside model burner for three different values of the volumetric heat transfer coefficient, in terms of the progress variable 156

5.14 Temperature distribution inside model burner for extreme values of the volumetric heat transfer coefficient 157

5.15 Temperature distribution inside model burner for very low and very high values of the volumetric heat transfer coefficient, in terms of the complementary progress variable 159

5.16 Major species distribution inside model burner in terms of the complementary progress variable, for two different values of the volumetric heat transfer coefficient 160

5.17 Minor species distribution inside model burner in terms of the complementary progress variable, for two different values of the volumetric heat transfer coefficient 161

5.18 Selected species (relevant to NO mechanisms) distribution inside model burner in terms of the complementary progress variable, for two different values of the volumetric heat transfer coefficient 162

5.19 Temperature distribution inside model burner for different values of the equivalence ratio 165

5.20 Temperature distribution inside model burner for different values of the equivalence ratio (rich flames up to $\Phi = 1.4$) 168

5.21 Major species distribution inside model burner for different values of the equivalence ratio (rich flames up to $\Phi = 1.4$) 169

5.22 Minor species distribution inside model burner for different values of the equivalence ratio (rich flames up to $\Phi = 1.4$) 170

5.23 Temperature distribution for different values of the firing rate for fuel rich inlet mixture ($\Phi = 1.1$) 173

5.24 Temperature distribution for different values of the firing rate for fuel lean inlet mixture ($\Phi = 0.9$) 175

5.25 Temperature distribution inside model burner for different values of the downstream oxygen mole fraction 177

5.26 Major species distribution inside model burner for different values of the downstream oxygen mole fraction 179

5.27 Minor species distribution inside model burner for different values of the downstream oxygen mole fraction 180

Figure Page

5.28 Influence of the emittance of the solid on the temperature distributions of the model burner . . . 183

5.29 Influence of the thermal conductivity of the solid on the temperature distributions of the model burner . . . 186

5.30 Influence of the extinction coefficient on the temperature distributions of the model burner . . . 188

5.31 Influence of the scattering coefficient on the temperature distributions of the model burner . . . 191

5.32 Temperature distribution inside the burner for two different fuels . . . 193

5.33 Major species distribution inside model burner for two different fuels . . 194

5.34 Minor species distribution inside model burner for two different fuels . . 195

Appendix Figure

B.1 Schematic of the single-blow apparatus used to measure the volumetric heat transfer coefficient of a porous sample. . . . 226

B.2 Single-blow technique: comparison between the measured and predicted temperature transients . . . 229

B.3 Volumetric heat transfer coefficient of a Nextel 312 fiber mat. The thickness of the sample was 10 *mm*. . . . 231

B.4 Volumetric heat transfer coefficient of a Nextel 312 fiber mat in terms on non-dimensional parameters. The thickness of the sample was 10 *mm*. . 232

C.1 Specific heat of Nextel 312 fiber mat. . . . 235

C.2 Specific heat of Fecralloy NIT100S and NIT200S fiber mats. . . . 236

D.1 Radiation thermometer calibration against a blackbody. . . . 238

NOMENCLATURE

a_1	preexponential coefficient in the modified Arrhenius expression, $[\frac{m^3}{kmol\ s\ K}]$ (bimolecular) or $[\frac{m^6}{kmol^2\ s\ K}]$ (termolecular reaction)
a_2	temperature exponent in the modified Arrhenius expression, dimensionless
A	cross sectional heater area, $[m^2]$
c	speed of light, $[\frac{m}{s}]$
c_p	specific heat at constant pressure, $[\frac{J}{kg\ K}]$
C	cross section, $[m^{-2}]$
$\mathcal{E}$	activation energy, $[\frac{J}{kmol\ K}]$
d	fiber diameter, $[m]$
F_{i-j}	(diffuse) view factor from surface i to surface j, dimensionless
$\mathcal{F}$	radiative heat flux, $[\frac{W}{m^2}]$
FR	firing rate, $[\frac{W}{m^2}]$
h	surface heat transfer coefficient, $[\frac{W}{m^2\ K}]$ or specific enthalpy, $[\frac{J}{kg}]$
h_v	volumetric heat transfer coefficient, $[\frac{W}{m^3\ K}]$
I	radiation intensity, $[\frac{W}{m^2\ sr}]$
k	effective thermal conductivity, $[\frac{W}{m\ K}]$
k_f	forward rate coefficient
K	total number of species, dimensionless
L	characteristic length, $[m]$
m	complex index of refraction, dimensionless
$\dot{m}$	mass flow rate, $[\frac{kg}{s}]$

$\dot{m}''$	mass flux, $[\frac{kg}{m^2 s}]$
$\hat{n}$	unit normal, pointing away from surface and into the medium, dimensionless
N	order of the discrete ordinates approximation, dimensionless
Nu	Nusselt Number $= \frac{h\,L}{k}$, dimensionless
Nu_v	volumetric Nusselt Number $= \frac{h_v\,L^2}{k}$, dimensionless
NTU	number of transfer units $= \frac{h_v L}{\dot{m} c_{pg}}$, dimensionless
p	pressure, $[Pa]$
PPC	number of pores per centimeter
PPI	number of pores per inch
Pr	Prandtl Number $= \frac{\mu\,c_p}{k}$, dimensionless
q''	heat flux, $[\frac{W}{m^2}]$
$\mathcal{R}$	universal gas constant $= 8314.510(70)\frac{J}{kmol\ K}$
Re	Reynolds Number $= \frac{\rho\,L\,u}{\mu}$, dimensionless
s	geometric path length, $[m]$
$\hat{s}$	unit vector in a given direction, dimensionless
t	time, $[s]$
T	temperature, $[K]$
u	velocity of the fluid mixture, $[\frac{m}{s}]$
V	diffusion velocity, $[\frac{m}{s}]$
w_i	quadrature weights, dimensionless
W	molecular mass, $[\frac{kg}{kmol}]$
x	spatial coordinate, $[m]$
Y	mass fraction, dimensionless
z	mixture fraction $\equiv \frac{\text{mass of material having its origin in the fuel stream}}{\text{mass of mixture}}$, dimensionless

Greek symbols:

α	thermal diffusivity, $[\frac{m^2}{s}]$
β	extinction coefficient $= \kappa_a + \sigma_s$, $[m^{-1}]$
$\Delta\chi$	variation, uncertainty or error in variable χ
Δp	pressure drop, $[Pa]$
ε	total emittance, dimensionless
ζ	progress variable as defined in Equation 5.1, dimensionless
η	efficiency as defined in Equation 2.2 or Equation 2.3, dimensionless
κ_1	resistance coefficient in Equation 3.1, $[m^{-2}]$
κ_2	resistance coefficient in Equation 3.1, $[m^{-1}]$
κ_a	absorption coefficient, $[m^{-1}]$
λ	wavelength, $[\mu m]$
μ	dynamic viscosity, $[\frac{kg}{m\ s}]$,
	or direction cosine of polar angle, dimensionless
ν	kinematic viscosity, $[\frac{m^2}{s}]$
ξ	incident angle of radiation beam in Equations 4.6 and 4.7
ρ	mass density, $[\frac{kg}{m^3}]$
	or reflectance, dimensionless
σ	Stefan-Boltzmann constant $= 5.670 \times 10^{-8} \frac{W}{m^2}$
σ_s	scattering coefficient, $[m^{-1}]$
Φ	equivalence ratio, dimensionless,
	or scattering phase function, dimensionless,
ϕ	porosity, dimensionless
χ	mole fraction, dimensionless
ω	single scattering albedo $= \frac{\sigma_s}{\beta}$, dimensionless
$\dot{\omega}$	species volumetric production rate, $[\frac{kmol}{m^3\ s}]$

Subscripts:

0	(variable) evaluated at $x = 0$
1	left boundary of computational domain (node 1)
a	absorption
b	blackbody
$extn$	extinction
g	gas mixture
i	free index for radiation intensity directions
in	inlet conditions
j	dummy index for radiation intensity directions
k	kth species
L	left boundary of solid domain, or (variable) evaluated at $x = L$
out	outlet conditions
R	right boundary of solid domain
rad	due to radiation
s	solid, or scattering
$surf$	solid surface
$surr$	surroundings
tot	total
w	wall (boundary)

Superscripts:

$\bar{\chi}$	mean value of variable χ

ABSTRACT

Leonardi, Sergio, Ph.D., Purdue University, August, 2000. Partially-Premixed Combustion in Porous Radiant Burners. Major Professors: Dr. Raymond Viskanta and Dr. Jay P. Gore, School of Mechanical Engineering.

Inert porous radiant burners are commonly employed in materials processing and manufacturing (drying, cooking, etc.) In spite of this extensive use, little knowledge was available concerning the operating characteristics and flame structure of such burners until recently. The advent of a new generation of natural gas-fired burners that include an active matrix introduces further challenges and opens new areas of research. The first catalytic heaters were diffusion-type; recent attempts to improve performance suggest that higher firing rates and efficiency can be attained in a *partially-premixed* mode. Yet, the effects of the partially-premixed air on the catalytic combustion process have to be determined.

The objective of the present work is to investigate theoretically and experimentally the performance characteristics of premixed and partially-premixed inert porous burners. A one-dimensional model for solving the conservation equations inside a porous material, including the detailed chemical kinetics for methane-air mixtures, is developed by modifying an existing burner-stabilized flame computer program. The chemical reactions are modeled using the GRI-Mech 2.11 mechanism. An energy equation for the solid matrix is introduced to the original system. The convection heat transfer between the gas and solid phases is characterized by means of a volumetric heat transfer coefficient.

The results of the experimental and theoretical investigation on metal-fiber porous radiant burners are presented. The experimental burner consisted of a specially-designed multi-diffuser housing capable of producing a very uniform gas flow distribution. Commercial-grade methane is used to simulate the natural gas. Radiation efficiency, gas and solid temperatures, and pollutant emissions data are obtained at atmospheric pressure for firing rates that cover the industrial operation range of interest. Fuel rich equivalence ratios naturally lead to a partially-premixed flame. It was expected that fuel lean and stoichiometric conditions would yield a conventional premixed flame structure. However, the heat transfer to the solid matrix led to some degree of partially-premixed burning for these conditions as well.

An extensive parametric study is carried out to investigate the effects of several parameters on a model burner performance. Emphasis is placed on thermal performance and parameters such as temperature distributions, flame location, the radiation efficiency and pollutant emissions.

1. INTRODUCTION

1.1. Background

Humans have controlled fire for several hundred thousand years (Weinberg, 1975). The prehistoric source of fuel was almost exclusively biomass (plant material and animal waste) and the primary heat transfer mode to objects outside the fire was radiation. A long time after the early humans learned to use fire, devices for burning a given fuel evolved from the open flame into more elaborate and intricate designs, such as stoves and burners. In the 18th century, Benjamin Franklin invented the notorious "Franklin Stove", also called the "Pennsylvania Fireplace". This was a revolutionary heating unit that, unlike a fireplace, was designed to sit in the middle of a room and radiate heat. The heavy iron of the stove absorbed much of the fire's heat, keeping the room warm long after the fire had died down, and its higher radiation output was an improvement over previous stoves (Lyons, 1987). Radiation has been an important mode of heat transfer throughout the ages, and an understanding of radiant heat transfer has become increasingly important for modern day technology (Viskanta, 1998).

Radiant burners have many industrial applications: drying of paper, textiles and food products, powder coatings, glass annealing, tempering and decorating, paint finishing and curing, plastic forming and stretching, etc. (Eclipse Combustion, 1992). Other applications include porous media reactors for the destruction of volatile organic compounds, and cores of fire-in-tube heaters in boilers (Howell et al., 1996). Their widespread use is mainly due to the possibility of high heat fluxes and the inherent energy savings of avoiding the multiple step conversion (heat-electricity-heat) of the electrical counterparts. The efficiency of electric power generation (≈40% maximum) and the losses in the transmission lines (ohmic losses and corona discharge can account for about 10%, and they are strongly dependent on external factors like the weather) motivate the search for a source of thermal radiation from a natural gas conversion device. Nevertheless, low energy costs, severe pollution emission requirements, and a lack of reliable radiant gas-fired heaters with acceptable control characteristics are leading to the conversion of the radiant heating market in the manufacturing sector to electrical resistance heating.

Alternatively, combustion catalysis[1] presents some differences with homogeneous (flame) combustion, making it worthy of consideration. In the last decades catalytic combustion has been vigorously explored as a route of the production of heat and energy in view of its capability to achieve effective combustion at much lower temperatures than in conventional flame combustion, thus allowing for simultaneous ultra-low emissions of NO_x, CO and unburned hydrocarbons (HC). For example, homogeneous gas combustion has an ignition temperature of $615°C$ for methane, but catalytic combustion has a light-off temperature of below $400°C$ even though it depends on the type of catalysts and the reaction conditions employed (Seo et al., 1999).

Various concepts of catalytic combustion have been investigated by many researchers, and they can be classified into the following three groups (Forzatti and Groppi, 1998):

1. Adiabatic lean-premixed catalytic combustion, which has attracted attention for power generation in gas turbines.

2. Non-adiabatic premixed catalytic combustion for the production of heat which is currently still under development for several applications including domestic burners and compact chemical reactor heaters.

---

[1] Catalytic effects are not studied in this dissertation. However, some attention to them is given here in this introductory chapter, since the need for improvements of catalytic radiant burners provides the foundation for the need of studying partially-premixed flames in inert porous burners.

3. Non-adiabatic diffusive catalytic combustion that has been commercially applied in radiant heaters.

Gas-fired catalytic infrared heating systems (the last two groups) have several distinctive characteristics that make them very attractive for a wide array of industrial applications. These systems operate at a relatively low temperature. Lower temperatures lead to a higher radiation peak intensity at longer wavelengths, which coincide with absorption characteristics of load materials. Burners operating at higher temperatures emit a higher fraction of their energy at shorter wavelengths, but the peak intensity at shorter wavelengths may not be absorbed by the material because of its lower spectral absorptance. The emission of the radiating medium in a gas heater can be also tuned with coatings or embedded materials (Tong and Li, 1995).

High radiation efficiency is another appealing feature of the catalytic burners. Because of the above mentioned characteristics, there are energy savings, process efficiency and productivity increases of up to 80 percent that have been reported in the industrial literature when comparing a catalytic oven with their convective or electric counterparts (Catalytic Industrial Systems, 1996).

These efficient, flameless gas burners are ideal for some industrial processes such as powder coating, where ignition of the chemicals by an open flame constitutes a serious explosion hazard. Catalytic infrared heaters are the leading choice for heating in hazardous areas in the oil and gas production and exploration industries and petrochemical storage and distribution facilities (Cis-Can Industries Ltd., 1998). Moreover, other operations like the thermo-forming of plastics can take advantage of the clean (in which no combustion-generated deposits appear on product due to ultra-low emissions; Dogwiler et al., 1999) and low temperature (which reduces the risk of burns) catalytic combustion.

One of the main problems faced by the diffusion-type catalytic burner users is the relatively narrow firing-rate operation range. When increasing the fuel inflow beyond the (low) nominal range, the gas slippage becomes significant and this results in a drastic deterioration of the efficiency and greatly increased pollutant emissions.

This lack of flexibility in the operating conditions limits more extensive use of this technology.

Another limitation of catalytic heaters is the maximum firing rate attainable using the state-of-the-art technology, which is currently at about 80 $\frac{kW}{m^2}$. Beyond this value blow-off occurs. This restricts possible applications for these type of burners/heaters.

It has been suggested that the diffusion of air is the limiting factor that prevents operation of catalytic heaters at higher firing rates. When the gas flows through the catalytic pad at the high velocities necessary to achieve the desired (high) energy output, the oxidizer cannot diffuse from the surrounding atmosphere into the reaction zone. As a result, analysis of emissions shows a large concentration of unreacted fuel and hydrocarbons in the exhaust stream (Ruff, 1964).

One possible method to counteract the aforementioned effect is to inject limited amounts of air into the fuel stream that is less than the amount required to obtain a stoichiometric mixture. In this manner, the heater becomes *partially-premixed*, i.e., it depends on both sources of oxygen, part entering the burner with the fuel and part diffusing from the front. This has been suggested in a patent for an infrared catalytic burner by Hardison (1967), but theoretical and experimental studies of catalytic burners are practically non-existent and have been mostly performed by burner manufacturers, who are reluctant to reveal their findings.

Partially-premixed open flames offer a wide variety of advantages over typical premixed and non-premixed flames, and it is possible that porous burners will benefit from them too. Partially-premixed flames are much shorter than the usual non-premixed flames (Gore and Zhan, 1996), thus reducing the overall volume of the system. The shorter flame length is a result of the reduced diffusion mixing time which accompanies the partial premixing. Additionally, partially-premixed flames are more stable than ultra lean premixed flames and do not require a large premixing section, and the dangers of flashback and auto-ignition are eliminated if the fuel-rich premixed portion is kept outside the rich flammability limit of the fuel. Finally, partially-premixed flames exhibit very low or even no soot formation in comparison to non-premixed flames, but the reason for this is not yet fully understood (Chambrion et al., 1996; Alder, 1996). Soot formation is a function of the fuel composition and the operating conditions, and some measurements for ethylene show that initial addition of air to the fuel stream causes the overall soot emission to increase, meaning that addition of air can have adverse effects at high equivalence ratios on sooting behavior of partially premixed flames (Mitrovic and Lee, 1998). Low NO_x emissions are another of the possible advantages under investigation.

1.2. Description of Different Types of Radiant Burners

A porous radiant burner consists of a pervious solid matrix, a material capable of operating at high temperatures, through which flows a gaseous fuel undergoing an exothermic chemical reaction. If the injected gas stream contains an oxidizer in a stoichiometric or more-than-stoichiometric proportion, it is said to operate in a *premixed* mode. On the other hand, if the gas stream contains only fuel (100% methane, for example) and all the oxidizer necessary for the combustion diffuses from the downstream boundary, the burner is said to operate in a *diffusion* mode. Intermediate situations, in which less-than-stoichiometric amounts of oxidizer are injected with the fuel and the rest is allowed to diffuse into the reaction zone, are called *partially-premixed.*

According to a classification from a different point of view, a gas burner is said to operate in a *radiant mode* if the combustion occurs inside the material, the permeable medium is heated to incandescence and emits a large portion of the energy input in the form of thermal radiation. In this situation, the conversion of chemical energy into radiant energy is enhanced. The opposite situation is referred to as a *surface combustion mode*: flames hover above the surface and release the major part of the energy into the combustion products; in this case, the solid phase anchors the flame at the surface or just below the surface. Figure 1.1 illustrates the difference between these two conditions. Viskanta (1995) included a third group in this classification, the *heat recirculating burner*, in which the presence of the solid extends the flammability limit and reduces gas temperature and pollutant emissions.

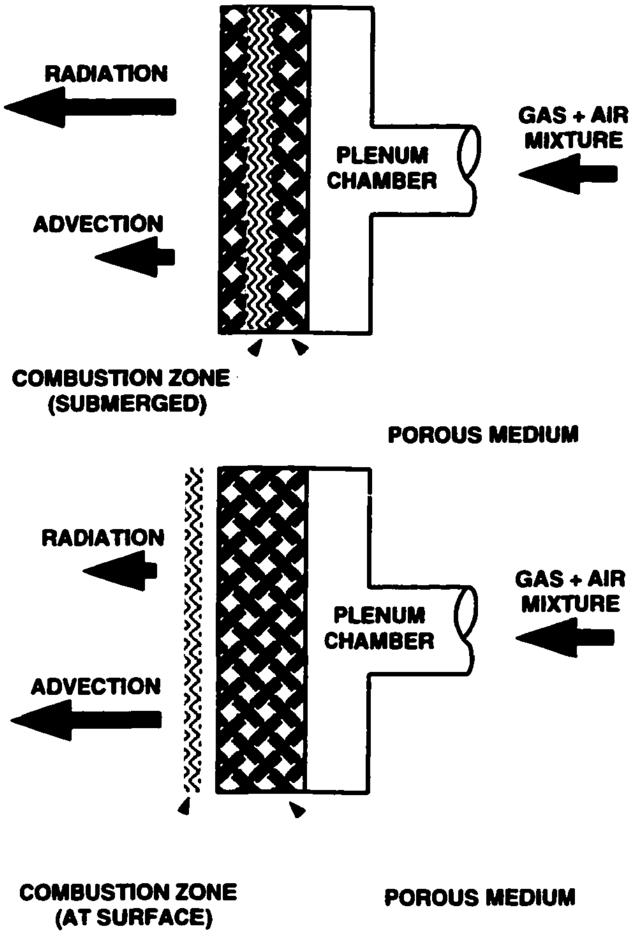

Figure 1.1. Schematic of two types of radiant porous burners: embedded or submerged flame (top); anchored surface flame (bottom).

Another pertinent classification corresponds to the possibility that the flame is opened (i.e., in contact with the heated load) or contained. In the first case, called *direct-fired* burner, the load is exposed to the combustion products. When the combustion zone is confined (usually inside a radiant tube) the burner is called *indirect-fired.* Figure 1.2 shows schematically the two configurations.

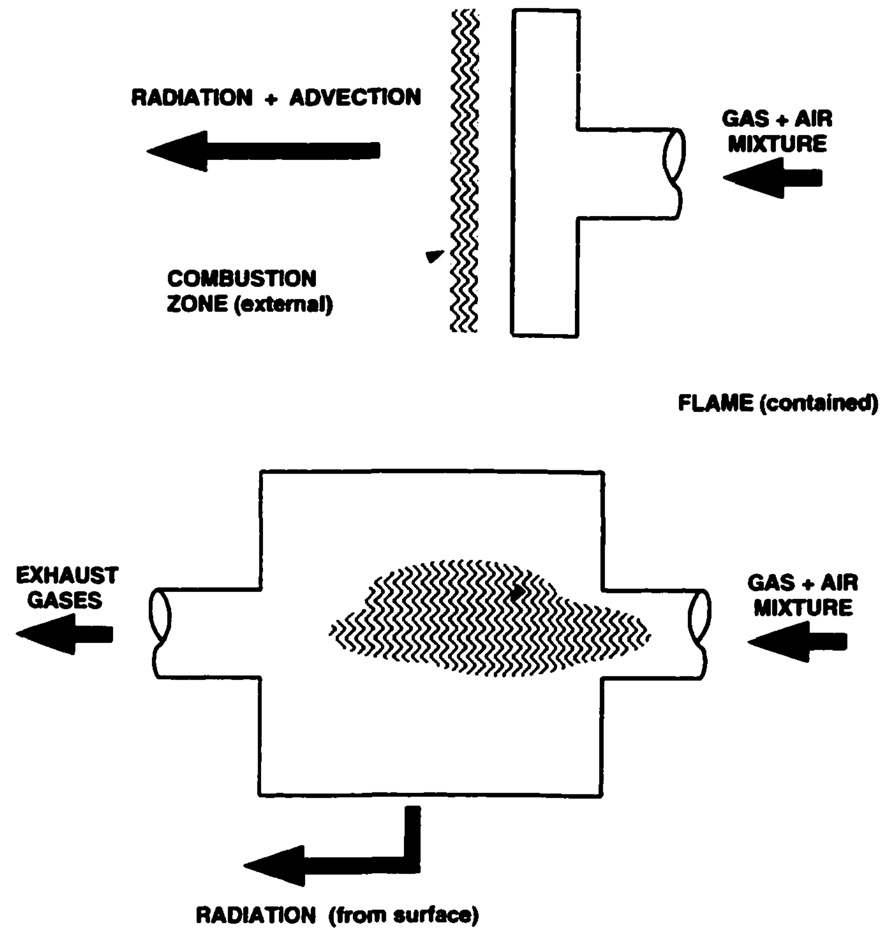

Figure 1.2. Schematic of two types of radiant burners: direct-fired (top); indirect-fired (bottom).

Among the direct-fired radiant burners, it is possible to distinguish between those in which the solid phase presents an array of perforations or ports that facilitate anchoring many flames (*ported burner*) and those in which the flammable mixture impinges on a solid matrix producing a single flame (Figure 1.3). A highly specific combination of material and configuration is normally required, and Cooper (1976) addressed this issue using pyramids machined on the surface of a ported burner, and identified optimal geometries and flame shapes.

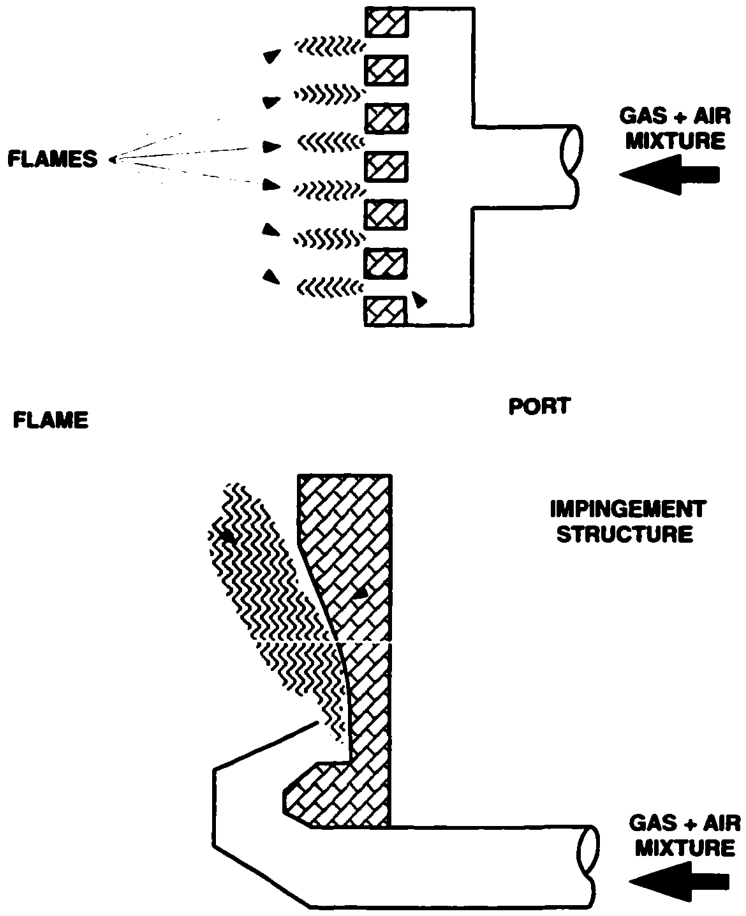

Figure 1.3. Schematic of two types of direct-fired radiant porous burners: ported or multi-flame (top); impingement (bottom).

Finally, another distinction can be made regarding the nature of the solid matrix. In an *inert* radiant burner, all chemical reactions are homogeneous, and the presence of the solid is relevant from the convection heat transfer point of view (and subsequent radiation.) A *catalytic* radiant burner has an active surface, on which heterogeneous chemical reactions take place, affecting significantly the kinetics of the combustion process.

1.3. Literature Review

1.3.1. Early Work on Porous Inert Radiant Burners

Porous inert radiant burners are being used industry for materials processing and manufacturing operations, but the scientific study of such burners has gained momentum only about three decades ago. Since then, various researchers have investigated mostly ceramic but also metal fiber radiant burners, both theoretically and experimentally. Models for premixed combustion within porous inert media are complicated by the highly non-linear radiative exchange in the solid matrix, in addition to the stiffness of the gas phase species conservation equations (Hsu and Matthews, 1993).

The first investigators that attempted the modeling for a porous burner were probably Kilham and Lanigan (1970), who developed a simple thermal model in a monolithic MoO_3 porous structure. They assumed that the gas and the solid were at different temperatures and they specified the convective heat transfer coefficient, but they did not account for radiation heat transfer or chemical reactions. A decade later, Echigo (1982) provided an early recognition of the ability of converting some of the enthalpy of a non-reacting hot gas to radiation from a porous material. He showed both analytically and experimentally that the radiation from a porous solid affected the temperature distribution of a hot gas flowing through that porous medium. His test section consisted of a 5 mm thick metal mesh screen placed in a $800°C$ air flow inside a circular duct. The temperature decrease along the duct was measured using screens of several different optical thicknesses, and the results were compared with the case with no screen. Temperatures at a location upstream the screen were as much as 60°C higher than those observed without a screen, indicating radiative feedback to the upstream gases. The feedback was stronger for thicker screens.

Some years later, Echigo et al. (1986) studied the extension of the lean flammability limit on an experimental porous burner that consisted of a ceramic plate encased in a permeable cylinder of stainless steel mesh.

In analytical work (Yoshizawa et al., 1988), using a single-step chemical reaction and a prescribed (assumed) flame location, showed that temperature profiles and burning velocities were highly dependent upon the optical properties of the porous matrix. Excess enthalpy flames (i.e., at temperatures in excess of the adiabatic flame temperature) were predicted due to the presence of the solid phase. According to their modeling, the single most important solid property governing the flame behavior was the absorption coefficient. In practice, the absorption coefficient can be increased by reducing the mean pore size of the matrix (Howell et al., 1996). Takeno and Moriyama (1986) used excess enthalpy theory along an extended reaction zone for a burner with an infinite heat transfer coefficient. Their model also incorporated the assumption of infinitely large thermal conductivity of the burner material, which could be interpreted as working against a narrowly restricted reaction zone of the type observed in metal fiber burners.

The excess enthalpy effect had been explained before by Weinberg (1971) as "borrowing" energy from a premixed flame in order to preheat the reactants; Takeno and Sato (1979) further elaborated on this topic of internal heat recirculation and preheating. The ability to extend the lean flammability limit and to achieve high reaction rates, leading to higher effective flame speeds than for open flames of similar composition, is mainly due to internal recirculation or recuperation of heat from the burned downstream region to the unburned mixture upstream of the reaction zone. The process also extends the flame stability range to burn otherwise non-flammable mixtures of low heat content. Hardesty and Weinberg (1974) showed theoretically that the flammability limits for a flame within a porous media is indeed beyond those of a conventional open flame. This idea created both interest and controversy (Fox, 1976; Hardesty and Weinberg, 1976). However, Howell et al. (1996) pointed out that while peak temperature can be higher than the adiabatic flame temperature, the exit temperature cannot, in agreement with the second law of thermodynamics.

A laminar premixed flame inside a honeycomb ceramic (cordierite of porosity 75%) was investigated experimentally and theoretically (Min and Shin, 1991) to provide the detailed data needed for computational approaches and to further the physical understanding of the mechanisms of heat transfer, particularly internal heat recirculation. The results showed that the ranges of flammability and flame stability were substantially extended without any external heating, when compared to the corresponding free flame. Two types of stable flames were observed, depending on the value of the equivalence ratio: one was nearly one-dimensional and the other was highly two-dimensional. Excess enthalpy flames were also reported in this case, but also the existence of the flame of low burning velocity and low temperature. Their analysis, based on a one-dimensional flame theory, reproduced reasonably well the experimental temperature profiles and flame behavior and revealed that heat was recirculated to the unburned mixture both by the conduction and the radiation of the solid phase. A stable flame was also predicted in the downstream region of the honeycomb ceramic, but was never observed in the experiments presumably due to the two-dimensional effects of heat losses. A later study regarding follow-up work confirmed photographically the presence of the downstream flame for $\Phi \approx 0.66$ (Lee et al., 1996).

Pioneer work in modeling a sintered metal fiber burner was done by Golombok et al. (1991). In addition to the highly refractory properties (i.e., ability to endure both the high temperatures and the thermal cycling associated with the burner operation), metal fibers have higher surface emittance than ceramic materials and are thus better radiant heaters (Golombok and Shirvill, 1990). Using 22 μm diameter Fecralloy fiber and a sample porosity of 80% (empirically determined to give close to optimum performance, according to what the authors claimed), they developed a one-dimensional model with single-step chemistry and obtained stable surface flames with firing rates in the range 100 to 700 $\frac{kW}{m^2}$. The main difference between their model and others consisted in the treatment of the effective solid thermal conductivity, resulting from the anisotropy of the fiber arrangement. Internal radiation was included by means of an enhanced conductivity, and the model equations were simplified using the method of activation energy asymptotics (i.e., the reduction of the burner to a sequence of boundary value problems). The reaction zone thickness and solid temperature were varied iteratively until the asymptotic boundary conditions at the exit were met. A similar study (Sathe et al., 1990b) modeled combustion in high-porosity isotropic burners made of alumina and silica, and the role of the thermal conductivity in controlling the flame speed and stability was emphasized. A subsequent study by Sathe et al. (1990a) identified an increase in thermal conductivity as a reason for an increase in the flame speed but leading to a net decrease in radiant efficiency due to a comparatively slow rise in radiant output. Because of this, Golombok et al. (1991) suggested that the relatively low effective conductivity of a metal fiber burner was of great interest in enhancing performance.

Another numerical study of the heat transfer characteristics of a porous radiant burner was performed by Tong and Sathe (1991), using a one-dimensional conduction, convection, and radiation model. The combustion phenomenon was modeled as spatially dependent heat generation, and non-local thermal equilibrium between the gas and solid phases was accounted for by using separate energy equations for the two phases. The solid matrix was assumed to emit, absorb, and scatter radiant energy, and the spherical harmonics approximation was used to solve the radiative transfer equation. They found that for a given rate of heat generation, large optical thicknesses and high volumetric heat transfer coefficients were desirable for maximizing radiant output. Furthermore, low solid thermal conductivities, scattering albedos and flow velocities, and high reflectivities produced the highest radiant output in their parametric calculations.

A different formulation for the heat transport in a fiber burner was developed by Andersen (1992). The model accounted for heat transfer by conduction in the fibers as well as in the gas, and the radiation inside the fibrous material was modeled by the two-flux formulation, i.e. isotropical scattering was not assumed. Conduction was not modeled, rather the solid conductivity was used in place of the effective property. but the main limitation was that a heat release function for the combustion inside the fibrous layer was used, instead of the one calculated from chemical kinetics. The reported predictions were only of a qualitative nature.

Hsu and Matthews (1993) first identified the necessity of using more realistic chemical kinetics. Prior researchers had simulated the gas-phase reactions using single-step chemistry (Echigo et al., 1986; Sathe et al., 1990b) or simulated the combustion process as a heat source (Andersen, 1992; Tong and Sathe, 1991), but Hsu and Matthews made predictions using both single-step and multi-step kinetics mechanisms. They concluded that it was essential to use multi-step kinetics if accurate predictions of the temperature distributions, energy release rates, total energy release, and composition profiles and emissions were sought. The authors showed that single-step kinetics was adequate for predicting all the flame characteristics except the pollutant emissions for the very lean conditions ($\Phi \approx 0.5$) under which equilibrium favors the more complete combustion process dictated by global chemistry. However, for higher equivalence ratios the errors were significant. For $\Phi = 1.0$, the error in the peak gas temperature could be several hundred of degrees. Hsu and Matthews (1993) modeled a 10.16 *cm* long partially-stabilized zirconia[2] cylinder, with 3.9 pores per cm, and they predicted for the first time NO and CO emissions for a porous inert burner, and then compared them with experimental data. The model estimated the CO emissions very accurately and predicted the NO trend correctly, but overestimated the NO emissions for $\Phi > 0.8$. The multi-step burner model did not accurately reproduce the data for the burning speed and NO emissions for non-dilute mixtures; the discrepancies could only be partially attributed to experimental uncertainties and/or imprecise knowledge of

---

[2] A ceramic foam with dodecahedral structure. A white crystalline compound, ZrO_2, used especially in refractories, in thermal and electric insulation, in abrasives, and in enamels and glazes - called also zirconium oxide.

the properties of the solid matrix. Thus, it was concluded that important aspects of the physical processes within porous burners were still not well simulated at the time.

An experimental and numerical investigation of premixed methane and air combustion within a non-homogeneous porous ceramic was carried out by Hsu et al. (1993a). Detailed chemical kinetics were utilized, with a 58-reaction mechanism involving 17 species, and a non-scattering gray medium with constant absorption coefficient was used for radiation heat transfer; however, the flame location was arbitrarily specified. The burner consisted of two porous ceramic cylinders of equal length and diameter that were stacked together and insulated around the circumference. Four series of experiments were performed to determine the lean limit using three different pore sizes in the downstream ceramic cylinder (10, 30, and 45 *PPI*), while the pore size in the upstream ceramic cylinder was maintained as a constant (65 *PPI*). The range of equivalence ratios used were $0.41 < \Phi \leq 0.68$ for the experiment and $0.43 < \Phi \leq 1.00$ for the simulations. The results demonstrated that porous ceramic burners provide a range of stable burning rates at a constant Φ and that the maximum flame speed inside the burners was much higher than the premixed, freely-burning adiabatic laminar flame speed. The lean limits in the porous burners were lower than that of the free flame. The numerical model in this study predicted with reasonable accuracy the combustion phenomena within the porous ceramics.

Another numerical investigation of premixed combustion within a highly porous inert medium was reported by Hsu et al. (1993b). They obtained results with a numerical model using detailed chemical kinetics and heat exchange between the flowing gas and the porous solid. The simulated burner was an 8 *cm* long partially-stabilized zirconia cylinder. An improved description of the thermophysical properties of the solid was used in the modeling, but the flame location was still arbitrarily prescribed. It was found that the preheating effect increased strongly with increasing convective heat transfer and with increasing effective thermal conductivity of the solid. The volumetric convective heat transfer was expected to increase with increasing number of cells per unit length of the porous matrix, but the absorption coefficient decreased with increasing cell size and decreasing cell density. Numerical simulations using baseline properties ($h_v = 10^7 \frac{W}{m^3K}$, $k_s = k_{air}$, $T_{surr} = 298K$) indicated that the lean limit can be extended to an equivalence ratio of about 0.36 for a methane-air flame. The peak flame temperature was generally higher than the adiabatic flame temperature, but not as high as it would have been predicted with single-step chemistry. The latter effect was more pronounced at lower equivalence ratios. The influence of the solid thermal conductivity, k_s, on the temperature distribution was found to be a weak one; however, the burning speed was affected by up to 20%.

1.3.2. Recent Studies on Porous Inert Radiant Burners

The global performance characteristics of reticulated ceramic burners were investigated by Mital (1996). He determined experimentally operating range, radiation efficiency, spectral intensity, exit gas temperature and velocity, and pollutant emissions. The results showed that submerged flame burners had 20 to 40% higher radiation efficiency than the available surface flame burners. For a fixed firing rate the efficiency increased with an increase in the equivalence ratio, and for a fixed equivalence ratio there was an optimum firing rate for maximum efficiency. The CO, NO_x and hydrocarbon emissions also increased with an increase in the equivalence ratio; NO_x emissions increased with increasing firing rate; however, beyond a certain firing rate the CO and HC emissions decreased. Flame structure measurements showed that, if the firing rate was increased above a certain level, the reaction zone moved upstream; this observation explained the importance of preheating as triggering factor for flashback at the higher firing rates. Mital also developed an effective thermal conductivity model (following the procedure of Vortmeyer and Schaefer, 1974) that predicted flame speed within 15% accuracy. He applied asymptotic analysis to gaseous and solid phase energy equations to predict the stability range and flame position within 20% and give a good qualitative match (within 25% of experimental data) for radiation efficiency.

Speyer et al. (1996) investigated experimentally the radiant efficiencies of four gas radiant burners using total and spectral radiation emission measurements as a function of the fuel-air mixture and combustion intensity. Ported ceramic tile and steel flame impingement plate burners, with oxidation-resistant downstream steel screens, showed the highest levels of efficiency (53.9% and 52.1%, respectively)[3]. A reticulated ceramic burner showed a moderate maximum efficiency (39.4%) (this is in agreement with the research of Mital, 1996), and a metal fiber burner was even lower at 28.4% (without a downstream screen). At combustion intensities above 250 $\frac{kW}{m^2}$, the efficiency of the impingement burner exceeded that of the ported ceramic, and was close to the theoretical maximum efficiency. Design of high-efficiency burners required a combustion product flow pattern around solid surfaces which caused extraction of sensible heat until gas and solid temperatures approached each other. Intense band emissions in spectral measurements of the metal fiber burner indicated a comparatively diminished convection heat transfer from combustion products to solid surfaces. A mixture preheated to 120°C resulted in approximately 3% increase in the value of radiation efficiency. NO_x emissions from reticulated ceramic burners increased with increasing firing rate, ranging from 16 to 38 PPM. But previous comparisons between ceramic burners and other combustion systems (Hulgaard and Damjohansen, 1992) had reported lower NO_x emissions.

A numerical study with special consideration of the pollutant emissions (Zhou and Pereira, 1997) of a porous burner concluded that NO and CO emissions depend mainly on the excess air ratio and firing rate. By assuming one-dimensional combustion and a 27-species, 73-reaction detailed mechanism of methane-air, they obtained results which show the effects of several parameters: excess air ratio, firing rate, solid conductivity and radiative heat transfer on the combustion and pollutants formation in inert non-homogeneous porous media. The peak flame temperature was reduced with the reduction of the solid conductivity resulting in a decrease of NO

---

[3] Note that these results seem to be higher than theoretically possible, maybe due to experimental errors, and they should probably be considered only qualitatively correct.

emissions. Zhou and Pereira concluded that NO emission could be decreased through the utilization of porous medium having a small solid conductivity. Radiative heat transfer was also significant for the combustion and heat transfer in porous media. The flame could be stabilized easily at the interface between two different porosity ceramic blocks due to the radiative heat feedback. Good agreement with experimental observations suggested that the numerical model was a useful tool to investigate combustion and pollutants formation in porous media as well as to achieve optimized porous combustion designs.

Two unsteady mathematical models of combustion and heat transfer within a submerged-flame porous radiant burner were developed and validated by Fu (1997). The first model was one-dimensional, and accounted for the interaction between convection, conduction, radiation and chemical reaction within a two-layer reticulated ceramic. The two flux approximation (Modest, 1993) was used to model the radiative heat transfer, and a single-step oxidation mechanism for methane was considered. The rate of fuel consumption was assumed to have the form suggested by Kuo (1986), and five chemical parameters (i.e., pre-exponential factor, activation energy, and exponents for the temperature and fuel and oxidizer concentrations) were either taken from the work of Westbrook and Dryer (1981) or adjusted to match the predicted species concentrations of Mital (1996). Fu tried to obtain a numerical solution of the model equations for a wide range of chemical parameters (pre-exponential factor and activation energy), but the resulting reaction zone was not stabilized within the support layer; either the combustion was extinguished or the flame was stabilized in the diffusion layer. Therefore, he assumed a top-hat (i.e., uniform) heat source equal in magnitude to the inlet firing rate, spread over a 2 mm thick region and located at an arbitrary position to match the experimental observations. Fu concluded that the thermal performance of a porous radiant burner was strongly dependent on the flame location, and an optimum distance from the downstream surface could be found to maximize the radiation efficiency. The radiation efficiency increased with increasing volumetric heat transfer coefficient, effective thermal conductivity of the solid matrix, equivalence ratio of the inlet mixture, and thickness of the support layer.

A two-dimensional model accounting for the transport of mass, momentum, energy, and species inside a cylindrical tube was also developed by Fu (1997). Local measurements in porous ceramics (Mital, 1996) had shown that pore-scale phenomena such as quenching of chemical reactions played a significant role in the physics of the system. Hence, Fu's goal was to provide fundamental understanding of the transport phenomena relevant to porous radiant burners, eliminating the uncertainty of a complex passage geometry that could not be described easily in mathematical terms. One-step global chemistry was used for methane oxidation, and the pre-exponential factor was adjusted so the flame location would match the experimental results of Min and Shin (1991). The results showed that the flame thickness in the tube was much broader than that of adiabatic combustion due to strong conduction and radiation feedback from the high temperature region to the preheat zone. The flame front was not plane (i.e., it was truly two-dimensional) because of the strong heat diffusion in the radial direction. Finally, he found that the variation of the radiation efficiency with any single parameter did not present a monotonic trend, which was attributed to the fact that one parameter affected the chemical heat release and all heat transfer modes.

Almost all radiant burner models used the one-dimensional flow and heat transfer assumption. But a two-dimensional model of two simple porous burner geometries was recently developed by Hackert et al. (1999) to analyze the influence of multi-dimensionality on flames within pore scale structures. The first of the geometries simulated a honeycomb burner, in which a ceramic was penetrated by many small, straight, non-connecting passages. The second geometry consisted of many small parallel plates aligned with the flow direction. The Monte Carlo method was employed to calculate the view factors for radiation heat exchange in the second geometry. This model compared well with experiments on burning rates, operating ranges, and radiation output. Heat losses from the burner were found to reduce the burning rate. The flame was shown to be highly two-dimensional, and limitations of one-dimensional models were discussed. The effects of the material properties on the peak burning rate in these model porous media were examined. The two-dimensional work of Hackert et al. (1999) is novel, but the trend in modeling (presently at least) seems to continue along the lines of the one-dimensional simulations, stressing the influence of chemistry and material properties.

A further simplification that is common to virtually all modeling efforts is to consider that the gas flow as laminar and radiatively non-participating. A recent literature overview of radiative and convective heat transfer in high temperature gas flows with primary thrust on its fundamentals (Viskanta, 1998) discussed the complex phenomena involving, not only spectrally selective radiative transfer in common gases, but also turbulent chemically reacting flows. The infrared radiation gas property models and methods for solving the radiative transfer equation were highlighted. Convective and radiative heat transfer in channels and chemically reacting high temperature hows were reviewed. The nonlinear effects of turbulent fluctuations in radiative transfer, and the influence of radiation on thermal turbulence spectra were also considered. Critical issues which need to be addressed for a more complete understanding of the processes were raised, and topics requiring research attention were identified, with their relation to current technological applications.

As a final remark, it is necessary to point out that good understanding of the physical phenomena governing porous radiant burners –allowing the design of devices with customized performance– will greatly simplify the construction and subsequent use of radiant furnaces. A strongly-coupled problem arises due to the combined convective, conductive, and radiative heat transfer during heating of a load in an industrial radiant oven (Fedorov et al., 1998), and heater characteristics play a fundamental role.

1.3.3. Catalytic Radiant Burners/Heaters

There has been not nearly as much research focus to understand the mechanisms that govern the behavior of a catalytic burners as compared to inert burners. The Ninth Symposium on Combustion (1963) contained no catalytic combustion papers, and by the Twenty-Third Symposium in the series, which was held in France (1991) there were just two. However, renewed industrial interest in low temperature and low pollutant emission radiant burners has inspired recently efforts in finding new suitable catalysts. In addition, the advent of more powerful computers that can handle the complex chemical mechanisms has furthered research on the problem also from the computational point of view.

The first diffusive catalytic combustion device may have been developed in France in 1916 as an engine warmer for airplanes, and currently catalytic heaters fueled by LPG are common worldwide (Sadamori, 1999). However, the burners fueled by natural gas (mainly methane) showed not only low combustion efficiency but also quick deterioration (Radcliffe and Hickman, 1975). In another report, pessimistic perspectives on the development of natural gas diffusive catalytic burners were published based on the reaction mechanism of methane in the burner (Dongworth and Melvin, 1976).

Subsequently, with the advent of porous materials made of alumina fibers coated with catalysts, which provided a large surface area concentration, the combustion performance of natural gas improved drastically. The large number of available active sites and a greatly increased uniformity allowed natural gas to compete with LPG on a more favorable basis (Sadamori, 1999).

Traditionally, the active ingredient of a catalytic burner was either platinum or palladium (Lee and Trimm, 1995). These precious metals were first identified to offer good selectivity for the catalytic combustion as no other products than carbon dioxide and water are formed. Several authors have reported that supported palladium catalysts show the highest activity (Anderson et al., 1961; Rudham and Sanders, 1972; Golodets, 1983), but little was known about its kinetics parameters. Often inaccurate values for activation energy were used, until van Giezen et al. (1999) measured them using truly differential conditions (micro-flow reactor and special attention paid to inhibition by water.)

Trimm and Lam (1980a) performed detailed studies on the kinetics of methane oxidation over a platinum-impregnated porous alumina catalytic medium, and then a numerical analysis of a burner with a one-dimensional flow model (Trimm and Lam, 1980b), but they failed to address the issue of reaction completeness and fuel slippage. More recently, Kang et al. (1994) studied experimentally the performance and durability of burners using alumina fiber mats coated with metals of the platinum group, and Sadamori (1999) concluded that future progress of the concept of a diffusion-type burner fueled by natural gas would be limited unless a much more efficient catalyst is developed.

Much work has been done recently regarding the search of a new efficient and durable catalyst. The use of a single chemical element as a catalyst has not produced satisfactory results, mainly because conventional noble-metal catalysts may become deactivated and/or poisoned in the presence of sulfur, halogens, phosphorus arsenic and some metals (Ryu et al., 1999).

Among the noble metal catalysts, palladium was early recognized as the most active catalyst for methane combustion (Anderson et al., 1961), but the sulfur content of natural gas (mercaptan used as odorant) caused premature deactivation (Hoyos et al., 1993). More recently, Arcoya et al. (1991) reported that the sulfur resistance of the Group 8-10 metal catalysts increased in the following order: Pt, Pd, Ni, Rh, Ru; and catalyst life decreased in the order Rh, Ru, Pd, Ni, Pt. Very recently, Ryu et al. (1999) determined that the addition of Rh did not noticeably improve the activity of the Pd compounds; on the other hand, addition of Ru enhanced the H_2S poison resistance without negative effects on the overall catalytic activity. They suggested that Ru metal blocked the accessibility of the poison to the Pd sites and concluded that the Pd/Ru bimetallic mixture was a good alternative to replace the more expensive Rh.

Noble metal foils have been use to promote catalytic oxidation of methane. A recent paper (Veser et al., 1999) compared ignition temperature and activity for platinum, palladium, rhodium and iridium, over the entire range of fuel-to-air ratios. While Pd showed the widest range of surface flammability (i.e., activity), Pt ignition temperatures were the lowest. Surface ignition temperatures were found to increase with an increasing metal-oxygen bond in the order Pt<Pd<Rh<Ir; the temperature generally decreased with increasing fuel-to-air ratio due to site competition between oxygen and hydrocarbon and the higher sticking probability of oxygen.

Another alternative being considered is the use of palladium catalyst supported on alumina-based transition metal oxides (copper, chromium, cobalt, iron, manganese and nickel). Widjaja et al. (1999) investigated the low-temperature catalytic combustion of methane. They founded that the catalytic activity was strongly dependent on the composition of the support material and that Pd/Al_2O_3–36NiO demonstrated excellent activity due to the small size of the palladium particles. They suggested that the stability of the active palladium species, PdO, at high temperatures is likely to correspond to an increase of the activity.

Alternatively, the alumina support could be replaced by zirconia (Muller et al., 1999). In this case, particle size was also identified as a significant parameter. The authors proposed a red-ox mechanism to model the catalytic reaction: CO_2 and H_2O were produced via a reaction of methane with oxidized catalysts, and then the re-oxidation of the resulting palladium with oxygen followed. The structural changes induced upon reduction were accompanied by altered physico-chemical and diminished activity.

Among a myriad of other possible catalysts currently under investigation for the combustion of methane, a few can be mentioned here. Artizzu et al. (1999) used copper oxide deposited onto high surface area magnesium aluminate. They observed good activity and no CO emission at the laboratory scale for a 1 vol% mixture of combustible gas and 10 vol% oxygen in nitrogen. Hoyle et al. (1999) reported combustion over polycrystalline powdered silica-supported catalysts containing platinum and other oxide promoters (like MnO_2). A series of chromium-based catalysts ($LaCrO_3$ and Cr_2O_3) over $LaAl_{11}O_{18}$ and alumina were applied to cordierite[4] were investigated by Zwinkels et al. (1999); they identified solid-state reactions between the active phase and the support, and suggested the passivation of the support surface (by thermal treatment) to achieve higher stability under combustion conditions. Lyubovsky and Pfefferle (1999) studied experimentally the influence of the reaction parameters on palladium activity using a zero-porosity alumina plate as support for the catalyst to minimize the aforementioned interaction, finding the reduced Pd to be more active than the oxidized form (PdO).

Hexaaluminates and hexaaluminate-supported palladium catalysts have been reported to have high activity for methane combustion and promising thermal stability (Machida et al., 1989; Machida et al., 1990; Groppi et al., 1993); Ba-Mn and Sr-La-Mn hexaaluminates were the most thermally stable and active in those studies. Jang et al. (1999) compared several methods of obtaining the catalysts, some of which were so complicated that were considered not commercially practical. Notoriously, the methane oxidation activities of La-Mn hexaaluminate with and without Pd substitution were comparable, but the stability of the former was poor, dropping from 93% to only 59% after a 100 hour test (at $525°C$).

Transition metal-based perovskites[5] have been shown over the last 15 years to be highly active for methane combustion (Arai et al., 1986; McCarty and Wise, 1990; Seiyama, 1992). Their low cost and potentially good resistance to sulfur made them an attractive option to the expensive platinum, with the additional benefit of the promotion of deep methane oxidation, i.e., no carbon monoxide formation, even in rich mixtures (Klvana et al., 1999).

A promising fully-premixed catalytic burner using Pd/NiO was tested by Seo et al. (1999). The catalyst was deposited on an alumina honeycomb structure of 400 cells

---

[4] From Pierre L. A. Cordier (died 1861) French geologist. A blue mineral of vitreous luster and strong dichroism that consists of a silicate of aluminum, iron, and magnesium

[5] From Count L. A. Perovskii (died 1856) Russian statesman. A yellow, brown, or grayish black mineral sometimes containing rare earth elements

per square inch. They observed that the temperature of the catalyst layer rose rapidly near the inlet and then slowly decreased. The maximum temperature increased with increasing excess air, and its position moved toward the exit. Two flame patterns occurred: the reaction was completed within the catalyst layer between stoichiometric and 50% excess air; flame combustion took place for excess air ranging from 75 to 100%. Catalytic combustion markedly depended on the active layer thickness, and stable burning was found for a 30 *mm* thick catalyst for firing rates between 80 and 160 $\frac{kW}{m^2}$ and excess air between 25 and 75%.

Another possible application of the surface reaction technology is the conversion of a conventional gas burner into a catalytic one. The addition of an oxidizing catalyst to an inert radiant burner might be able to increase its operating range and stability. Beneficial surface reactions can be encouraged by coating part of the flame support layer with a suitable catalyst, thereby anchoring the flame in a position that optimizes the system performance. Kendall et al. (1992) conducted a preliminary experimental investigation on partially-catalytic burners (where both homogeneous and heterogeneous reactions coexist) that showed increased radiant efficiency and reduced pollutant emissions than for similar but inert radiant burners. They applied a dilute solution of hydrogen hexachloroplatinate (H_2PtCl_6) on the surface of a ceramic burner; radiant output increased and NO and CO emissions decreased.

Rumminger et al. (1999) modeled a partially-catalytic burner using detailed chemical kinetics. They used a reduced gas phase mechanism with 19 species for methane combustion (Kazakov and Frenklach, 1998) that was accurate to predict flame structure when the nitrous oxides were not significant. Surface chemistry was implemented with Surface CHEMKIN subroutines (Coltrin et al., 1990). They assumed that the catalyst was evenly distributed and that no deactivation (sintering or poisoning) occurred. Additionally, they considered that the mixing of the gas phase was such that the system was not mass-transfer limited; therefore, no solution of a mass diffusion equation was needed. Their results showed that radiant efficiency gains were obtained when the catalyst was placed on the downstream edge of the porous slab and that only a thin layer of catalyst was required for efficiency improvements of up to 10%.

1.3.4. Partially-Premixed Flames

The term "partially-premixed flame" can be applied to describe a wide variety of situations in which fuel and oxidizer are mixed in less-than-stoichiometric proportions. Among those are counterflow diffusion flames, coflow jet flames, lifted jet diffusion flames, and flames involving liquid fuel droplets and sprays. All the aforementioned situations share the common feature of having some oxidizer mixed at the molecular level with the fuel before it enters the reaction zone to undergo combustion. While diffusion flames and fully-premixed flames are relatively widely studied and well understood, partially-premixed flame knowledge is still in its early stages of development (Sun, 1997).

One of the pioneering studies on partially-premixed combustion was performed by Libby and Economos (1963). A hydrogen-oxygen mixture was injected in a laminar boundary layer through a porous plate. A two-zone model (unreacted and product equilibrium zones) together with single-step chemical reaction and large activation energy assumptions, were used to compare a diffusion flame ($\Phi = \infty$) and a partially-premixed one ($\Phi = 8$). The partially-premixed temperature profiles were wider and slightly higher than in the purely diffusion case, and in both cases the reaction zone broadened with increasing injection flow rates. Several years later Peters (1976) reached similar conclusions using asymptotic analysis techniques to solve for the temperatures on both sides of the equilibrium flame zone. The reaction zone can be idealized as a two-dimensional equilibrium region, bounded by two non-equilibrium layers of negligible thickness that ensure the transition to the outer equilibrium zones (Peters, 1979).

Yamaoka and Tsuji (1975) used the outer surface of a porous cylinder to stabilize a methane-air partially-premixed flame. A lateral, low-turbulence (secondary) air flow was present to provide enough oxidizer for complete combustion. Equivalence ratios between 1.5 and 3.0 for a constant flow rate were studied. and appearance of the flame. its location. temperature and major species profiles were examined for atmospheric pressure conditions. A double structure (an inner, rich premixed flame. surrounded by a diffusion-controlled outer flame) was observed for the lower Φ. The distance between the two flames decreased and the temperature profile became thinner with increasing Φ. Stable species concentrations were measured and it was observed a non-zero O_2 concentration throughout the field. A further study showed that the reaction rate profiles for $\Phi = 3$ did not differ much of those of a diffusion flame (Yamaoka and Tsuji, 1976). For mixtures inside the flammability limit ($1.6 < \Phi < 2.7$) the inner premixed methane flame supplied hot fuel (CO and H_2) to the outer diffusion flame. Outside the flammability limit, when a double flame was present, the two fronts were close and coupled; the inner flame was not self-sustaining (Yamaoka and Tsuji, 1977).

Stability analysis of a non-premixed flame concepts were applied to find the extinction characteristics of a local partially-premixed flame by Peters (1984), assuming a single-step irreversible chemical reaction. Diffusion flamelets were found to be independent of the variation of the mixture fraction for certain conditions. A numerical calculation showed that partial premixing made the flamelets more susceptible to stretching, and their quenching (due to merge into the diffusion flame layer) appeared to be the relevant stabilization mechanism for jet flames.

Seshadri et al. (1985) continued the study of extinction experimentally with flat, partially-premixed flames stabilized in an opposed-flow methane burner. The composition of the streams was such that the overall fuel-to-oxidizer ratio was equivalent as in the corresponding purely diffusion flame. The results showed that partial premixing increased the sensitivity to flamelet stretch, in agreement with Peters (1984). The extinction criterion for counterflow partially-premixed flames was investigated also by Hamins et al. (1985). Based on previous experimental evidence of a double flame, they showed theoretically that the two flame fronts must merge together before extinction. However, Law et al. (1989) later demonstrated that this is not necessarily the case.

An analytical and experimental study of counterflow premixed and non-premixed flames showed that the separation between the double flame fronts decreased with increasing flow rates (Law et al., 1989). Furthermore, the flame zones were almost together prior to extinction. An interesting finding was that the maximum temperature of the diffusion flame was independent of the mass flow rate, but the temperature of the premixed front increased with the flow rate, because of the reduced separation between the flames. This finding verified the previous results of Yamaoka and Tsuji (1975). Law et al. (1989) demonstrated the great complexity and subtlety of the flame behavior in realistic partially-premixed gaseous mixtures. They suggested that further effort was needed for the modeling of more complex problems, such as turbulent flames.

Further information regarding gas temperature and species concentrations was obtained by Araki et al. (1990), when they examined and demonstrated the practicality of using coherent anti-Stokes Raman spectroscopy (CARS) to obtain data on the structure of partially-premixed flames. Later Makino et al. (1991) used CARS to study the blow-off limit of rich fuel-air flames established in the forward stagnation region of a porous cylinder from which premixed methane and air were ejected into a uniform air stream. They studied counterflow rich flames, and showed that the blow-off limit was governed by two different phenomena depending on the equivalence ratio: for $\Phi \leq 1.3$ it was due to a decrease in the maximum temperature; for higher equivalence ratios ($1.6 \leq \Phi \leq 3.0$), it was controlled by the system heat loss.

A numerical simulation based on asymptotic analysis was carried out by Bui-Pham et al. (1992). They used a four-step mechanism to model the kinetics of lean and rich flames without additional air to complete combustion. They divided the flame into four regions: a preheat zone, an inner layer where the fuel is completely consumed, an H_2 oxidation layer characterized by the burning of the intermediate hydrogen, and a CO-oxidation layer. The results showed that the inner layer became thinner when increasing the equivalence ratio (the studied range was from $\Phi = 0.5$ to $\Phi = 1.4$), but the H_2 and CO oxidation layers increased the flame thickness. Interestingly, they found that the O_2 concentration in the burnt gases mixture was effectively reduced to zero after the equivalence ratio was increased beyond $\Phi = 1.1$.

The relative structural sensitivity of partially-premixed counterflow flames for methane fuel was investigated by Tanoff et al. (1996). They tracked the local species concentrations (i.e., the structure) of the flame experimentally and theoretically, showing that small perturbations in the amount of premixing may result in large changes in the overall behavior. For instance, the flames were observed to change drastically in structure and character as the fuel stream equivalence ratio was perturbed slightly below $\Phi \approx 1.4$, from a single, merged flame in the vicinity of the stagnation plane to a double flame consisting of a premixed-type, fuel-side flame and a stagnation-region diffusion flame. Accordingly, the mode and amount of NO_x formation changed severely. This duality in flame structure was further discerned by monitoring the relative locations of CH and OH profiles, as these were considered as indicators of specific flame chemistry. The exact value of the "changeover" equivalence ratio depends upon the flame strain rate and, in fact, flames close enough to extinction remained as a merged flame structure even at the lowest equivalence ratio. The maximum fuel-side velocity gradient was shown to be an extremely sensitive and sharp indicator of flame character, being completely insensitive to fuel-stream equivalence ratio above certain strain-dependent values, but varying sharply with equivalence ratio below these values. Other parameters, such as the width of the temperature or product species profiles, were shown to be indicators of flame structure, also, but were not nearly as sharply responsive as the fuel-side velocity gradient. Tanoff et al. (1996) suggested that these results could have important implications for design criteria of commercial burners, as well as for applications to the prediction of turbulent flame structure, including suppression and extinction.

Laminar partially-premixed methane-air jets surrounded by an outer coflow air stream (over-ventilating) were studied by Zhan (1994) and Gore and Zhan (1996).

They measured visible flame heights, global radiative heat loss fractions, distributions of mole fractions of stable gas species, and pollutant emission indices while burning various fuel-rich mixtures. They obtained major species data (the mole fraction profiles of CO_2, CO, H_2, O_2, N_2, CH_4, C_2H_4 and C_2H_2), using sampling and gas chromatography, at several radial locations at three different heights above the fuel tube for a fixed fuel flow rate and six different fuel tube equivalence ratios. The mole fractions of H_2O were inferred from the dry-based measurements. They reported the following effects when increasing the levels of partial premixing: 1) the flame height and luminous sooting decreased dramatically, and the overall flame color changed from yellow to blue; 2) the radiative heat loss fraction first decreased and then reached a constant value; 3) the mole fractions of CO decreased and those of CO_2 and H_2O increased in the lean parts of the flame; the mole fractions of C_2H_2 decreased and those of C_2H_4 first increased and then decreased in the rich parts of the flame; 4) the mole fractions of CO and H_2 first decreased slightly and then increased in the rich parts of the flame; and 5) the O_2 mole fractions at the point of negligible fuel mole fraction decreased. A moderate level of partial premixing ($\infty > \Phi > 5.0$) resulted in a modified diffusion flame structure; at $\Phi = 3.5$, the methane was consumed within rich mixtures before reaching the stoichiometric zone, and at $\Phi = 2.0$ the fuel was fully consumed in very rich zones coinciding with the CO and H_2 peaks. They also reported that the emission indices for NO, NO_x, CO and HC showed that an optimum level of partial premixing exists for a fixed fuel flow rate and overall equivalence ratio.

Similar results regarding the flame height reduction with air premixing were observed by other researchers (Kim et al., 1995). NO formation in laminar partially-premixed ethane-air flames was investigated as a function of the amount of air introduced into the central fuel tube of an annular coflow burner. Flames with an overall equivalence ratio of 0.5 and fuel-tube equivalence ratios varying from 1.1 up to 10 were measured for a fixed fuel flow rate. Local NO number densities data were obtained as a function of both radial position and height above the burner. An intermediate dual-flame pattern was identified which minimizes the NO emission index, and NO production was found to occur primarily between an inner premixed and an outer non-premixed flame front, which constitutes the dual-flame structure. These results suggested that the optimum burner-tube equivalence ratio occurred because of a compromise between prompt and thermal formation of NO in the predominantly premixed and non-premixed flame regions, respectively.

Heberle et al. (1995) observed that when increasing the amount of air premixing in a laminar methane-air flame, the concentration of OH radicals also increased, which suggested that more premixed flames exhibited faster reaction kinetics. Most of this OH radical increase was attributed to an inner rich premixed cone, since the OH concentration in the outer diffusion region did not vary much with Φ. Nguyen et al. (1996) studied a laminar methane-air Bunsen flame and obtained axial and radial profiles of temperature, major species, OH and NO. They found that the peak centerline OH concentration for a $\Phi = 1.70$ flame was higher than the corresponding to $\Phi = 1.52$ and $\Phi = 1.38$, contradicting the findings of Heberle et al. (1995). Nguyen et al. (1996) measurements indicated that the inner unburned fuel-air mixture experienced significant preheating as it traveled up into the conical flame zone surrounding it. Consequently, the centerline axial temperatures were typically 100–150K higher than predicted by adiabatic equilibrium for reactants at an initial temperature of 300K. They also used a one-dimensional premixed laminar flame model incorporating finite-rate chemistry, which satisfactorily predicted properties such as the temperature, CO, OH, and NO concentrations at the inner flame.

An extension of Zhan's (1994) work was conducted by Ramakrishna et al. (1996). They found higher flame peak temperatures and wider reaction zones when more air was added to the fuel stream. Using identical flames and absorption spectroscopy, Blevins and Gore (1996) discovered that the overall CH radical concentrations increased with increasing air premixing (changing from $\Phi = 3.5$ to $\Phi = 2.0$). These CH radicals were believed to be a major contributor to NO_x production. Later, Blevins and Gore (1999) used a numerical simulation to investigate the NO formation in partially-premixed counterflow burner. They reported that, for $\Phi > 2.5$, the flame structure could be described as a methane-air premixed flame merged with a CO-H_2-air non-premixed flame. When $\Phi < 2.5$, the two flame zones existed on opposite sides of the stagnation plane, and the CO-H_2-air non-premixed flame was characterized by hydrocarbon concentration peaks on its fuel-side edge. Also, broad NO destruction regions, caused primarily by CH_i + NO reactions, existed between the resulting double hydrocarbon concentration peaks. The fuel-side equivalence ratio was identified as the most important indicator of how rapidly NO was destroyed relative to how rapidly it was formed, and NO destruction reactions were more important in pure diffusion flames than in partially-premixed flames for the low strain rate computations.

In addition to the double-flame structure characteristic of partially-premixed combustion (reported in numerous papers, for instance, Yamaoka and Tsuji, 1975; Hamins et al., 1985; Law et al., 1989; Nishioka et al., 1994), the presence of three distinct reaction layers was noted in a recent article by Libby (1998). By means of an asymptotic analysis of laminar flames in opposed streams (under the circumstances of fast chemistry and/or low rates of strain and of high Reynolds numbers), Libby predicted two premixed and one non-premixed flames, the latter centered on the stagnation plane. These layers separated inviscid, chemically inert regions with constant gas properties. The state variables in each region were determined by the reactants exiting from each jet. If the location of the two premixed reaction layers was known, the velocity distributions in the four regions could be readily calculated. Comparison of the asymptotic analysis was made with a large scale computation of triple flames, and agreement with the distributions of the velocity components was satisfactory; however, as a consequence of the idealized chemistry assumed, the temperature distributions in the two high temperature regions were only roughly correct. The analysis showed that the changes in jet velocities and equivalence ratio of the fuel-rich reactant stream influence the most the location of the premixed reaction layers and the velocity distributions.

Partially-premixed flames stabilized on a burner were investigated by Vanoostendorp et al. (1991). They used laser-induced fluorescence imaging of CO and OH to study the influence of ambient air entrainment. Later, Gollahalli and Subba (1997) conducted an experimental study of the effects of using a triangular port (instead of the standard circular ports) in a laminar partially-premixed natural gas burner. Their results showed that the triangular ports increased air entrainment by 30%, decreased nitrogen oxides emission by less than 15%, and increased carbon monoxide emission by 20%. The effects were explained in terms of the changes in the flow structure and instabilities caused by the non-circular geometry and sharp corners of the burner exit port.

To the knowledge of the author, there are no studies of partially-premixed combustion within porous media or, in other words, research on coupled heat transfer in porous materials using fuel-rich flames. Partially-premixed flames are usually investigated as a modification of a purely diffusion flame, in an attempt to improve some of their characteristics (stability, pollutant emissions, etc.) On the other hand, the study of combustion within porous inert materials has, until now, exclusively dealt with fully-premixed (stoichiometric) or fuel-lean (i.e., some excess air premixed with the fuel at the inlet) gas mixtures. There is an open research opportunity where these two areas meet.

1.4. Objectives and Scope of Study

1.4.1. Motivation

Porous radiant burners have been extensively studied in the past, and current interest in the topic to enhance performance for some specific applications has resulted in two modifications to their design: 1) active (catalytic) porous matrix, and 2) injection of some oxidizer into the fuel stream to operate in a partially-premixed mode.

Chemists have used catalysts to enable a chemical reaction to proceed at a faster rate or under different conditions (usually lower temperature) than otherwise possible. Identical purpose is intended in the case of fuel oxidation in a burner.

On the other hand, it has been observed that the characteristics of a diffusion flame are altered substantially when some air is added to the fuel. A similar phenomenon is suspected to occur in a porous burner when operated in a partially-premixed mode.

However, there is little available information regarding the interaction between these two modifications in the burner design and operation, specifically when trying to account for the effects of each separate change in the output of the burner/heater, on efficiency and pollutant emissions. These are the factors that determine the selection of the given burner for a specific industrial application. In addition, flame structure characteristics are needed to gain a better understanding of the physico-chemical phenomena in porous radiant burners operating in partially-premixed mode, and they are unknown at present time.

1.4.2. Specific Objectives

The objective of this study is the theoretical and experimental investigation of laminar, partially-premixed flames inside inert porous media, without considering catalytic effects.

The experimental investigation (Chapter 2) has two main components. The first one is to obtain global flame structure measurements with standardized instrumentation and techniques. A specially designed burner/heater is used for that purpose. The objective is to measure the radiation efficiency, gas exhaust and surface solid temperatures, and pollutant emissions for the purpose of validating the numerical model. The burner/heater is described in Chapter 2. Additionally, the volumetric heat transfer coefficient of several fibrous (porous) materials is measured using a single-blow technique (Appendix B). This parameter is required for the purpose of correctly modeling the convective heat transfer between the gas stream and the solid matrix.

The numerical solution of a one-dimensional reacting flow inside a porous material, using detailed chemistry and finite-rate kinetics, is performed with a modified version of the PREMIX code. Details of the code structure, modifications and present work are included in Chapter 3. Radiation heat transfer within the porous matrix (considered gray) is modeled using the discrete ordinates method, which can be easily carried out to arbitrary order and accuracy. The relevant thermophysical and optical properties needed for the modeling are obtained either from the manufacturer (e.g., thermal conductivity), measured (e.g., specific heat) or estimated (e.g., extinction coefficient).

The experimental results obtained with a prototype metal fiber burner (exhaust gases and solid matrix surface temperatures, radiation efficiency, pollutant emissions) are compared with the results of the numerical simulations (Chapter 4) to assess the usefulness of the model.

A parametric study is included in Chapter 5, to evaluate the benefits of changing the operating conditions (firing rate, inlet equivalence ratio, etc.) on the overall performance. In addition, the effects of the relevant material properties is analyzed, with the double purpose of assessing the dependence of the solution on the uncertainties in those parameters (sensitivity analysis), and also the possibility of enhancing the performance by fine-tuning the solid matrix characteristics (thermal conductivity, emittance, etc.)

Finally, the conclusions and recommendations for future work are summarized in Chapter 6.

2. EXPERIMENTS

2.1. Introduction

The objective of this chapter is to describe the experimental setup and the procedure necessary for characterizing the combustion and thermal performance of a porous radiant burner/heater prototype. The data are required for comparison to the numerical predictions and, therefore, validation of the model to be developed (Chapter 3). Probing of the thin porous matrix for the flame structure is exceedingly complex; therefore, standardized instrumentation and techniques are used to measure radiant flux (and obtain multi-point radiant efficiency), solid surface temperature, gas spectral radiation intensity (to obtain the exit gas temperature), and pollutant emissions (CO, NO_x, unburned hydrocarbons). A wide range of firing conditions (i.e., equivalence ratio, air premixing, fuel mass flow, etc.) are used for the characterization.

2.2. Burner Selection

A suitable burner was built in order to measure the actual combustion phenomena so that the data could be compared with numerical simulations. Initially, for that purpose, the $0.30\ m \times 0.30\ m$ stainless steel housing of an old Vulcan[1] catalytic porous burner/heater was modified to accommodate new flame support pads. The housing was selected because the original fiber pads can be easily removed and replaced with the desired materials. Figure 2.1 depicts a schematic of this burner prototype.

However, soon after the beginning of the experimental program, it was found that the design was less than desirable. The gas flow non-uniformities produced by

---

[1] Vulcan Catalytic Infra-red Heaters, Portsmouth Business Park, Portsmouth, RI 02871

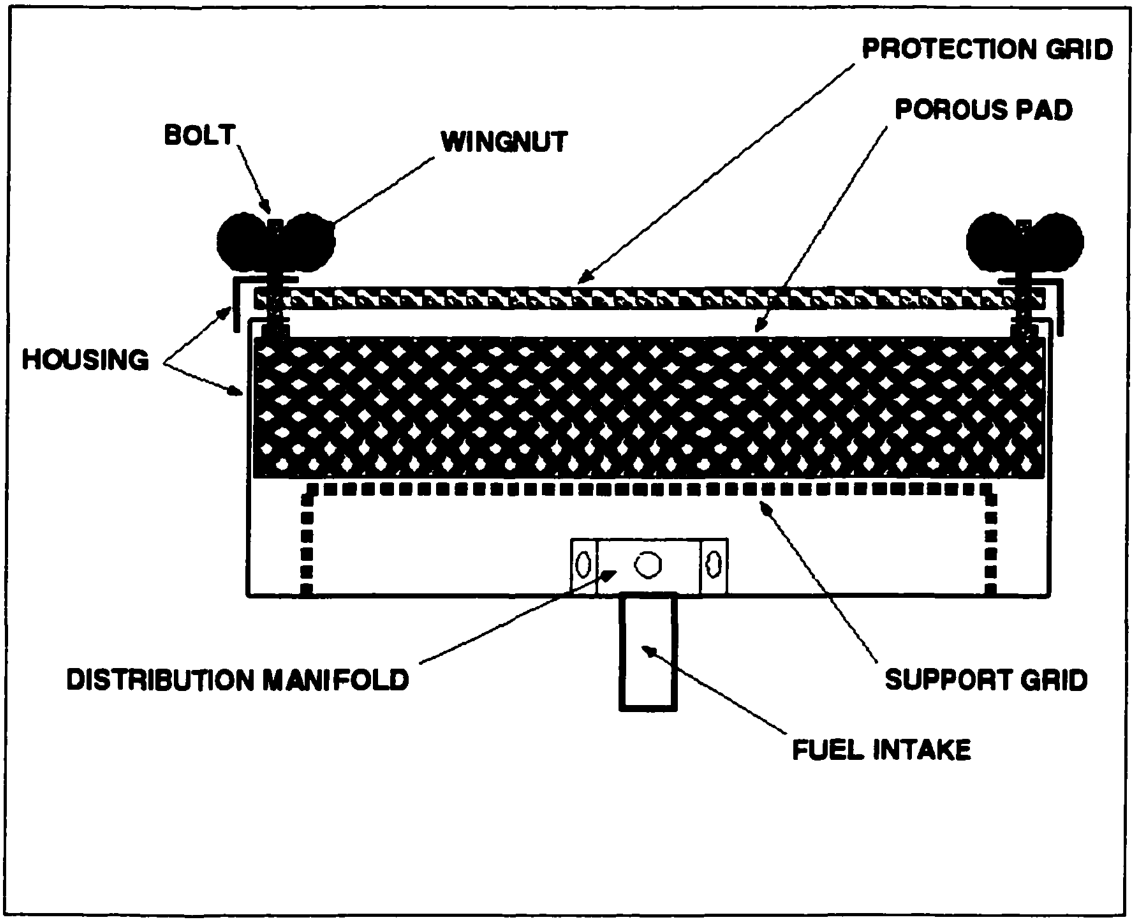

Figure 2.1. Schematic of the prototype radiant gas burner and its main components (not to scale).

the inlet manifold were not attenuated by the high porosity flame support pads: the pressure drop induced by these high porosity materials at the relatively low gas flow velocities (of a few $\frac{cm}{s}$) was not sufficient to produce a uniform gas velocity profile. Increasing the induced pressure drop by stacking more layers of porous materials (diffusion layers) did not improve the situation.

A set of preliminary measurements was performed using the 0.30 $m \times 0.30$ m burner that was specially built to compare the experimental data with numerical simulations. Figure 2.2 shows a photographic image of the burner for stoichiometric combustion ($\Phi = 1.0$) using a single Fecralloy NIT200S layer for a firing rate of 70 $\frac{kW}{m^2}$. The combustion reaction took place at the surface, heating the metal fibers only partially. A problem with the flow non-uniformity was observed, since there was no flame occupying the center of the fiber mat. Radiation efficiency was estimated to be poor in this case. Surface temperature was about $490°C$ at the hottest point.

Figure 2.3 shows a photographic image of lean combustion with 20% excess air ($\Phi = 0.8$) using a single Nextel 312 layer with a metal grid for a firing rate of 60 $\frac{kW}{m^2}$. In this case, the flame was buried inside the fiber pad, which was heated to incandescence in a large part. However, flow non-uniformity was noticed once again, especially at the center. The maximum surface temperature was about $470°C$.

Figure 2.4 shows a situation identical to the one of Figure 2.2 (stoichiometric combustion and a firing rate of 70 $\frac{kW}{m^2}$), but Nextel 312 was used underneath the Fecralloy to act as a diffusion layer. The combustion reaction was partially stabilized inside the solid near the edges, heating the metal fibers to the extent that they glowed, but blue-lifted flames were also present. Surface temperature was about $540°C$ at the hottest point. The flow distribution problem was observed also in this design.

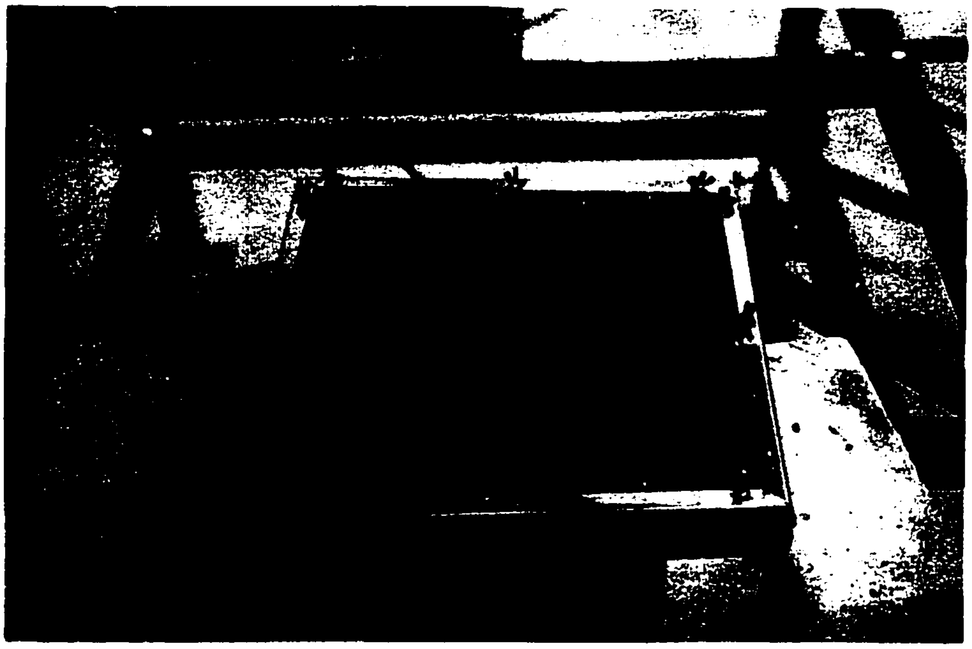

Figure 2.2. Fecralloy NIT200S prototype burner; $\Phi = 1.0$, firing rate of 70 $\frac{kW}{m^2}$.

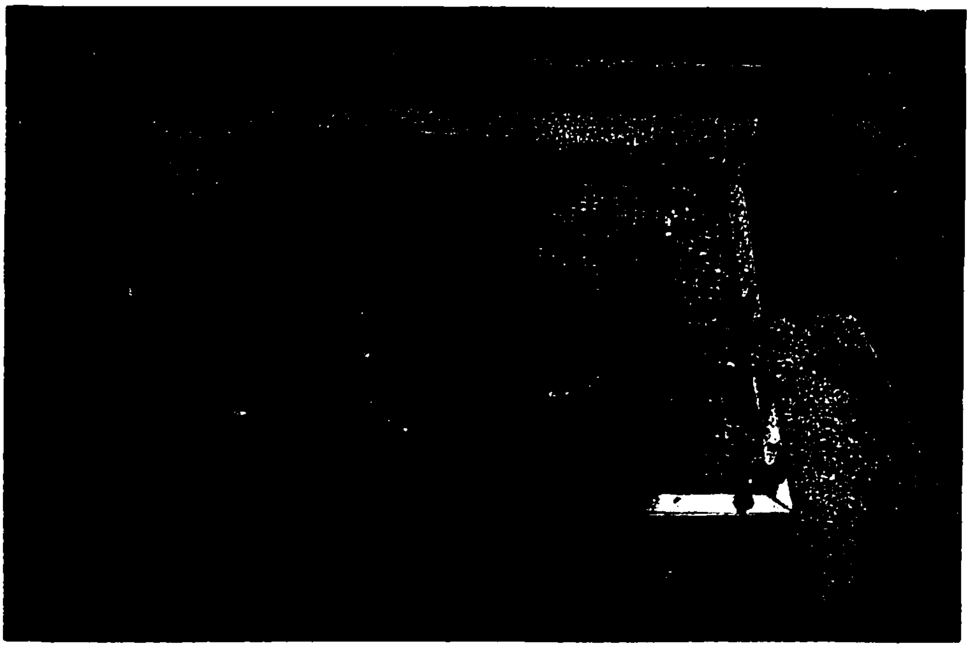

Figure 2.3. Nextel 312 prototype burner; $\Phi = 0.8$, firing rate of 60 $\frac{kW}{m^2}$.

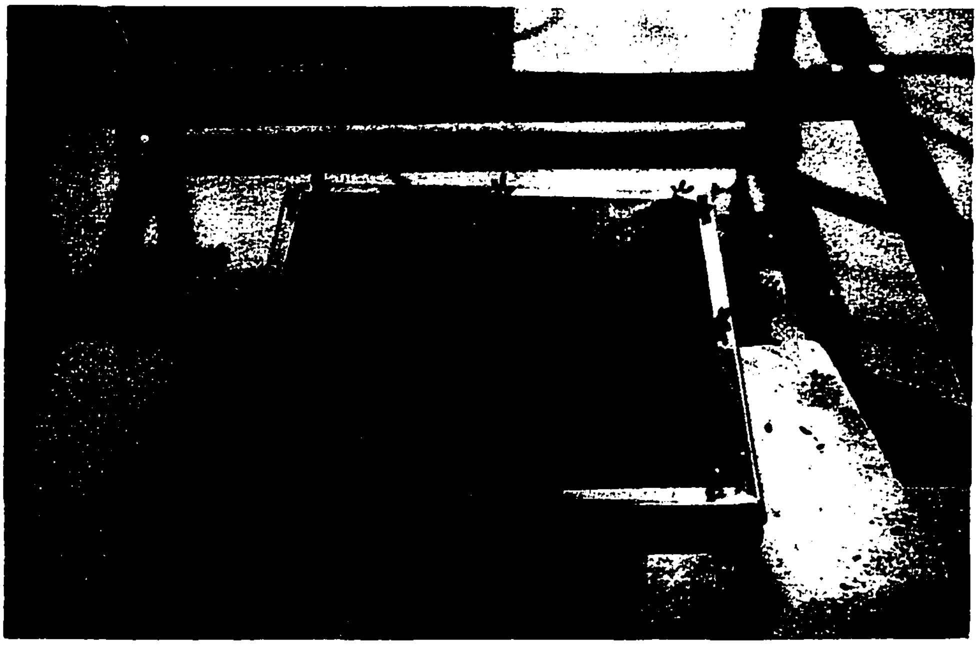

Figure 2.4. Fecralloy NIT200S prototype burner with a Nextel 312 diffusion layer; $\Phi = 1.0$, firing rate of 70 $\frac{kW}{m^2}$.

Commercial porous gas burners usually have one (relatively small) inlet nozzle and a distributor with multiple holes to inject the fuel into a (relatively large) plenum. Even though screens and baffles are often used in some designs, it is impossible to assure uniform gas flow to the solid matrix with this configuration. Other designs include thick porous diffusion layers upstream the flame support layer, with the purpose of inducing a pressure drop that will produce a more uniform flow. However, at low firing rate conditions, gas velocities are too low to create a significant difference in the performance. The problem is accentuated when high-porosity fibrous materials are used (Leonardi et al., 2000), as it is clearly seen in Figures 2.2 to 2.4. Pressure drop was usually less than 250 *Pa* (one inch of water in manometer reading) for the selected materials at the burner operating conditions.

These findings suggested that a new flow distribution concept was necessary if operation in a wide range of firing rates was desired: a design that is not dependent of the inlet velocity (Plesniak, 1999).

For both conical and rectangular diffusers, a total included angle of 7 degrees provides the optimum pressure recovery without separation, as long as the ratio of total diffuser length to inlet width does not exceed about 25 (Kline et al., 1959; Robertson and Fraser, 1960; Barlow et al., 1999). This well-known 7-degree diffuser geometry eliminates boundary layer separation at any constant[2] gas flow rate; therefore, it could be used at the burner inlet to achieve uniform flow. However, the use of such a diffuser results in large burner housing dimensions, which are undesirable in industrial applications. A novel inlet plenum design is presented here. It consists of using several small diffusers in parallel, which assure uniform gas flow distribution at any flow rate, while keeping the burner housing dimensions relatively small.

In order to assess the viability of the new burner concept, preliminary numerical simulations were carried out using a two-dimensional CFD model. FLUENT (Release 5.0.2) was used to solve the momentum equations for several plenum geometries. An adiabatic solution of the model equations using cold air as the working fluid

---

[2] "Constant" flow rate, since boundary layer separation can still occur for pulsating flows

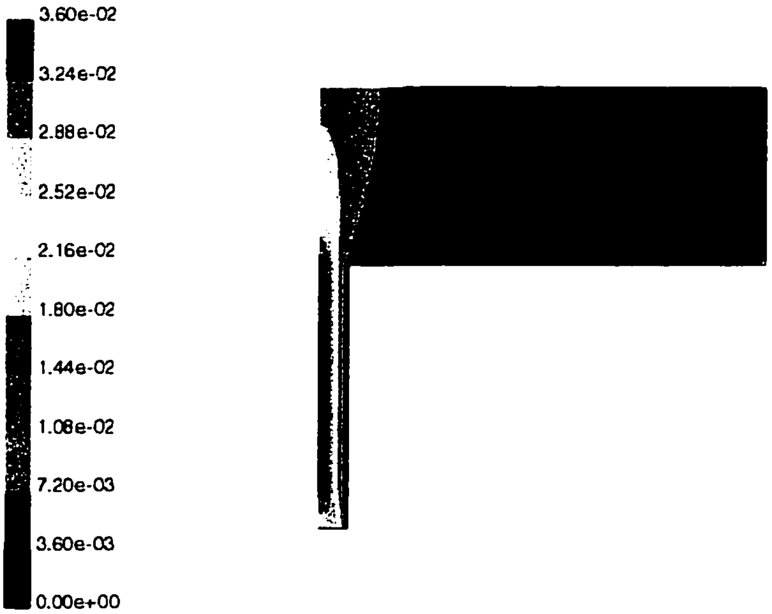

Figure 2.5. Flow distribution results based on FLUENT when a fuel jet enters a rectangular inlet plenum. Note that the exit velocity is highly non-uniform. Velocities are in $\frac{m}{s}$.

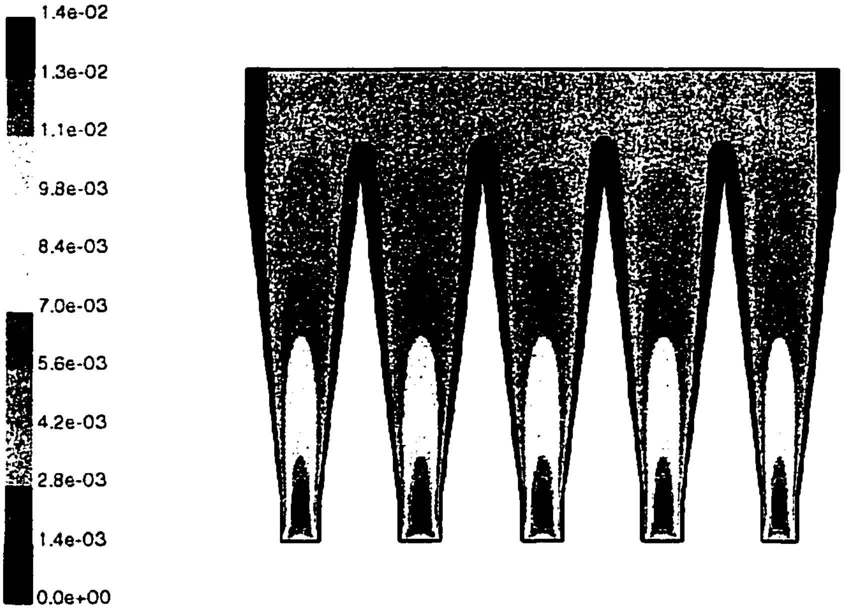

Figure 2.6. Flow distribution results based on FLUENT when a fuel jet enters a diffuser-based burner inlet plenum. Note that the exit velocity is highly uniform, except for thin boundary layers along the side walls. Velocities are in $\frac{m}{s}$.

was selected, since only the flow patterns were required. Figure 2.5 shows a typical situation, in which a single jet entered an empty (i.e., without any fibrous material) rectangular cavity, creating a highly uneven exit velocity profile. Figure 2.6 shows the velocity distribution in a multi-diffuser configuration. The simulations showed that the diffuser-based burner housing was able to provide a uniform flow to the flame support pad, without relying on any induced pressure drop, i.e., the presence of the porous mat was not necessary to establish an adequate gas flow profile at the burner exit.

A housing configuration using four 7-degree diffusers in parallel was selected for the burner prototype, since it allows significant length reduction when compared to a single diffuser, but without the increased complexity (due to too many inlets) of a 3 × 3 array, as shown in Figure 2.7. A photograph of the housing prototype is depicted in Figure 2.8, where a detail of the four-way distribution inlet manifold and a flame arrestor can be seen.

Figures 2.9 to 2.11 show photographs of the surface of the new prototype, diffuser-based, burner operating at three different conditions. A significant improvement of the flame uniformity across the surface with respect to the original burner design was achieved (compare to Figures 2.2 to 2.4). The reaction uniformity produced such a uniform burner glowing that it became difficult to clearly distinguish the difference in firing rate with the naked eye. A burner with a single-layer Fecralloy flame support pad at a firing rate of 300 $\frac{kW}{m^2}$ for a stoichiometric mixture can be seen in Figure 2.9. A double-layer arrangement at a firing rate of 270 $\frac{kW}{m^2}$ for a fuel lean mixture ($\Phi = 0.9$) is depicted in Figure 2.10. Finally, a fuel rich ($\Phi = 1.1$) situation is shown in Figure 2.11 for a lower firing rate of 170 $\frac{kW}{m^2}$, using only one Fecralloy layer.

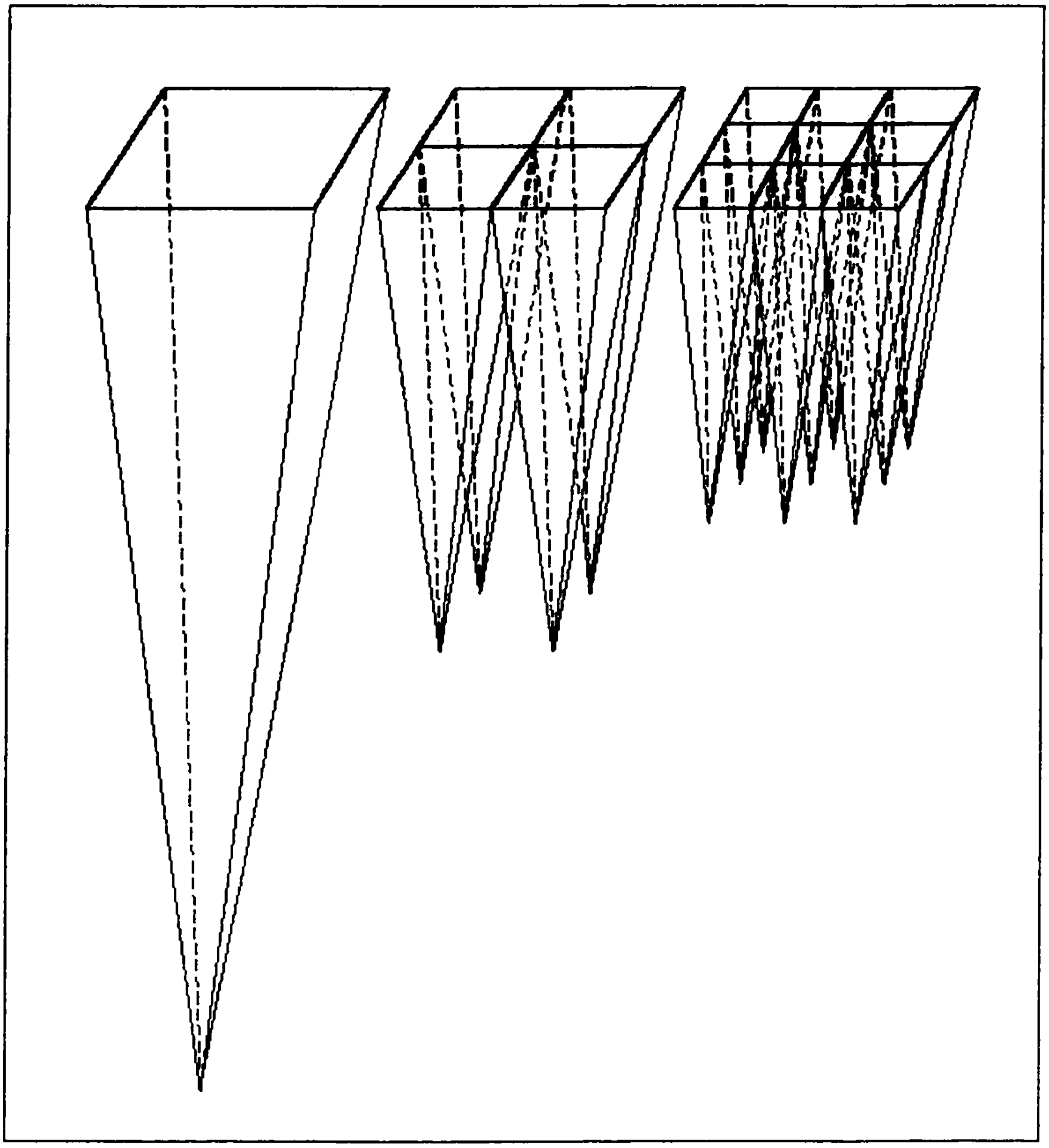

Figure 2.7. Schematic of a diffuser-based burner inlet plenum. Note that the length of the diffusers for a single, 2×2 and 3×3 arrangements follows a 1.00 : 0.50 : 0.33 ratio.

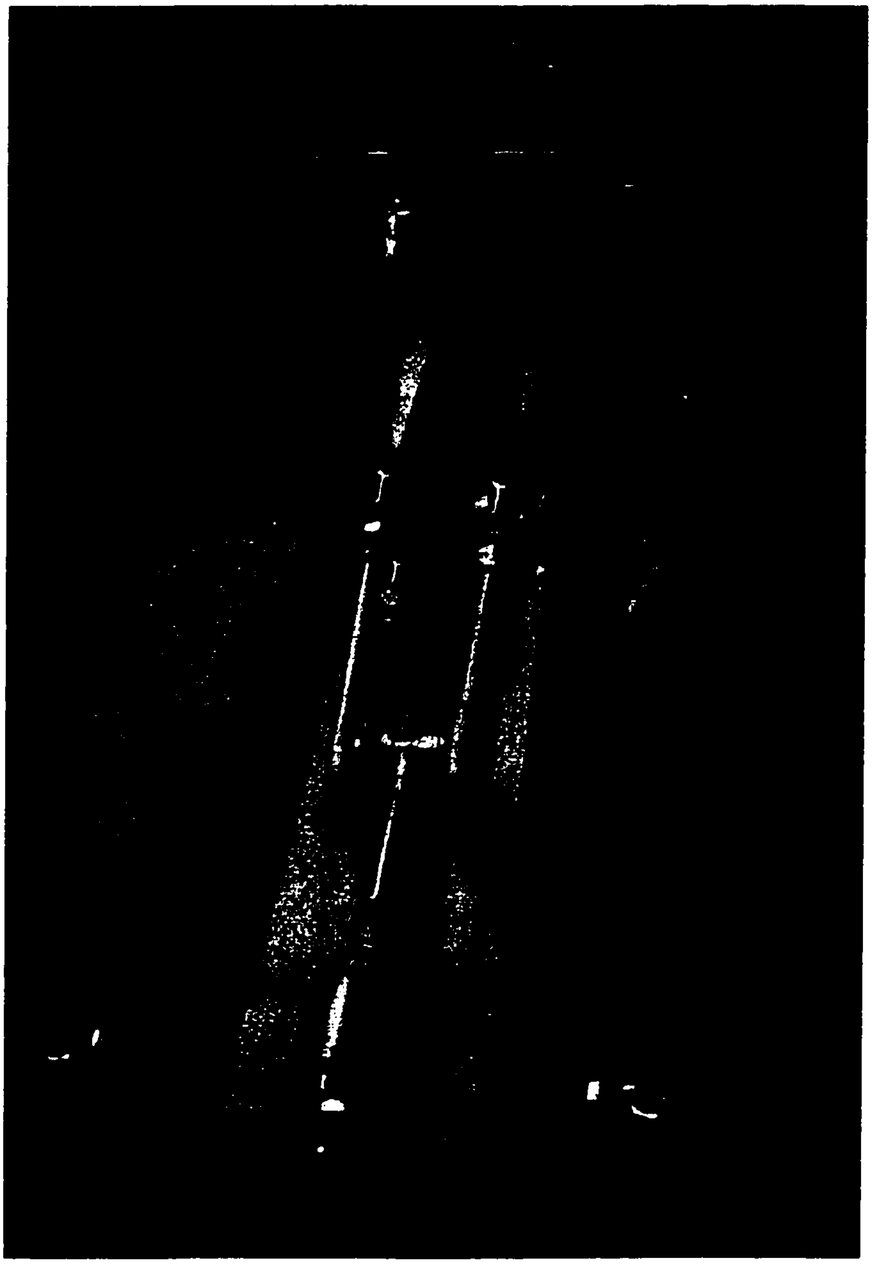

Figure 2.8. Rear view of the diffuser-based housing for the prototype burner. Note the four-way (symmetric) inlet manifold and the flame arrestor at the inlet.

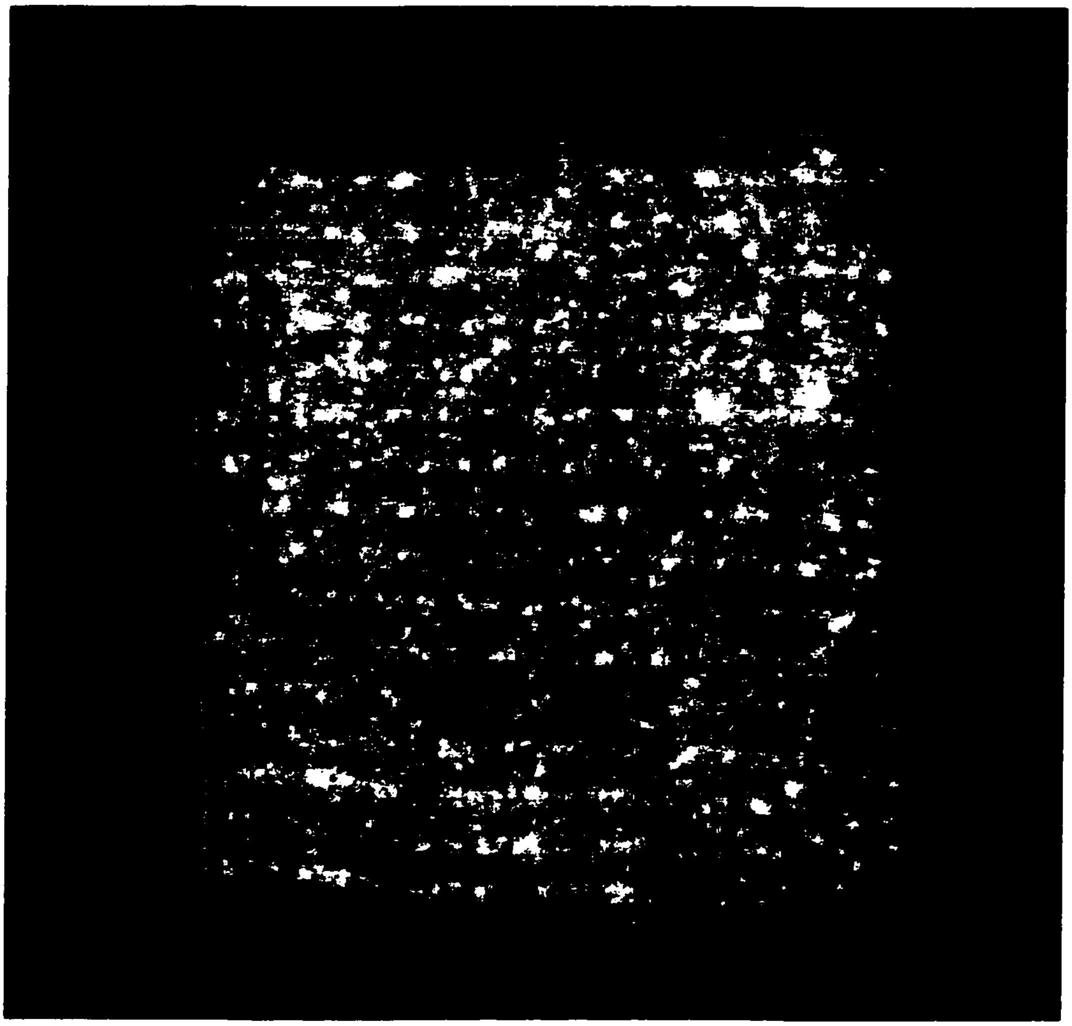

Figure 2.9. Single-layer Fecralloy NIT200S prototype burner; $\Phi = 0.9$, firing rate of 300 $\frac{kW}{m^2}$.

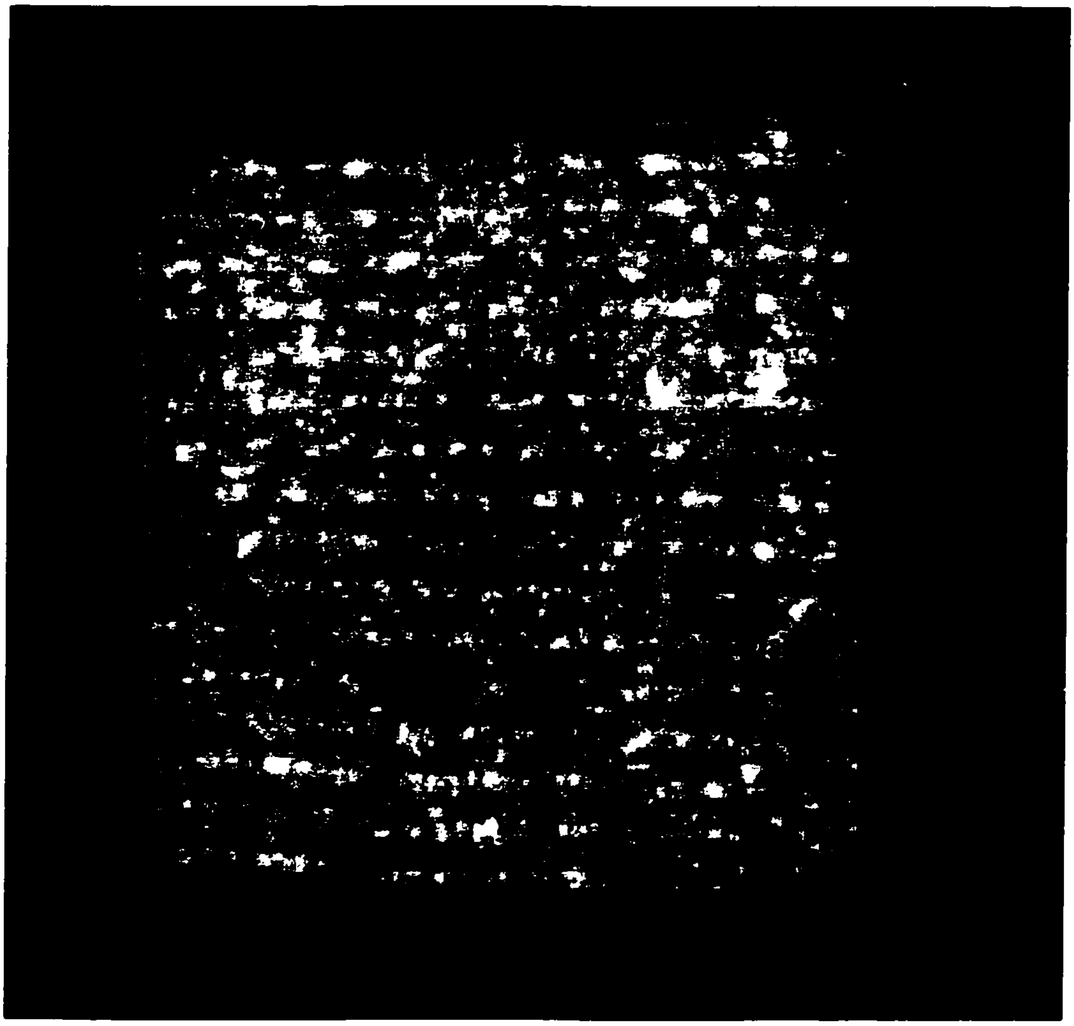

Figure 2.10. Double-layer Fecralloy NIT200S prototype burner; $\Phi = 1.0$, firing rate of 270 $\frac{kW}{m^2}$.

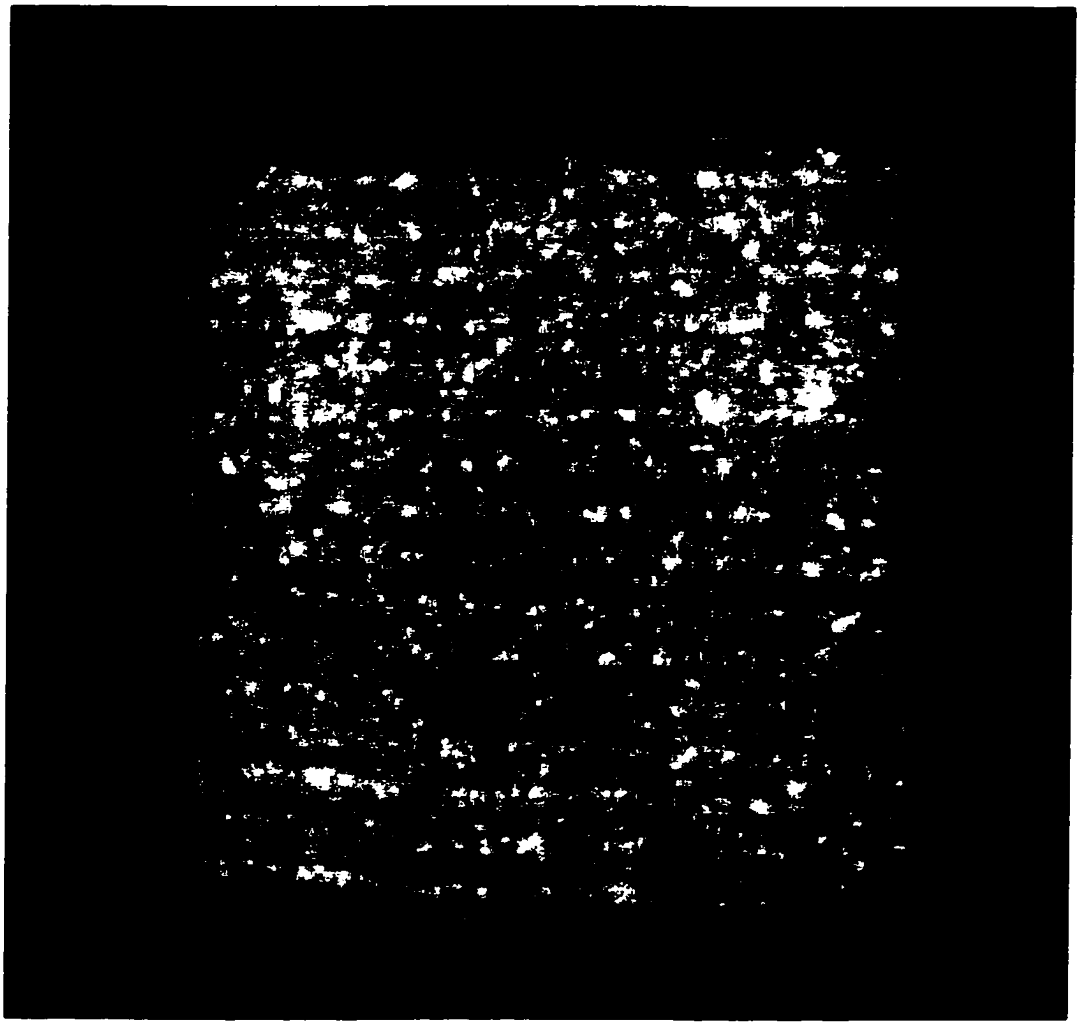

Figure 2.11. Single-layer Fecralloy NIT200S prototype burner; $\Phi = 1.1$, firing rate of 170 $\frac{kW}{m^2}$.

2.3. Experimental Arrangement

A diagram of the experimental arrangement needed to fire the burner is shown in Figure 2.12. The system consisted of a custom built arrangement of valves, orifice-plate based flowmeters and pressure gauges to regulate and measure gas and air supply flows in the ranges of interest. The fuel source was a "grade 1.3" methane tank (93% CH_4 nominal). A mixing chamber consisted of a 3 *m* tube length (6.35 *mm* nominal diameter), and a flame arrestor was placed immediately before the heater to prevent flash-back.

The orifice plates were carefully calibrated against a positive-displacement flowmeter. The gas or air volume that flows during a given period of time was measured for each orifice at choke-flow conditions.

Two porous materials were initially selected to be used as flame support: Nextel non-woven (3M Corporation[3]) and Fecralloy (Acotech Corporation[4]). The relevant properties are listed in Table 2.1. Nextel and Fecralloy compositions are shown in Table 2.2 and Table 2.3, respectively. Nextel fibers have been used in prototype diffusion-type catalytic burners at the University of Minnesota (Goralski, 1998), but not for premixed firing conditions until very recently (Redenius, 1999); Fecralloy fibers are used for commercial fully-premixed gas burners by Acotech Corporation. The metal fiber burner mats are produced by Acotech in accordance with the requirements of the European Quality Standard EN 29001. Fecralloy is an alloy registered by the UK Atomic Energy Authority. This refractory steel was selected for its outstanding oxidation resistance at temperatures above $1000°C$. Of special importance in the alloy composition is the yttrium element which anchors the protective surface alumina layer to the base metal in a very firm, tenacious way.

Since the maximum pad thickness for the materials is small, about 9 and 2 *mm*, respectively, and larger thicknesses are not available at this moment, some burner

---

[3] 3M Ceramic Fiber Products, 3M Center, Building 207-1S-02, St. Paul, MN 55144.

[4] A Shell and Bekaert joint venture: Acotech, 1395 S. Marietta Parkway, Building 500 Suite 100, Marietta, GA 30067.

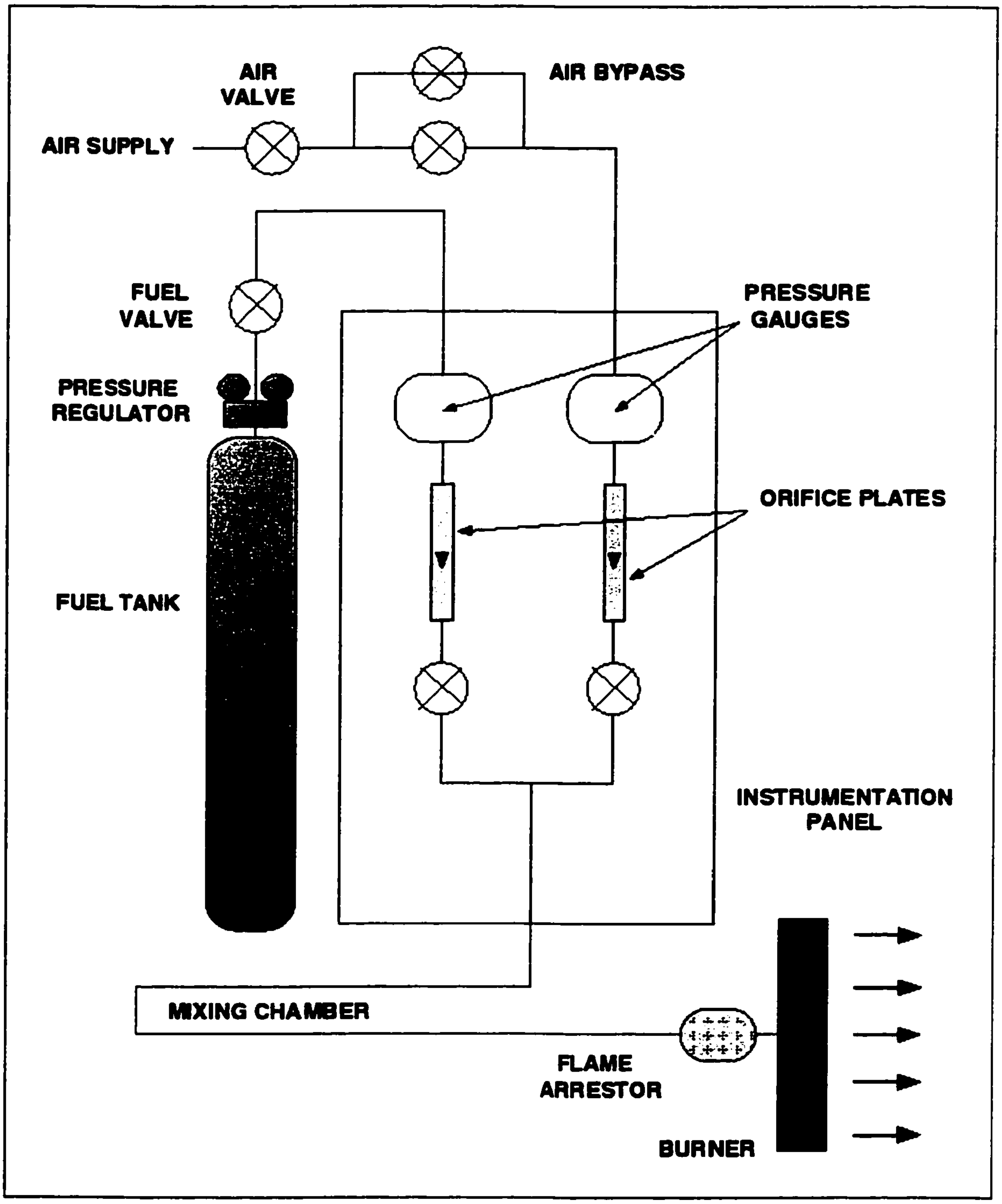

Figure 2.12. Schematic of the experimental arrangement for burner operation.

configurations consisting of one or more layers were studied to determine the merit of using thicker flame support pads.

Table 2.1. Fibrous materials properties according to the manufacturers (3M Corporation and Acotech, respectively, except for c_p, which was independently measured: see Appendix C.)

Property	Nextel		Fecralloy	
	312	440	NIT100S	NIT200S
ρ $\frac{kg}{m^3}$	120	136	540	600
c_p $\frac{J}{kg\ K}$	881 $(333K)$		432 $(333K)$	422 $(333K)$
k $\frac{W}{m\ K}$	0.17 $(300K)$	0.18 $(300K)$	0.13	0.13
d μm	7.5 to 13.5	7.9 to 13.8	35	35
ε —	0.88	0.87	0.65	0.65
ϕ —	0.96		0.91	0.91

2.4. Description of Global Measurements

Ideally, local measurements of temperature and species concentrations would be highly desirable to compare with the numerical results. Mital (1996) has made detailed determination of the temperature and species concentrations inside reticulated ceramic pads. However, due to the nature of the materials used for the flame support layer in this work, which are quite thin and flexible and of small inter-fiber spacing, it was impractical to do so without disrupting the flame structure. The physical limitations caused by the solid matrix for both optical and mechanical probes are

Table 2.2. Nextel fiber composition (wt. %).

	Nextel 312	Nextel 440
Al_2O_3	62%	70%
SiO_2	24%	28%
B_2O_3	14%	2%

significant (Howell et al., 1996). In view of this, global measurements, i.e., at the exit of the burner, were used to compare to the numerical predictions.

2.4.1. Radiant Flux

The radiant flux was measured using a 150° view angle radiometer with a sapphire window (Medtherm[5] Series 64, Model 64P-1-22). This heat flux transducer was selected for the direct measurement of heat transfer rates because of its linear output (which is directly proportional to the heat transfer rate), accuracy, ruggedness, reliability and convenient mounting.

The sensor was a Gardon-type[6] gauge, 25.4 *mm* in diameter. Gardon gauges absorb heat in a thin metallic circular foil and transfer the heat radially (parallel to the absorbing surface) to an integral heat sink attached at the periphery of the foil, and they are widely used for radiation measurements (Prasad et al., 1991; Rawson, 1993). The difference in temperature between two points along the heat flow path is proportional to the heat being transferred and, therefore, to the heat being absorbed; in this case, that difference is taken between the center and the edge of the foil. Medtherm transducers have thermocouple junctions that form a differential

---

[5] Medtherm Corporation, P.O. Box 412-TR, Huntsville, AL 35804

[6] This sensor design takes its name from a one-dimensional radiation-conduction model originally developed by Gardon (1956).

Table 2.3. Fecralloy fiber composition (wt. %).

	NIT100S, NIT200S
Cr	20.00%
Al	5.00%
Y	<0.10%
Si	0.30%
Mn	0.08%
Cu	0.03%
C	0.03%
Fe	balance

thermoelectric circuit providing a self-generating potential between the two leads; no reference junction is needed. The radiometer specifications are provided in Table 2.4.

A sapphire window attachment was added to eliminate convective heat transfer. The window reduced the sensitivity of the basic transducer to a nominal fraction of the original, in this case to 79%, thus extending the bare sensor rage from 11.4 $\frac{kW}{m^2}$ (1 $\frac{Btu}{ft^2 s}$) to 14.4 $\frac{kW}{m^2}$. The window transmitted 85% (nominal) of the spectrum in the wavelength range from 0.15 to 5.0 μm.

The radiometer was connected to a universal heat flux meter (Medtherm H-201) that amplifies the signal. The H-201 is recommended for steady-state or slowly-varying measurements. The specifications are shown in Table 2.5.

A schematic diagram of the heater and radiometer orientation is shown in Figure 2.13. The heater was mounted vertically for this radiant flux measurement and the heat flux incident on multiple points was measured by changing the position of the detector, which was mounted on vertical and horizontal positioners. The flux meter gain was usually set to 250, and the output was processed by an A/D converter and stored in a personal computer (IBM compatible, 486 processor). It was important

Table 2.4. Radiometer specifications.

Range	$11.4\ \frac{kW}{m^2}$
Output signal (full range)	$(10.0 \pm 1.5)\ mV$
Maximum operating temperature	$478K$ ($400°F$)
Repeatability	±0.5%
Accuracy	±3%
Overrange capability	500%
Maximum non-linearity	±2% of full range
Sensor absorptance	92% (0.5 to 15.0 μm)
Response time	$< 0.3\ s$
Nominal impedance	$< 10\ \Omega$

to keep the radiometer at a sufficient distance from the burner face to minimize the convective heat transfer. The distance between the heater surface and the radiometer was usually about 1 m.

Since the dimensions of the radiometer window were small, the radiant flux measurement domain for this configuration could be considered as a rectangular box aligned with the heater. Taking advantage of this geometry, the entire plane was divided into four quadrants and four different view factors were computed. According to Modest (1993), the view factor from a differential planar element, $d1$, to a finite parallel rectangle of dimensions $a \times b$, separated by a distance c, when the normal to the element passes through a corner of a rectangle, can be computed as:

$$F_{d1-2} = \frac{1}{2\pi}\left(\frac{X}{\sqrt{1+X^2}} \arctan\frac{Z}{\sqrt{1+X^2}} + \frac{Z}{\sqrt{1+Z^2}} \arctan\frac{X}{\sqrt{1+Z^2}}\right), \qquad (2.1)$$

where $X = a/c$ and $Z = b/c$. Note that when the detector was centered with respect to the burner area, the view factors to the four quadrants became identical.

Table 2.5. Heat flux meter specifications.

Range	Determined by linear sensor
Output signal (full range)	2.0 V
Maximum operating temperature	323K (50°C)
Warmup time	5 min
Accuracy	±0.5% of full range
Input impedance	$> 100\ M\Omega$

Multi-point measurements were obtained by moving the detector to different positions and obtaining the radiant flux[7]. Typically 9 to 13 positions were used: detector aligned with the center of the burner, the four corners, the midpoint of the four edges, and the center of the four quadrants. Maximum detector signal strength corresponded to the situation when the sapphire window was aligned with the center of the burner (since the view factor becomes maximum).

One of the most important measures of the thermal performance of the burners/heaters is the radiation efficiency, η_{rad}, which is defined as the ratio of the emitted radiation in the forward direction to the chemical energy input or firing rate, *FR*:

$$\eta_{rad} = \frac{\text{radiant flux}}{FR} . \qquad (2.2)$$

2.4.2. Combined Radiation and Convection

Calorimetric measurements can be used to determine the combined (i.e., convection plus radiation) flux. The heater was mounted horizontally, facing upward, parallel to a 0.61 m diameter water-cooled calorimeter, which was placed directly above the heater (Figure 2.14). The aforementioned calorimeter was coated black so

---

[7] A significant difference in the radiant flux measurement for different positions of the detector can be indicative of surface non-uniformities.

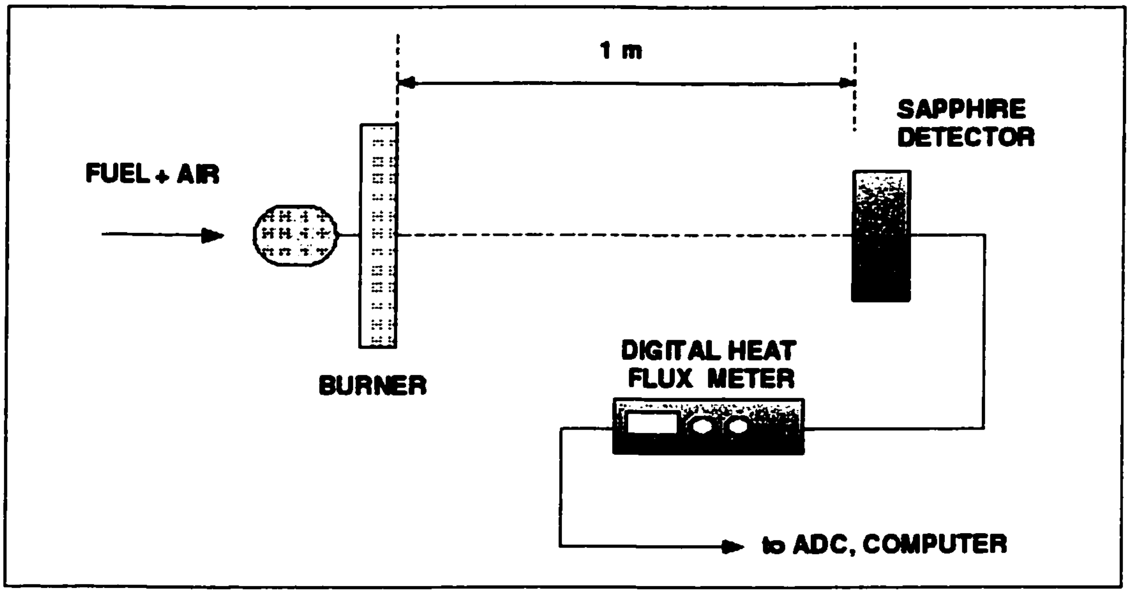

Figure 2.13. Schematic of the heater and radiometer orientation.

that the surface absorptivity became large (about 0.96). Water was then circulated through the calorimeter, and the burner/heater transferred energy by convection and radiation to the water through the calorimeter plate. Condensation of water from the exhaust stream on the calorimeter surface was avoided by installing an immersion heater in the input water line and keeping the calorimeter plate at a temperature above the dew point (about $318K$). The distance between the calorimeter plate and the heater surface was maintained at 0.025 m, which was close enough to minimize room air entrainment, and large enough to allow for the remotion of the combustion products.

2.4.3. Burner Surface Spectral Intensity

The spectral intensity measurement technique is shown schematically in Figure 2.15. The heater was mounted vertically, facing the spectrometer. The setup includes a changeable detector since different devices were needed for each wavelength range: PbS detector (for wavelengths from 1.08 to 3.00 μm), a PbSe detec-

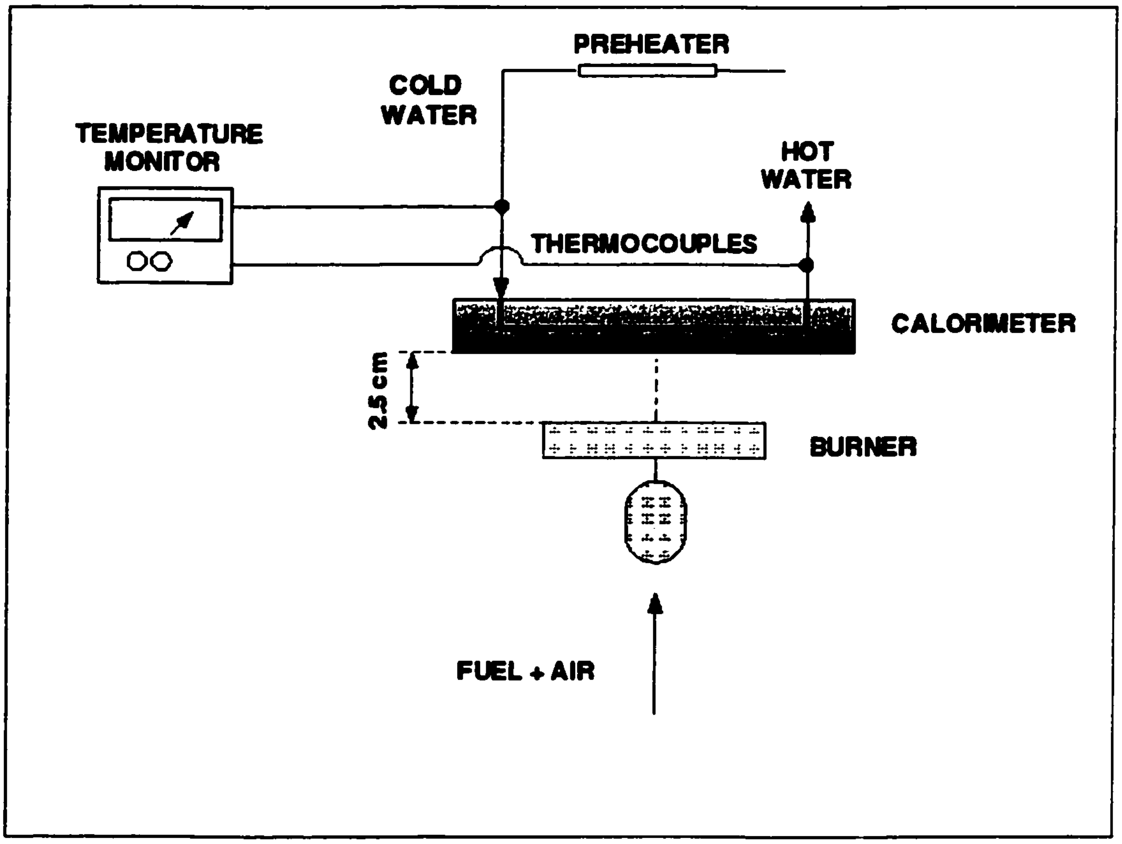

Figure 2.14. Schematic of the heater and calorimeter orientation.

tor (from 3.36 to 5.12 μm) and a thermopile detector (from 5.28 to 10.40 μm). A monochromator (Oriel[8] Model 77250) with three monochromator gratings (one for each wavelength of interest), three order sorting filters, a six-blade rotating optical chopper and a shielded collection probe (a $5mm$ inner diameter tube inserted through black cardboard) completed the detection system. The chopper was necessary because the PbSe detector responds only to modulated signals. The order sorting filters were used to eliminate monochromator order artifacts from the data. All the optics were mounted on a precision optical slide to facilitate alignment.

The system was aligned using a He-Ne (632 nm) laser and then calibrated using a blackbody at $1200K$. For PbS and PbSe detectors, the signal was chopped at 250 Hz and sent into the filter set at 125 Hz. The output of the filter was fed into a lock-in amplifier. The output from the amplifier passed through a low-band pass filter set at 100 Hz, before being fed into a data acquisition program and simultaneously being observed on an oscilloscope.

For the thermopile detector, no chopper or lock-in amplifier was used. The calibration constant was obtained by dividing the output voltage with the blackbody intensity at that particular wavelength at $1200K$.

The spectral radiation intensity measurements were made by replacing the blackbody with the heater. The heater was operated at the different desired conditions. The voltage signal from the heater was collected in the wavelength range of 1.08 to 10.40 μm. Using the calibration constant, the voltage was converted into radiation intensity.

2.4.4. Exhaust Gas Temperature and Spectral Intensity

The measurement of the exhaust gas temperature in the neighborhood of the strong thermal radiation field emitted by the burner surface is usually a difficult problem from the experimental point of view. It is not possible to use a simple

---

[8] Oriel Instruments, 250 Long Beach Blvd., P.O. Box 872 - Dept. TR, Stratford, CT 06497.

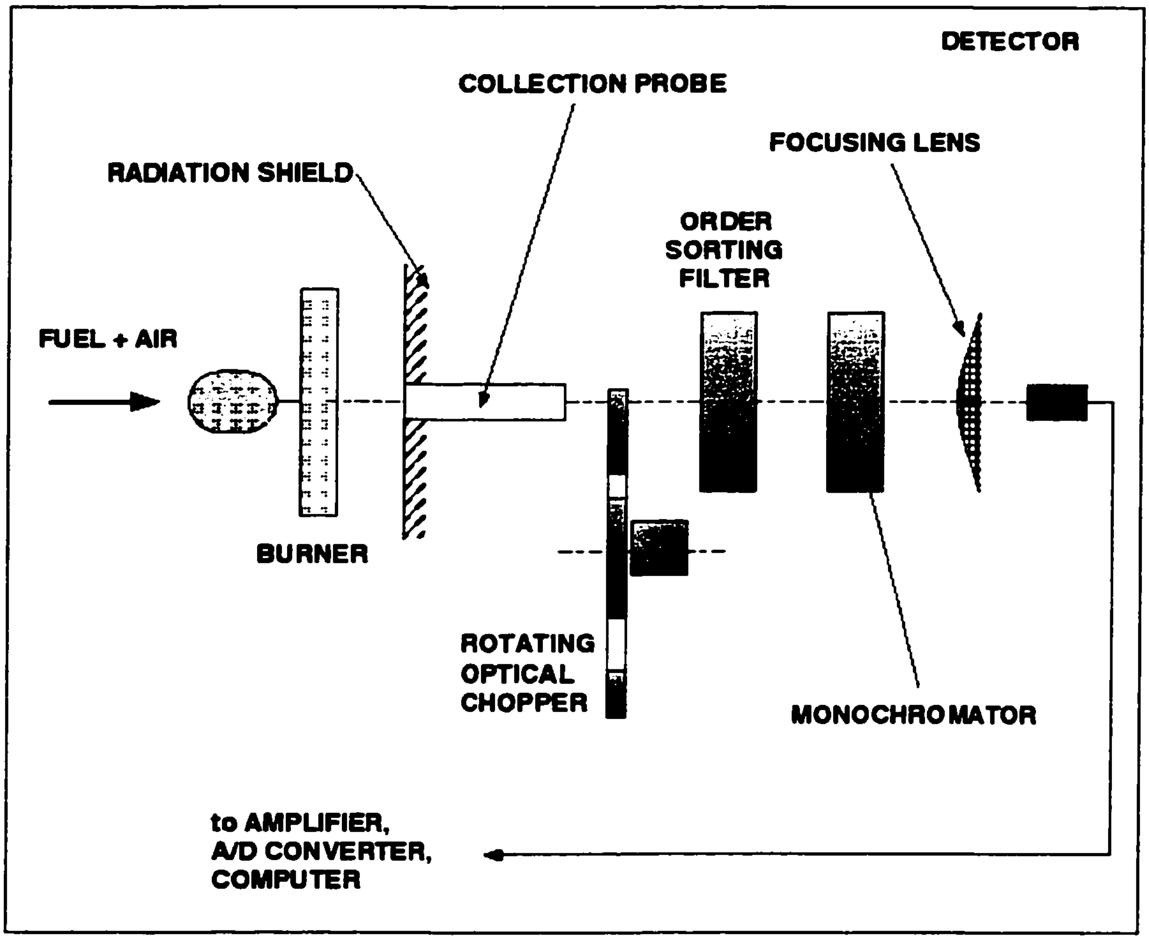

Figure 2.15. Schematic of the spectral intensity measurement apparatus.

thermocouple because a radiation correction becomes significant (Holman, 1971) and prone to uncertainty. More sophisticated methods are necessary.

Mital (1996) used three thermocouples of different bead sizes to measure the exhaust gas temperature, and then extrapolated the data to "zero bead diameter" to eliminate the effects of radiation and heat conduction. However, uncertainties in the bead diameter, need for three measurements and the fact that the temperature has to be extrapolated (as opposed to interpolated) can be sources of errors.

Thin filament pyrometry, originally introduced by Vilimpoc and Goss (1988), has the potential to provide better than 5 to $10K$ precision and possibly accuracy for flame temperature measurements (Pitts, 1996). The technique is based on the blackbody emission of a small ceramic filament (about 15 μm in diameter) which is introduced into the flow field under study (Goss et al., 1988). Because the emission along the entire length of the filament is recorded, the complete spatial temperature distribution (or average) is measured. As a possible drawback, Pitts et al. (1998) reported performance degradation due to the effects of soot deposition on the filament for diffusion flames.

A third method consists in using a "fast infrared array spectrometer" (FIAS) to simultaneously measure spectral radiation intensities over the 1.8 to 4.9 μm wavelength range. This range covers two important bands of CO_2 and one important band of H_2O radiation. Radiation from the flame (the detector is placed in such a way that its view line is parallel to the burner surface, to avoid the direct radiation from the solid matrix) is directed and dispersed over a staggered 160-element linear array PbSe detector. A tuning fork chopper at a fixed frequency of 390 Hz is used; during each chopper cycle, ten scans are initiated over the 160-pixel linear array PbSe detector. Extensive details about the instrumentation description, specifications and calibration procedure were reported by Ji et al. (2000a). Once the gas emission spectrum is available, species concentrations were assumed to be those of complete combustion, and a narrow band analyses in RADCAL (Grosshandler, 1993) was used to back-calculate the gas temperature through an inverse iterative procedure. A more recent model (Soufiani and Taine. 1997) does not improve the results (Ji et al., 2000b). Recently, they compared several adiabatic turbulent lean premixed flame temperatures measured with thin filament thermometry to the RADCAL results, and excellent agreement was obtained between the two methods and also with the adiabatic flame temperature.

Based on the success of the last technique reported by Ji et al. (2000b), the temperature of the exhaust gases for the present study was measured following that same procedure. The heater was mounted in a horizontal position (facing upwards) to allow the hot gases plume to raise vertically. The detector was oriented in a way that only the emission from the gases (and not from the solid surface) was within the view angle, at a distance of approximately 2.5 *cm* from the burner to minimize the entrainment of (cold) room air. Emission spectra were acquired for several firing rates and equivalence ratios. Figure 2.16 illustrates the experimental arrangement.

2.4.5. Pollutant Emissions

The heater was mounted horizontally, facing upward. The emissions of CO, NO, NO_x and unburned hydrocarbons (CH_4 equivalent) from the heater were measured for various operating conditions by sampling the gases either in a collection hood placed above the burner or by direct sampling very near the surface (at about 1.5 *cm*). The samples were collected after the steady state was reached.

A schematic diagram of the experimental setup is shown in Figure 2.17. The sample was drawn from the exhaust and passed through a chiller to remove water vapor before directing it to a gas-filter-correlation based CO emission analyzer.

A flame-ionization-detector based hydrocarbon analyzer (with a temperature-controlled heated zone to eliminate condensation) was used. A sample conditioner was used for the chemiluminescence based NO_x analyzer. The CO analyzer (Model

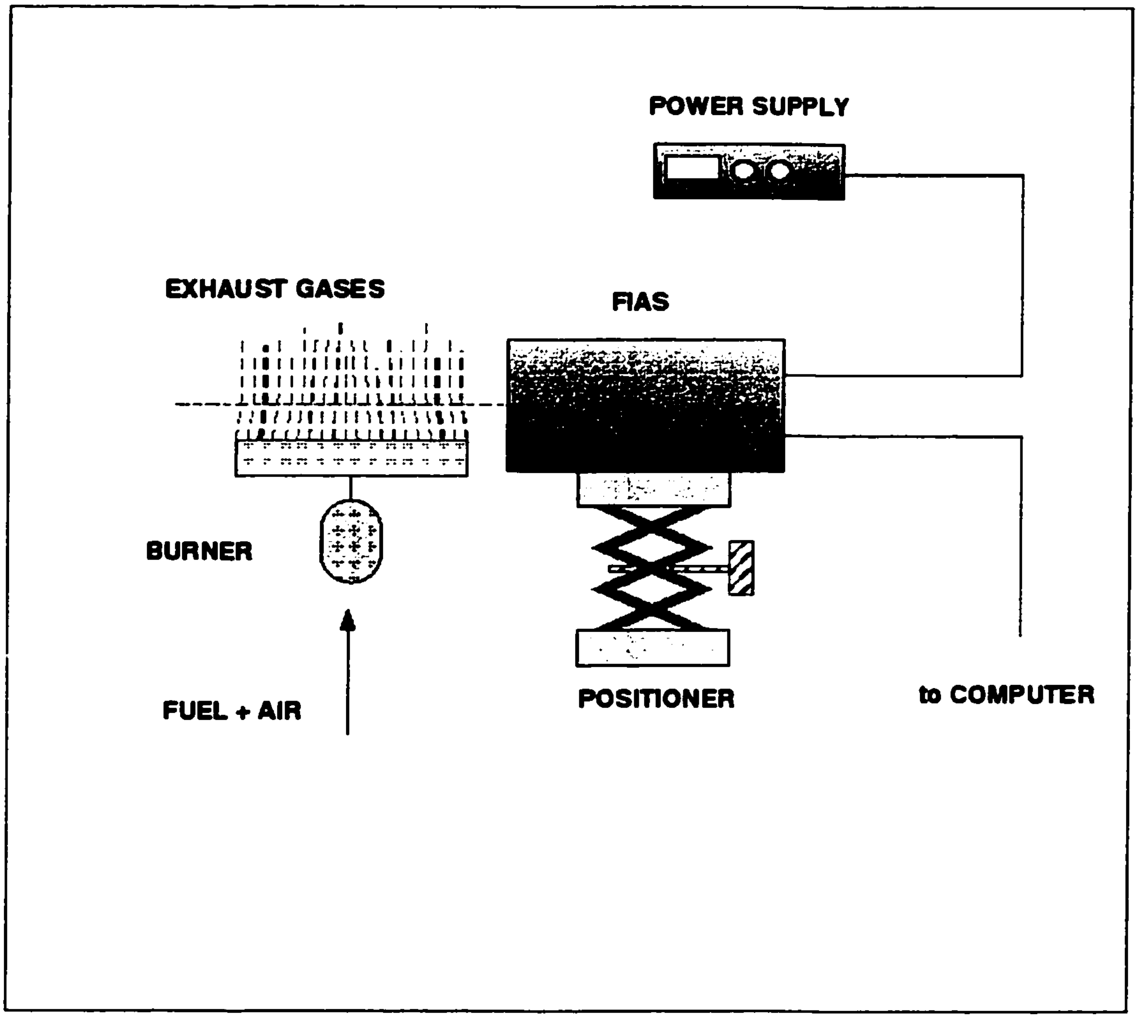

Figure 2.16. Schematic of the fast infrared array spectrometer experimental arrangement.

48), HC analyzer (Model 51), NO_x analyzer (Model 42) and the sample conditioner (Model 800) were all from Thermo-Environmental Instruments[9].

The recommended flow rate range for the CO analyzer was 8.3 to 16.6 $\frac{cm^3}{s}$. The flow rate in the NO/NO_x analyzer was maintained such that the steel ball of a rotameter in the oven unit of the analyzer was always in buoyant motion. In the hydrocarbon analyzer, air and hydrogen were provided at pressures of 207 kPa (30 psi) and 414 kPa (60 psi), respectively. The zero and span readings of all the analyzers in the appropriate ranges were calibrated before each test.

2.4.6. Burner Temperature

The burner surface temperature can be measured relatively easily utilizing different methods. One of them consisted of using an radiation thermometer (Ircon[10] Ultimax UX-81, in the range 40–400°C; Raytek[11] Raynger ST8, in the range 0–540°C; Ircon Ultimax UX-81, in the range 500–2800°C). The radiation thermometers were calibrated against a blackbody (Infrared Systems Development, model 563/201, with a temperature controller model 112/201), and the correspondence between the thermometer readings and the blackbody temperature is shown in Figure D.1 of Appendix D. Another technique is based on finding the temperature at which the Planck's blackbody distribution function closely matches the measured spectral intensity described in Section 2.4.3.

It is necessary to mention here that what it is referred in the text as "burner temperature" or "surface temperature" is in fact an "apparent surface temperature" and not the actual thermodynamic temperature of the ideal surface of the flame support pad. The concept of surface cannot be easily applied to a porous material; additional complications arise from the fact that radiation is emitted from within the volume of the semitransparent material.

---

[9] Thermo Environmental Instruments, Inc., 8 West Forge Pkwy., Franklin, MA 02038.

[10] Ircon, Inc., 7300 N. Natchez Ave., Niles, IL 60714.

[11] Raytek Corporation, 1201 Shaffer Rd., P.O. Box 1820, Santa Cruz, CA 95061.

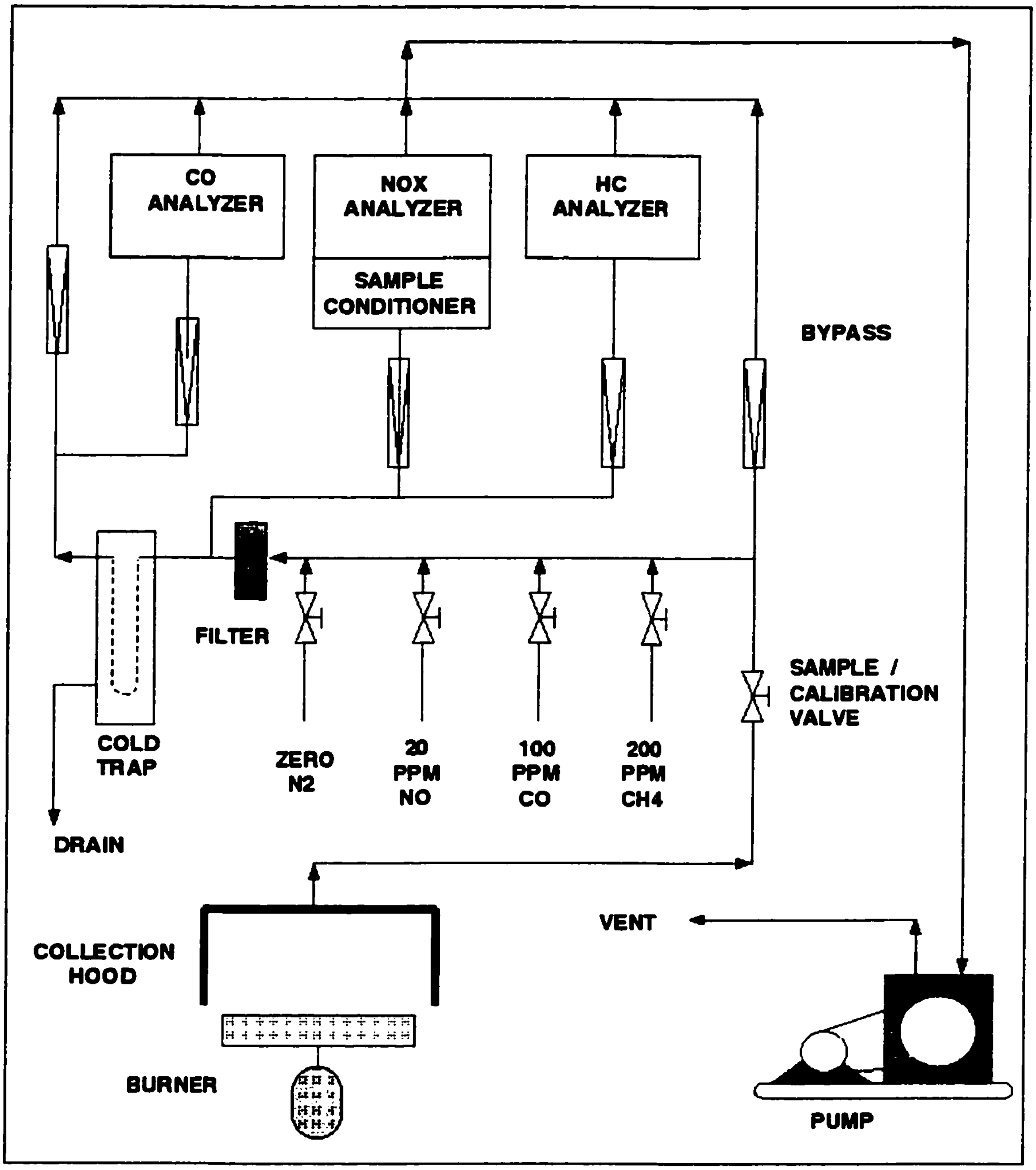

Figure 2.17. Schematic of the pollutant emission analysis apparatus.

2.5. Experimental Data

2.5.1. Partially-Premixed Commercial Catalytic Burner

The experimental determination of the influence of partially-premixing the fuel on a commercial, diffusion-type catalytic burner was performed. The burner was originally designed to operate below 25 $\frac{kW}{m^2}$; beyond that, methane slippage became significant and the radiation efficiency (defined in Equation 2.2) dropped significantly (Figure 2.18). The figure shows that the efficiency was improved noticeably by adding air to the fuel stream, which effectively broadened the range in which this type of burner/heater could be operated.

2.5.2. Prototype Fiber Burners

In order to obtain experimental data to validate the numerical model presented in Chapter 3, a test matrix was prepared for the testing of a Fecralloy burner. Seven firing rates covering the range from 170 to 340 $\frac{kW}{m^2}$[12], three inlet equivalence ratios from about 10% excess air for a fuel lean flame up to 10% defect air for a fuel rich flame ($\Phi = 0.9, 1.0, 1.1$), and two flame support pad thicknesses (2 mm for a single layer, 4 mm for a double layer) were used.

2.5.2.1. Radiation Efficiency for the Prototype Burners

Figure 2.19 depicts the measured variation of the multi-point radiation efficiency as a function of the firing rate. The difference in radiation efficiency for different positions of the radiant flux detector was less than 0.5%, indicating the reaction uniformity across the surface.

---

[12] Radiant burners used in industrial furnaces usually operate at a nominal firing rate of 100 $\frac{kBtu}{ft^2h}$ ($\approx 315\frac{kW}{m^2}$). The selected range allowed for the test matrix to include typical industrial conditions from 50% to 100% of that nominal power.

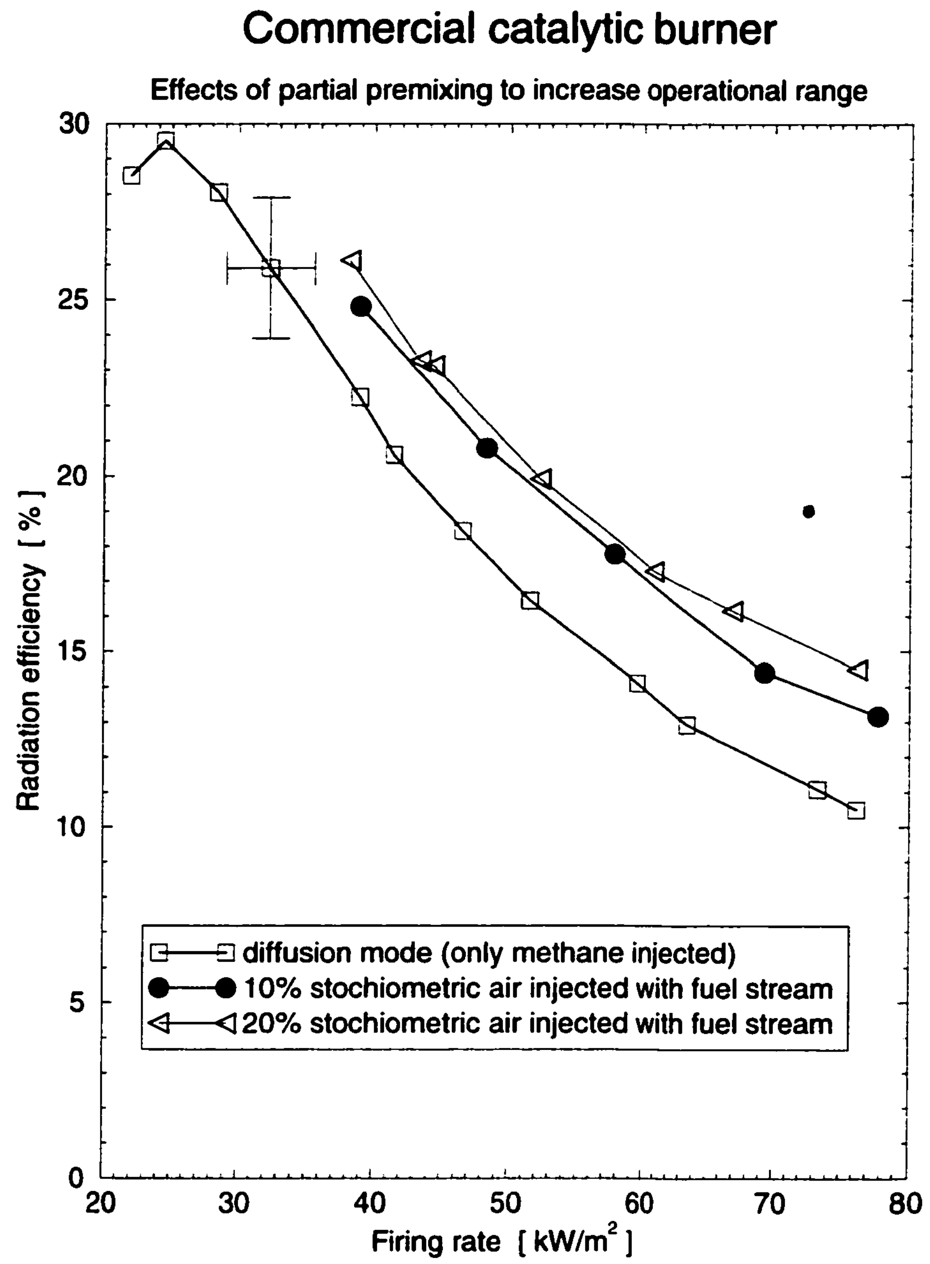

Figure 2.18. Effect of partially premixing fuel and air on a diffusion-type catalytic burner: dependence on the firing rate. Note that there is a significant increase in the radiation efficiency even when a small fraction of the stoichiometric air is injected with the fuel stream. The error bars represent the best estimate of the experimental uncertainty: ±2% in the radiation efficiency and ±3 $\frac{kW}{m^2}$ in the firing rate.

The experimental uncertainty, obtained by error propagation (Appendix A) of an estimated maximum 10% error in the fuel flow rate setting and a 3% error in the radiometer readings, was less than 2% for all conditions.

At the lower range, up to 225 $\frac{kW}{m^2}$, there was an increase in the efficiency for all inlet mixture and configuration combinations, indicating that heat losses from the burner housing to the surroundings were significant. Additionally, effects of more incomplete chemistry at the lower temperatures can be present (more details are given in Section 4.3.3). At higher firing rates, the radiation efficiency was approximately constant in the range 18-26%.

It was observed that the burners with the thicker flame support pad (double Fecralloy layer) had a higher radiation efficiency than the thinner counterparts, at the same operating conditions. This performance increase was probably a combination of two factors: a longer gas mixture residence time in the high temperature region resulted in a more complete combustion (see Section 2.5.2.5, where the unburned hydrocarbon emissions are compared); additionally, an effective increase in the pad volume allowed for a larger fraction of thermal radiation emission, since radiation is emitted not only from the surface but also from within the semitransparent material. Radiation efficiency for the double-layer burner was about 2% to 3% higher than when using the single-layer pad.

Finally, for both single- and double-layer pads, the radiation efficiency increased when increasing the equivalence ratio (in the studied range $\Phi = 0.9$ to 1.1, i.e., near stoichiometric conditions[13]). The same trend was noted for all firing rates. This observation agrees with the fact that the maximum adiabatic flame temperature occurs not at stoichiometric, but rather at a slightly rich equivalence ratio, as a consequence of both the heat of combustion and the heat capacity of the products

---

[13] Only fuel mixtures similar to those used in industry were studied here; richer flames ($\Phi > 1.1$) were not considered. By avoiding the burning of mixtures with higher fuel content, the deposit of soot particles in the porous matrix was minimized, keeping the prototype burner clean and the experiments highly reproducible. Equivalence ratios in excess of 1.1 are investigated numerically in Section 5.3.

declining beyond $\Phi = 1.0$. For equivalence ratios between $\Phi = 1.0$ and $\Phi(T_{max})$, the heat capacity decreases more rapidly than the heat of combustion (Turns, 1996).

The results compared reasonably well to those obtained with commercial metal-fiber burners. Singh (1999) performed extensive measurements using industrial burners, and obtained similar radiation efficiency results for stoichiometric and 10% excess air inlet mixtures, at firing rates beyond 250 $\frac{kW}{m^2}$. He observed increased radiation efficiencies at lower firing rate conditions ($> 30\%$), which were probably due to a combination of two factors: commercial gas heaters are more compact than the prototype used for the present study; therefore, they have lower heat losses to the surroundings (which are significant at low firing rates); and errors in his measurement of the natural gas flow rate, since his experimental apparatus was more suitable for large flow rates (Gore, 1999).

2.5.2.2. Combined Efficiency for the Prototype Burners

Figure 2.20 shows the measured variation of the combined (or total) efficiency as a function of the firing rate. The total efficiency is defined as the ratio of the total energy transferred to the load (i.e., radiation and convection) to the chemical energy input or firing rate:

$$\eta_{tot} = \frac{\text{radiant flux} + \text{convective flux}}{FR} \,. \tag{2.3}$$

The experimental uncertainty, obtained by error propagation of an estimated maximum 10% error in the fuel flow rate setting, a 5% error in the water flow rate through the calorimeter, and a $1K$ uncertainty in the temperature difference between the inlet and the outlet, was less than 5% for all conditions.

It is important to point out here that the magnitude of the measured combined efficiency is somewhat dependent on the calorimeter size and design. Large, black calorimeters (as the one utilized here, see Section 2.4.2) are more effective in absorbing

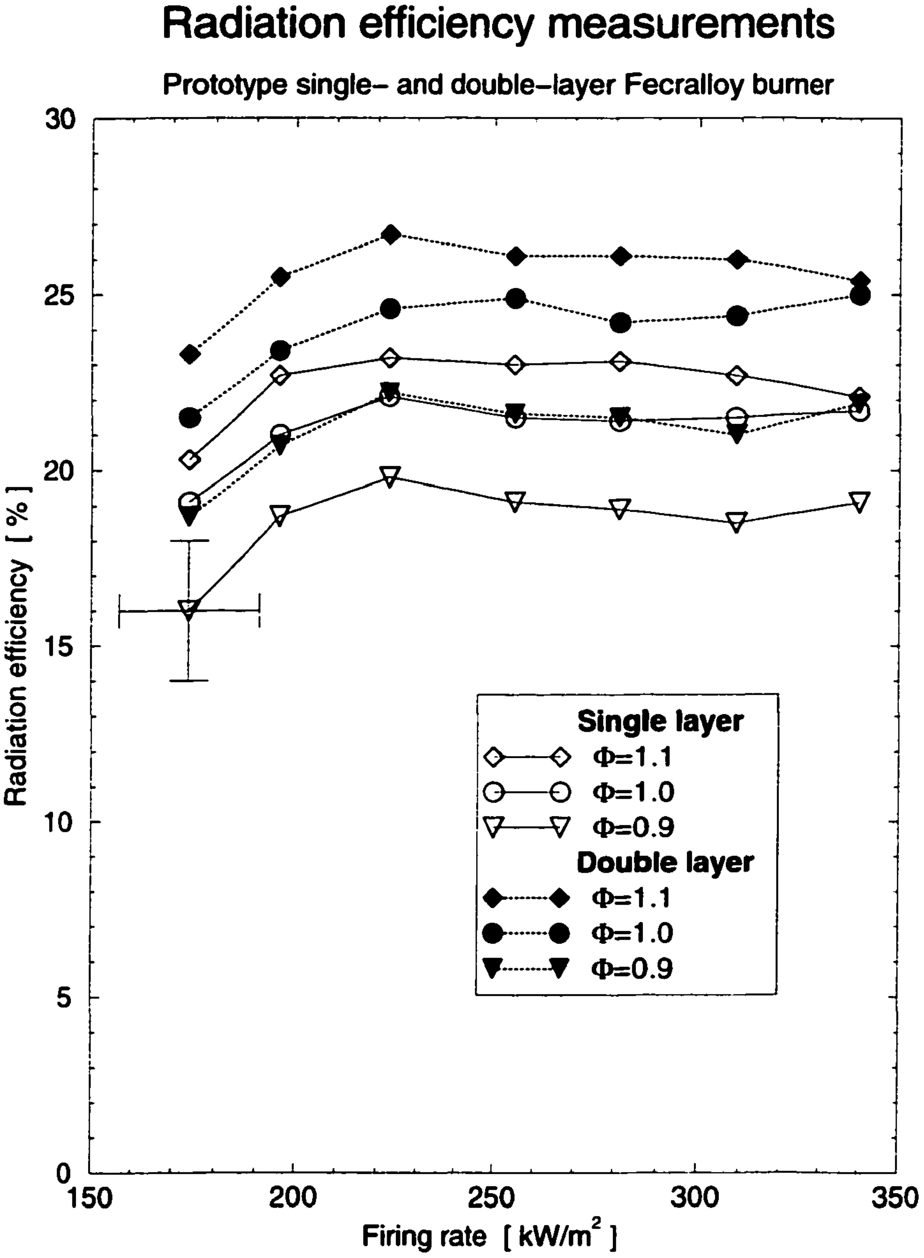

Figure 2.19. Radiation efficiency for the Fecralloy burner: dependence on the firing rate. Experimental uncertainty was ±2%.

the energy emitted by the burner (by both convection and radiation) than smaller and/or non-black calorimeters. Therefore, the data obtained in this case should be very close to the actual total efficiency. In spite of the possible differences, the experimental trends are correctly captured.

At the lower firing range, up to 225 $\frac{kW}{m^2}$, there was an increase in the efficiency for all inlet mixture and configuration combinations. The trend is similar to the one observed for the radiation efficiency. This is another indication that the heat losses from the burner housing to the surroundings were significant at the low firing rates. At higher firing rates, the combined efficiency was approximately constant, about 75–87%, i.e., about the same fraction of the input energy was transferred to the "load" (the black calorimeter described in Section 2.4.2) by any of these two competing modes. An increase in radiation flux resulted in a decrease in the convective flux, and conversely. Note that even though the burner face and the calorimeter were placed very close to each other, still there was cold ambient air entrained that caused convective losses. The magnitude of the total efficiency for the prototype burner was comparable to that of commercial woven metal fiber units, between 75 and 80%, as reported by Leonardi et al. (1998).

No definite trend was observed when changing the burner pad thickness, but a tendency to higher total efficiency for slightly fuel rich mixture ($\Phi = 1.1$) was evident.

2.5.2.3. Surface Temperature for the Prototype Burners

The experimental results showing the variation of the burner surface temperature (measured as described in Section 2.4.6) as a function of the firing rate are reported in Figure 2.21. The burner temperature increased with the firing rate for all inlet mixture and configuration combinations, as expected, since more heat was released when more fuel was available.

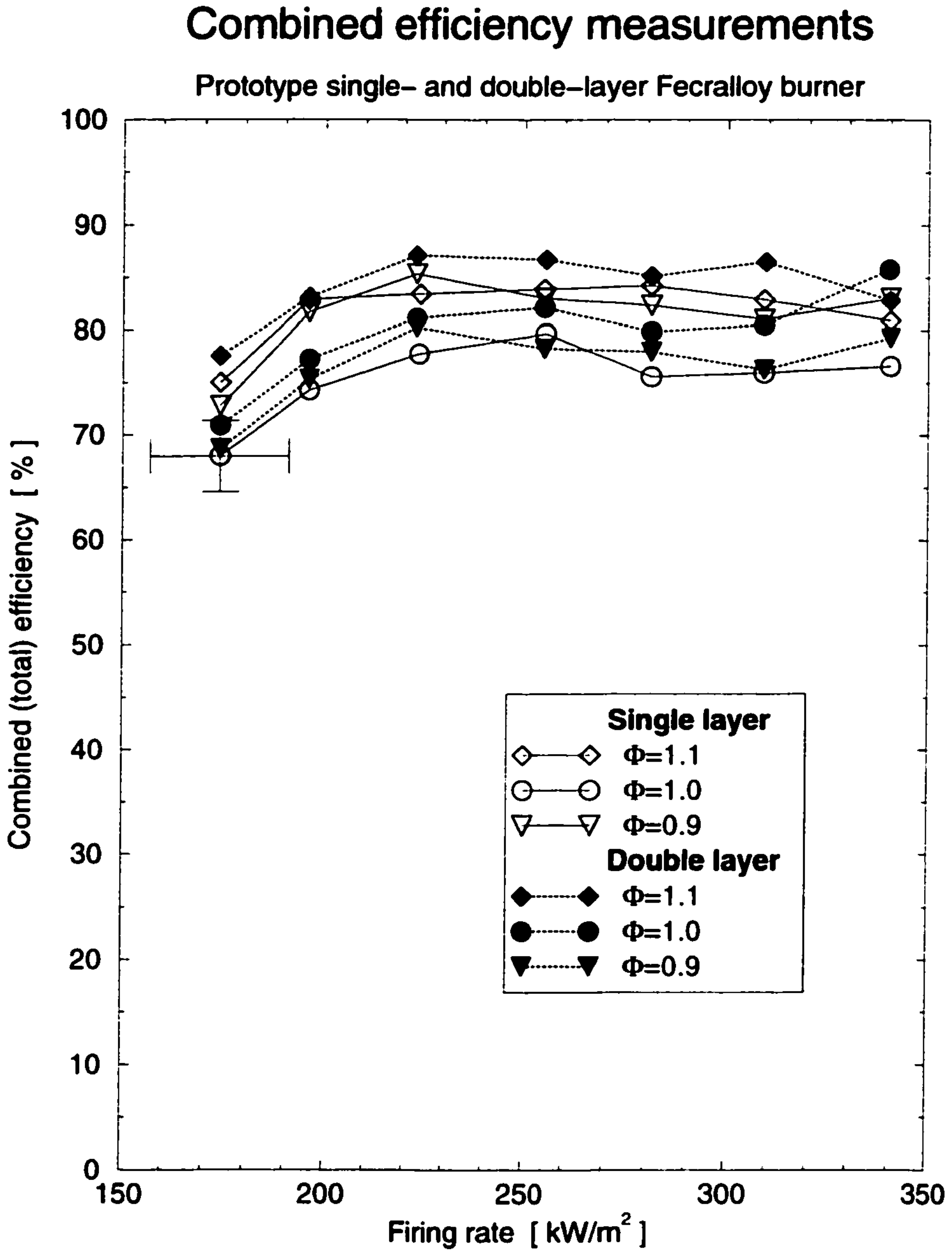

Figure 2.20. Combined efficiency for the Fecralloy burner: dependence on the firing rate. Experimental uncertainty was ±5%.

Experimental uncertainty was estimated by error propagation of the assumed maximum 10% error in the fuel flow rate setting and the radiation thermometer reading error. Since this reading was less than the $30K$ surface temperature variation across the burner surface (due to inhomogeneity of the burner material), the magnitude of the error bars was considered to be $30K$.

The burners with the double-layer flame support pad had a higher surface temperature than the equivalent single-layer burner at the same operating conditions. This increase was consistent to the trends in radiation efficiency, and it can be attributed to the same factors (more complete combustion and greater radiation emitting volume), as described in Section 2.5.2.1.

For both single- and double-layer pads, the pad temperature increased whit the increasing equivalence ratio (from $\Phi = 0.9$ to 1.1), for all firing rates. Again, this is analogous to the radiation efficiency dependence, due the maximum adiabatic flame temperature occurring not at stoichiometric, but rather at a slightly rich equivalence ratio (Turns, 1996).

2.5.2.4. Temperature of the Exhaust Gases

The temperature of the exhaust gases was measured according to the procedure described in Section 2.4.4, using a "fast infrared array spectrometer" (FIAS) with the detector at a distance of approximately 2.5 *cm* from the burner surface. A typical spectrum is shown in Figure 2.22, where the distinctive peaks of CO_2 and H_2O can be easily identified. There is a small difference in the height and width of the peaks for the measured conditions, which result in a small temperature difference among the different conditions, since the sensitivity of the temperature near the maximum (occurring at slightly rich conditions, $\Phi \approx 1.05$) is low.

Figure 2.23 shows that the exit gas temperature increased with the firing rate. The double-layer burners and the richer fuel mixtures both resulted in higher gas

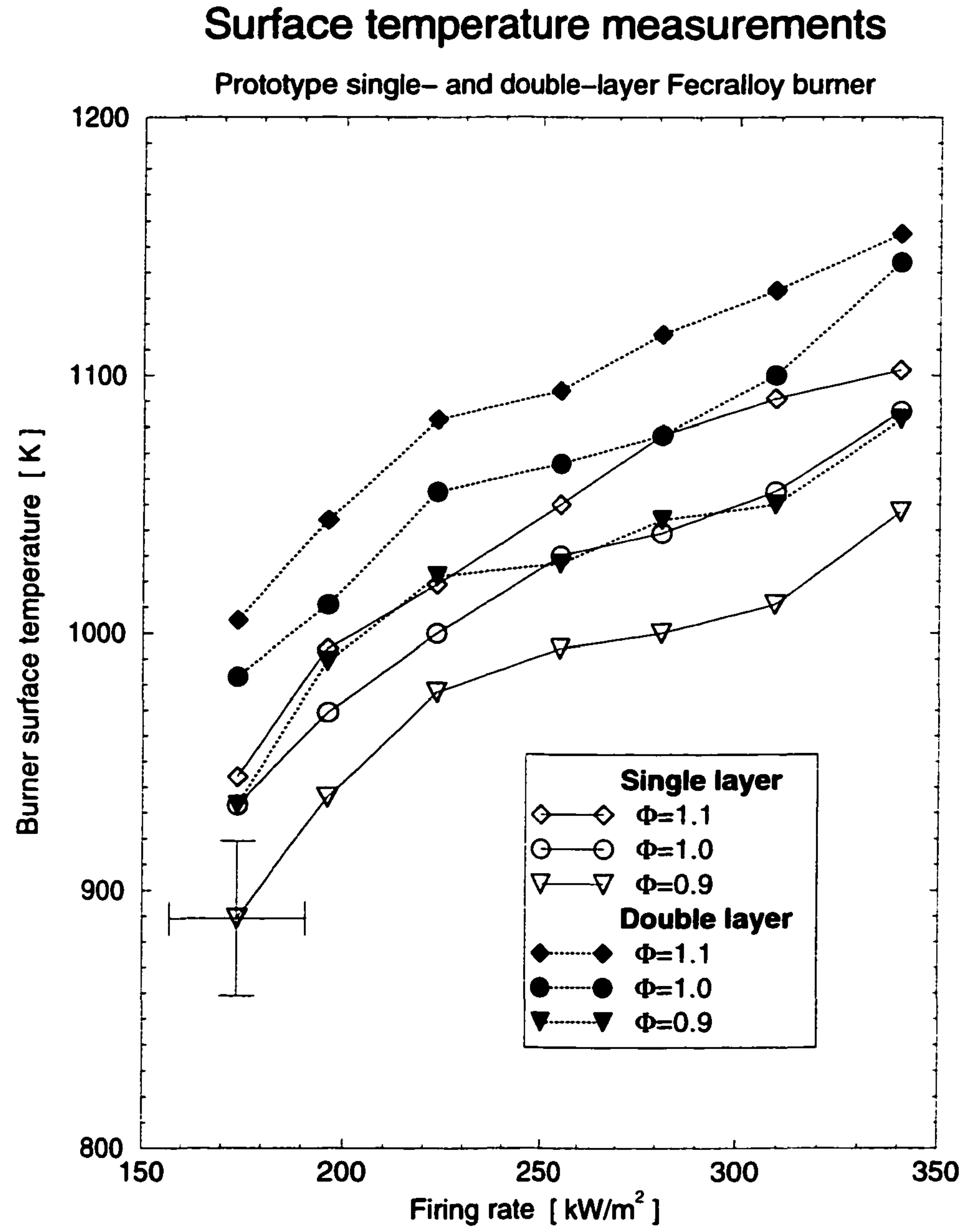

Figure 2.21. Surface temperature for the Fecralloy burner: dependence on the firing rate. Experimental uncertainty was $\pm 30K$.

temperatures, coinciding with the observed surface temperature (Section 2.5.2.3). Note that the gas temperature appeared to be less sensitive to the firing rate change (i.e., the curves were less steep) than the solid surface temperature, possibly indicating that chemical reactions were still occurring after the combustion products left the burner.

The uncertainty in the gas temperature measurements was difficult to estimate, since the FIAS experimental technique and subsequent RADCAL inverse-problem solution was quite involved. However, upon examining the success reported by Ji et al. (2000b), who compared the measured flame temperatures at adiabatic conditions to the corresponding theoretical adiabatic temperatures, it was concluded that the largest source of uncertainty in the present study was the fuel flow rate measurement. A $\pm 30K$ error (same as calculated in Section 2.5.2.3) was considered to be the best estimate in this case.

2.5.2.5. Pollutant Emissions

The variation of the CO, NO and unburned hydrocarbons emissions with the firing rate are shown in Figures 2.24 to 2.26, respectively. All reported concentrations are corrected to a 3% O_2 level in the product stream and expressed on a dry basis. The purpose of correcting to a specific O_2 level is to remove the effects of various degrees of dilution so that true comparison of emission levels can be made, while still retaining a familiar mole-fraction-like variable (Turns, 1996).

The CO emissions increased almost linearly with the firing rate, from about 100–220 PPM[14] at 170 $\frac{kW}{m^2}$ to 400–700 PPM at 340 $\frac{kW}{m^2}$. This increase is attributed to the increased fuel slippage. Note that the radiation efficiency did not increase with the firing rate (except at the lower range, as explained in Section 2.5.2.1), but it was rather constant; therefore, more CO was present at the burner exit for the larger

---

[14] The given range covers the different equivalence ratio and pad thickness conditions.

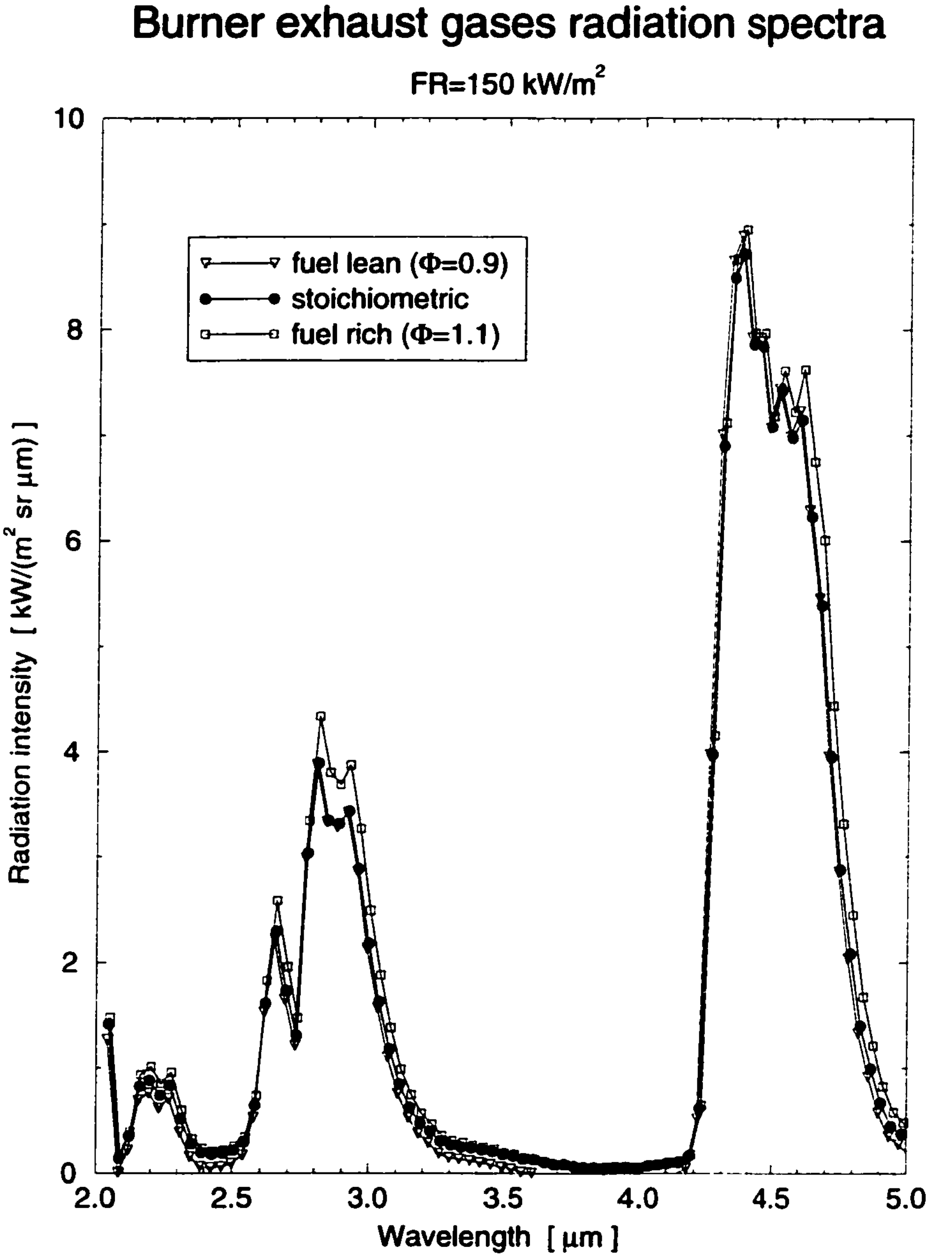

Figure 2.22. Typical emission spectrum for the burner exhaust gases for three different equivalence ratios. Note that there is a small difference in the height and width of the peaks for the measured conditions, which result in a small temperature difference among them.

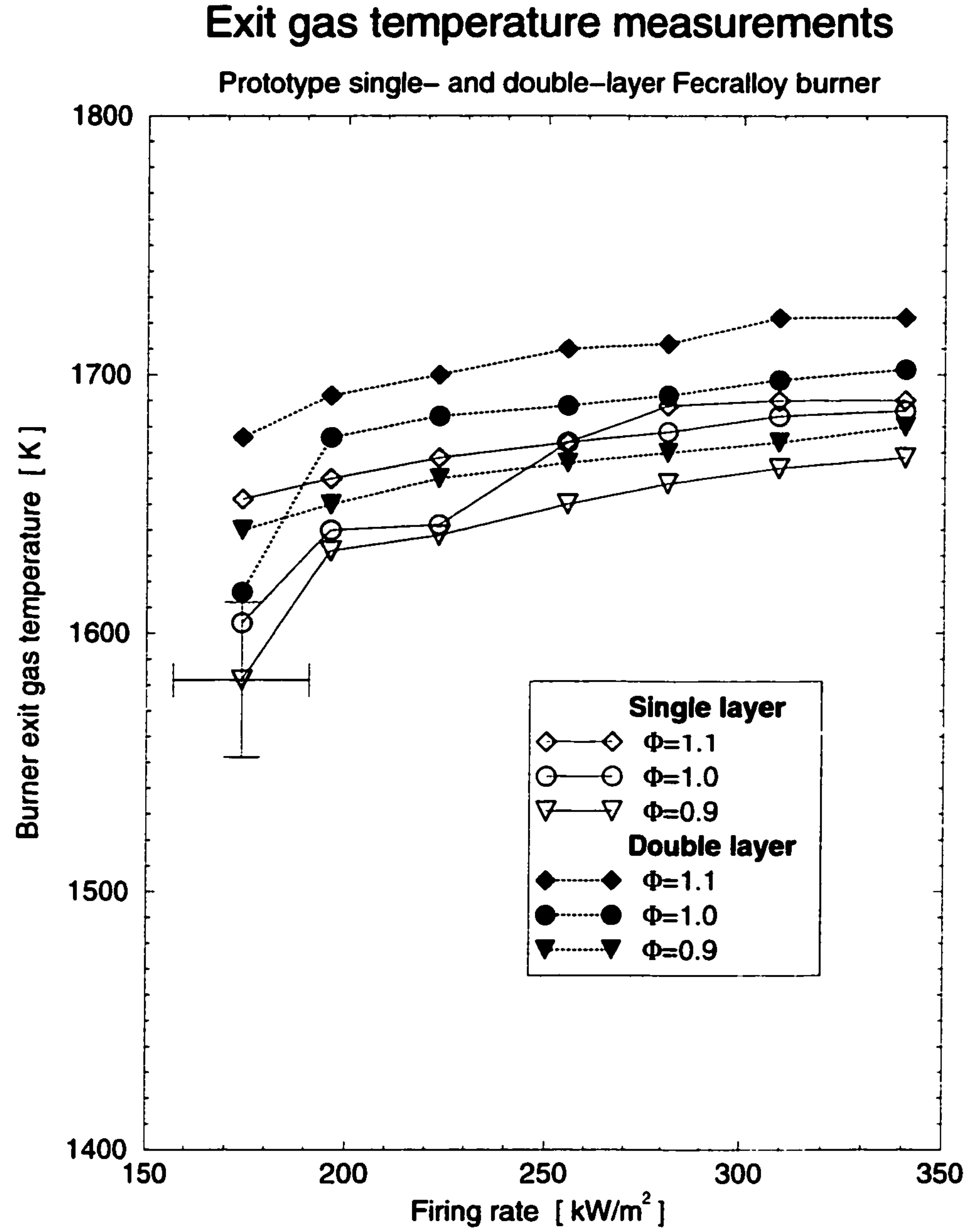

Figure 2.23. Exhaust gases temperature for the Fecralloy burner: dependence on the firing rate. Experimental uncertainty of this measurements based on the spectral intensity was estimated at $\pm 30K$.

firing rates. Little or no difference with the equivalence ratio was observed when a single Fecralloy pad was used. When a double pad was employed, CO emissions were higher for the richer mixtures.

The NO emissions[15] also increased almost linearly with the firing rate, from 5–40 PPM at 170 $\frac{kW}{m^2}$ to 30–140 PPM at 340 $\frac{kW}{m^2}$. This increase followed the same trend as the temperature of the porous pad, as expected, since NO is produced in the high temperature region. Relatively small differences in the NO emissions were measured for the different inlet equivalence ratios for the single-layer burner, but these differences increased at higher firing rates. On the other hand, the double-layer burner showed strong dependence on the inlet mixture compositions, and resulted in higher emissions with increasing equivalence ratio.

---

[15] Since all NO_x was in the form of NO, NO_x results were identical to those for NO.

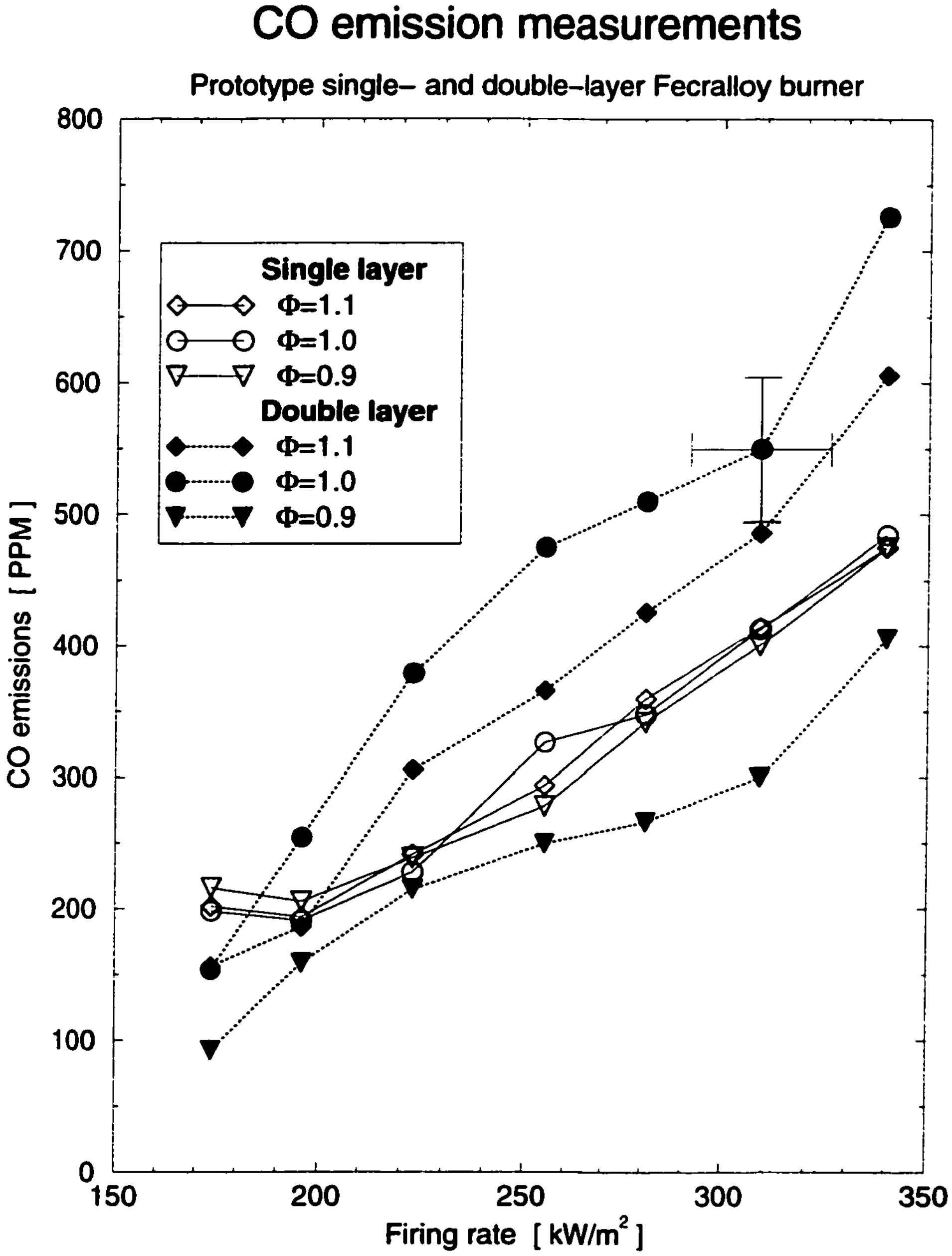

Figure 2.24. Carbon monoxide emissions for the Fecralloy burner: dependence on the firing rate. Experimental uncertainty was estimated to be 10%.

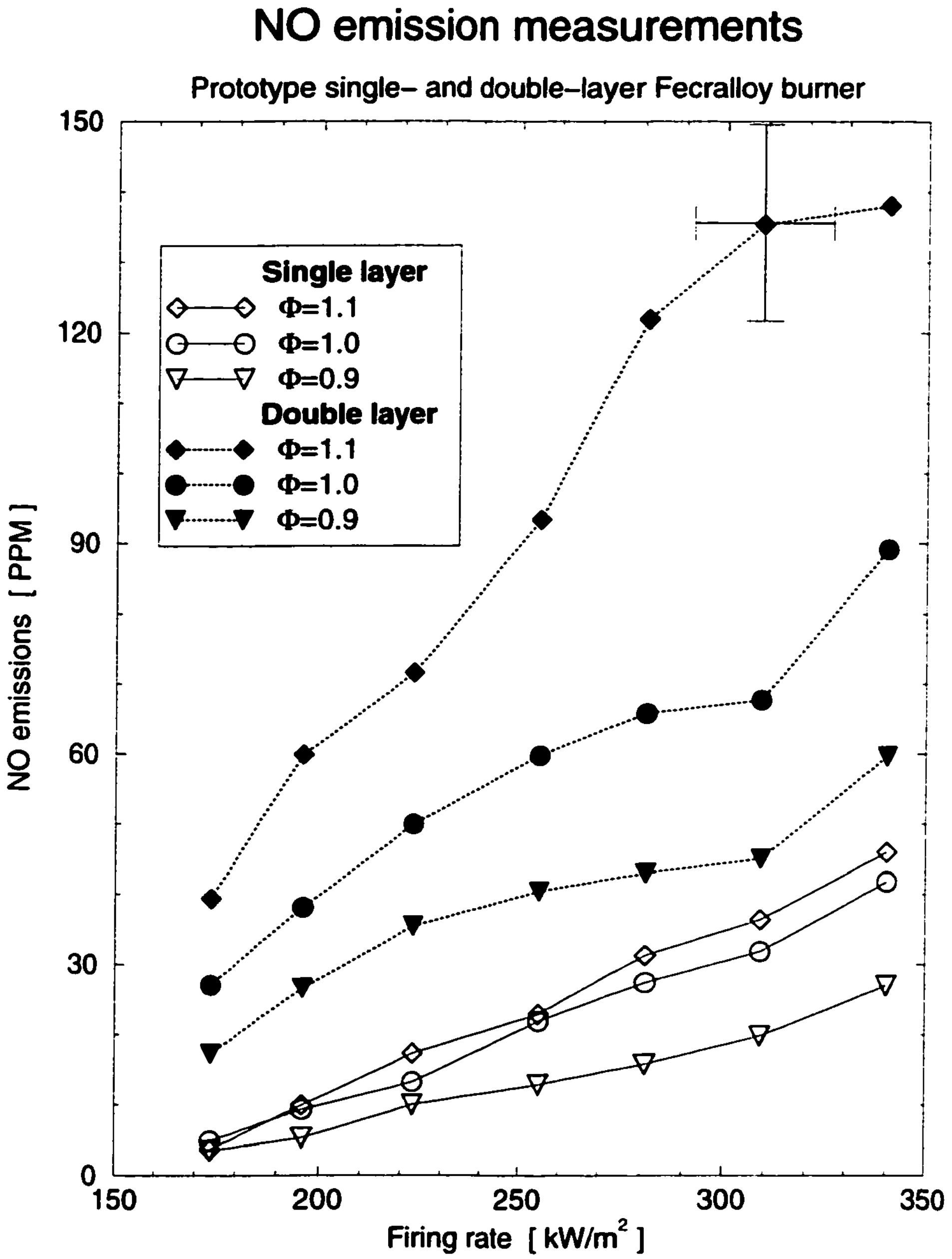

Figure 2.25. Nitrous oxide emissions for the Fecralloy burner: dependence on the firing rate. Experimental uncertainty was estimated to be 10%.

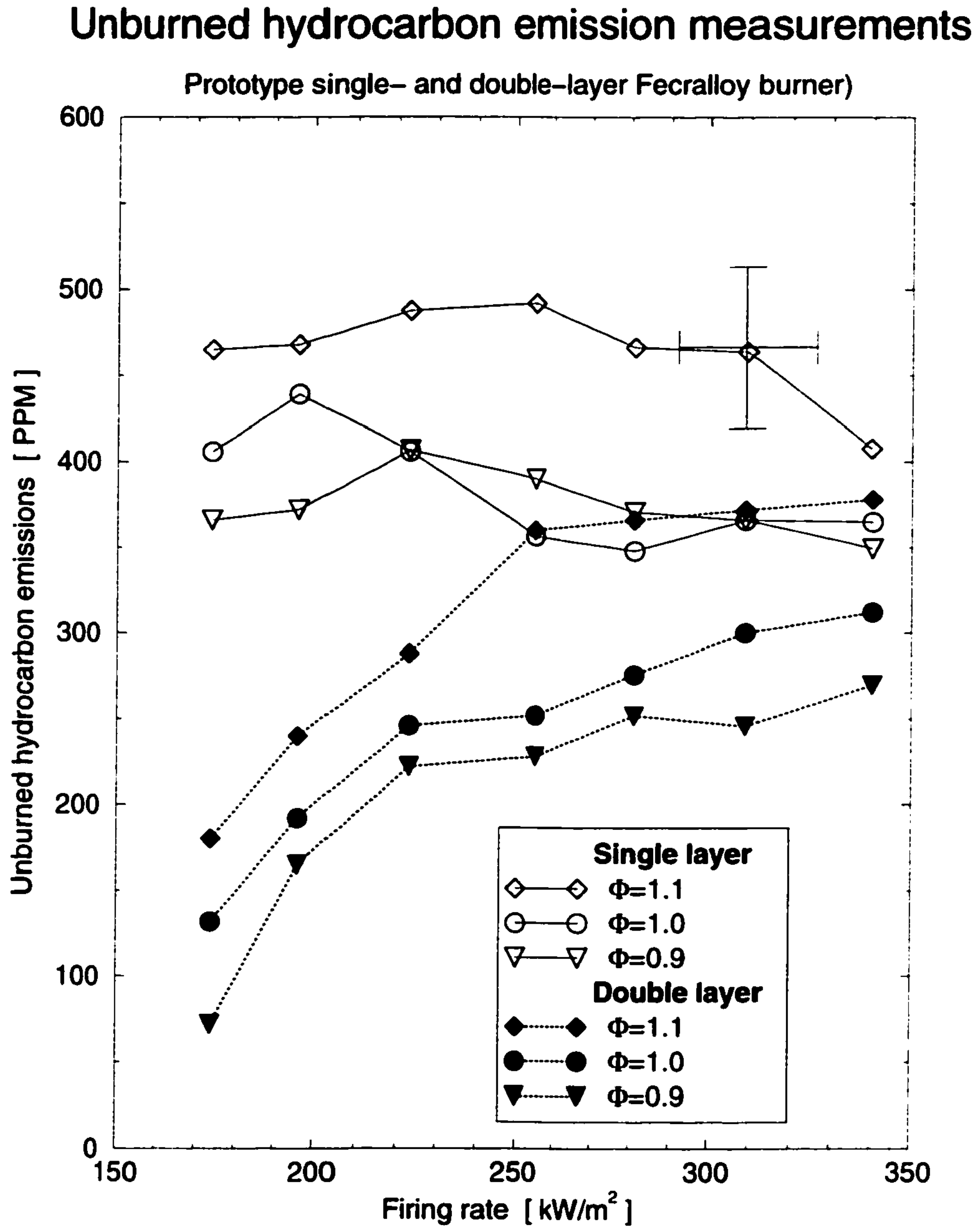

Figure 2.26. Unburned hydrocarbon emissions for the Fecralloy burner: dependence on the firing rate. Experimental uncertainty was estimated to be 10%.

3. MATHEMATICAL MODELING OF A POROUS RADIANT BURNER

3.1. Introduction

A direct-fired porous radiant burner consists of a pervious solid matrix through which a gaseous fuel stream can flow while undergoing an exothermic chemical reaction. The solid can be either a reticulated ceramic, sintered metal or fibrous medium, and the stable flame can be submerged inside of the porous matrix or at the surface.

Gas burners made of reticulated ceramics have been studied in the past (Mital, 1996; Rumminger, 1996; Fu, 1997). When the flame is submerged within the porous solid, convection from the gas to the solid is increased and energy losses due to hot combustion gas exhaust are reduced, creating the conditions for high radiant energy emission. A large surface area per unit volume is desired to enhance the convective heat transfer between the gas and solid phases.

The highest radiation efficiency is attained when the flame is stabilized at an optimum distance from the burner surface. This distance is a function of many system parameters, and a thermal model is required to calculate the most favorable operating conditions. Except for a limited number of attempts, like those made by Mohamad et al. (1994), most combustion models applied to submerged flames have either artificially specified the reaction zone location or thickness, as mentioned in Sections 1.3.1 and 1.3.2. In addition, they have not been successful in predicting the limiting flash-back or blow-out conditions.

When a mixture of gaseous fuel and air flows through the porous matrix and is ignited, a steady-state condition can be achieved if there is a balance between the energy released by the chemical reaction at a certain location and the removal of that energy by a combination of advection, conduction, convection and radiation. Of course, if no such balance is attained, the flame will be extinguished by either flash-back or blow-out phenomena.

The problem of solving a complex system of equations involving chemically reacting flow inside a very complicated (and not very well determined, except for average parameters) geometry, the conjugate effects of several heat transfer modes, with strong property changes due to temperature feedback, and a fully detailed chemistry, becomes almost intractable. Earlier efforts used a simplified overall (one-step chemistry) mechanism (Westbrook and Dryer, 1984), reduced mechanisms (Rumminger, 1996), or even a combination of reduced mechanisms, with post-calculation of the nitrogen oxides emissions (Bouma et al., 1995).

3.2. Mathematical Description

A schematic of a one-dimensional porous radiant burner and the relevant heat transfer modes is shown in Figure 3.1. The one-dimensional formulation used by Singh et al. (1991) has been extended to investigate the thermal performance of the porous radiant burner with an embedded flame. A mixture of gas and air enters an inert porous material at the left (x=0). The material consists of a homogeneous matrix, comprised of one or more layers. The chemical reactions take place within the solid and the flame is anchored at a location that is not known a priori, but rather determined by the interaction of conduction, convection, advection, radiation and chemical energy release due to combustion. As the chemical energy is released in the gas phase, a fraction of it is transferred to the solid (by convection) and subsequently converted to thermal radiation.

3.2.1. Assumptions

A number of assumptions are needed to cast the problem in a form suitable for a *relatively* simple numerical solution.

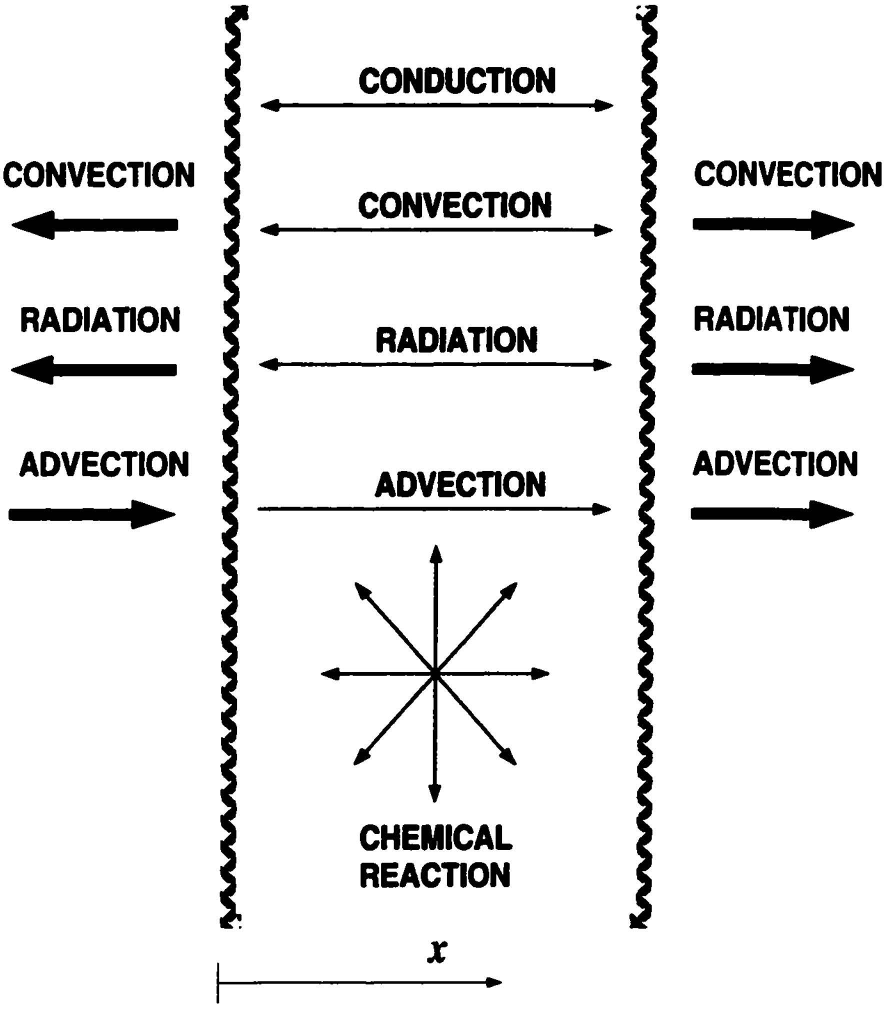

Figure 3.1. Schematic of a one-dimensional porous burner. The relevant heat transfer modes are indicated with arrows: advection by the gas; convection and radiation from the faces; conduction (two phases), convection, radiation and chemical release inside the solid domain.

- The main interest consists of obtaining the performance of the burner in steady-state operation and not during transient situations. Therefore, the model is formulated on a steady-state basis.

- The burner is considered to be very large in directions perpendicular to the inlet velocity so that one-dimensional flow and heat transfer can be assumed. This is a very good assumption since the flame zone is much thinner than the non-axial dimensions of the porous medium.

- Gas flow is unperturbed by the presence of the porous matrix.

- Combustion gases behave as ideal gases.

- Isobaric conditions: the pressure drop across the solid matrix and the changes due to the chemical reaction are negligible. Even though some models include the pressure drop across the solid matrix (e.g., Bouma et al., 1993) using a Darcy-Forchheimer equation (Coulaud et al., 1988):

  $$\frac{dp}{dx} = \kappa_1 \mu u + \kappa_2 \rho_g u^2 \, , \tag{3.1}$$

  which can be justified when modeling ceramic foams, the very small flow resistance induced by the fibrous materials (Nextel and Fecralloy, Section 2.2) make this isobaric assumption a valid simplification.

- Heat losses to the sides of the burner are negligible in comparison to the heat release.

- Homogeneous chemical reaction takes place only in the gas phase; no surface (catalytic) reactions are considered.

- Inlet velocities are small and they remain small enough in spite of the acceleration due to the property changes for the flow to be laminar.

- Solid and gas phases are not in thermal equilibrium, i.e., there is a net exchange due to convection within the matrix. The volumetric heat transfer coefficient is considered to be constant throughout the porous pad, i.e., not a function of the local gas velocity.

- The solid matrix is considered spectrally gray and its thermophysical properties are taken as constant.
- The pore dimensions are small; therefore, the gas opacity is also small, and hence the gas phase can be considered as radiatively non-participating.
- The index of refraction of the medium is assumed to be unity.

Note that no simplification has been made regarding the chemical reaction, which can include any number of elementary steps and intermediate species. The treatment of the chemical kinetics is given in Section 3.4.

3.2.2. Model Equations

The physicochemical problem of a reacting flow across a permeable layer was described in Section 3.1. Then, the equations governing a steady, isobaric, one-dimensional (constant area) flame propagation inside a porous material may be written, using the aforementioned assumptions, as follows (Kee et al., 1988):

Continuity:

$$\dot{m} = \rho_g u A \ . \tag{3.2}$$

(The heater area, A, is considered to be unity in this one-dimensional formulation.)

Species ($k = 1, ..., K$):

$$\rho_g u \frac{dY_k}{dx} + \frac{d}{dx}\left(\rho_g Y_k V_k\right) - \dot{\omega}_k W_k = 0 \ . \tag{3.3}$$

Energy for gas:

$$\rho_g u c_{pg} \frac{dT_g}{dx} - \frac{d}{dx}\left(k_g \frac{dT_g}{dx}\right) + \sum_{k=1}^{K} \rho_g Y_k V_k c_{pk} \frac{dT_g}{dx} + \\ + \sum_{k=1}^{K} \dot{\omega}_k h_k W_k - h_v (T_g - T_s) = 0 \ . \tag{3.4}$$

Energy for solid:

$$\frac{d}{dx}\left(k_s\frac{dT_s}{dx}\right) + h_v(T_g - T_s) - \frac{d\mathcal{F}}{dx} = 0 \ . \tag{3.5}$$

Radiative transfer:

$$\frac{d\mathcal{F}}{dx} = 4\kappa_a\sigma T_s^4 - 2\pi\kappa_a\int_{-1}^{1} I(x,\mu)d\mu \ . \tag{3.6}$$

Equation of state:

$$\rho_g = \frac{p\bar{W}_g}{\mathcal{R}T} \ . \tag{3.7}$$

Equation (3.3) states the balance between (from left to right) advection, diffusion and source (or sink) for each of the K species. In the gas energy equation, Eq. (3.4), the equilibrium between advection, conduction, interdiffusion, heat release and convection to the solid phase is enforced. The solid energy equation, Eq. (3.5), accounts for the balance between conduction, convection to the gas phase and radiation. Note that these equations are tightly coupled[1]. The same convective term, $h_v(T_g - T_s)$, appears as a source in the solid energy equation and as a sink in the solid energy equation. The generation term for the kth species (last term on the left-hand-side of Equation (3.3), $\dot{\omega}_k W_k$) multiplied by the enthalpy of that species, h_k, is included in the gas energy balance. Additionally, the mass continuity equation, Eq. (3.2), is coupled to all species and gas energy balances through the advection terms.

3.2.3. Radiative Transfer

The radiative transfer equation, Eq. (3.8), is given in terms of the radiation intensity, I. A separate problem needs to be solved to determine I.

By performing an energy balance on the radiative energy propagating in a direction $\hat{s}$ within a small pencil of rays, the change in intensity, I, is found by summing the contributions from emission, absorption, scattering away from the direction $\hat{s}$ (outscattering), and scattering into the direction $\hat{s}$ (inscattering). The radiative transfer equation can be expressed as (Modest, 1993):

---

[1] These are 53 coupled equations: continuity, gas energy, solid energy, radiant energy and 49 species.

$$\frac{1}{c}\frac{\partial I}{\partial t} + \frac{\partial I}{\partial s} = n^2 \kappa_a I_b - \kappa_a I - \sigma_s I + \frac{\sigma_s}{4\pi}\int_{4\pi} I(\hat{s}')\Phi(\hat{s}',\hat{s})d\Omega' \, . \tag{3.8}$$

In the above expression, the emission and absorption coefficients (first two terms on the right-hand-side) were considered to be identical. The availability of the absorption coefficient, κ_a, scattering coefficient, σ_s, and the scattering phase function. $\Phi(\hat{s}',\hat{s})$, for porous materials is discussed in Section 4.2.

The discrete ordinates (also known as S_N) method (Siegel and Howell. 1992; Modest, 1993) is used to transform the equation of radiative transfer, Equation (3.8), into a set of simultaneous ordinary differential equations. First proposed by Chandrasekhar (1960) in his book on stellar and atmospheric radiation, the discrete ordinates method was first extensively applied to neutron transport (Lee, 1962; Lathrop. 1966; Carlson and Lathrop, 1968). An advantage of this method over other approximations is that it may be carried out to any arbitrary order and accuracy.

The discrete ordinates (S_N) method is based on a discrete representation of the directional variation of the radiation intensities. A solution to the transport problem is found by solving the equation of transfer for a set of individually distinct directions spanning the total solid angle range of 4π. It is simply a finite differencing of the directional dependence of the radiative equation of transfer, and the integrals over the solid angles are approximated by numerical quadratures.

The one-dimensional version of Equation (3.8) is solved here for a set of N different directions $\hat{s}_i = 1, 2, ..., N$, and the integrals over direction are replaced by the numerical quadratures, that is,

$$\int_{4\pi} f(\hat{s})d\Omega \approx \sum_{i=1}^{N} w_i f(\hat{s}) \, , \tag{3.9}$$

where the w_i are the quadrature weights associated with the directions $\hat{s}_i$. Using the approximation given by Equation (3.9), realizing that the time dependence of the radiative intensity may be neglected when accounting for the heat transfer within a porous burner[2], and since the index of refraction was assumed to be unity, Equation (3.8) becomes:

$$\mu_i \frac{dI(x,\mu_i)}{dx} = \kappa_a(x) I_b(x) - \beta I(x,\mu_i) + $$
$$+\frac{\sigma_s(x)}{4\pi} \sum_{j=1}^{N} w_j I(x,\mu_i) \Phi(x,\mu_i,\mu_j) \ , \ i = 1,2,\ldots,N \ , \tag{3.10}$$

(with $\beta = \kappa_a + \sigma_s$) subject to the boundary conditions:

$$I(x_w,\mu_i) = \phi I_b(T_{surr}) + (1-\phi)[\varepsilon_w I_b(x_w) + \frac{\rho(x_w)}{\pi} \sum_{\hat{n}\cdot\hat{s}_j} w_j I(x,\mu_j)\mu_j] \ , \ \hat{n}\cdot\hat{s}_j > 0 \ . \tag{3.11}$$

Equations (3.10) together with the boundary conditions given by Equations (3.11) constitute a set of N simultaneous, first-order, linear ordinary differential equations[3] for the unknown intensities in the discretized directions. If scattering is present ($\sigma_s \neq 0$), the equations are coupled in such a way that generally an iterative solution scheme is necessary.

The discrete ordinates methodology is capable of accommodating different types of quadrature schemes, such as the traditional Gaussian, Lobatto, Chebyshev, Newton-Cotes (Kopal, 1961) or newer types like the one developed by Fiveland (1987). The differences between the various quadratures lie in the values of the weights (w_j) and the direction cosines (μ_j). The user must generally use a few different quadratures and orders to assess which is the most suitable for the given problem (Kumar et al., 1990). Fiveland (1987) and Truelove (1987) have observed that different sets of ordinates may result in considerably different accuracy. According to Modest (1993), the choice of the quadrature scheme is arbitrary, but it is customary to choose sets of weights and directions that are completely symmetric (i.e., invariant after any 90° rotation) and that satisfy the zeroth, first and second moments. The weights and

---

[2] The factor $1/c$ in the first term of Equation (3.8) is so small that the time dependence term may be safely neglected in almost all heat transfer applications (Modest, 1993).

[3] They are partial differential equations in 2D or 3D. Additionally, in multi-dimensional geometries, $N(N+2)$ equations are needed for a given order N.

ordinates used here for the one-dimensional problem are taken from Lathrop and Carlson (1965) and are shown in Table 3.1.

Table 3.1. Discrete ordinates for the one-dimensional S_N approximation.

Order of Approximation	Ordinates μ_i	Weights w_i
S_2	0.5773503	6.2831853
S_4	0.2958759	4.1887902
	0.9082483	2.0943951
S_6	0.1838670	2.7382012
	0.6950514	2.9011752
	0.9656013	0.6438068
S_8	0.1422555	2.1637144
	0.5773503	2.6406988
	0.8040087	0.7938272
	0.9795543	0.6849436

3.2.4. Boundary Conditions

The appropriate boundary conditions for the burner-stabilized system of equations presented in Section 3.2.2 may be deduced from the early work of Curtiss and Hirschfelder (1949). Boundary conditions are needed for the dependent variables: mass flow rate, $\dot{m}$, species concentrations, Y_k, gas temperature, T_g, and solid temperature, T_s. Note that the boundary conditions for the separate problem of finding the radiation intensity, I, were given in Section 3.2.3.

The mass flow rate, $\dot{m}$, is a known constant determined by the desired firing rate and equivalence ratio. The gas temperature at the inlet is found enforcing that all the heat conducted downstream is advected back into the computational domain:

$$\dot{m}\, c_{pg}(T_1 - T_{in}) = k_{g1}\left.\frac{dT}{dx}\right|_1 .$$

Note that a simple Dirichlet boundary condition (as in the original PREMIX code) does not work properly due to unaccounted heat losses. The temperature gradient at the inlet is not zero in some cases (especially at low firing rates), and the fixed-temperature boundary condition results in energy conducted upstream that does not return into the computational domain.

The species concentrations boundary conditions at the cold boundary are determined by a balance between advection and diffusion, which corresponds to specifying the mass flux fractions, $Y_k + \rho_g Y_k V_k A/\dot{m}$, for all species. These quantities are zero for all species except CH_4, O_2 and N_2.

Vanishing gradients are imposed for the gas temperature and the mass fractions at the outlet boundary (beyond the front face of the burner), except for the O_2 and N_2, which are set to specified values to allow for back-diffusion.

The solid faces are subjected to convective heat transfer to the gas and also exchange radiation with the surroundings. It should be mentioned here that the effect of the reduction of the solid surface area due to porosity should be accounted for in the convection and conduction terms; however, since the fibers are of small dimensions and thus optically very thin, the entire area (and not only the fraction $1-\phi$) is considered to exchange thermal radiation with the surroundings:

$$(1-\phi)h_L(T_{gL} - T_{sL}) + (1-\phi)k_s\left.\frac{dT_s}{dx}\right|_L = \varepsilon_L\sigma(T_{sL}^4 - T_{surr,in}^4) , \qquad (3.12)$$

$$(1-\phi)h_R(T_{gR} - T_{sR}) + (1-\phi)k_s\left.\frac{dT_s}{dx}\right|_R = \varepsilon_R\sigma(T_{sR}^4 - T_{surr,out}^4) . \qquad (3.13)$$

3.3. Volumetric Heat Transfer Coefficient

The thermal coupling between the solid and gas phases is affected through the volumetric heat transfer coefficient, h_v. It is difficult to predict the coefficient for the complex, irregular geometries of fibrous materials. This parameter plays an important role in determining the nature of the solution; therefore, it is necessary to obtain the data through experimentation (Appendix B). Under certain assumptions, a "single-blow technique" and an inverse-problem solution can be used to determine the coefficients for a given material (Fu et al., 1998b).

3.4. PREMIX Chemical Mechanism Description

In order to close the system of differential equations (Equations (3.2) to (3.7)), it is necessary to model the source terms. The net chemical production rates, $\dot{\omega}_k$, of each species results from a competition between all of the chemical reactions involving that species. The PREMIX code (Kee et al., 1988) (part of the CHEMKIN package) was used to solve the partial differential equations. A detailed account of the program modifications is included in Section 3.5.

The chemical kinetics was simulated assuming that each reaction proceeded according to the law of mass action and that the forward rate coefficients, k_f, were in the modified Arrhenius form:

$$k_f = a_1 T^{a_2} \exp\left(-\frac{\mathcal{E}}{\mathcal{R}T}\right) . \tag{3.14}$$

The details of the chemical reaction equations and the thermochemical properties were found in the user's manual for CHEMKIN (Kee et al., 1980).

The constants a_1, a_2 and $\mathcal{E}$ for the Arrhenius expressions were obtained from the GRI-Mech 2.11 mechanism (Bowman et al., 1996). GRI-Mech 2.11 is a compilation of 277 elementary chemical reactions and associated rate coefficient expressions and thermochemical parameters for the 49 species in the reactions (Appendix E). It differs from the version 1.2 release in that it includes nitrogen chemistry relevant to natural gas chemistry and reburning[4].

The thermophysical properties of the individual species, such as thermal conductivity and diffusion coefficient, were evaluated using Stockmayer potentials. An extended Euken-Hirshfelder correction for polyatomic species was also included. A more detailed description can be found in Kee et al. (1983). The gas mixture thermal conductivity was determined from the individual component conductivities by means of an empirical combination averaging formula, as done by Mathur et al. (1967).

3.5. Computer Program Modifications

The original code was designed to simulate a premixed burner-stabilized flame. Several modifications on the computer code were necessary in order to simulate a partially premixed flame embedded in a porous matrix.

In addition to the equations corresponding to mass continuity (Equation (3.2)), species conservation (Equation (3.3)) and gas energy balance (Equation (3.4)), an additional energy equation for the solid phase (Equation (3.5)) was included in the computer program. This new equation was coupled to the gas energy equation through a convective term of the form $h_v(T_g - T_s)$. Note that this term appears with opposite signs at the rightmost position of the right-hand-side of Equations (3.4) and (3.5). There were then a total of 53 coupled equations: continuity, gas energy, solid energy, radiant energy and 49 chemical species.

The treatment of the radiation heat transfer is of great importance in the modeling. The discrete ordinates method (Equations (3.10), with boundary conditions given by (3.11)) was used in an external subroutine. This subroutine was called only after several iterations (about 50 to 100) of the energy equations, to avoid the numerical

---

[4] GRI-Mech 3.0 became recently available. It is a compilation of 325 elementary chemical reactions and associated rate coefficient expressions and thermochemical parameters for the 53 species involved in them. It replaces the previous releases of GRI-Mech, both versions 1.2 and 2.11. It differs from the previous release in that kinetics and target data have been updated, improved, and expanded. Propane and C2 oxidation products have been added, and new formaldehyde and NO formation and reburn targets included.

instabilities[5]. The radiation intensity results were used to calculate the radiant energy source (last term on the left-hand-side of Equation (3.5)) using Equation (3.6).

The downstream boundary conditions for O_2 and N_2 species were changed from the zero gradient used for a premixed flame to a non-zero gradient or fixed-value type, as indicated in Section 3.2.4.

Another important change was that the solid phase solution domain was not set to be the same as the gas phase domain, since the former is smaller than the latter. This feature allowed to ensure that an embedded flame represented a stable "true" solution and not a forced one. Gas-only regions of arbitrary size are considered ahead and after the porous structure.

The input data file containing the problem definition was also modified to include the many additional parameters needed for solving the new problem. Volumetric heat transfer coefficient, length of the solid phase, thermophysical and radiative properties of the solid material, and oxygen and nitrogen concentrations downstream were all included in the input file. A sample input is provided in Appendix F.

The original PREMIX uses an adaptive grid selection scheme that adds new points, actually partitioning in half the intervals at which the tolerances (in value or gradient change) for the significant variables are not satisfied. However, this algorithm does not eliminate unnecessary points during the iterative solution procedure (see Section 3.6) and, consequently, when the flame location changes substantially, a large concentration of grid points appears at the old flame location, even though there is no need for them (gradient and curvature for all variables are small). This increase in the size of the numerical problem results in an increased computational expense and, many times, in the exhaustion of the allocated memory space. Hence, a new subroutine was added after new grid points are inserted by the adaptive grid scheme. A quick verification for their usefulness is performed and, if unnecessary grids

---

[5] The convergence speed of the numerical algorithm for the 52 coupled equations was much slower than the convergence speed in solving the radiative transfer equation, which is only dependent on the temperature distribution of the solid. If the radiative source term was updated too often, convergence was hindered, since the modified dampened Newton method had to chase a "moving" target solution. A brief description of the modified dampened Newton method is included in Appendix G.

are detected, they are eliminated. In this manner, some solutions that required 200 points when using the original program could be accurately described with less than 70 after modifying the gridding routine. Extensive grid-independence studies were carried out to verify that both solutions were identical and that further convergence tolerance reductions did not change the numerical results.

Finally, the output and restart files were also altered to include the solid temperature data.

Figure 3.2 shows schematically the most relevant modifications for the computer program: the new parameters, equations, boundary conditions and subroutines that transformed the premixed burner stabilized program into a radiant burner code. A simplified flow chart for PREMIX is shown in Figure 3.3.

3.6. PREMIX Solution Strategy

The resulting system of equations was stiff and it was difficult to obtain a converged solution if the initial estimate was not appropriate. In view of this fact, and using the restart capabilities of PREMIX, a converged solution from a similar problem was used as an initial approximation, and the variables were changed in steps until the desired conditions were achieved.

For example, the solution for a surface, burner-stabilized flame at a desired firing rate was used to solve for the flame inside the high-porosity matrix with $h_v = 10^7 \frac{W}{m^3 K}$; the emittances of the solid faces were also set to zero. The high value of h_v guaranteed that the solid temperature was almost identical to the gas temperature, which coincided with the initial guess for that variable; the zero emittance avoided the large temperature gradients at the two faces due to the radiative losses from high temperatures solid faces.

After this, and using the previous solution as a starting point, the emittance ε was increased in many steps up to the final value (0.88 for Nextel, 0.65 for Fecralloy); usually between a few hundred to several thousand steps were needed. Then, the

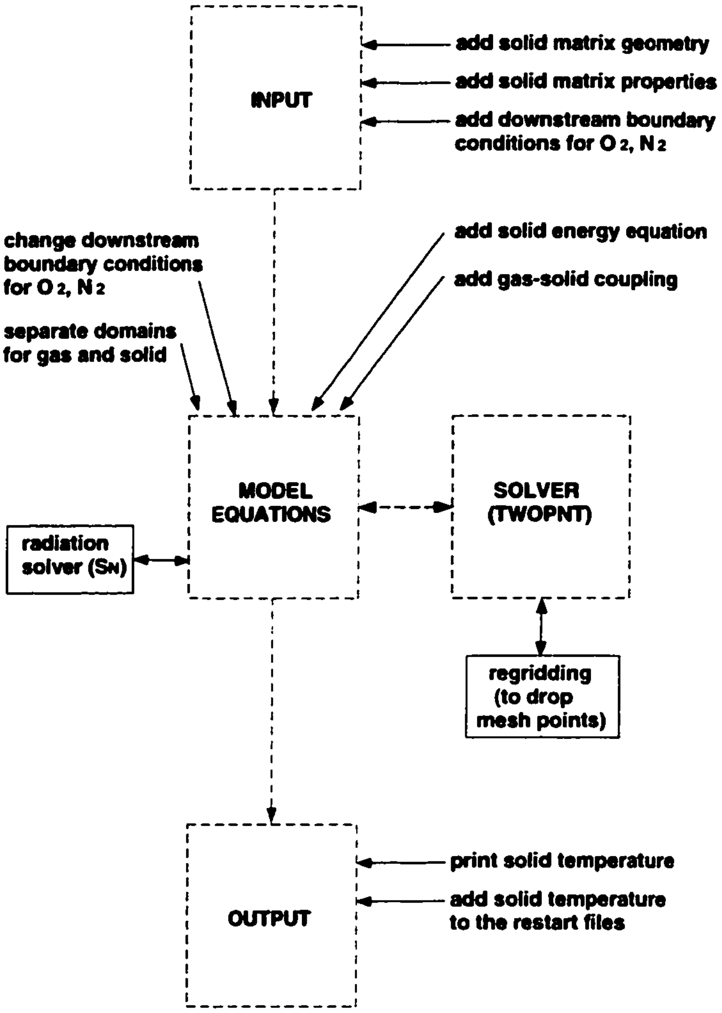

Figure 3.2. Diagram of the changes implemented in the PREMIX computer program. The gray dashed boxes correspond to the original code; the black solid lines indicate the necessary modifications and new subroutines to solve a radiant burner.

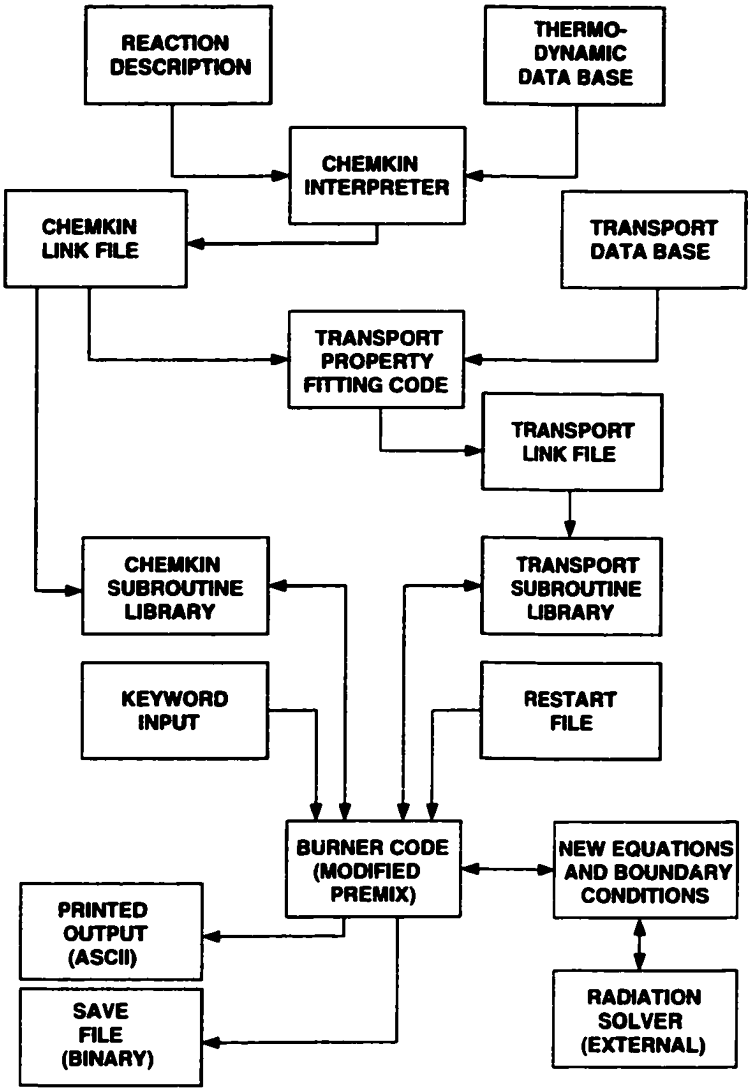

Figure 3.3. A flow chart for the PREMIX computer program. The reaction description and thermodynamic and transport data bases are given by GRI-Mech 2.11. The CHEMKIN interpreter generates the "link" files that become the libraries to be compiled together with the burner code. The user supplies the problem parameters (initial guesses, material properties, flow rate, boundary conditions, numerical algorithm parameters) in the "keyword input", and the results are printed to both ASCII and binary files. Alternatively, the initial guesses can be obtained in a more detailed way from a restart file (which is the binary output of a previous problem solution.

volumetric heat transfer coefficient h_v was decreased in steps of about 10 $\frac{kW}{m^3K}$ (about 1% of the baseline value, larger steps became unstable) until the desired value was attained.

The same procedure was used to vary other parameters: inlet gas flow rate, equivalence ratio, extinction coefficient, solid thermal conductivity, etc.

A special note regarding the nodalization of the computational domain is that "clustering" of between 5 to 10 grid points at the upstream face of the solid phase was necessary. These nodes helped to "lock" the flame solution inside the solid material at the beginning of the simulation, when the overall grid was coarse. Otherwise, the numerical propagation speed of the reaction zone across that initial coarse grid was too fast and resulted in a gas-phase-only flame upstream of the burner[6]. It is important to stress that this did not result in a physically unacceptable solution. Once a solution was obtained, the flame characteristics were independent of the discretization scheme.

3.7. Code Validation

The computer code was verified in several simple ways[7]. First, both the overall and local energy balances were corroborated. According to the global balance, the energy transported to the burner (i.e., chemical and sensible energy of reactants) leaves the burner in the form of chemical and sensible energy of the products, plus the radiation from the solid matrix. The local energy budget was also audited, and the typical magnitude of the different components are compared in Figures 3.4 and 3.5, for the gas and solid phases, respectively. Positive quantities indicate that the corresponding heat transfer mode increases the local temperature; conversely, negative sign indicates a local temperature reduction. Note that the coarse convergence (i.e., the curves are not smooth) is mainly due to the presence of derivatives in the terms. Temperature distributions are smooth (see, for example, Figure 5.1), but the

---

[6] Since PREMIX is a steady-state code, the actual transient that occurs when a burner is lit in the laboratory was artificially reproduced here.

[7] More details regarding the validation of the code against a radiant burner prototype, including how all properties were obtained and/or estimated is included in Chapter 4.

numerical differentiation and the non-uniform grid spacing cause the oscillations in the energy budget terms.

The major component in the gas energy balance (Figure 3.4) is given by the chemical source, which peaks at the flame location. In a free flame, stabilization results from balancing the heat release with the heat conduction (Turns, 1996). In an embedded flame, however, the fraction of heat removed by conduction is less than that for a free flame, since the other mechanisms (mainly advection and convection to the solid phase[8] also remove heat from the gas. It is interesting to note that both the conduction and convection components change sign at some location upstream of the flame; they are greater than zero at the entrance (i.e., contributing to the preheating of the fuel mixture) and then become negative to stabilize the reaction zone by removing the chemical energy release. The advection component is negative at the entrance, since the incoming gas mixture is being heated. Downstream of the reaction zone, the gas temperature does not change significantly and the advection component becomes small. Finally, it can be seen that the local energy change due to species interdiffusion is negligible.

The solid phase energy budget is given by the balance between convection (from the gas), conduction and radiation. As expected, the convection component has the largest magnitude, and its peak coincides with the flame location, as seen in Figure 3.5. There is an entrance region (approximately $x < 0.06\ cm$) where this component is negative, indicating that the solid matrix is actually transferring energy to the gas (i.e., preheating.) The other two heat transfer modes, conduction and radiation, follow similar trends but are opposite to that of convection. They are greater than zero in the preheat region, since they provide the means for the heat from the flame region to be transfered upstream, and they are negative at the reaction zone, where they remove the heat supplied by the gas. Note that positive values correspond to energy gain for the porous matrix element at the given location. For

---

[8] Gas phase radiation has been neglected in this analysis, according to the simplifying assumptions listed in Section 3.2.1.)

example, at $x = 0.1$ *cm*, the temperature of the solid increases by convection (at the expense of the gas energy), but decreases by radiation and conduction (to other parts of the participating porous material, which are at lower temperature).

After auditing the local and global energy balances, two limiting cases were verified. First, when the convective heat transfer coefficient vanishes, the solution becomes identical to the original code solution for a burner-stabilized flame at the given firing rate and reactant mixture composition; second, when the volumetric heat transfer coefficient is set to a large value, gas and solid temperature distributions were identical. Additionally, the temperature distributions corresponding to very low or very high firing rates were the trivial solution; with no energy release, there is no change in temperature and composition due to flame extinction and blow-off, respectively.

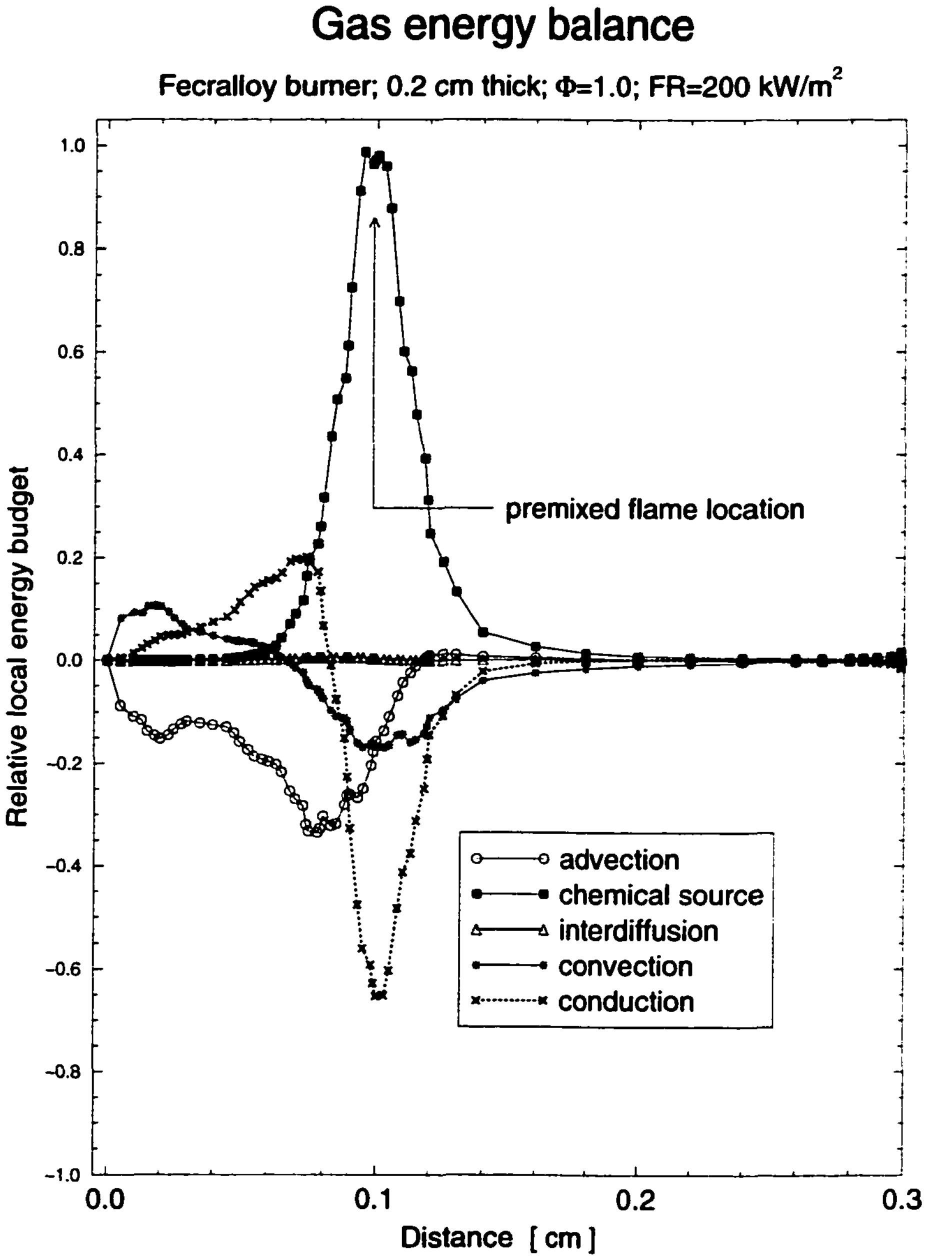

Figure 3.4. Local energy budget (gas phase) inside a radiant burner. The different components have been normalized to make the peak chemical heat release equal to unity. Note that radiation from the gas phase has been neglected. The small oscillations are due to the coarser convergence of the derivatives.

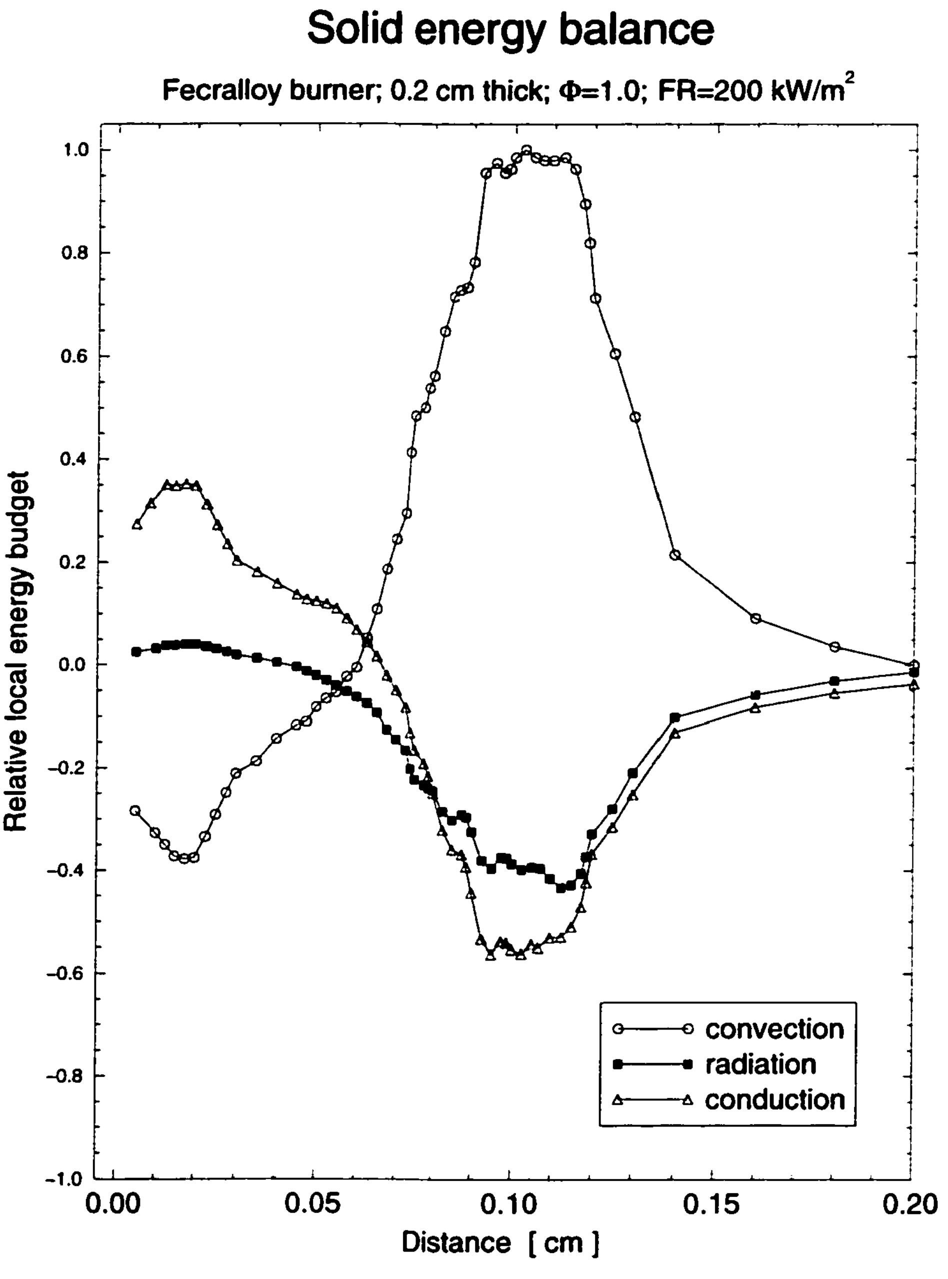

Figure 3.5. Local energy budget (solid phase) inside a radiant burner. The different components have been normalized to make the peak convection equal to unity. Note that positive values correspond to energy gain for the porous matrix element at the given location. The small oscillations are due to the coarser convergence of the derivatives.

4. COMPARISON OF MODEL PREDICTIONS WITH EXPERIMENTAL DATA

4.1. Introduction

In order to asses the computational model, the experimental results obtained with a prototype woven metal fiber burner were compared with the results of the numerical simulations. The Fecralloy burner is described in detail in Section 2.5. The main difficulty involved determining all the necessary properties for the porous flame support pad material, some of which were not readily available, as discussed in the following section.

4.2. Characteristics of Porous Matrix

The high sensitivity of chemical reactions and radiative transfer to temperature required careful consideration of the properties of the porous medium (Rumminger, 1996). For the model described in Chapter 3, the following properties were needed: effective thermal conductivity (k_s), extinction coefficient (β), scattering coefficient (σ_s), porosity (ϕ), and volumetric (convective) heat transfer coefficient (h_v). Additionally, at least approximate values for the specific heat (c_p) and density (ρ_s) were needed (even though the sought solution corresponded to a steady-state condition and, therefore, the term containing $\rho_s c_{p,s}$ was not included in the model equation for the solid phase, Equation (3.5)), since the numerical algorithm resorted to time-stepping to shift the solution domain closer to the convergence region.

Some of the properties were provided by the manufacturer of the flame support material and were included in Table 2.1. However, the volumetric heat transfer coefficient and the radiation properties (extinction and scattering coefficients) were not available from the aforementioned source.

4.2.1. Volumetric Heat Transfer Coefficient

An attempt to measure the volumetric heat transfer coefficient using the single-blow technique (Appendix B) did not result in a useful correlation for Fecralloy, as described in Appendix Section B.5.

Measurements of heat transfer between single heated wires 20 μm in diameter in an air stream perpendicular to the wire axis have been carried out by Jakob and Hawkins (1957), to obtain the relationship $Nu = 0.88 Re^{0.31}$ for $Re < 1$. The coefficient decreased and the exponent increased as the Reynolds number became larger.

A pad comprised of small diameter of woven wires is rather different from a single isolated wire, and experimental data on small diameter metallic wires at low Reynolds numbers are scarce. Golombok and Shirvill (1990) carried out a study using a regenerator technique for sintered Fecralloy fibers (porosity 80%). They also obtained a power-law relationship between the Nusselt and Reynolds numbers:

$$Nu = 0.04 Re^{0.53}, \quad \text{for} \quad Re < 0.4 \ , \tag{4.1}$$

$$Nu = 0.10 Re^{1.64}, \quad \text{for} \quad Re > 0.4 \ . \tag{4.2}$$

Equation (4.1) is in good agreement with the results reported by Žukauskas (1972), who suggested that an exponent of 0.5 was applicable at low Reynolds numbers (Hausen, 1983).

At the thermal input range of interest for fiber burners (i.e., < 1500 $\frac{kW}{m^2}$ of equivalent natural gas with $Re < 0.3$), the applicable correlation is given by Equation (4.1). The volumetric heat transfer coefficient is related to the Nusselt Number as (Golombok et al., 1991):

$$h_v = 4Nu\frac{k_g(1-\phi)}{d^2} \; . \tag{4.3}$$

For a given burner pad, the local volumetric heat transfer coefficient takes a wide range of values. At the inlet, the gas is "cold" (low viscosity, low thermal conductivity) and the velocity is relatively low. After the reaction zone the gases are "hot" (high viscosity[1], high thermal conductivity) and the velocity is considerably higher due to the increased volume. Table 4.1 contains some representative volumetric heat transfer coefficient values, where the thermophysical properties of air were used for the calculations[2].

Equation (4.1) (or (4.2)) can be combined with the definition of the volumetric transfer coefficient in terms of the Nusselt number (Equation (4.3)), and rearranged to explicitly show the dependence of the thermophysical properties on h_v for a given fibrous material (i.e., fixed porosity and fiber diameter):

$$h_v \propto (\rho u)^{0.53}\left(\frac{k_g}{\mu^{0.53}}\right) \quad \text{for} \quad Re < 0.4 \; , \tag{4.4}$$

or

$$h_v \propto (\rho u)^{1.64}\left(\frac{k_g}{\mu^{1.64}}\right) \quad \text{for} \quad Re > 0.4 \; . \tag{4.5}$$

For a given low Re flow rate, the volumetric heat transfer coefficient increases with the gas temperature as shown in Table 4.1, since the thermal conductivity increases faster than viscosity.

In view of the results included in Table 4.1, for the present study an "average" value of $h_v = 1{,}000 \; \frac{kW}{m^3 K}$ was selected as a reasonable estimate for the baseline case comparison with the experimental data. The effect of this choice is analyzed parametrically in Chapter 5.

---

[1] Note that the viscosity of a *gas* at low density *increases* with increasing temperature, whereas the viscosity of a *liquid* decreases with increasing temperature (Bird et al., 1960).

[2] Inlet gas mixture is over 90% air and less than 10% methane (in volume) for stoichiometric conditions. Including a correction due to the presence of methane, based on the pseudo-critical properties method (Hougen and Watson, 1947; Bird et al., 1960), did not significantly change the coefficients.

Table 4.1. Local values of the volumetric heat transfer coefficient (h_v) according to Equation (4.3), based on the local temperature and flow velocity. The properties of air (viscosity, density, thermal conductivity) were used. The mass flux was 0.35 $\frac{kg}{m^2 s}$, corresponding to an inlet (i.e., cold gas mixture) velocity of 0.4 $\frac{m}{s}$.

T $[K]$	u $[\frac{m}{s}]$	μ $[\frac{N\,s}{m^2}]$	k_g $[\frac{W}{m\,K}]$	Re	Nu	h_v $[\frac{kW}{m^3 K}]$
400	0.4	230×10^{-7}	34×10^{-3}	0.333	0.022	562
1000	1.0	424×10^{-7}	67×10^{-3}	0.181	0.016	801
1500	1.5	557×10^{-7}	100×10^{-3}	0.138	0.014	1040
1800	1.8	637×10^{-7}	120×10^{-3}	0.120	0.013	1160

It is necessary to point out here that the constant volumetric heat transfer coefficient represents a very simplistic (but useful) concept of the relevant energy transport phenomena in porous media. For heat transfer within a cylindrical pore, the wall and the flowing gas behave as a multimode heat exchanger system in which three modes, i.e., convection, conduction, and radiation, occur simultaneously. Fu et al. (1998a) predicted numerically the temperature contours for methane combustion in a cylindrical tube, showing that reversed gradients (i.e., the wall is hotter than the gas) occur at the same axial location where the gas mixture reaches the maximum temperature. In this context, the concept of gas bulk temperature for defining the volumetric heat transfer coefficient loses its meaning. Understanding the usefulness and limitations of the convection heat transfer modeling in a system with local volumetric heat release, it becomes evident than the numerical results should be interpreted carefully.

4.2.2. Radiation Properties

So far there has been little information about the extinction and scattering coefficients and scattering phase function, which are the two most important radiative properties of dispersed media (Viskanta and Mengüç, 1989), for porous media containing metallic fibers.

Experimental data of radiation properties of porous materials that are suitable for flame support pad are limited. Most studies deal with porous materials suitable for insulation (among many others: Tong et al., 1983; Cain and McKay, 1991; Viskanta and Mengüç, 1987) and none of them include metallic fibers. In a noted work, Mital et al. (1996) determined the extinction coefficient and the single scattering albedo[3] of selected cellular (reticulated) ceramics that are candidates for use in radiant burners, in the 1200 to 1400K temperature range. They measured the total radiation intensities leaving layers of the heated reticulated materials (placed in a tube furnace) using two different boundary conditions, and then used an inverse radiation approach involving the two-flux approximation (assuming a gray, isotropically scattering medium) to obtain the radiative properties from the measured intensities. This method was particularly sensitive for optically thin layers. The single scattering albedos varied from 0.68 to 0.88 (±7% uncertainty), whereas the extinction coefficients varied from 81 to 270 m^{-1} (±11%). Mital et al. (1996) also reported that the variations in the radiation properties were not significant in the range of temperatures investigated.

There have also been many theoretical attempts to calculate the radiation properties of fibrous materials from first principles (Tong and Tien, 1980; Tong and Tien, 1983; Wang et al., 1987; Kurosaki and Yamada, 1991). The extinction and scattering characteristics of a single particle can be described after the solution of the electromagnetic field equations. Kurosaki and Yamada (1991) summarized the procedure for analytically computing the extinction and scattering cross sections per unit length for a cylinder, provided that its composition (which determines the complex index of refraction), size parameter ($\pi d/\lambda$) and surrounding medium are all known:

$$C_{extn}(\lambda, m, \xi_0) = \frac{2\lambda}{\pi}\, \Re\{T(0)\}\ , \tag{4.6}$$

$$C_s(\lambda, m, \xi_0) = \frac{2}{\pi^2} \int_{\theta=2\pi} i(\xi_0, \theta) d\theta\ , \tag{4.7}$$

---

[3] The single scattering albedo is the fraction of energy lost from an incident beam due only to scattering (Kerker, 1969), i.e., the ratio between the scattering and extinction coefficients.

where m is the complex index of refraction of the cylinder relative to the medium, λ is the wavelength of the incident radiation, ξ_0 is the incident angle measured with respect to the cylinder axis, and $T(0)$ and $i(\xi_0, \theta)$ are the amplitude and intensity functions, respectively. $T(0)$ and $i(\xi_0, \theta)$ are complicated functions that involve integral order Bessel functions[4], which are beyond the scope of this thesis and and are described in detail in the literature (Kerker, 1969).

Once the single-fiber cross sections are determined, they can be used to calculate the fibrous medium (i.e., multi-fiber) parameters by summing (or integrating) the intensity attenuated by every fiber element (Kurosaki and Yamada, 1991). The effect of fiber length distribution (Komori and Makishima, 1978) and orientation (Komori and Makishima, 1978; Lee, 1986) can also be accounted.

To predict radiative properties from electromagnetic theory, the complex index of refraction, m, must be known, either from direct measurements or from dispersion theory predictions (Modest, 1993). The main problem with using the method described by Kurosaki and Yamada (1991) is that the very basic information regarding the optical behavior of the Fecralloy fibers, i.e., their complex index of refraction is not known. Additionally, Fecralloy fibers consist in a multi-component alloy (Table 2.3), and the extra complication of the protective, yttrium-bonded, surface alumina layer (Section 2.3). Scattering by stratified cylinders can be treated in a manner which is formally similar to that for spheres (Kerker, 1969). However, there is no simple solution for oblique incidence (Samaddar, 1970).

The Fecralloy fibers that form the prototype burner pad are neither parallel nor randomly arranged, which further complicates the calculation of the radiation properties from first principles. They form a cloth-like structure[5], a weave of twisted, interlacing multi-fiber strands that constitute the woven metal fiber pad. Figure 4.1 depicts this structure, and also the sintered version used by Golombok et al. (1991) for comparison purposes.

---

[4] Bessel functions (of the first kind), Neumann functions (or Bessel functions of the second kind), and Hankel functions.

[5] The material is actually produced using a textile processing technique.

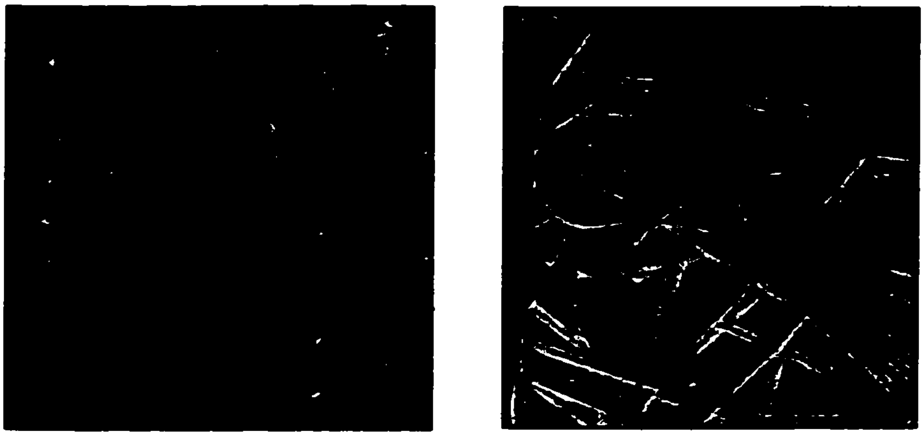

Figure 4.1. Fecralloy fiber pad structure: compare the textile-like knitted fiber structure on the left (used for the prototype burner in this investigation) with the randomly-oriented sintered fiber medium on the right (the material used by Golombok et al., 1991). Note that the latter has been magnified to show the 22 μm fibers in detail.

Therefore, and given the difficulty of the analytical calculations and the uncertainty in the involved information (specifically in the complex index of refraction, m), reasonable estimates of the optical properties were used for the present study. A baseline case using $\beta = 200\ m^{-1}$ and $\omega = 0.1$ (i.e., $\sigma_s = 20\ m^{-1}$) was used to compare predictions with experiments (Section 4.3). A sensitivity analysis was performed and is included in Chapter 5. In addition, isotropic scattering was assumed.

4.3. Comparison of Model Predictions with Data

4.3.1. Temperature of the Exhaust Gases

The comparison between the model predictions and the exit gas temperature experimental data for a single-layer Fecralloy burner is shown in Figures 4.2 to 4.4, for equivalence ratio of $\Phi = 1.1$, 1.0 and 0.9, respectively. The general trend in all cases is that the gas temperature increases with increasing firing rate, since the flame temperature increases and its location is almost constant. The model predictions tend to capture this general behavior.

For the rich flame case (Figure 4.2), the numerical results present initially a steep gradient, but the increase in gas temperature moderates (and eventually decrease) at the higher firing rates. This particular deviation from the general trend at the higher end of the firing range can be explained by realizing that the reaction zone stabilizes further away from the burner face, deeper inside the solid matrix; therefore, the peak flame temperature increase is not enough to compensate for the additional convective heat losses (since the hot gases are in contact with the porous medium for a longer time.) This change in the flame location is shown in Figure 5.23 of Section 5.4, where the effect of the firing rate is studied.

An excellent agreement is observed for the stoichiometric case (Figure 4.3), where data and the predictions are identical at a firing rate of 300 $\frac{kW}{m^2}$. On the other hand, the lean mixture case (Figure 4.4) shows that the gas temperature is underpredicted for firing rates between 220 and 340 $\frac{kW}{m^2}$; below this range, the calculated results are much higher than the data, since the program predicts that the flame stabilizes outside the solid matrix instead of within the pad (and, therefore, heat losses from the gas phase become considerably smaller), as shown in the next chapter in Figure 5.24. This behavior can be reproduced in the laboratory, but at firing rates around 100 $\frac{kW}{m^2}$, which is about one half of the value at which the code predicts that the flame emerges out of the solid. Flame location and burning mode changes are the hardest to predict with approximate property values.

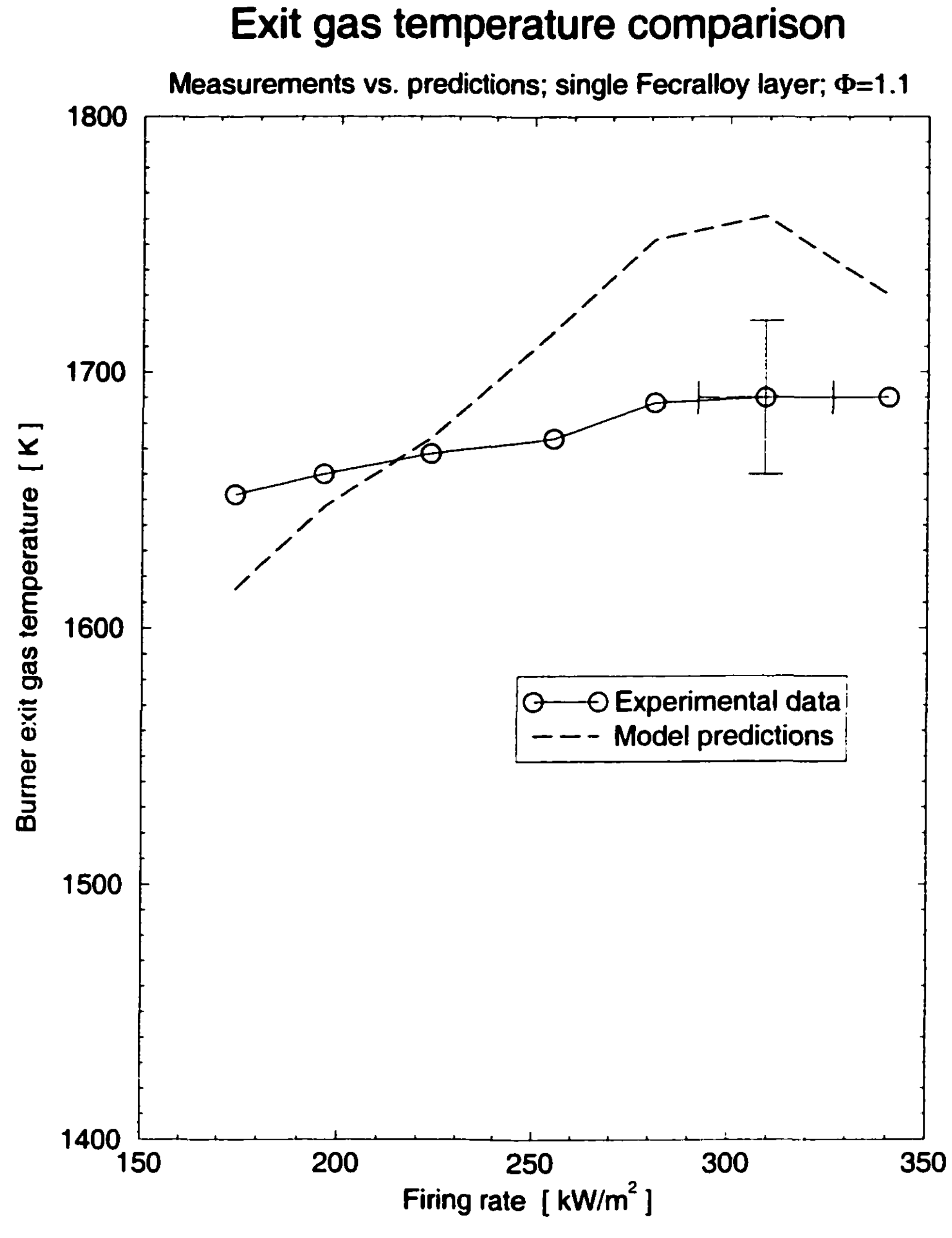

Figure 4.2. Comparison of the exit gas temperature between the model predictions and the experimental data, for a fuel rich ($\Phi = 1.1$) inlet mixture.

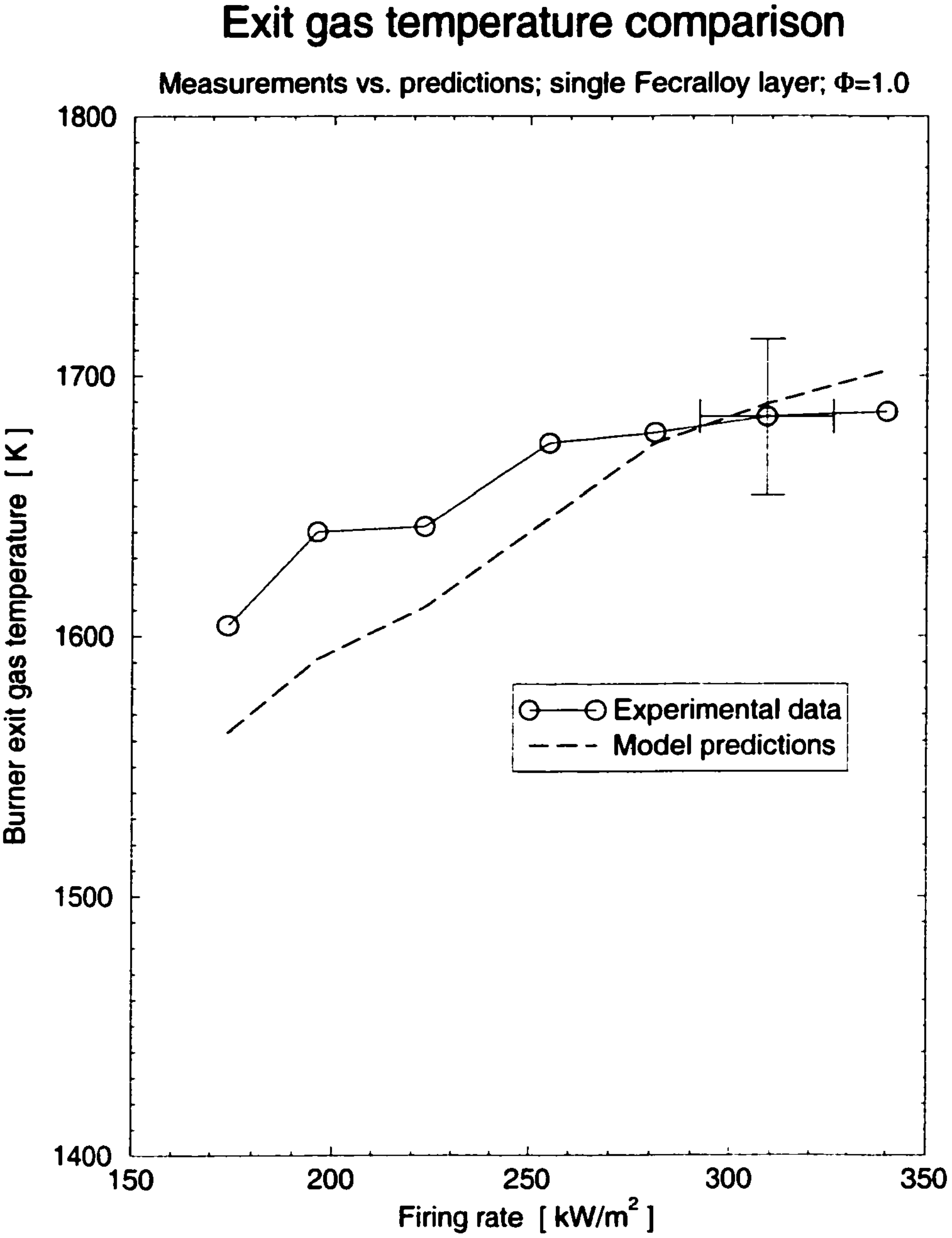

Figure 4.3. Comparison of the exit gas temperature between the model predictions and the experimental data, for a stoichiometric ($\Phi = 1.0$) inlet mixture.

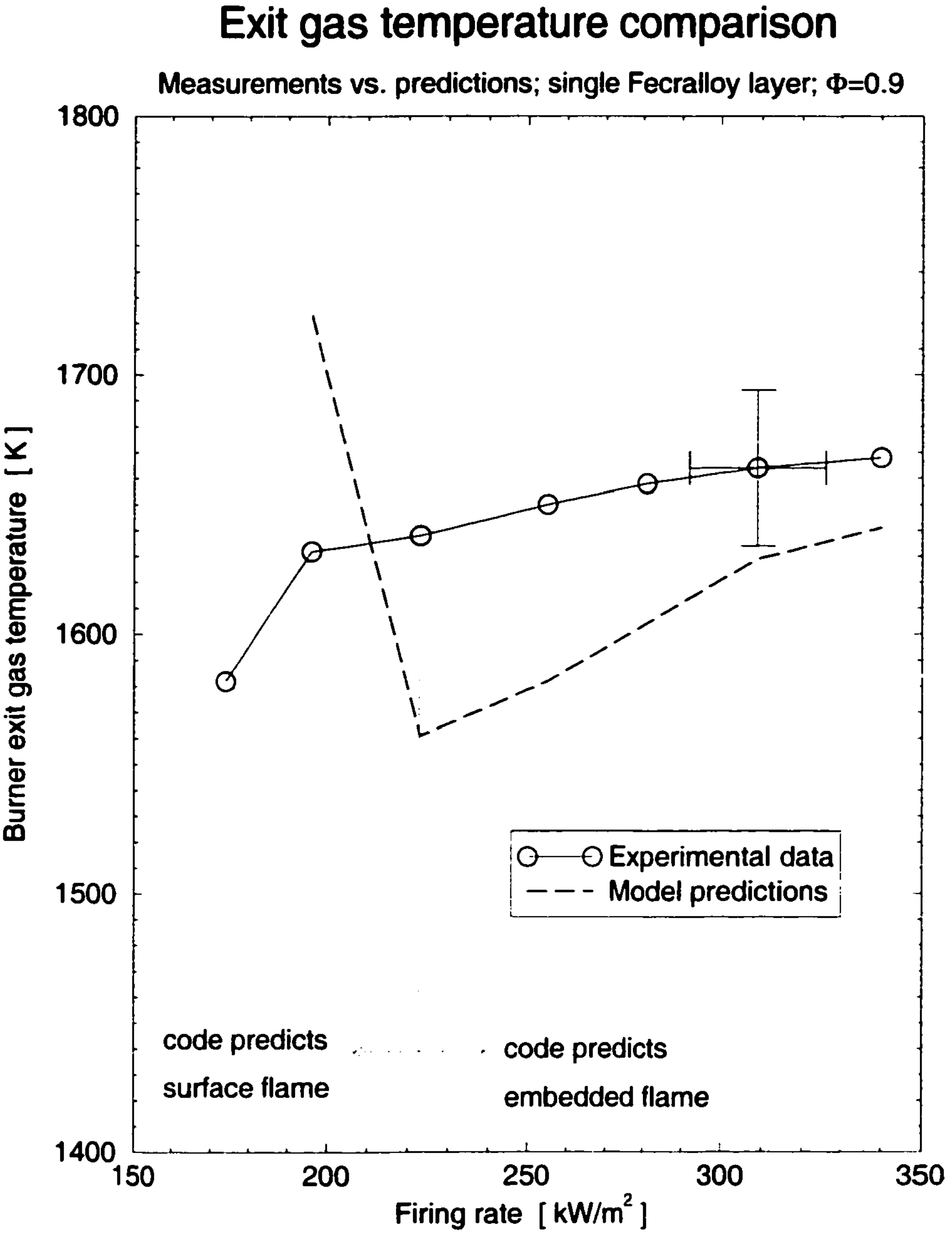

Figure 4.4. Comparison of the exit gas temperature between the model predictions and the experimental data, for a fuel lean ($\Phi = 0.9$) inlet mixture.

4.3.2. Solid Surface Temperature

The predictions of the surface temperature of the solid matrix are plotted together with the experimental data in Figures 4.5 to 4.7, for equivalence ratios of $\Phi = 1.1$, 1.0 and 0.9, respectively. For all inlet mixtures, the surface temperatures increase with an increase in the firing rate, and the simulations capture this trend. Note that the predicted surface temperature (i.e., the temperature of the last grid point of the solid matrix) is always about $200K$ below the data, but the experimental results always lie between the calculated surface and maximum temperatures. As mentioned in Section 2.4.6, the experimental technique relies on comparing the radiant flux emitted by the burner to that of a blackbody; the fact that the measurements are in between the calculated surface and maximum temperatures is indicative of radiation being emitted not only from the "surface"[6] but partly from the bulk of the matrix.

A sharp reduction of the predicted solid temperatures is observed in Figure 4.7 for firing rates below 220 $\frac{kW}{m^2}$, which corresponded to the flame being stabilized outside the porous matrix. This effect of the flame becoming a "surface flame" was discussed previously in Section 4.3.1.

4.3.3. Radiation Efficiency

The radiation efficiency for ideal burners (without heat losses from the sides and assuming complete combustion) resembles, for larger-than-zero firing rates, a hyperbolic curve (Fu et al., 1999): it decreases with increasing firing rates, since the extra fuel fraction causes a less-than-proportional increase in the efficiency. When heat losses are considered, the ideal burner presents a local maximum in the radiation efficiency. The radiation efficiency increases when reducing the firing rate, up to the point when the heat losses from the housing become significant and curve that behavior; eventually, the radiation efficiency drops to zero for zero firing rate.

---

[6] The concept of surface is not straightforward for a porous medium.

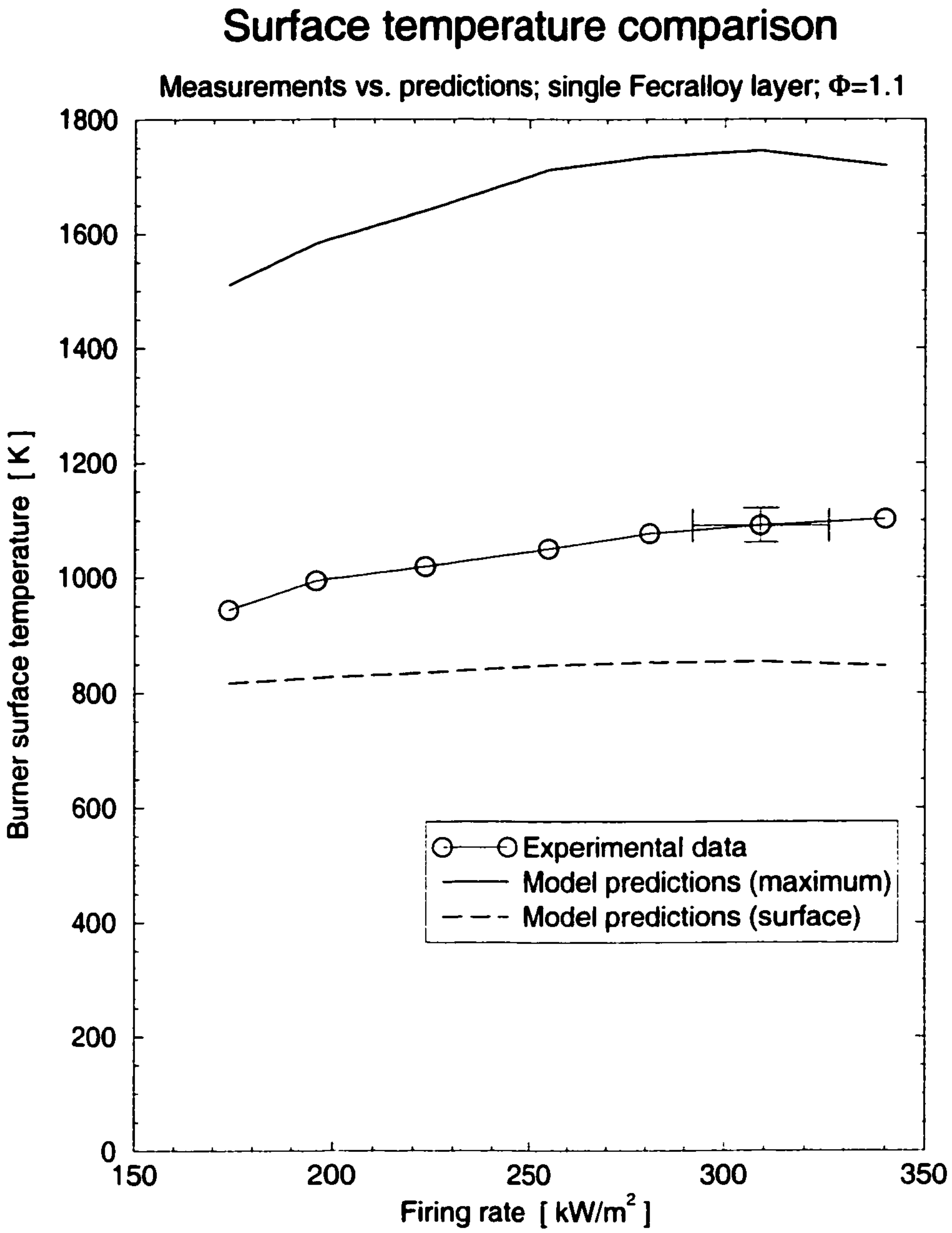

Figure 4.5. Comparison of the burner surface temperature between the model predictions and the experimental data, for a fuel rich (Φ = 1.1) inlet mixture. The maximum solid matrix temperature is included for comparison.

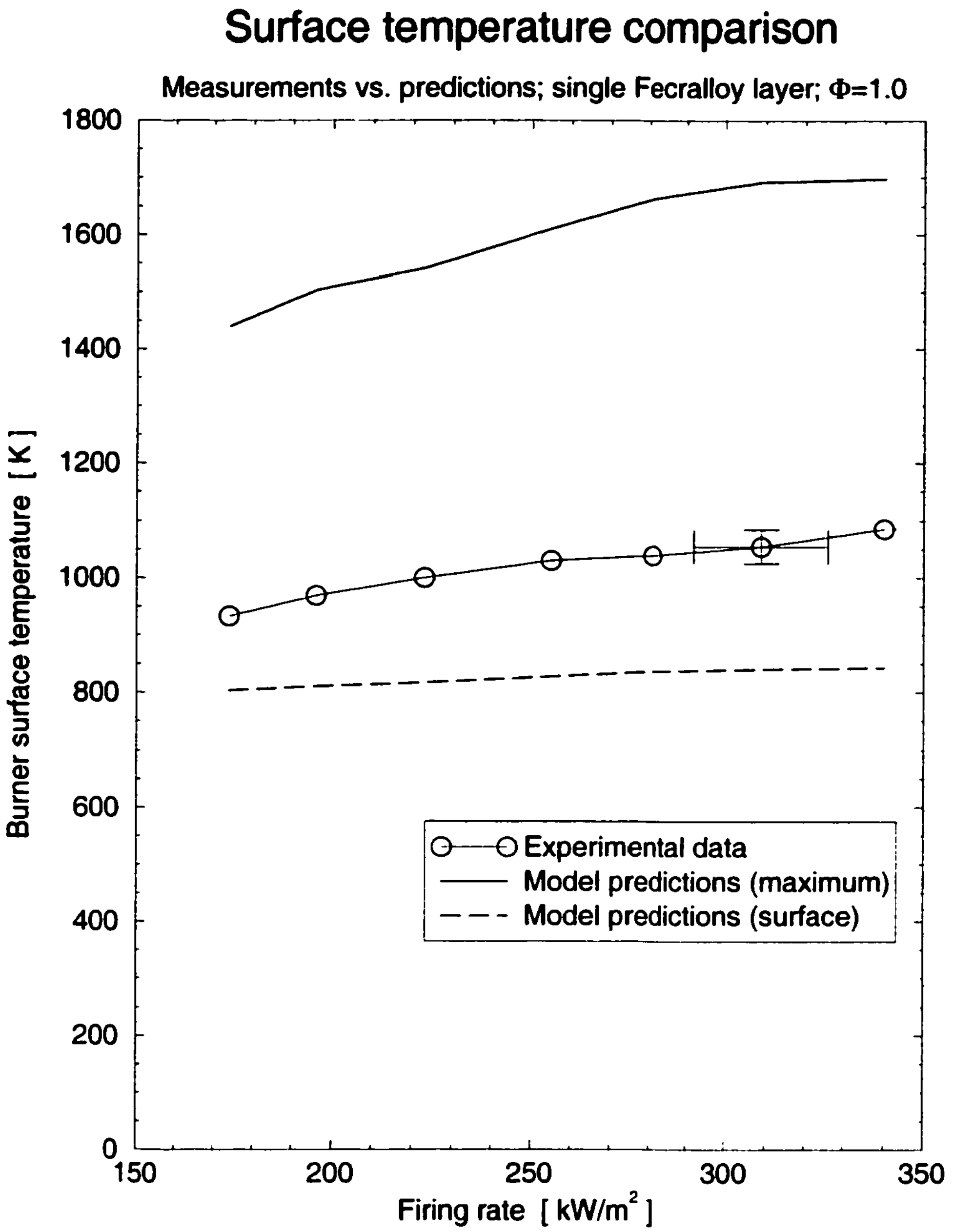

Figure 4.6. Comparison of the burner surface temperature between the model predictions and the experimental data, for a stoichiometric ($\Phi = 1.0$) inlet mixture. The maximum solid matrix temperature is included for comparison.

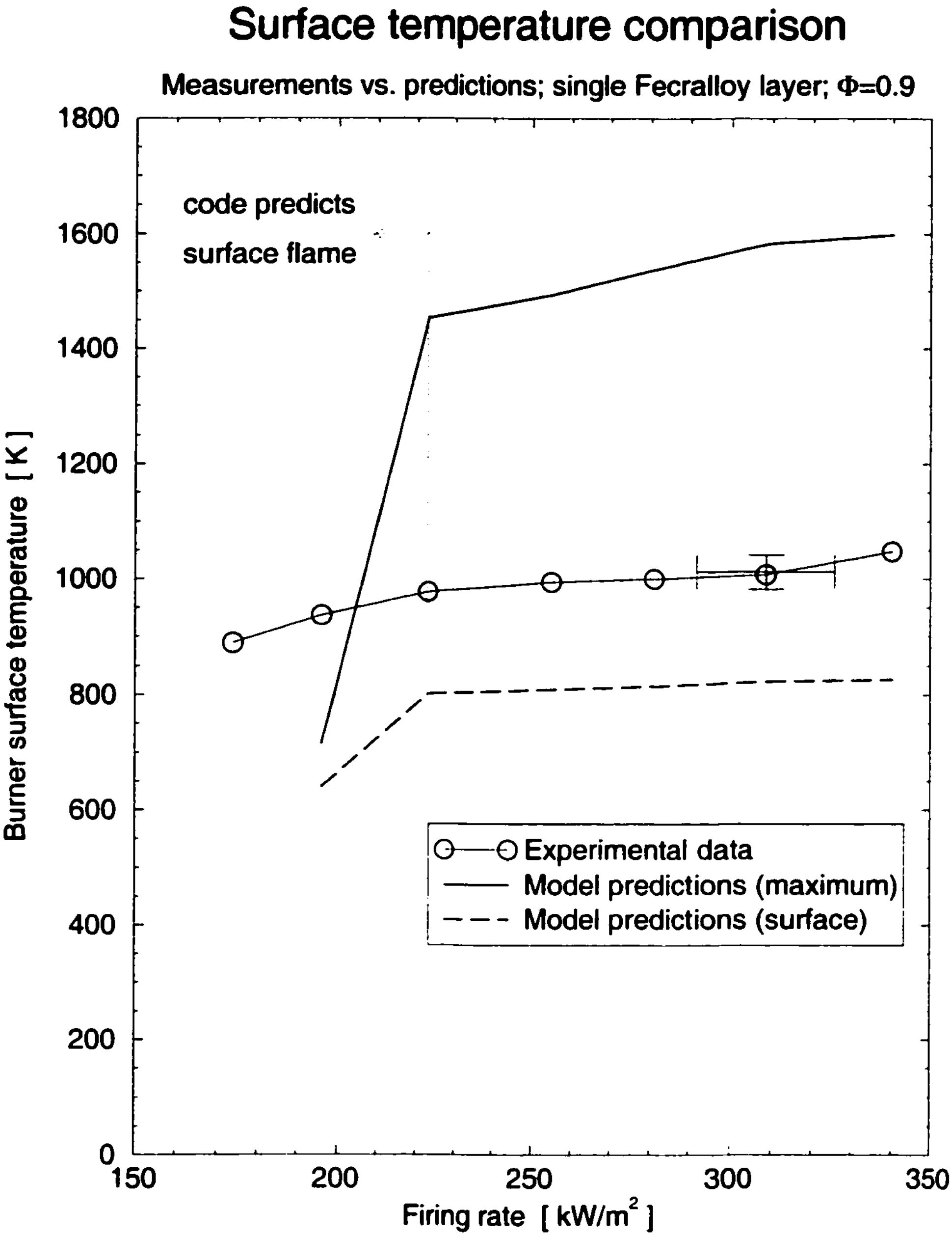

Figure 4.7. Comparison of the burner surface temperature between the model predictions and the experimental data, for a fuel lean ($\Phi = 0.9$) inlet mixture. The maximum solid matrix temperature is included for comparison.

A real burner presents a local maximum in the radiation efficiency, which is usually attributed to the aforementioned heat loss effect. However, chemistry effects are also present and should be included in the analysis. When multi-step chemistry is considered in a numerical simulation, a maximum in the radiation efficiency can still be produced, even in the absence of heat losses from the burner housing. In fact, in a porous radiant burner, a relatively low firing rate flame subjected to heat loss (i.e., convection to a solid matrix) cannot achieve full oxidation of all species. Then, the relative pollutant emissions increase and overall efficiency decreases. At large firing rates, the behavior approaches that of the ideal burner.

The aforementioned local maximum was observed in the laboratory at firing rates of about 220 $\frac{kW}{m^2}$, independently of the equivalence ratio. However, the numerical predictions show that the firing rate at which the maximum occurs decreases slightly with increasing equivalence ratio, from 310 $\frac{kW}{m^2}$ for $\Phi = 0.9$ to 280 $\frac{kW}{m^2}$ for $\Phi = 1.1$, as shown in Figures 4.8 to 4.10.

Radiation efficiency is predicted reasonably well for a stoichiometric mixture (Figure 4.9). Agreement is not as good for rich and lean mixtures, being over- and underpredicted, respectively (Figures 4.8 and 4.10). Note that there is a significant radiation efficiency drop for the case when the flame is not embedded in the solid matrix, but rather anchored to the burner surface ($\Phi = 0.9$ and $FR < 220$ $\frac{kW}{m^2}$, Figure 4.10), which confirms the fact that submerged flames are desired for an optimum radiant burner operation.

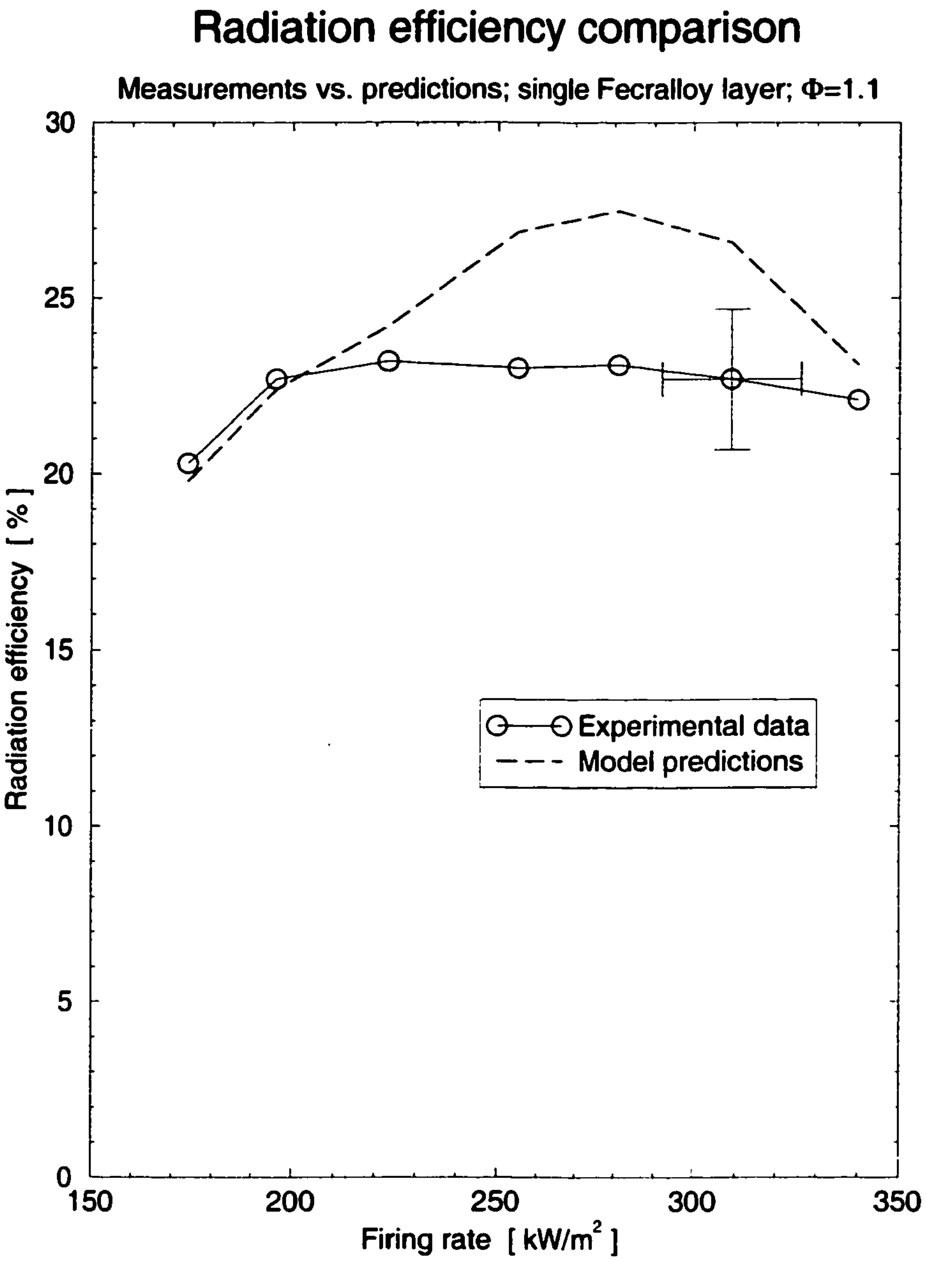

Figure 4.8. Comparison of the radiation efficiency between the model predictions and the experimental data, for a fuel rich ($\Phi = 1.1$) inlet mixture.

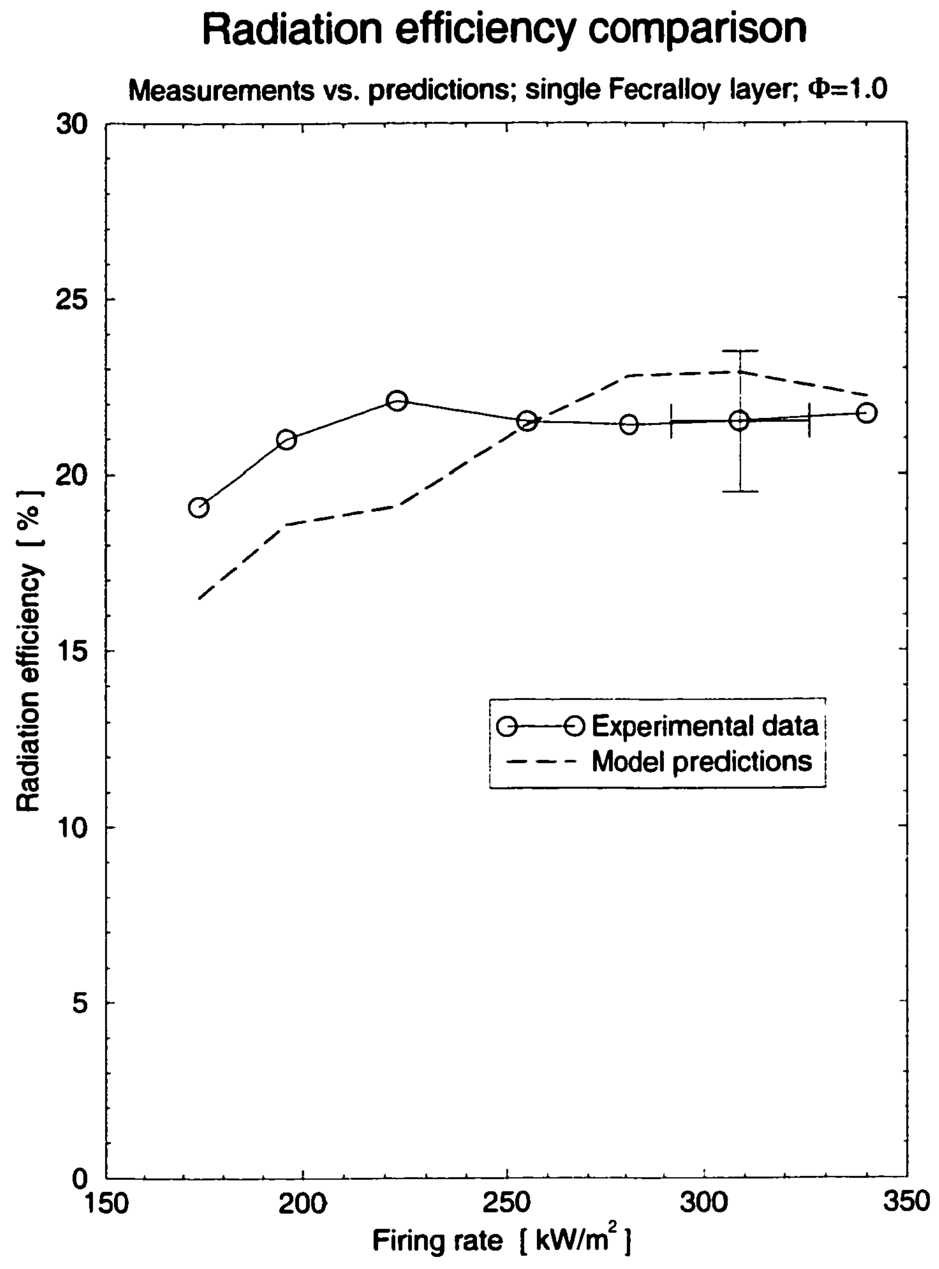

Figure 4.9. Comparison of the radiation efficiency between the model predictions and the experimental data, for a stoichiometric ($\Phi = 1.0$) inlet mixture.

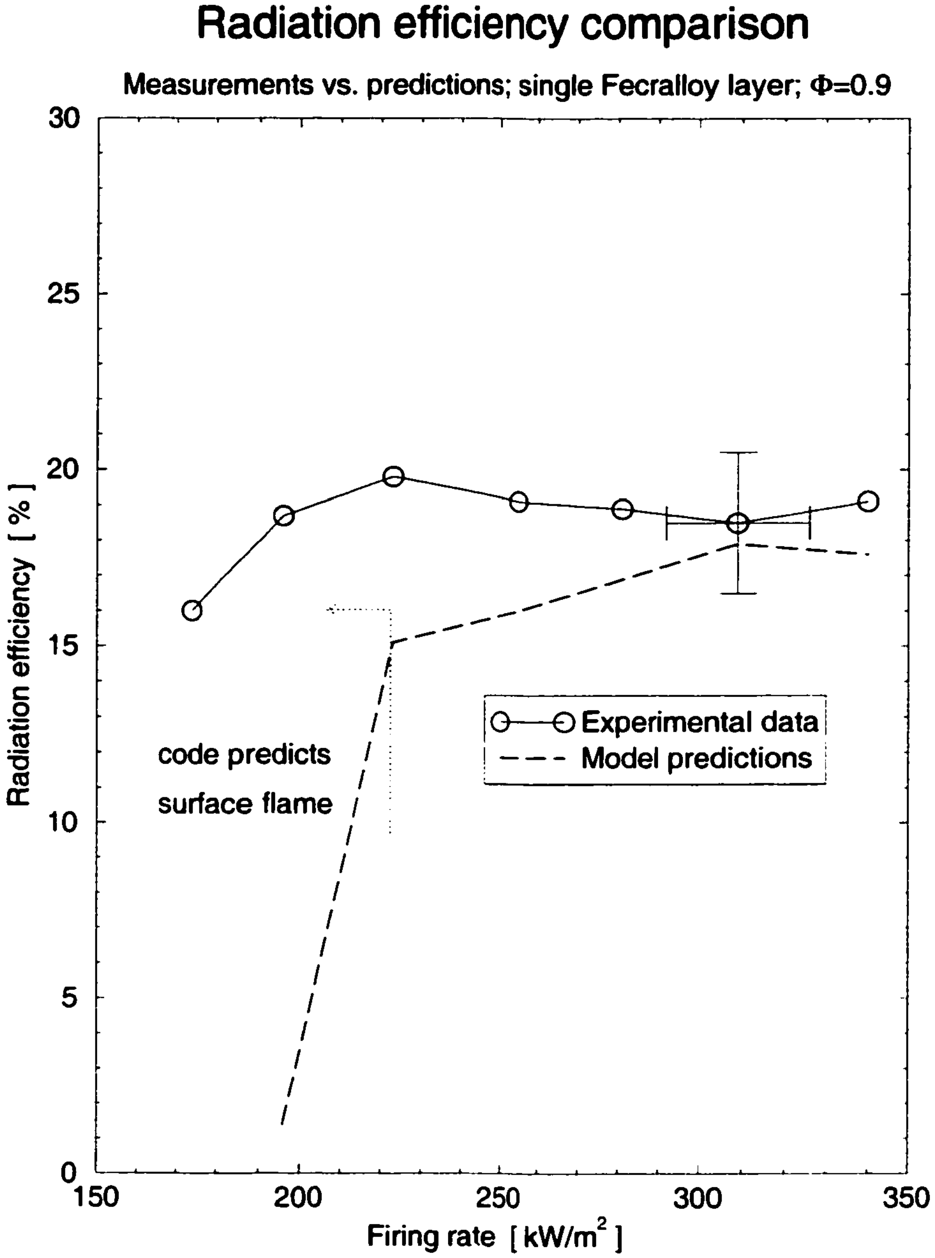

Figure 4.10. Comparison of the radiation efficiency between the model predictions and the experimental data, for a fuel lean ($\Phi = 0.9$) inlet mixture.

4.3.4. NO Emissions

The emission of NO is strongly related to the gas temperature; the production mechanisms are summarized in Section 5.1. Therefore, a similar success to that achieved for the temperature predictions is seen for this quantity. Figures 4.11 to 4.13 show the numerical predictions and the data for equivalence ratios of $\Phi = 1.1$, 1.0, and 0.9, respectively, corrected to 3% O_2 (dry basis)[7]. The NO emissions increase with increasing firing rate for all the embedded flames. Note, that when the flame stabilizes outside the porous material (at the lowest calculated firing rate for a lean flame, Figure 4.13), the NO emissions increase due to the corresponding temperature increase.

Both magnitude and trend show good agreement with the firing rate for the three equivalence ratios, but the slope of the predicted curves is somewhat lower than that for the data.

4.3.5. CO Emissions

Figures 4.14 to 4.16 depict the measured CO emissions variation with the firing rate, for equivalence ratios of $\Phi = 1.1$, 1.0, and 0.9, respectively, corrected to 3% O_2 (dry basis). In this case, the model results are not close to the experimental measurements; CO emissions are over-predicted by about one order of magnitude.

The experimental data show that CO emissions increase with increasing firing rate. The model results predict the same increasing trend for all the embedded flames when $\Phi \geq 1.0$ (Figures 4.14 and 4.15), but a rather flat profile for the lean mixture, $\Phi = 0.9$ (Figure 4.16). The numerical result becomes very poor when the predicted flame is not submerged in the porous material.

A possible explanation for the difference is that the GRI-Mech 2.11 reaction rates for the CO oxidation steps are low, making it "harder" for the code to complete the

---

[7] As mentioned in Section 2.5.2.5, the purpose of correcting to a specific O_2 level is to remove the effects of various degrees of dilution so that true comparison of emission levels can be made, while still retaining a familiar mole-fraction-like variable (Turns, 1996).

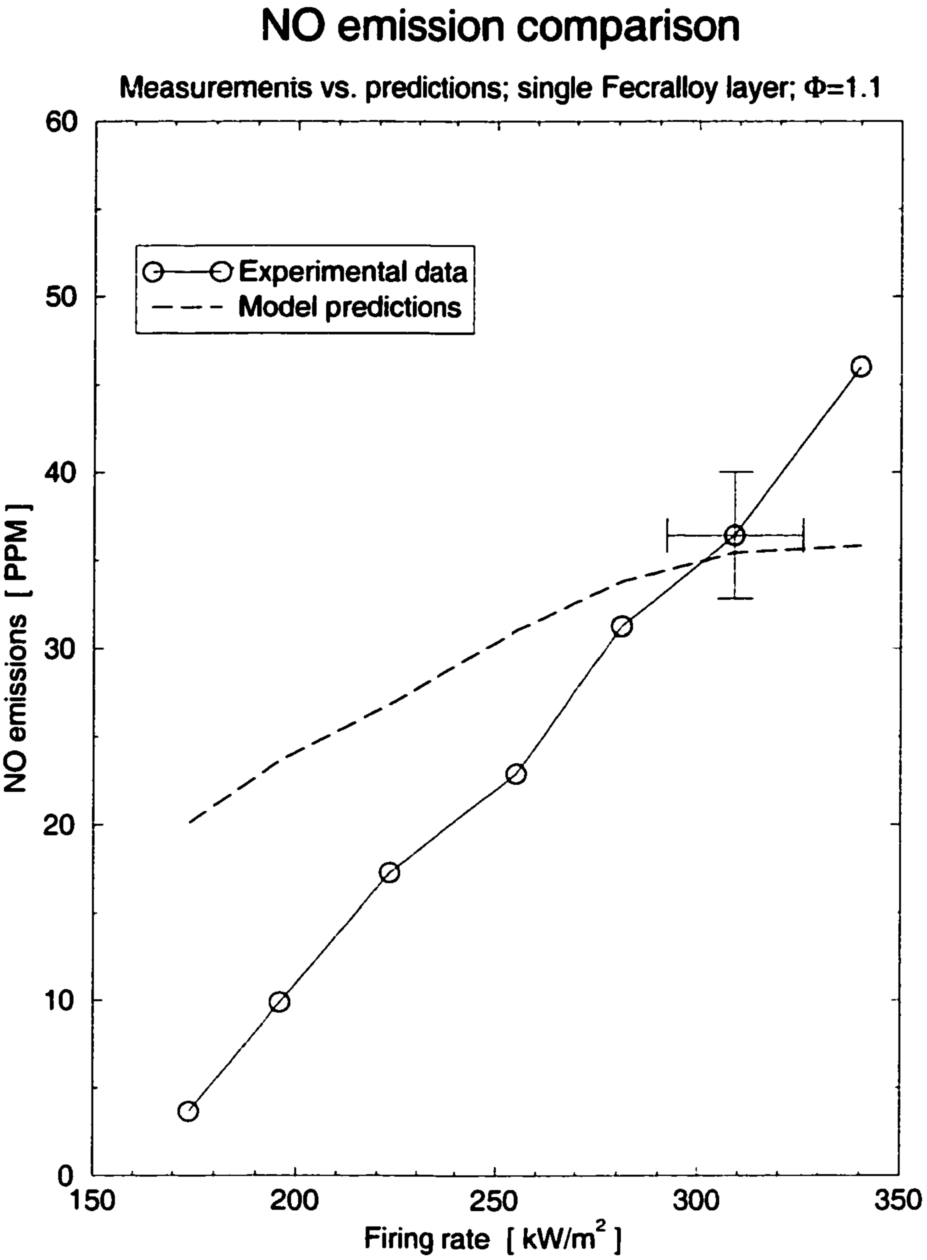

Figure 4.11. Comparison of the NO emissions between the model predictions and the experimental data, for a fuel rich ($\Phi = 1.1$) inlet mixture. Concentrations are corrected to 3% O_2 (dry basis).

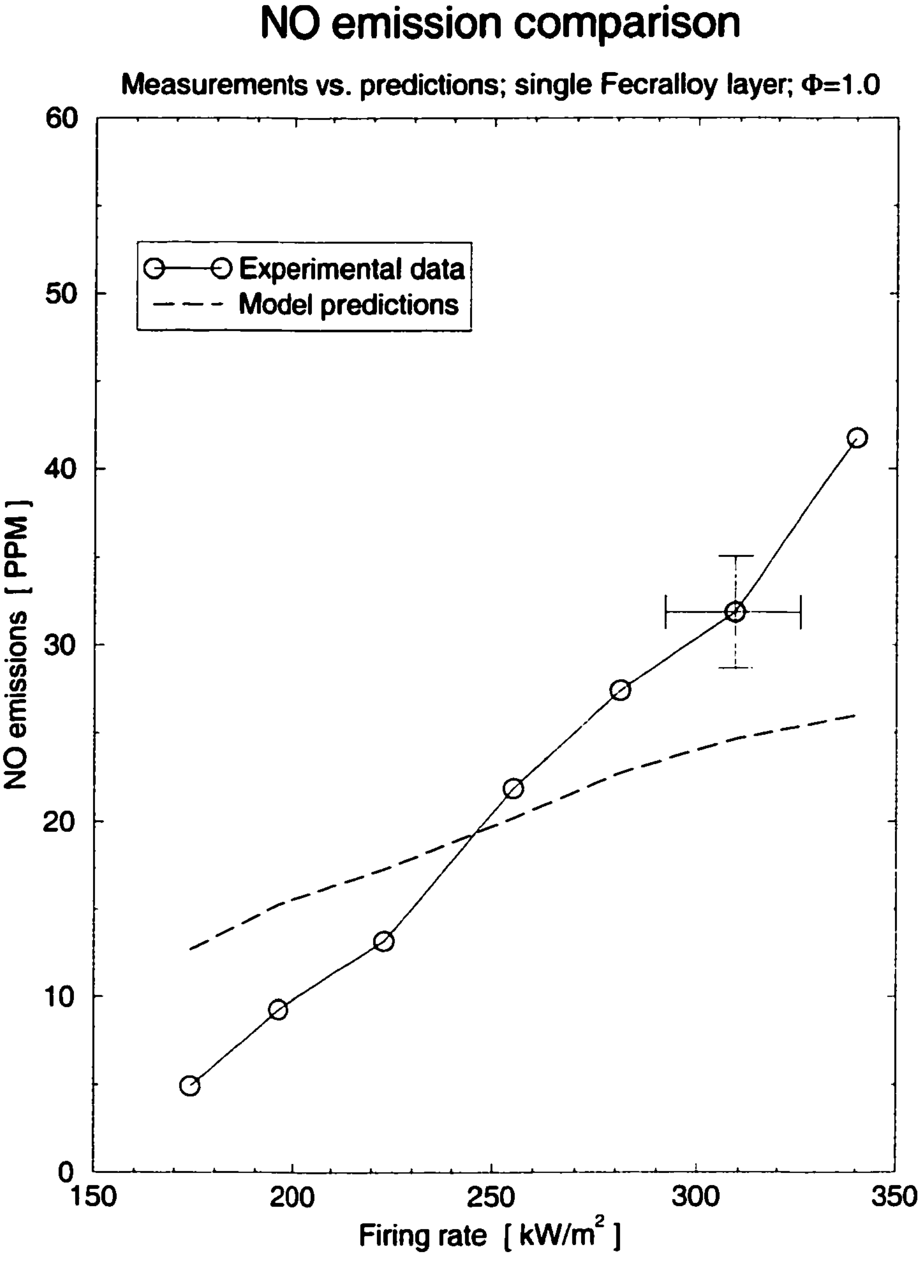

Figure 4.12. Comparison of the NO emissions between the model predictions and the experimental data, for a stoichiometric (Φ = 1.0) inlet mixture. Concentrations are corrected to 3% O_2 (dry basis).

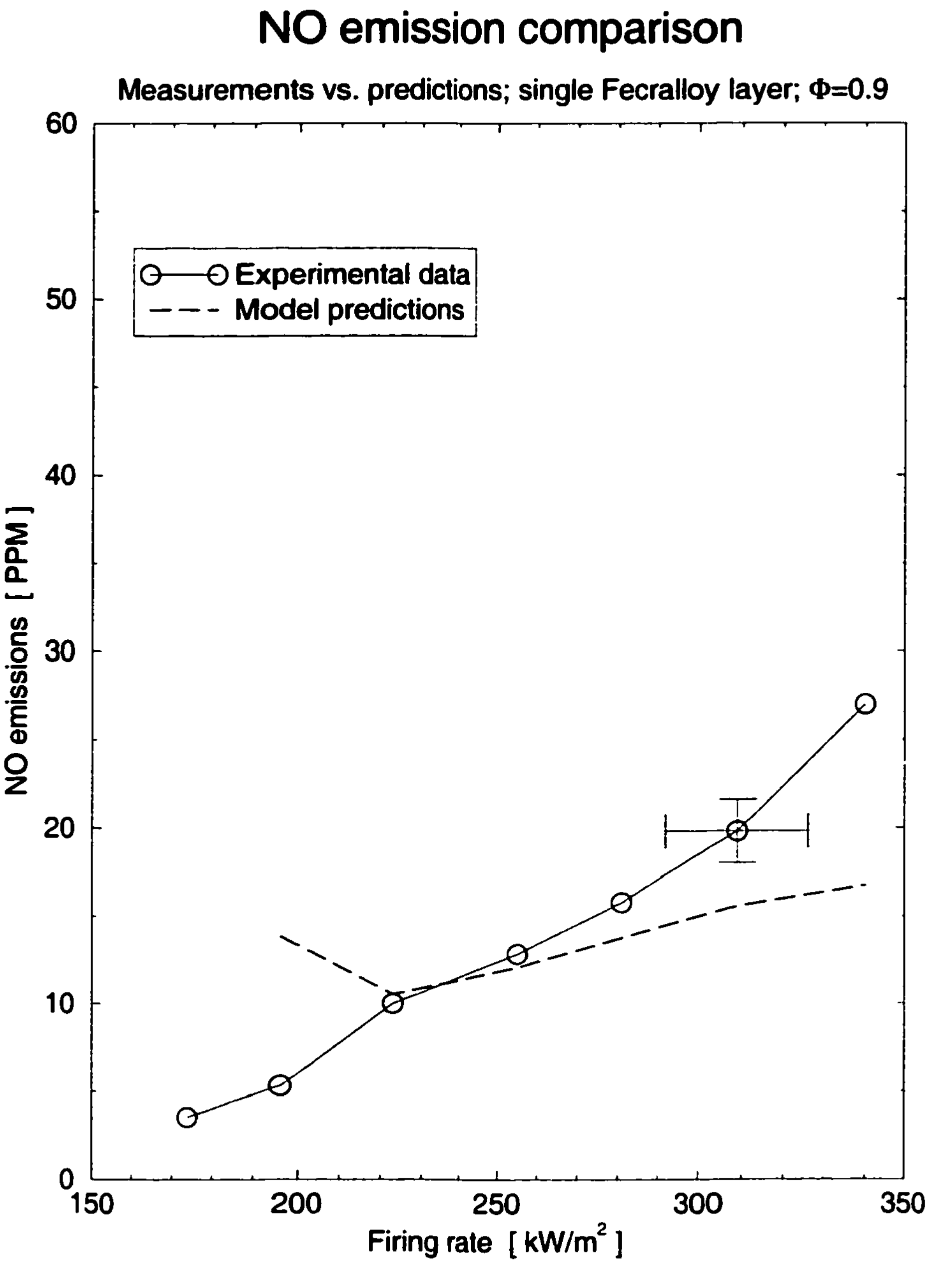

Figure 4.13. Comparison of the NO emissions between the model predictions and the experimental data, for a fuel lean ($\Phi = 0.9$) inlet mixture. Concentrations are corrected to 3% O_2 (dry basis).

process. The rates have been obtained and optimized for use in adiabatic flames. and their extension to non-adiabatic situations has not been thoroughly studied.

4.3.6. Unburned Hydrocarbons Emissions

The numerical results for the unburned hydrocarbon emissions[8] are plotted with the experimental data in Figures 4.17 to 4.19. All concentrations are corrected to 3% O_2 level (on a dry basis). The difference between the experimental data and the simulations is of several orders of magnitude. The code predicts virtually no emissions, but the measurements are in the range of 360 to 480 PPM.

There are several possible explanations for this large discrepancy. First. following a similar reasoning as before for CO emissions (Section 4.3.5), it can be argued that the chemical mechanism rates are too large. making it "easy" for the code to complete the oxidation of the hydrocarbons. Additionally. and even though the sampling probe in the experimental setup was located near the center of the burner. it is possible that some methane which slipped near the cold edges of the burner could have been aspirated into the sample stream (thus elevating the readings). Finally. the numerical model assumed pure methane as fuel. when natural gas (a "grade 1.3" methane tank, 93% CH_4 nominal) was used in the laboratory. According to Zhou (1999), who recently performed a gas chromatography analysis. the gas composition (Table 4.2) contains some ethene (C_2H_4) that can lead to the increased pollutant emissions. Unburned hydrocarbon emissions from natural gas and from methane are investigated in more detail using the modified PREMIX code in Section 5.10.

4.4. Discussion of the Comparison

The one-dimensional model for the Fecralloy radiant burner described in Chapter 3 predicts reasonably well the radiation efficiencies. exhaust gas temperatures and NO emissions in the studied range of firing rate (170 to 340 $\frac{kW}{m^2}$) and equivalence ratio (Φ =

---

[8] Mostly methane; non-zero but negligible levels of C_2H_2, C_2H_4 and C_2H_6 are also present.

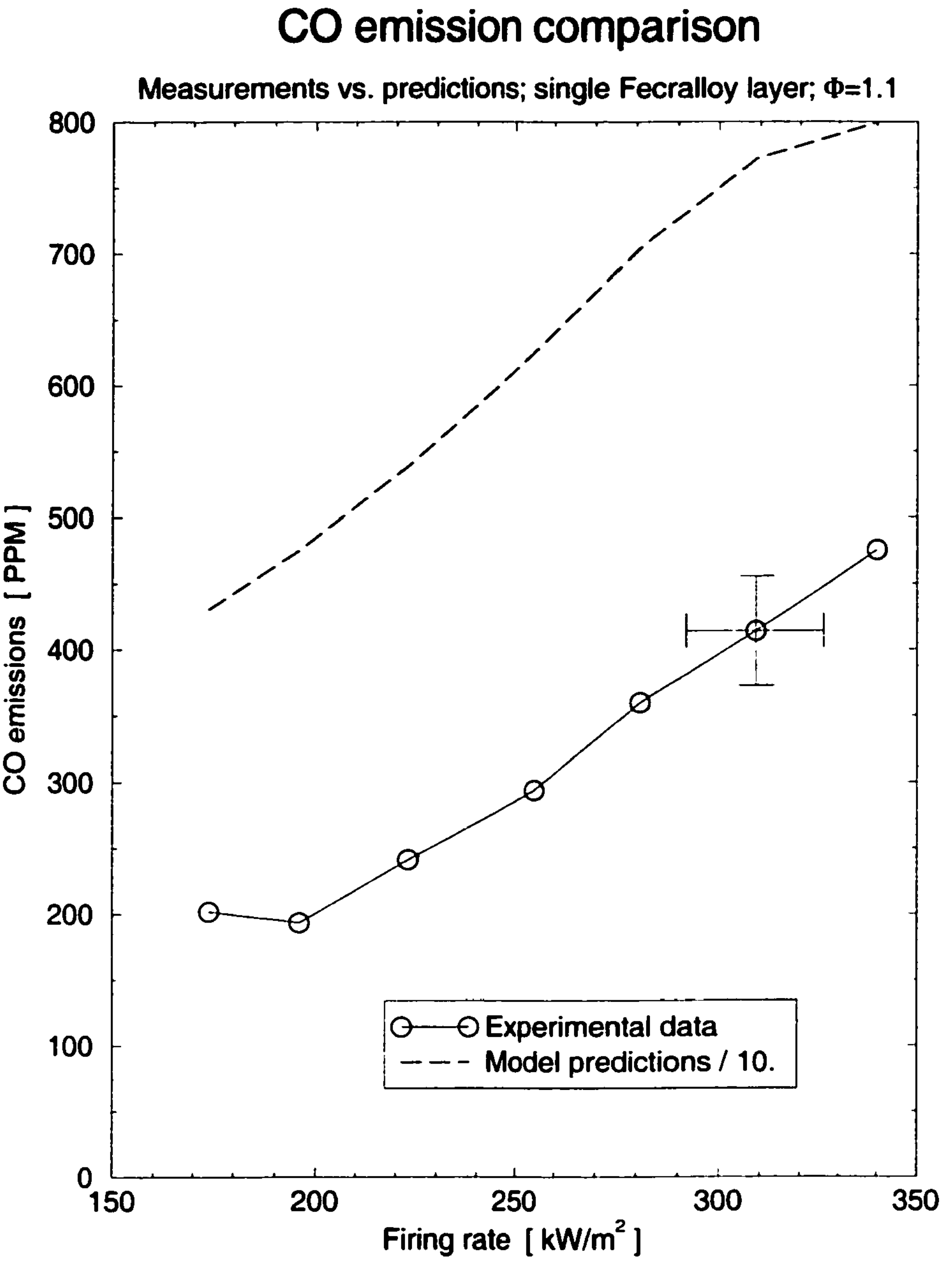

Figure 4.14. Comparison of the CO emissions between the model predictions and the experimental data, for a fuel rich ($\Phi = 1.1$) inlet mixture. Concentrations are corrected to 3% O_2 (dry basis).

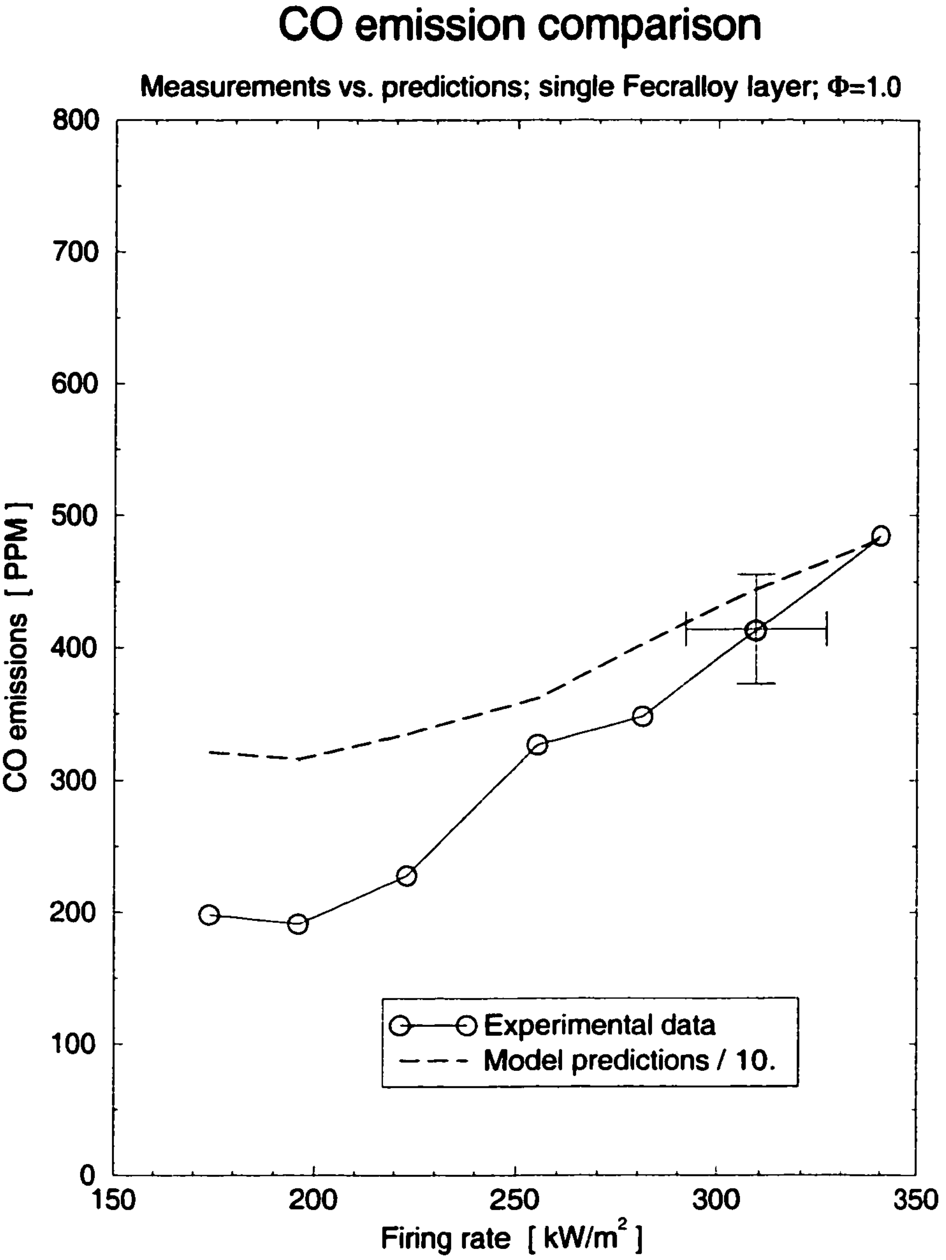

Figure 4.15. Comparison of the CO emissions between the model predictions and the experimental data, for a stoichiometric ($\Phi = 1.0$) inlet mixture. Concentrations are corrected to 3% O_2 (dry basis).

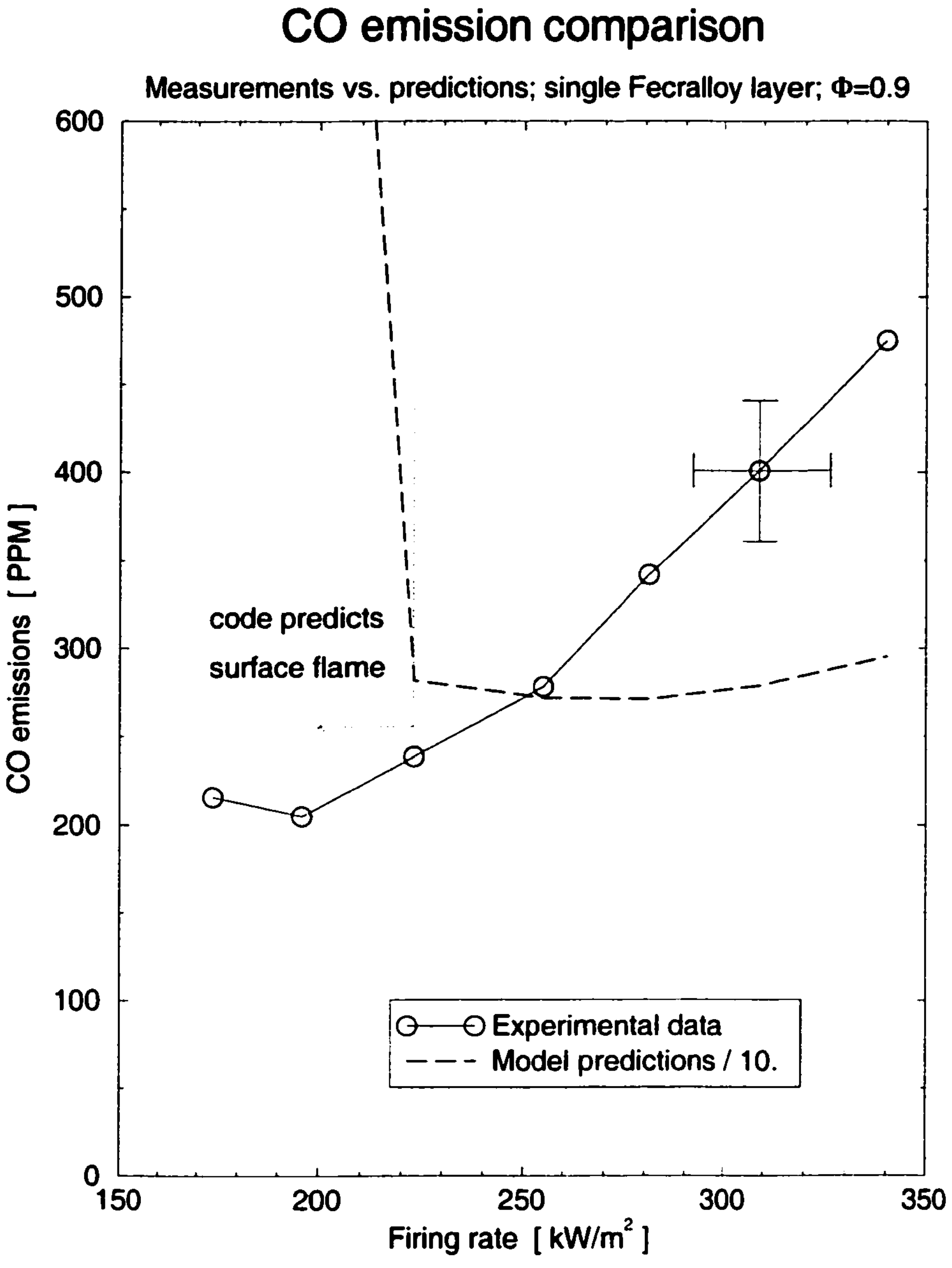

Figure 4.16. Comparison of the CO emissions between the model predictions and the experimental data, for a fuel lean ($\Phi = 0.9$) inlet mixture. Concentrations are corrected to 3% O_2 (dry basis).

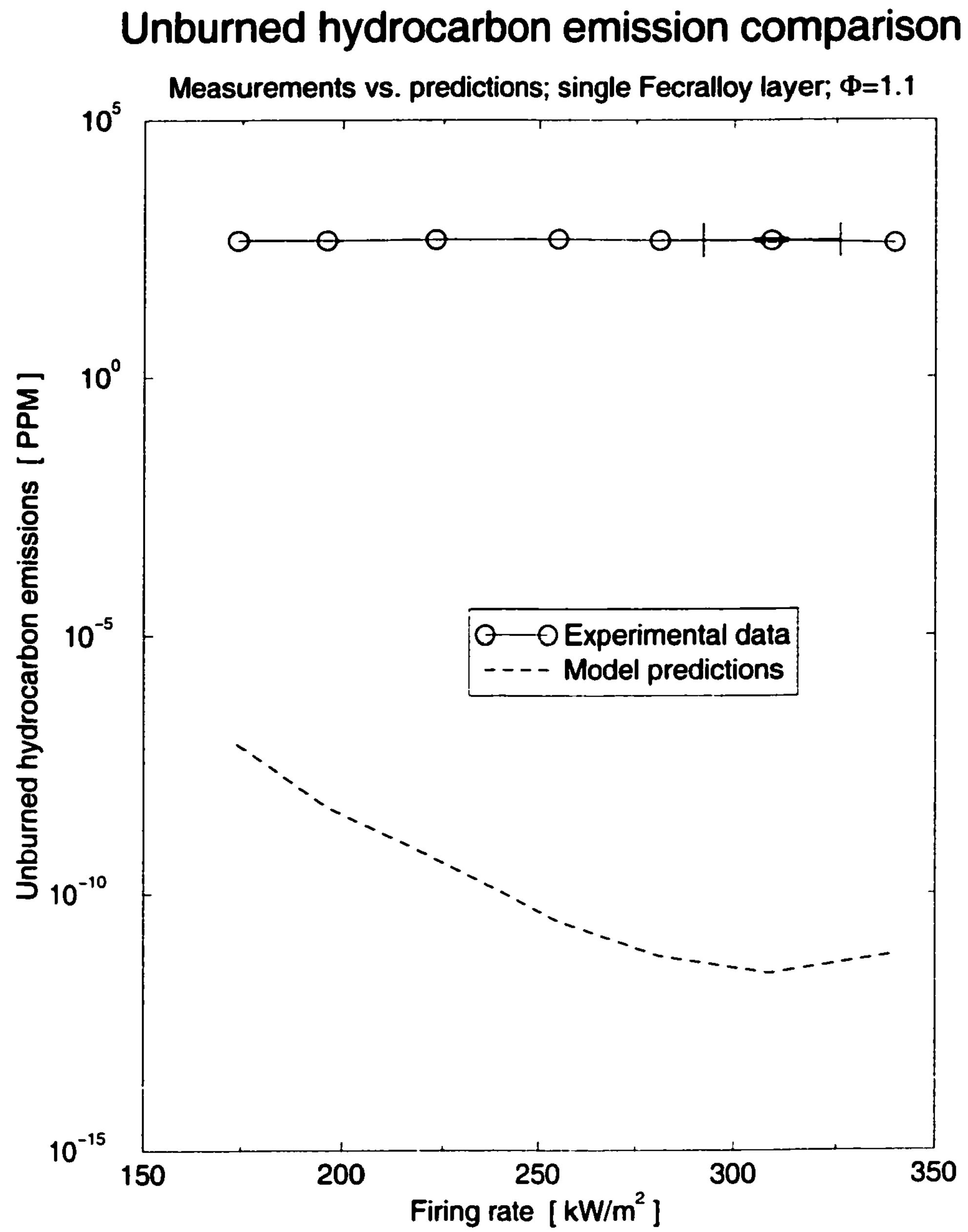

Figure 4.17. Comparison of the UBH emissions between the model predictions and the experimental data, for a fuel rich ($\Phi = 1.1$) inlet mixture. Concentrations are corrected to 3% O_2 (dry basis).

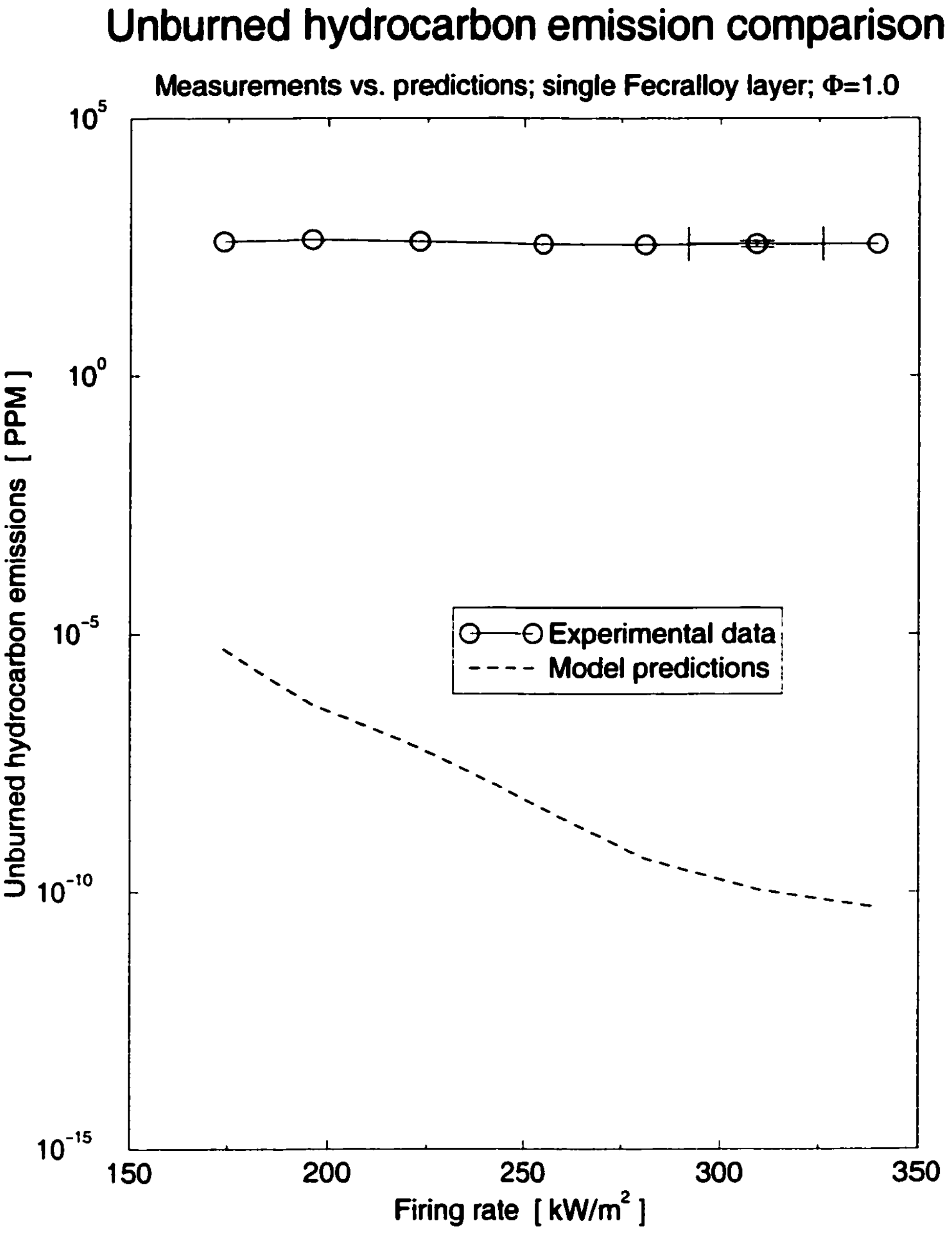

Figure 4.18. Comparison of the UBH emissions between the model predictions and the experimental data, for a stoichiometric ($\Phi = 1.0$) inlet mixture. Concentrations are corrected to 3% O_2 (dry basis).

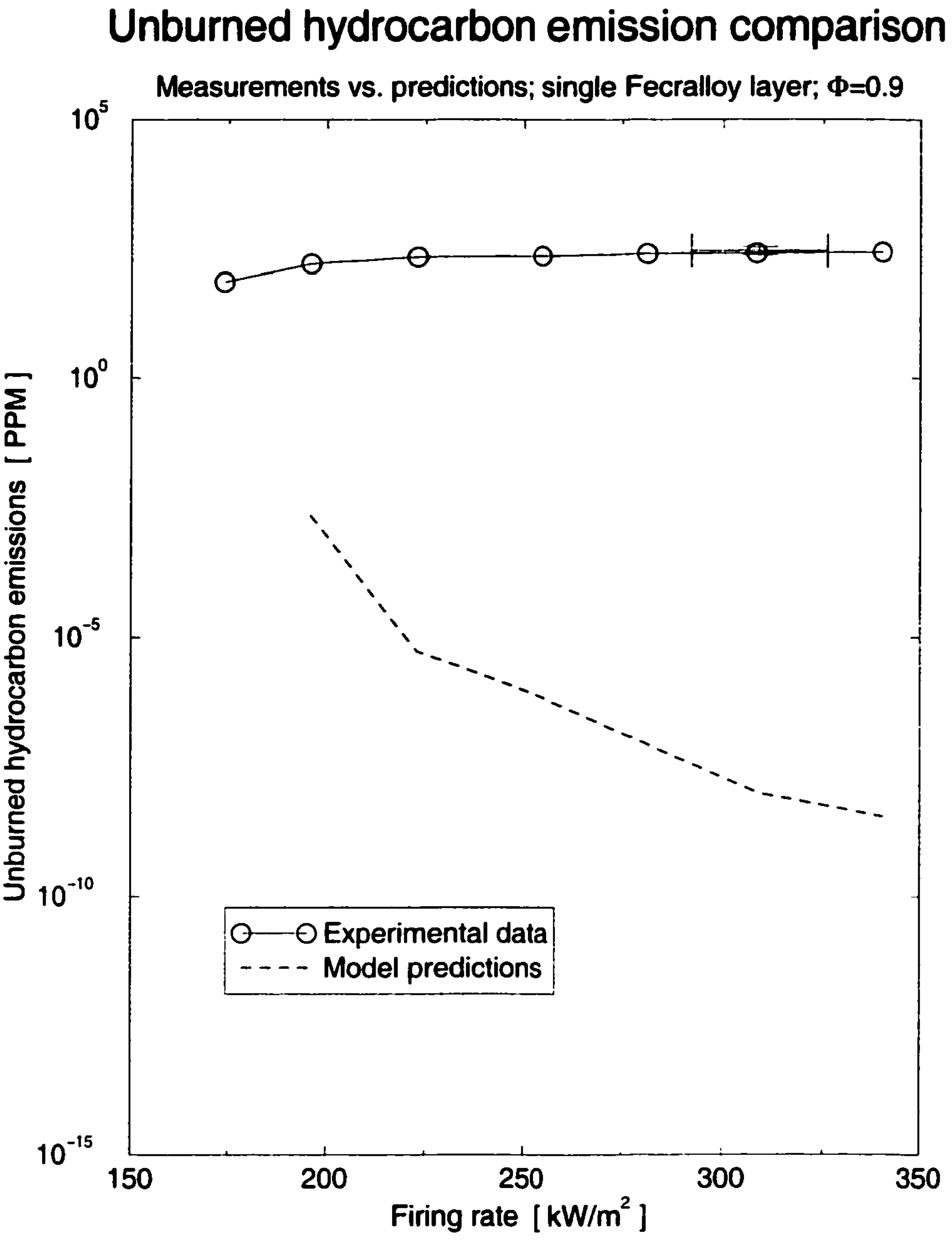

Figure 4.19. Comparison of the UBH emissions between the model predictions and the experimental data, for a fuel lean ($\Phi = 0.9$) inlet mixture. Concentrations are corrected to 3% O_2 (dry basis).

Table 4.2. Natural gas composition (vol. %) according to Zhou (1999).

Component	Volume %
CH_4	92.2
C_2H_4	3.3
N_2	3.9
CO_2	0.6

0.9 to 1.1). Some differences at the lower firing rates can be attributed to significant heat losses from the burner housing, which are not included in the modeling. In one case (fuel lean, low firing rate), the calculations suggest that the flame moves outside of the porous matrix, changing the nature of the solution; this effect was observed in the laboratory but at much lower firing rates.

The solid surface temperature is predicted qualitatively correctly. The experimental data are always about $200K$ higher than in the calculations, and lies between the numerical surface and maximum temperatures. This is because a significant fraction of the thermal radiation is emitted from the bulk of the solid matrix, and the concept of "surface" for a porous material is not straightforward. The measured quantity takes an intermediate value because it assigns an equivalent solid surface to the porous medium.

Emissions of CO and unburned hydrocarbons are not simulated very successfully. The CO is overpredicted by about one order of magnitude by the numerical code, and the hydrocarbons are severely underpredicted (by several orders of magnitude). A possible source for the discrepancy is that the chemical mechanism rates were optimized for adiabatic flames, and they might not be applicable to non-adiabatic processes. On the other hand, the elevated experimental data on the hydrocarbon emission can be caused by impurities in the fuel (natural gas instead of pure methane. as described in Section 4.3.6). It should be mentioned here that. even though the computed CO emissions are not accurate in magnitude. the trends with the firing rate are correct (for $\Phi \geq 1.0$).

5. PARAMETRIC STUDY

In this Chapter, the effects of certain model parameters affecting the thermal performance of the burner/heater are investigated. A solution for a baseline case is presented in order to assess the changes in the results after modifying one of the parameters of interest. Sensitivity calculations are performed for variations in volumetric heat transfer coefficient, equivalence ratio, firing rate, downstream oxygen concentration, surface emittance, thermal conductivity of the solid, extinction and scattering coefficients.

5.1. Choice of Baseline Parameters

The solution of the model equations require specifying the properties of the solid and the composition of the fuel stream. For this purpose, a single, 0.2 *cm* thick Fecralloy layer was considered as the flame support material, which started at $x = 0.2$ *cm* and ended at $x = 0.4$ *cm*; the computational domain extended up to $x = 0.5$ *cm*[1]. The gas-only region (from $x = 0$ to $x - 0.2$ *cm*) served to model the inlet plenum. The incoming fuel mixture was selected to be of an equivalence ratio of 1.1, which resulted in relatively fast computations[2] due to the lack of the complex NO_x chemistry of richer flames, but it still allowed the study of the effects of partial premixing. Effectively, this slightly fuel rich ($\Phi = 1.1$) mixture was selected purposely to avoid a fully-premixed solution and thus emphasize the role of the oxidizer back-diffusion

---

[1] For plotting purposes, however, the inlet plenum (i.e., the initial 0.2 *cm*) is not included. This is done in order to show in more detail the remaining of the computational domain, where the changes actually occur.

[2] "Fast" in this case meant between 5 and 10 CPU hours in an IBM RISC 6000 machine.

and partial-premixing, but, at the same time, remaining close to the stoichiometric conditions that are commonplace in normal radiant burner operation.

The relevant model parameters were summarized in Table 5.1. The volumetric heat transfer coefficient was selected for this base case to be 1,000 $\frac{kW}{m^3K}$, based on the analysis presented in Section 4.2.1; its influence is described in more detail in Section 5.2. The extinction coefficient was selected to be $\beta = 200\ m^{-1}$, as discussed in Section 4.2.2. The scattering phase function was taken to be unity (i.e., isotropic). Discrete ordinates equations were carried up to order 4 (S_4); symmetric and non-symmetric S_2 were not accurate enough[3], and higher order approximations did not improve the accuracy of the solution. Downstream O_2 concentration was assumed to be 0.2. In addition, the surface emittance for these calculations was chosen as $\varepsilon = 0.65$, the value provided by the manufacturer. Note that the concept of "surface" for a fibrous material can be ambiguous and often requires a more clear definition. It can refer to the whole surface of the material, or only the fraction of the area occupied by the uppermost layer of fibers. The former definition is used here.

Figure 5.1 depicts the temperature distribution inside the burner. The numerical solution of the model equations to the desired tolerance (absolute tolerance of 10^{-9}, relative tolerance of 10^{-4}, assuring four digits of accuracy) required using 67 mesh points for the gas phase: 45 points were used for the upstream preheat and flame zone, 7 for the two-phase region after the flame, and the remaining 13 for the downstream gas-only zone. The solution in the solid domain needed 54 points. It is interesting to note that there is a region with a relatively high accumulation of mesh points at the exit of the domain (at the right), due to the presence of a second (diffusion) flame, and the the need of matching the imposed Dirichlet boundary condition that specifies the O_2 and N_2 concentrations there.

The temperature profile of the gas shows a rapid, quasi-linear increase at the burner entrance. It peaks at the flame location ($x \approx 0.09\ cm$, a premixed flame)

---

[3] These are equivalent to the two-flux method and the Schuster-Schwarzschild approximation, respectively (Modest, 1993).

Table 5.1. Base case parameters for sample calculations.

Solid	
L $[m]$	0.002
ϕ	0.91
ε	0.65
h_v $[\frac{W}{m^3K}]$	10^6
k_s $[\frac{W}{mK}]$ (effective)	0.13
$\rho_s c_{p,s}$ $[\frac{J}{m^3K}]$	253,200
β $[m^{-1}]$	200
h $[\frac{W}{m^2K}]$ (at faces)	50
Gas stream	
Firing rate $[\frac{kW}{m^2}]$	200
Φ	1.1
Inlet T $[K]$	400
Surroundings	
χ_{O2} (downstream boundary)	0.2
T $[K]$	400

and then decreases since the flame loses energy to the solid. These losses are larger than the still ongoing chemical heat release. After leaving the solid matrix. the gas temperature rises again. mainly due to the reburning of CO_2 and H_2 (diffusion flame). The premixed flame inside a porous burner is considerably thicker[4] than a free flame. mainly because the preheating takes place over a broader region.

The temperature distribution in the solid matrix is roughly parabolic. with a subtle inflection point near the entrance of the burner, where the gas temperature. initially low, reaches the temperature of the solid. Peak temperature of the solid matrix is reached some distance downstream of the maximum gas temperature. at about $x \approx 0.012\ cm$. Radiation efficiency (as defined in Equation 2.2) is 22.4%.

Figure 5.2 illustrates the behavior of the temperature difference between the gas and the solid matrix. There is an entrance region ($x < 0.05\ cm$) where the porous solid is at a higher temperature than the gas mixture, actually preheating it. The initial positive slope of the curve shows that the gas temperature is increasing at a faster rate than the solid matrix temperature. A local maximum occurs at $x \approx 0.08\ cm$. indicating that the trend is reversed. i.e.. the temperature of the solid starts to increase faster. There is another local extremum (in this case. a minimum) at $x \approx 0.12\ cm$, after which the temperature difference increases significantly. corresponding to the region near the burner face. where the solid matrix temperature decreases due to radiative losses (even though the hot gases are still transferring energy to the solid by convection.) Exit temperature difference is about $700K$.

---

[4] The flame thickness does not have a significant influence in the thermal performance of the burner/heater and it is not investigated in this dissertation.

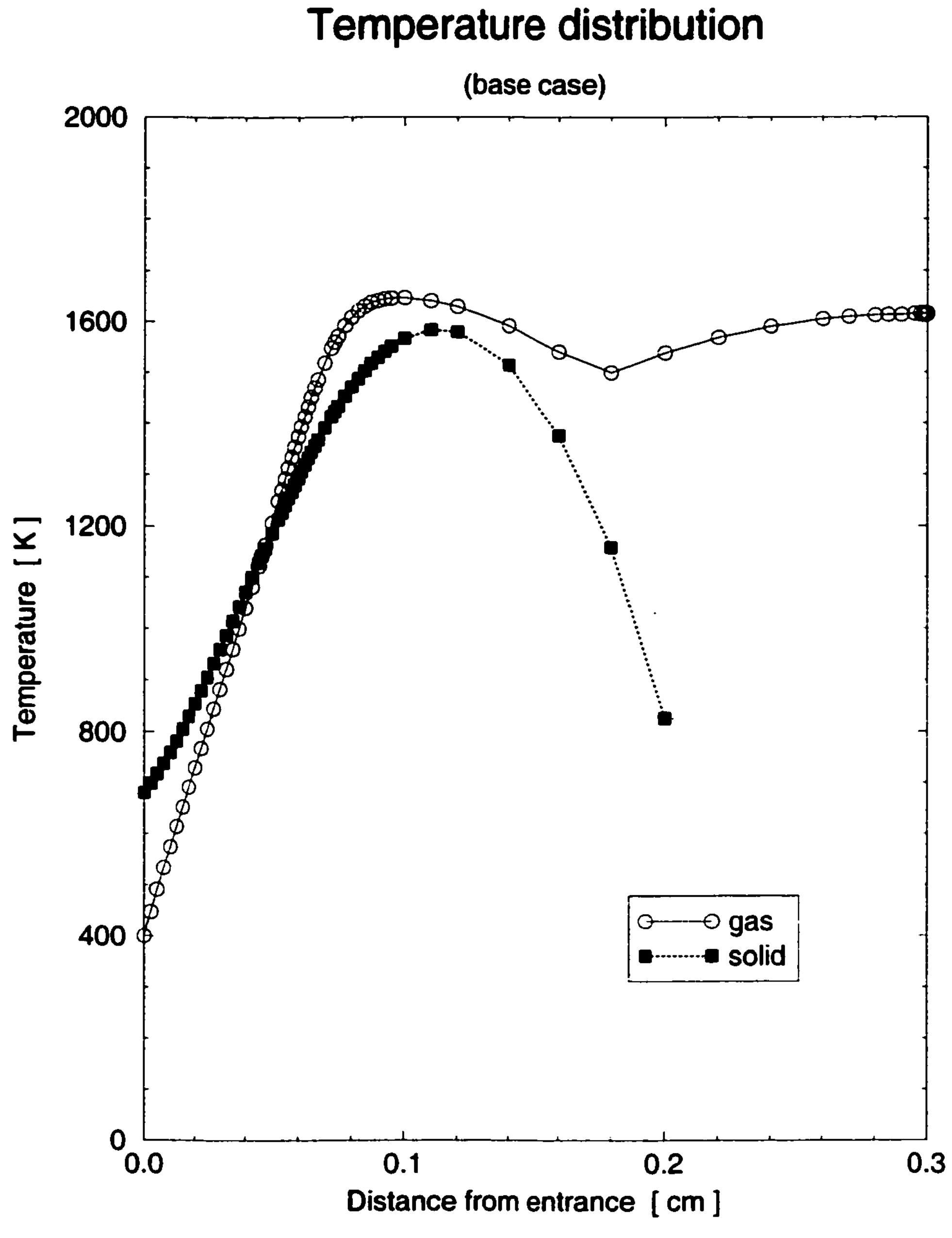

Figure 5.1. Gas and solid matrix temperature distribution inside the model burner.

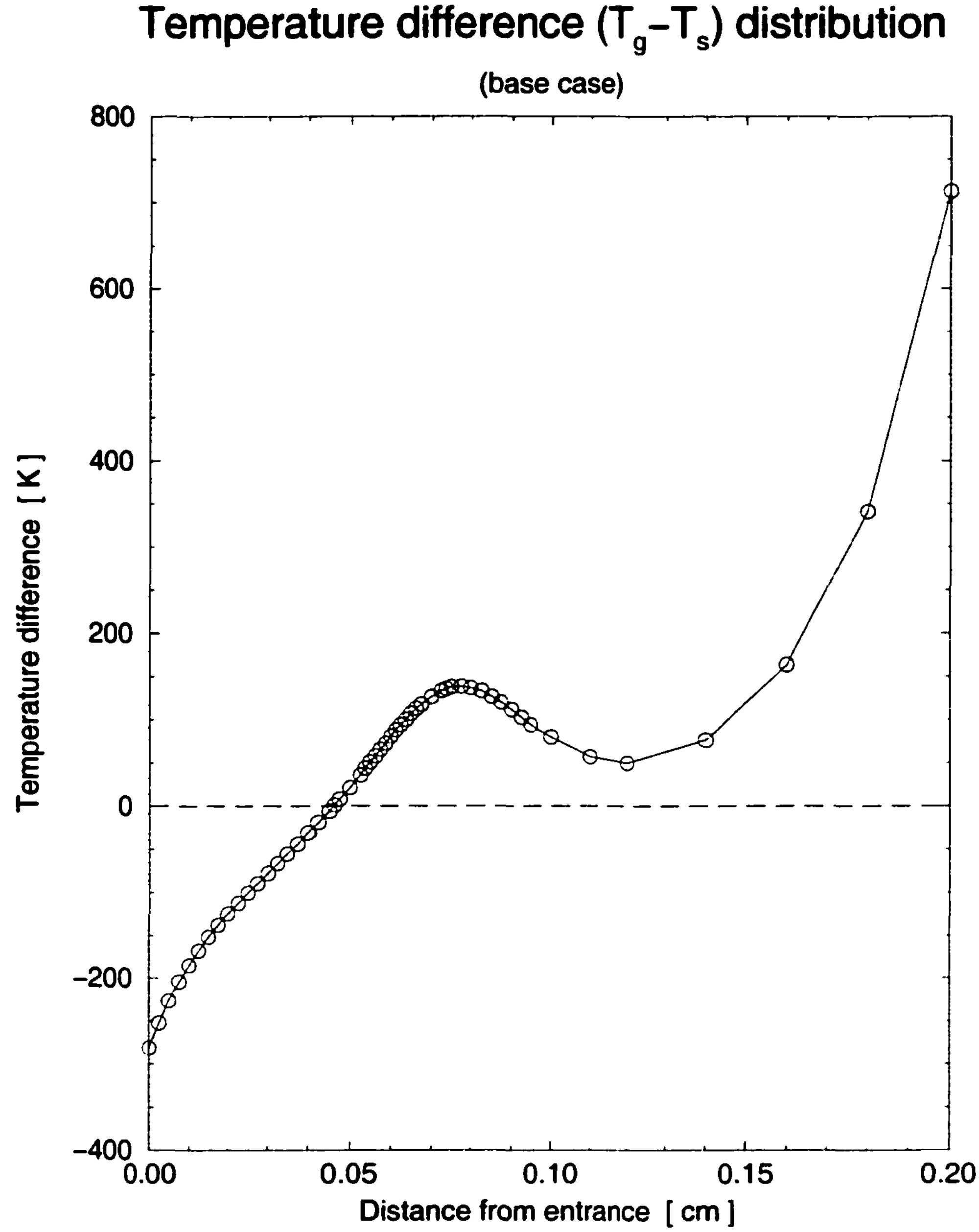

Figure 5.2. Temperature difference (between the gas and the solid matrix) distribution inside the model burner. A negative value (as seen for $x < 0.05$ *cm*) indicates that the porous pad is at a higher temperature than the incoming gas, therefore preheating the flow.

Figure 5.3 shows the variation of the local velocity along the computational domain: inlet value is almost $20\frac{cm}{s}$, a peak at the flame center reaches about $75\frac{cm}{s}$, and then decreases at the outlet to about $70\frac{cm}{s}$. A local minimum for the gas velocity is present right at the burner face, where the temperature reaches also a local minimum. It is interesting to compare that the velocity ratio (maximum/inlet) is about 4, somewhat lower than that of a free flame, which is around 6[5]. In Figure 5.4 it can be seen that the local gas density presents the opposite trend: it decreases from a maximum at the entrance to a minimum at the flame center, and then starts to increase again (when the products of combustion cool down by transferring energy to the solid matrix) and, finally, after exiting the solid layer the density decreases once again.

Selected "major" species are plotted in Figure 5.5, and "minor" species are presented in Figure 5.6. The fuel and oxidizer fractions change relatively quickly at the flame location ($x \approx 0.09$ cm). O_2 reaches a minimum (non-zero) value right after the premixed flame, in between one region where the injected oxidizer was consumed and another where O_2 diffuses from the downstream boundary.

The mole fraction of CO reaches a maximum at the premixed flame location, being consumed thereafter. Radicals (O, H, OH) increase rapidly at that same position, with a peak a small distance downstream of the flame, and they decay in the post-flame zone. But not all these radicals indicate the same trend after leaving the porous material: while the H diminishes monotonically, O and OH show second peaks during the reburning stage.

Hydrogen (H_2) is quickly generated in the fuel-rich entrance region, and then is monotonically consumed roughly in three equal parts: 1/3 at the premixed flame, 1/3 in the post-flame region inside the burner, and the remaining 1/3 at the diffusion flame during reburning.

---

[5] The maximum gas temperature inside the burner is usually lower than the temperature of a free flame. Therefore, the velocity (density) ratio for a flame submerged in a porous burner is smaller (larger).

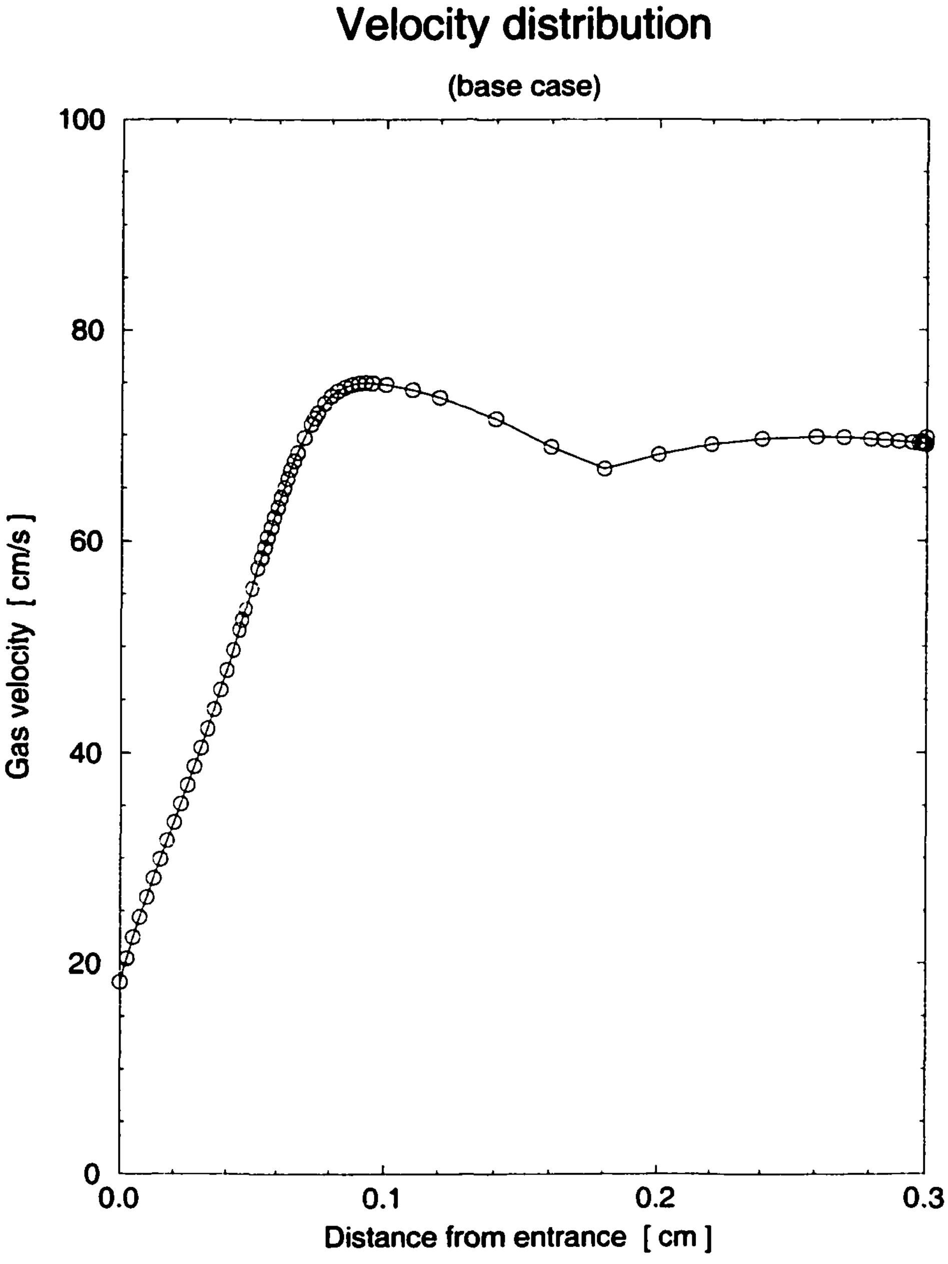

Figure 5.3. Gas velocity distribution inside the model burner.

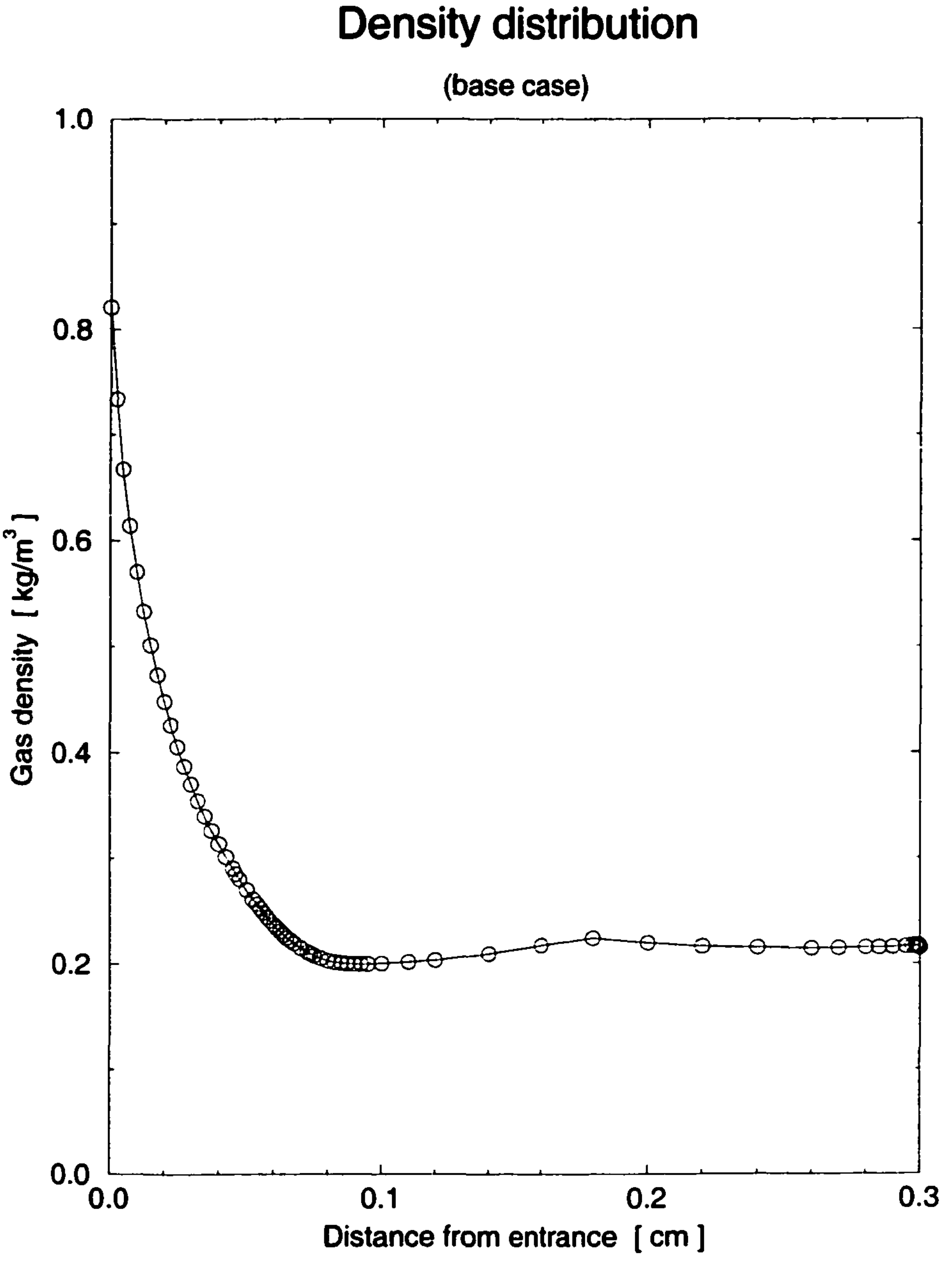

Figure 5.4. Gas density distribution inside the model burner.

Main combustion products (CO_2 and H_2O) initially increase, but their mole fractions decrease after the main reaction zone due to the back-diffusion of air. Formation of NO pollutant also increases initially following the temperature rise at the flame front, but it becomes consumed in the lower temperature diffusion flame. Another important pollutant, NO_2, shows rapid formation before the flame front, followed by rapid destruction at the flame front (due to the decomposition into NO at high temperature.) A slight NO_2 concentration recover occurs later in the colder post-flame zone.

There are several mechanisms by which NO is created in a flame. In all cases, NO is the primary species formed, and NO_2 production always requires NO as a reactant.

1. *Thermal* (or Zeldovich) mechanism (Miller and Bowman, 1989) is given by the reactions 178, 179 and 180 of GRI-Mech 2.11 (Appendix E):

$$\mathrm{N + NO = N_2 + O} \ ,$$

$$\mathrm{N + O_2 = NO + O} \ ,$$

$$\mathrm{N + OH = NO + H} \ .$$

   This mechanism has a large activation energy and is not important below $1800K$ (Correa, 1992).

2. *Prompt* (or Fenimore) mechanism occurs within the flame zone, and it is initiated by the attack of N_2 by CH radicals. The details of the mechanism are not fully established (Lyle, 1997), but the four most important initiating reactions are believed to be (Miller and Bowman, 1989) numbers 238, 239, 240 and 242 of GRI-Mech 2.11:

$$\mathrm{H_2CN + N = N_2 + CH_2} \ ,$$

$$\mathrm{C + N_2 = CN + N} \ ,$$

$$\mathrm{CH + N_2 = HCN + N} \ ,$$

$$\mathrm{CH_2 + N_2 = HCN + NH} \ .$$

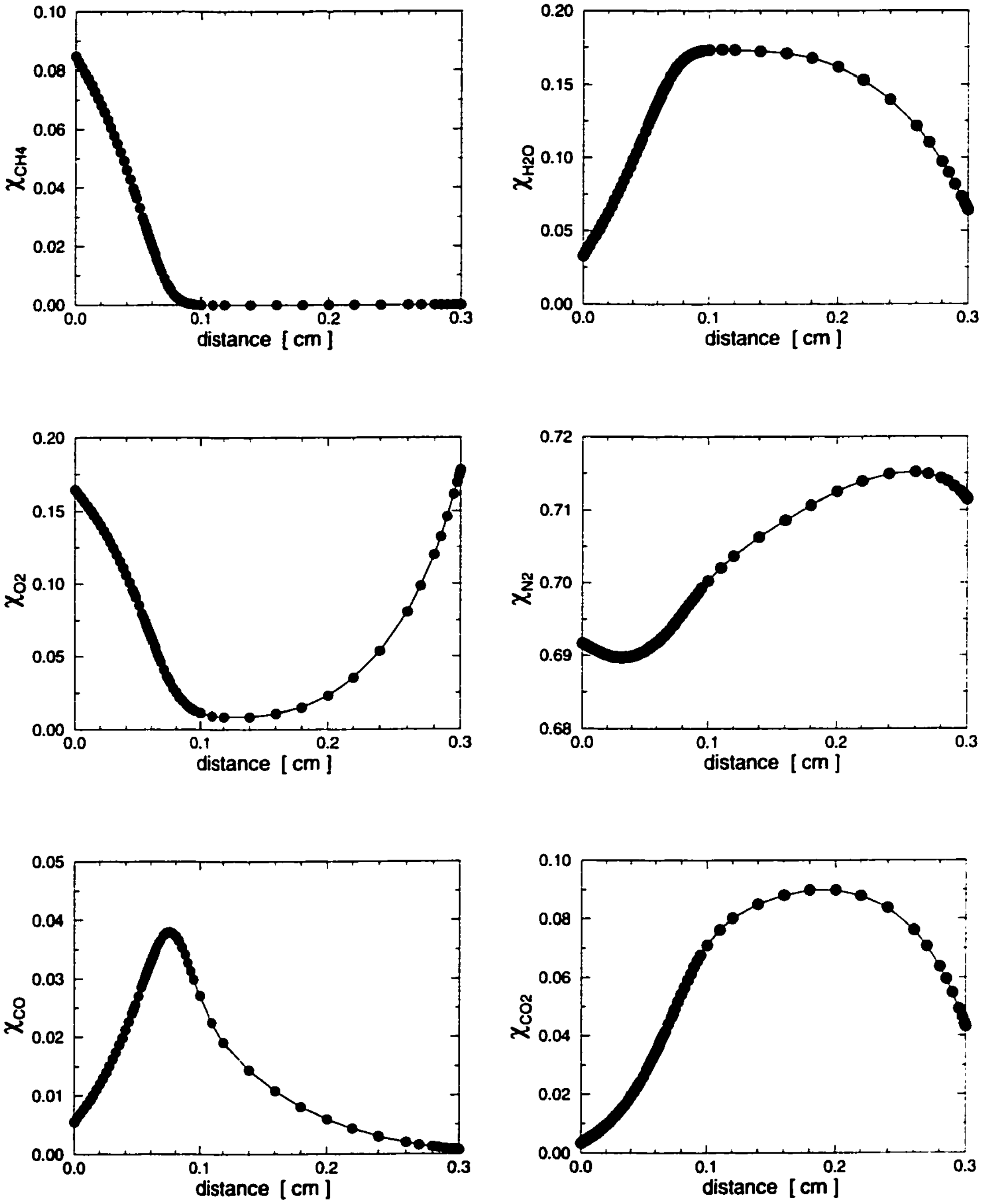

Figure 5.5. Selected (major) species distributions inside the model burner.

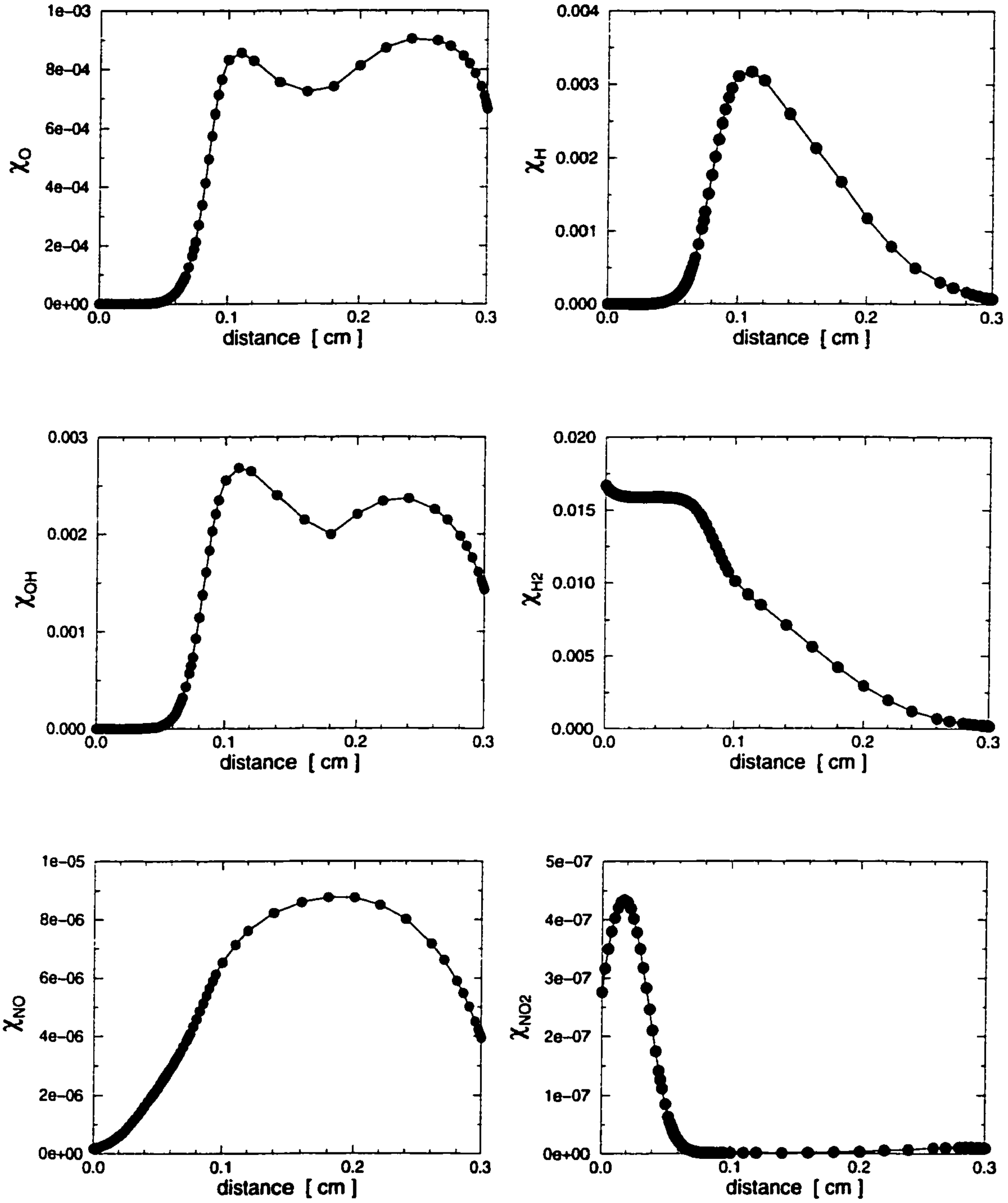

Figure 5.6. Selected (minor) species distributions inside the model burner.

3. Another NO generation pathway is through the *nitrous oxide* mechanism, which involves the conversion of intermediate N_2O into NO. One of the major production routes for N_2O is the recombination of N_2 and O in the presence of a third body (reaction number 185 of GRI-Mech 2.11):

$$N_2O + M = N_2 + O + M \ .$$

N_2O can then react with other species to form NO according to reactions 182, 199 and 228 (Nishioka et al., 1994):

$$N_2O + O = 2NO \ ,$$

$$N_2O + H = NH + NO \ ,$$

$$N_2O + CO = NCO + NO \ .$$

This mechanism is usually not significant except in very lean, low-temperature flames (Correa, 1992).

Nishioka et al. (1996) discussed contributions of different reaction steps to NO production in counterflow flames. Lim (1998) used that information to show that the prompt mechanism contributed even more when the temperature was increased due to steam addition. He also pointed out that, since reaction 178 was highly sensitive to temperature, the sensitivity of NO_x emissions resulted from this reaction step. Additionally, CH and HCN (from reaction 240) were identified as significant species in the overall nitrogen oxides chemistry (Lim, 1998).

Figure 5.7 depicts the profiles of some of the relevant species for the aforementioned mechanisms, in terms of the local coordinate. Since most of the change takes place within a small region (at the flame location), a fuel-based progress variable[6] (ζ, defined below in Equation 5.1) is used to show in more detail the variation of the mole fractions

---

[6] Because of the definition of the progress variable, ζ, the both the premixed flame and the downstream diffusion flame are collapsed together. Note that it is common to work with a normalized form of the fuel mass fraction, i.e., the progress variable (Neuber et al., 1998), which is useful to describe premixed flames in terms of a single thermochemical variable (Prasad et al., 1999).

with the reaction progression (Figure 5.8). Mole fractions for CH and H_2CN behave similarly, presenting a narrow peak with a maximum at $\zeta \approx 0.95$, and diffusing toward the low ζ values; rapid destruction occurs as $\zeta \rightarrow 1.0$. Mole fraction for HCN shows a gradual, almost linear increase from $\zeta = 0$ up to $\zeta \approx 0.95$, then a sharp decrease.

After a slow increase to about 50% of its maximum value, the NO species are characterized by a very narrow peak at $\zeta = 1.0$. The NO_2 reveals a broad peak around $\zeta = 0.20$, which is associated with the oxidation of NO at low temperatures. The N_2O mole fraction is more symmetric, implying that the diffusion and formation rates ($\zeta < 0.40$) are of the same order as the destruction rates ($\zeta > 0.40$). More on the use of the progress variable follows in Section 5.2.

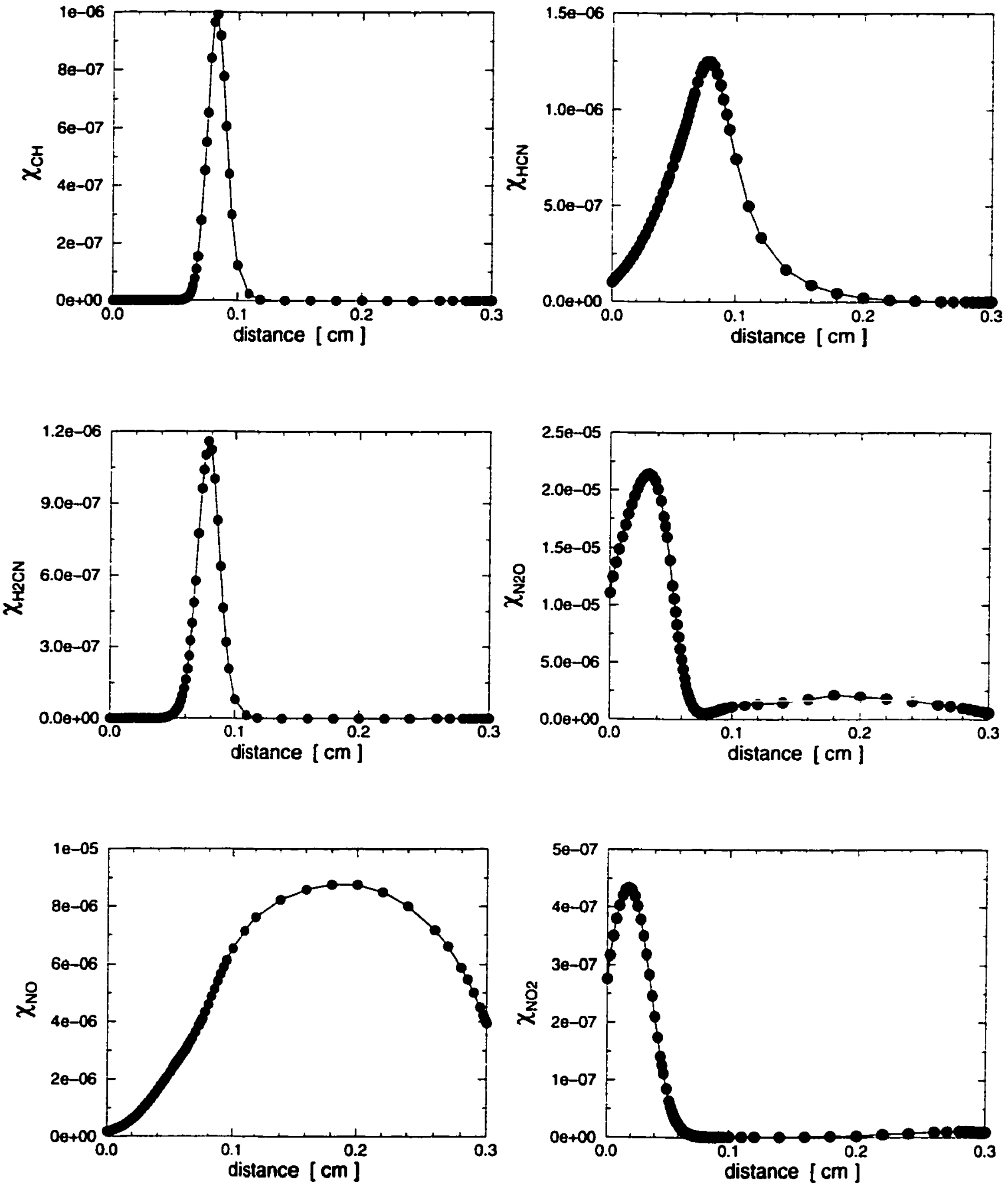

Figure 5.7. Selected species (relevant to NO mechanisms) distributions inside the model burner.

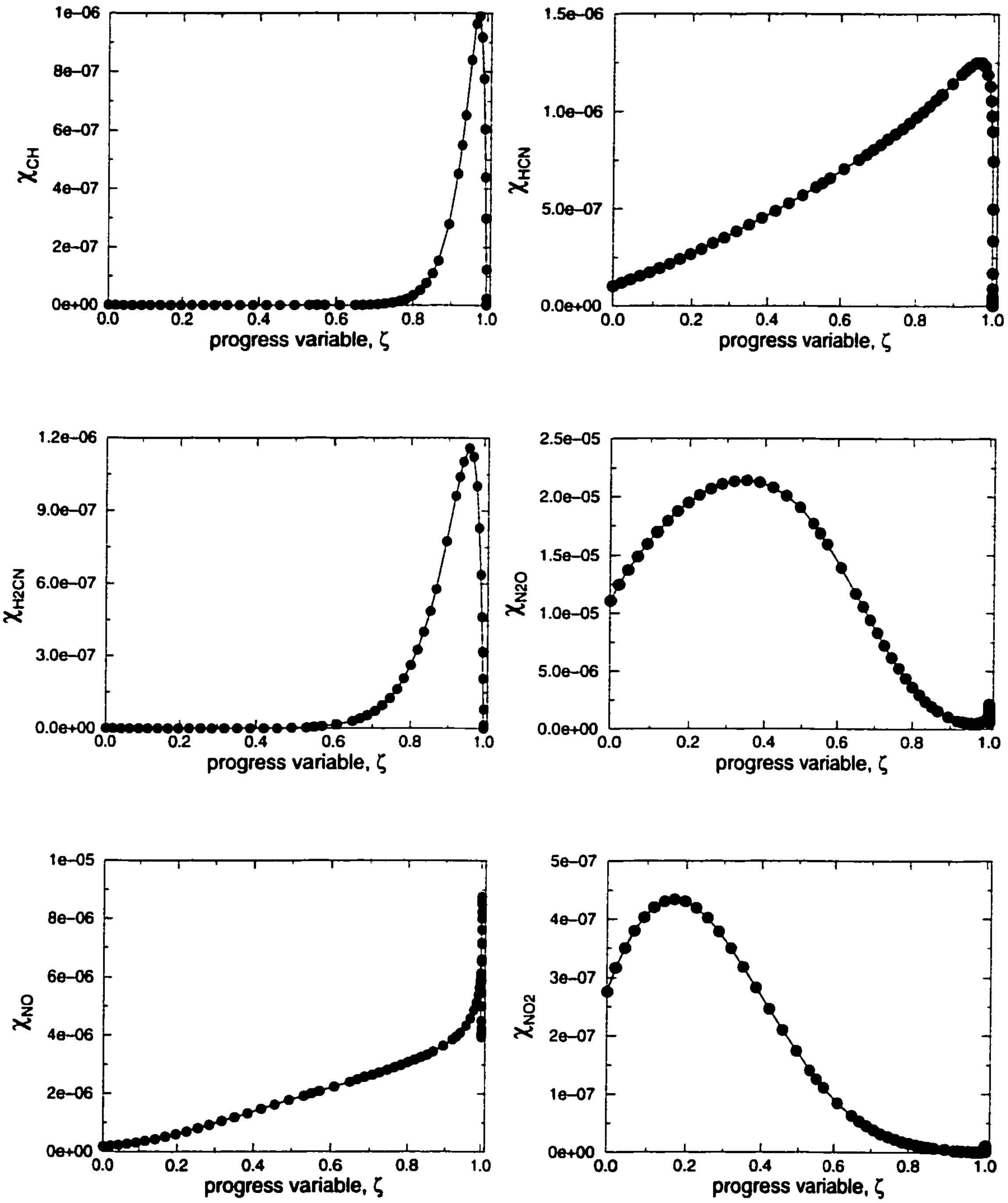

Figure 5.8. Selected species (relevant to NO mechanisms) distributions inside the model burner, in terms of the progress variable, ζ.

5.2. Influence of the Volumetric Heat Transfer Coefficient

The effect of the volumetric heat transfer coefficient, h_v, is discussed in this section. Figure 5.9 shows the changes in the temperature profiles for the gas and solid phases when increasing h_v by 50% (to 1,500 $\frac{kW}{m^3K}$) or decreasing it to 50% of the base case value (500 $\frac{kW}{m^3K}$). It is apparent that the temperature of the gas mixture is not too sensitive to the value of the volumetric heat transfer coefficient. The peak flame temperature is hardly affected by the changes, and the exit temperature difference between the two limits (when h_v differs by 200%) is less than $100K$. The variation in the volumetric heat transfer coefficient, however, causes a small shift in the flame location. When h_v decreases, the reaction zone stabilizes deeper in the matrix; for larger values, the flame moves toward the inlet. The change in the flame location can be attributed to the preheating of the mixture: larger convective heat transfer allows faster preheating, therefore, accelerating ignition. It has been observed in the numerical experiments that the subsequent increase of h_v beyond 1,500 $\frac{kW}{m^3K}$ has no influence on the flame location.

The temperature of the solid matrix is strongly affected by the value of the volumetric heat transfer coefficient. Even though an increase of h_v beyond the baseline value is not significant, a considerable effect is observed for lower values. The maximum temperature drops almost $200K$ when h_v is reduced to 50% of the base case value.

The change in the temperature profiles caused by a variation in the volumetric heat transfer coefficient produces a corresponding shift in the species profiles (Figures 5.10 and 5.11.) Since the gas temperature remains almost constant for these three cases, the species profiles are quite similar. Most notably, the temperature change outside the porous material affects the radicals O and OH_2 levels. The CH_4 and O_2 consumption occurs more slowly for low h_v, resulting in a stronger diffusion flame on the burner surface.

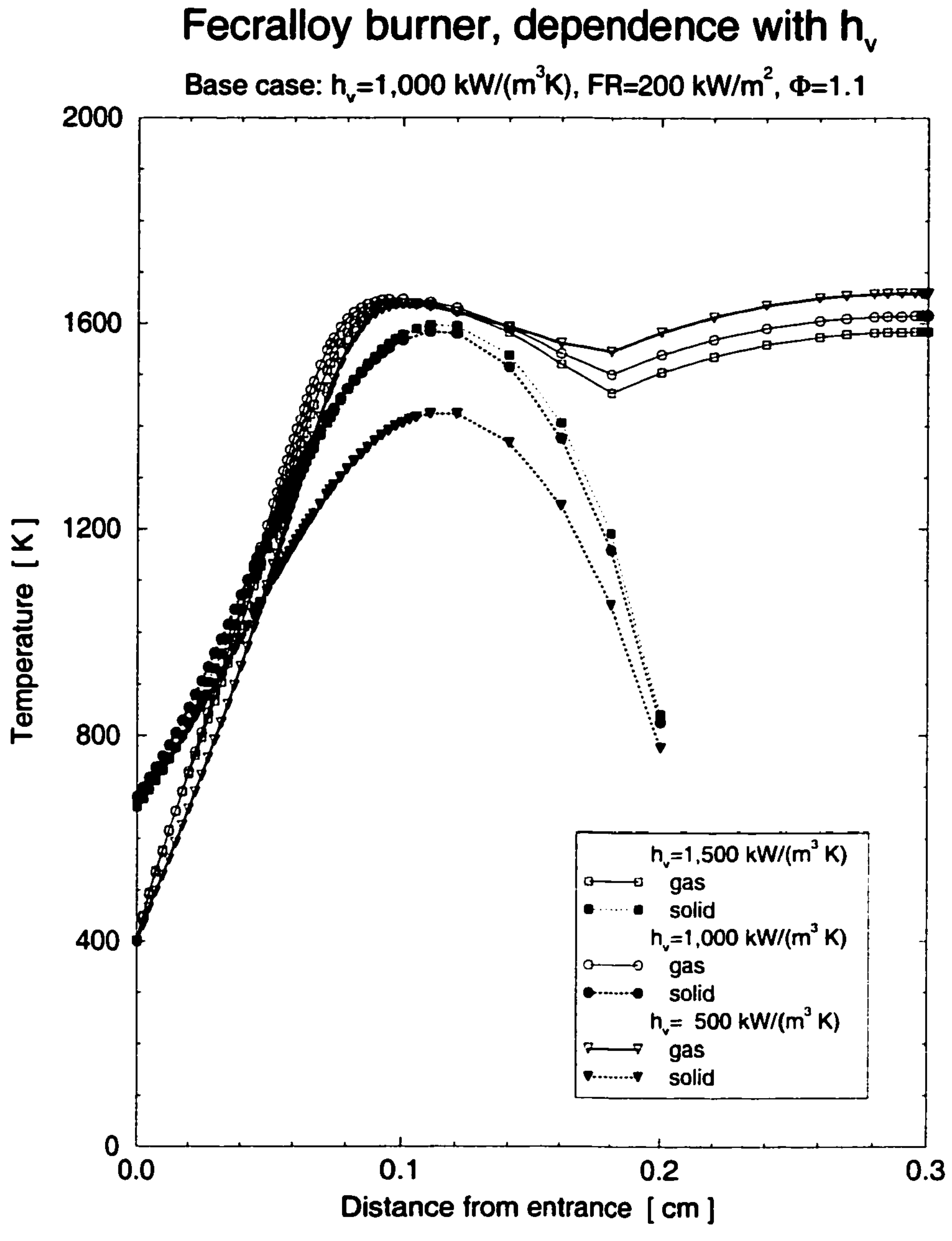

Figure 5.9. Temperature distribution inside the model burner for three different values of the volumetric heat transfer coefficient.

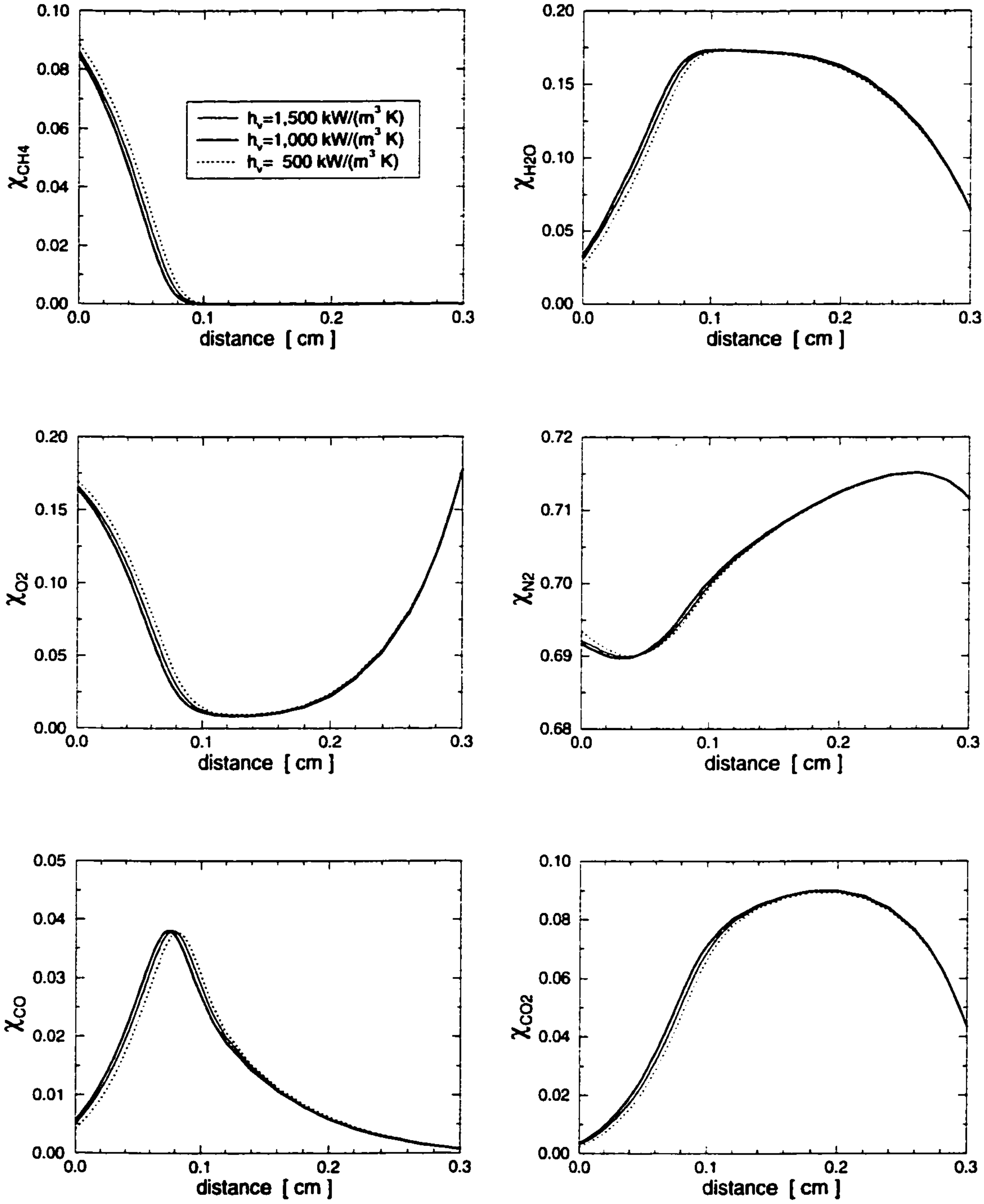

Figure 5.10. Major species distribution inside the model burner for three different values of the volumetric heat transfer coefficient.

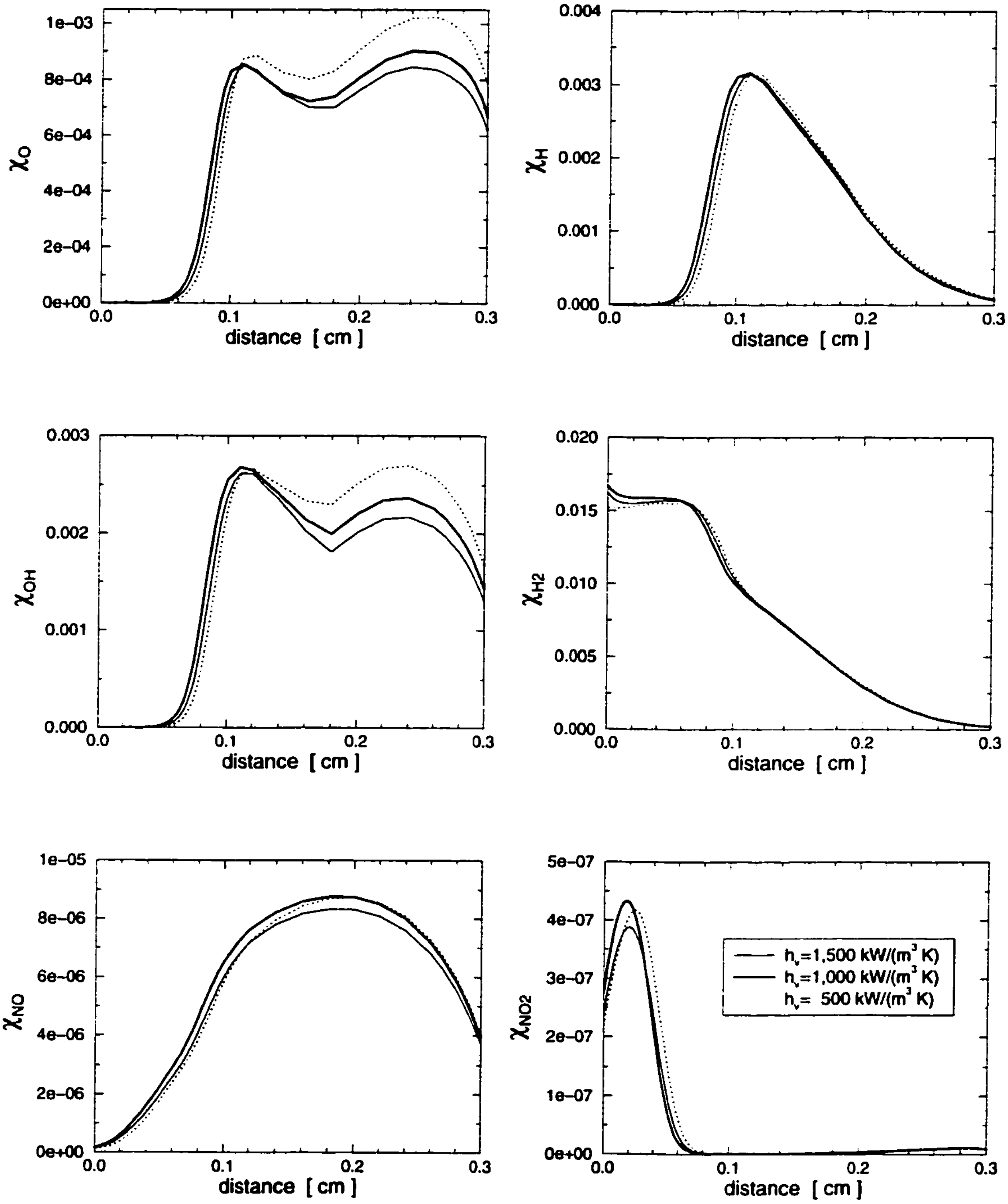

Figure 5.11. Minor species distribution inside the model burner for three different values of the volumetric heat transfer coefficient.

An interesting way of studying the effects of the heat loss on chemistry is by using a suitable progress variable. In this manner, the effects of other variables such as flame location, flame thickness, etc., can be eliminated.

Free adiabatic flames allow the definition of a progress variable in terms of the gas temperature; however, since the gas temperature in the non-adiabatic case is maximum inside the domain (and not at the exit), such progress variable becomes non unique, because the same value is obtained during the gas mixture heating and cooling. According to Gouldin (1996), a progress variable may be defined in terms of a mass (mole) fraction of a species[7]. Therefore, a convenient definition in terms of the fuel molar fraction is:

$$\zeta = \frac{\chi_{CH4} - \chi_{CH4,in}}{\chi_{CH4,out} - \chi_{CH4,in}}, \tag{5.1}$$

which ranges from 0 to 1, and it is effectively unique in the domain.

Figures 5.12 and 5.13 show the same results as those presented in Figures 5.10 and 5.11 but in terms of the progress variable, ζ. The effects of the different flame location for the different values of h_v vanish, and all three curves virtually collapse on top of each other. The three solutions with different values for the volumetric heat transfer coefficient deviate from similarity only slightly in the case of NO_2, due to the sensitivity of this species to the maximum gas temperature. Especially successful is the collapse of the radicals O and OH, which present significantly different profiles along the diffusion flame region ($x > 0.2$ cm, Figure 5.11), but become virtually indistinguishable in terms of ζ (Figure 5.13).

The injected species (CH_4, O_2, N_2) present a negative gradient at $\zeta = 0$ due to the advective transport; all other species show positive gradients, which is characteristic of the diffusive transport in the upstream direction and is particularly strong for N_2O. The CO sharp decrease at $\zeta = 1.0$ actually corresponds to the oxidation in the diffusion flame. The peaks in O_2 and N_2 at $\zeta = 1.0$ are due to the downstream source

---

[7] The use of different species for the definition of the progress variable will give different results in the presence of differential diffusion; see, for example, Cant et al. (1994).

for those species that drive the back-diffusion process (the decrease in H_2O and CO_2 mole fractions is linked to the same effect). Radicals O, H and OH peak out shortly before both the premixed and the diffusion flames, but only the former can be seen in this representation.

The NO profile shows a peak at the end of the reaction zone ($\zeta \approx 1$) due to the thermal production. The pollutant diffuses upstream where is converted to NO_2 by recombination at lower temperatures (maximum at $\zeta \approx 0.2$).

The resulting temperature distributions obtained when using very high and low values for the volumetric heat transfer coefficient are presented in Figure 5.14. The premixed flame is submerged more deeply within the solid matrix when h_v is low, since the preheating of the gas mixture occurs more slowly, and thus the gas mixture has more time before being ignited. Gas temperatures increase with a reduction in h_v, due to the diminished heat loss. On the other hand, the solid temperature decreases considerably when the thermal coupling to the gas phase is reduced.

A subsequent decrease in h_v (below 250 $\frac{kW}{m^3K}$) causes the flame location to move further downstream, very near the front face of the burner. The excessive heat losses cannot be sustained in this case and the reaction either extinguishes or becomes one for a surface (burner stabilized) flame, depending on the firing rate.

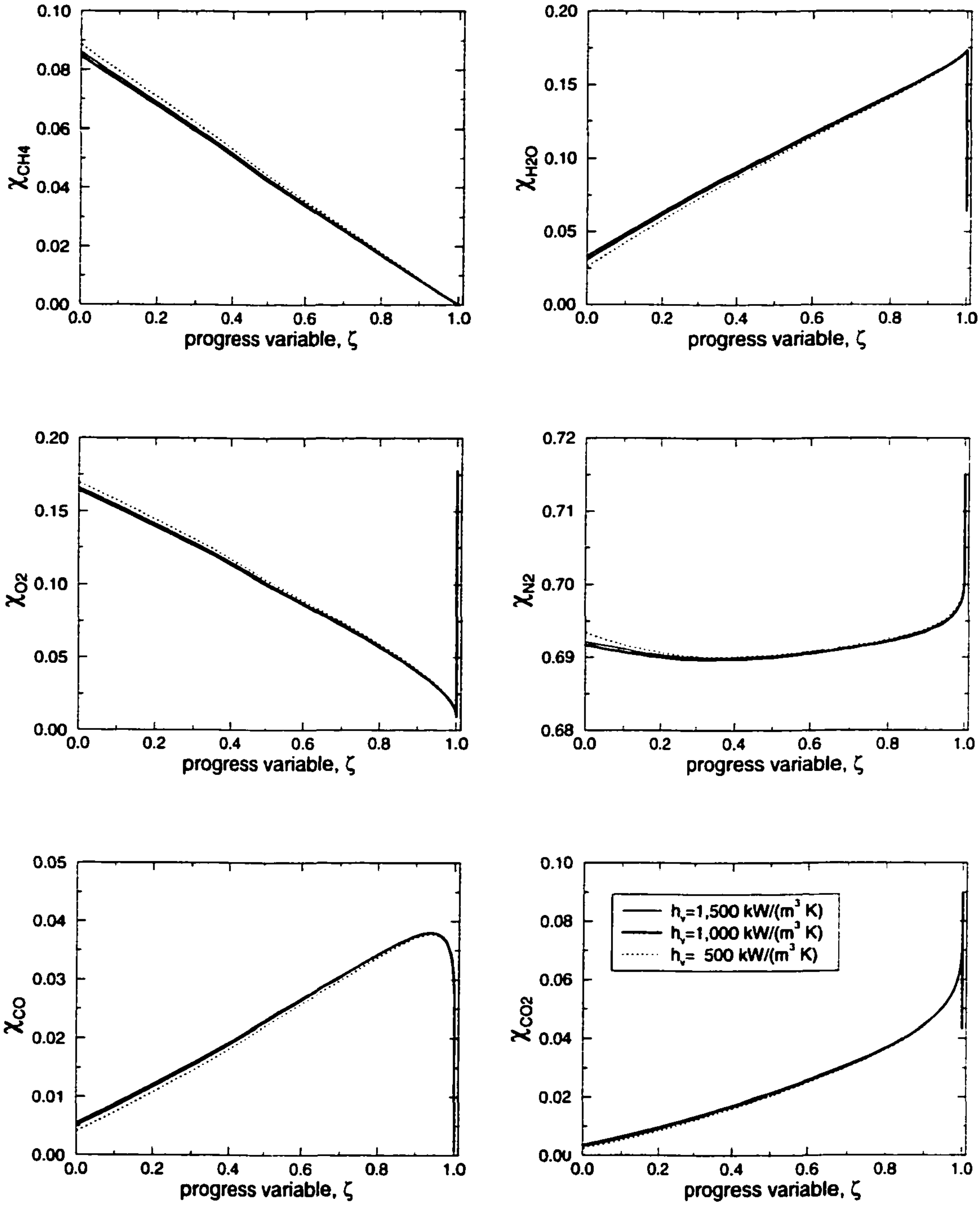

Figure 5.12. Major species distribution inside the model burner in terms of the progress variable, ζ, for three different values of the volumetric heat transfer coefficient, h_v. Note that all the separate curves shown in Figure 5.10 collapse on top of each other in this representation.

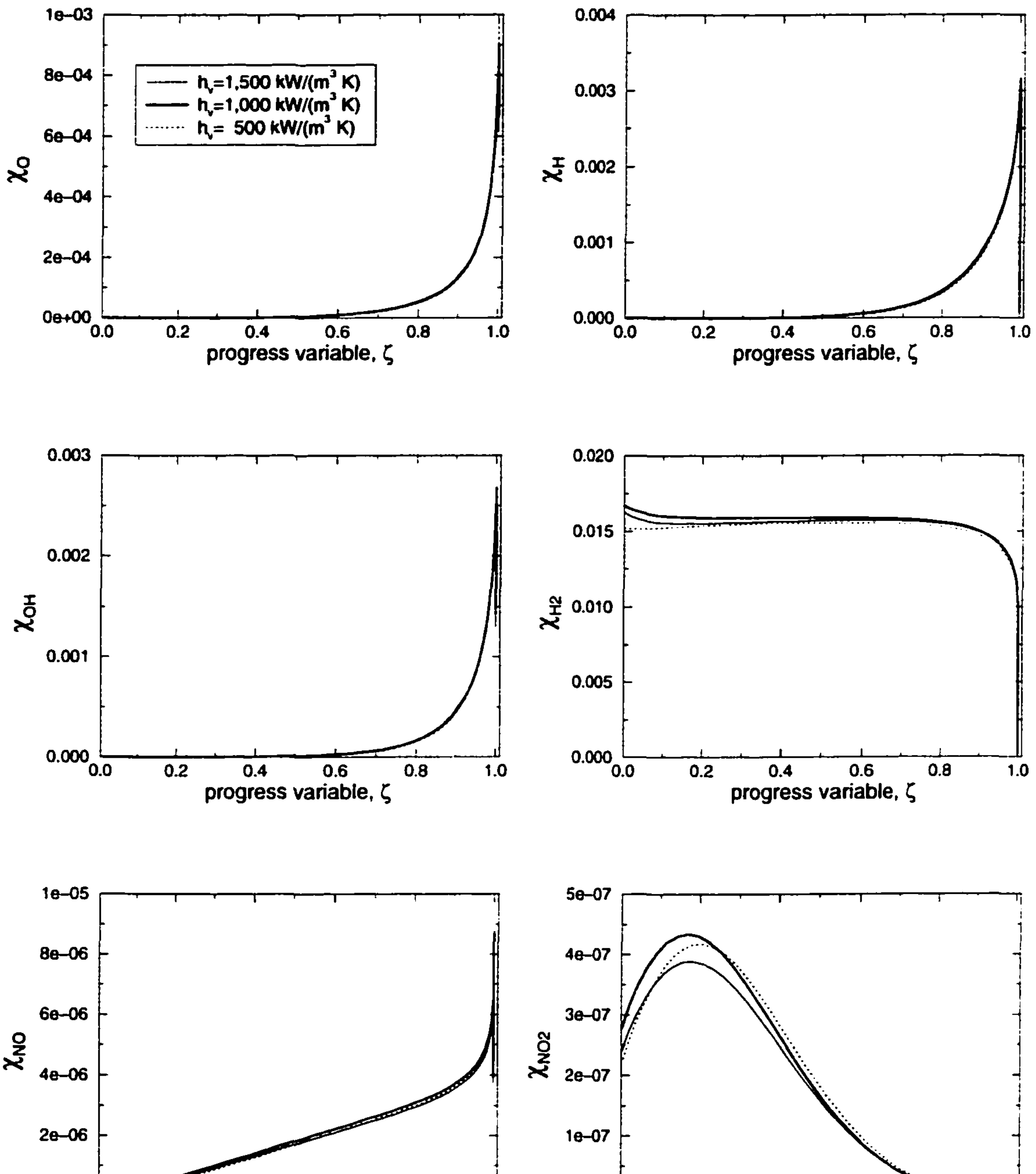

Figure 5.13. Minor species distribution inside the model burner in terms of the progress variable, ζ, for three different values of the volumetric heat transfer coefficient, h_v. Note that all the separate curves shown in Figure 5.11 collapse on top of each other in this representation.

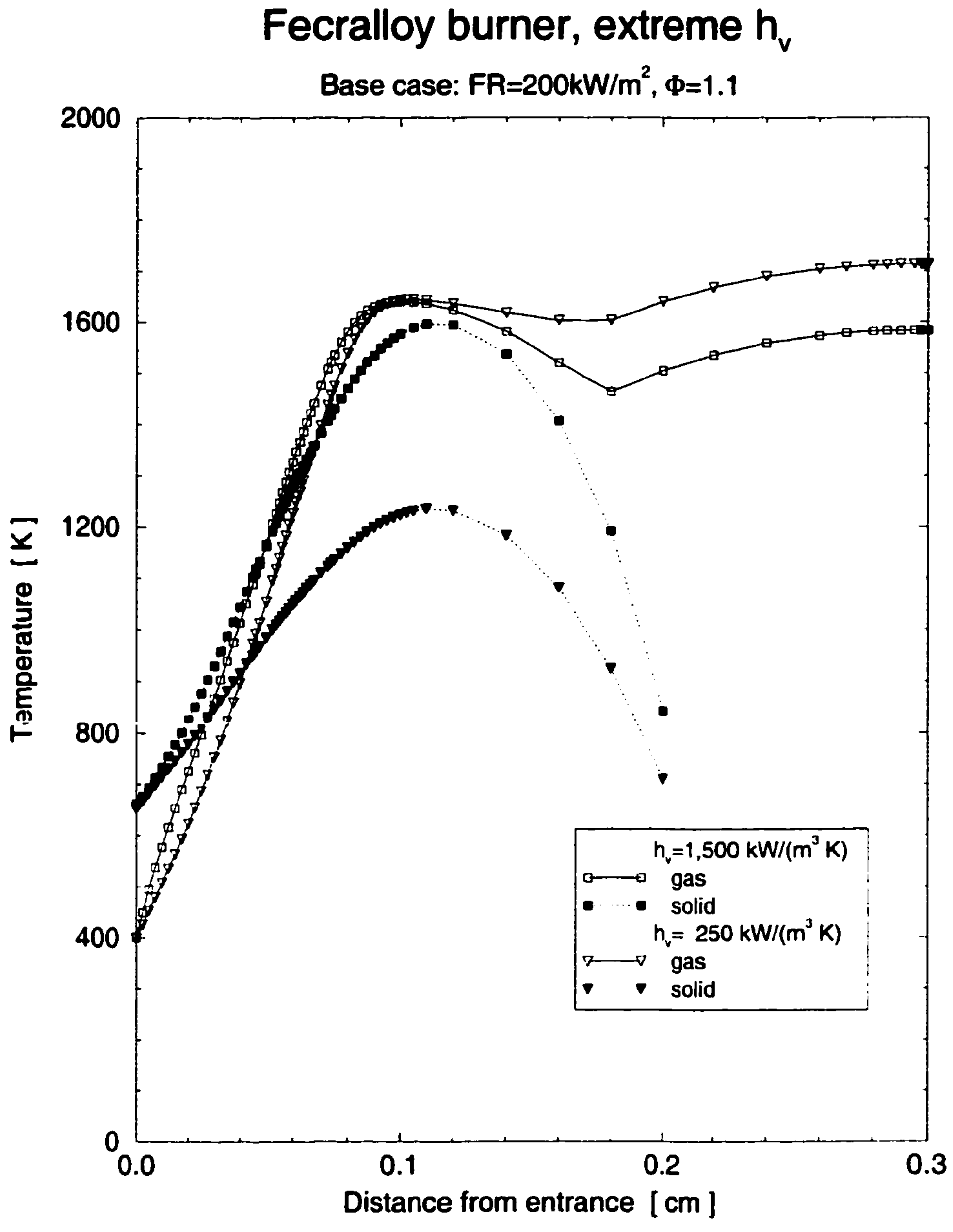

Figure 5.14. Temperature distribution inside the model burner for extremely high and low values of heat transfer coefficient, h_v.

The gas temperature distributions included in Figure 5.14 are plotted in Figure 5.15 now in terms of the complementary progress variable, $1-\zeta$. Selected species concentrations are depicted in Figures 5.16 to 5.18, also as a function of $1-\zeta$. In this representation, the high-temperature (i.e., flame) region (which lies to the left of the plots) is expanded to emphasize the differences caused by the heat loss, where $\zeta \approx 1.0$).

The gas temperature distributions inside the Fecralloy model burner are virtually identical except for $\zeta > 0.999$ (or $1-\zeta < 10^{-3}$), where the results for the lower h_v value reveal higher temperatures due to the reduced heat transfer to the porous matrix. Major species (Figure 5.16) are completely analogous. The profiles for both values of h_v are identical. Selected minor species are compared in Figure 5.17. The H and H_2 are not affected by the differences in the heat loss, but the radicals O and OH show some difference for $1-\zeta < 10^{-2}$. The NO profiles begin to differ from the very beginning, showing about 10% excess of this pollutant for $1-\zeta = 10^{-6}$ in the case with the lower h_v (when the resulting gas temperature is higher). The NO_2 distributions are similar, virtually zero, except in the narrow region $0.1 < 1-\zeta < 1.0$, where the local (low) gas temperature favors the recombination of NO into NO_2. When h_v is low, there is more NO available and, therefore, more NO_2 is produced. Some of the species that contribute to the formation of NO are plotted in Figure 5.18, along with NO and NO_2 fractions. No significant differences are observed in CH, HCN, H_2CN and N_2O, suggesting that the NO and NO_2 formations are the result of many reaction paths combined.

The radiant burner results have been compared to those of a free (burner stabilized) flame. The main difference between them is that the free flame generates a greater amount of NO, mainly due to its higher peak temperature.

The radiation efficiency of the model burner decreases with an increase in the volumetric heat transfer coefficient. As expected, a stronger thermal coupling between the reactive flow and the porous matrix results in more energy being transferred to the solid phase, which then emits a larger fraction of the energy supplied to the

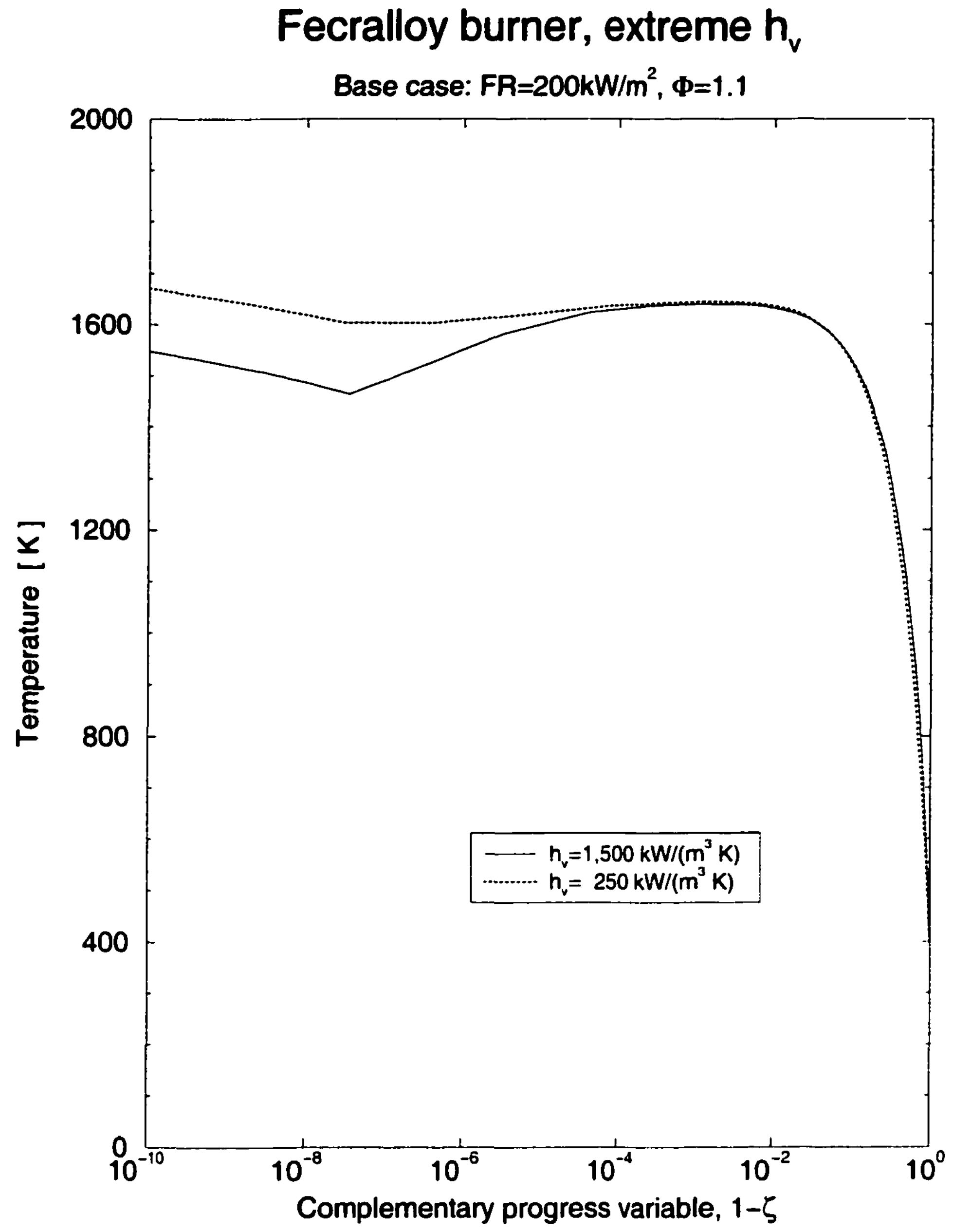

Figure 5.15. Temperature distribution inside the model burner for very low and very high values of the volumetric heat transfer coefficient, h_v, as a function of the complementary progress variable, $1-\zeta$.

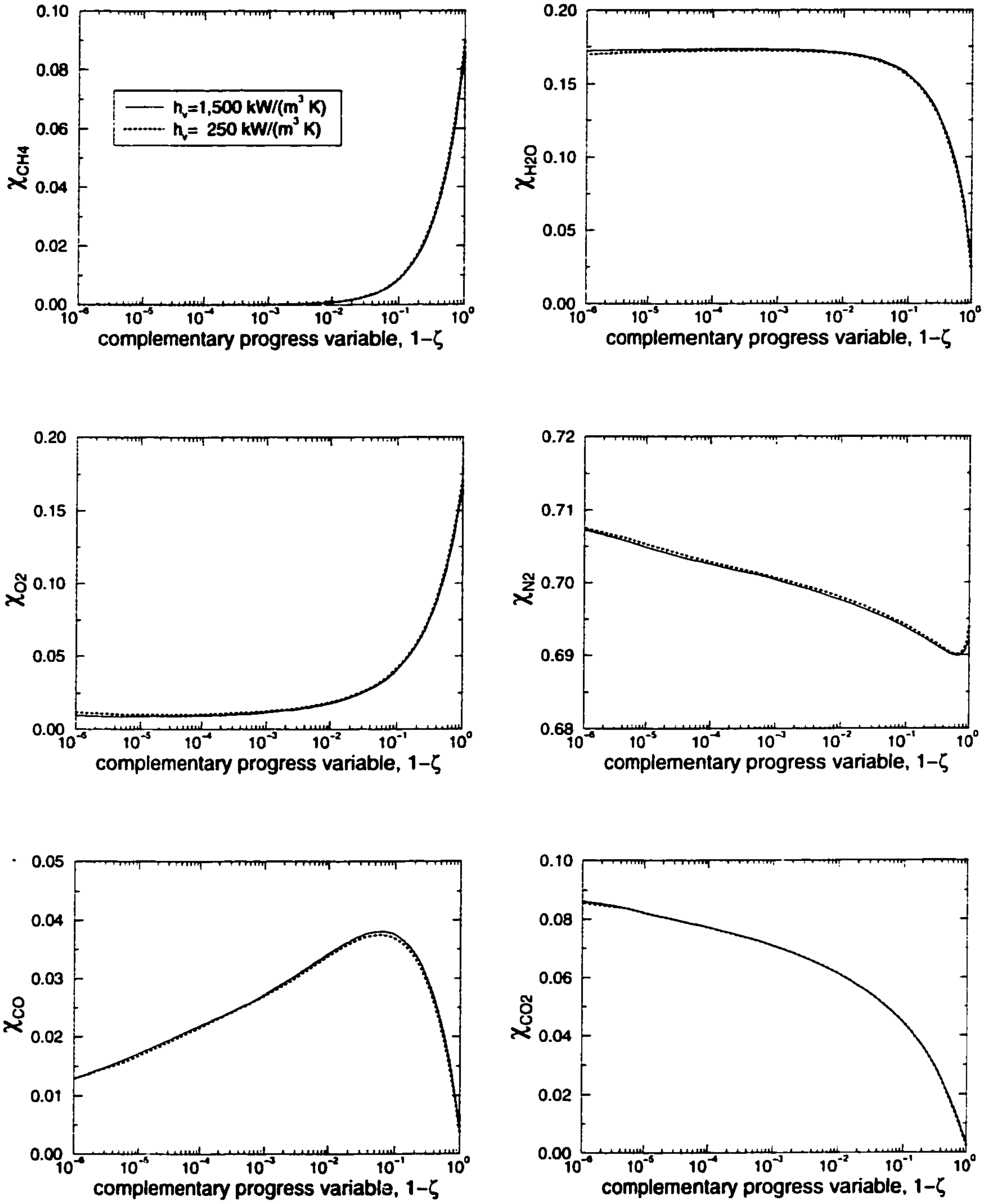

Figure 5.16. Major species distribution inside the model burner in terms of the complementary progress variable, $1-\zeta$, for two different values of the volumetric heat transfer coefficient, h_v.

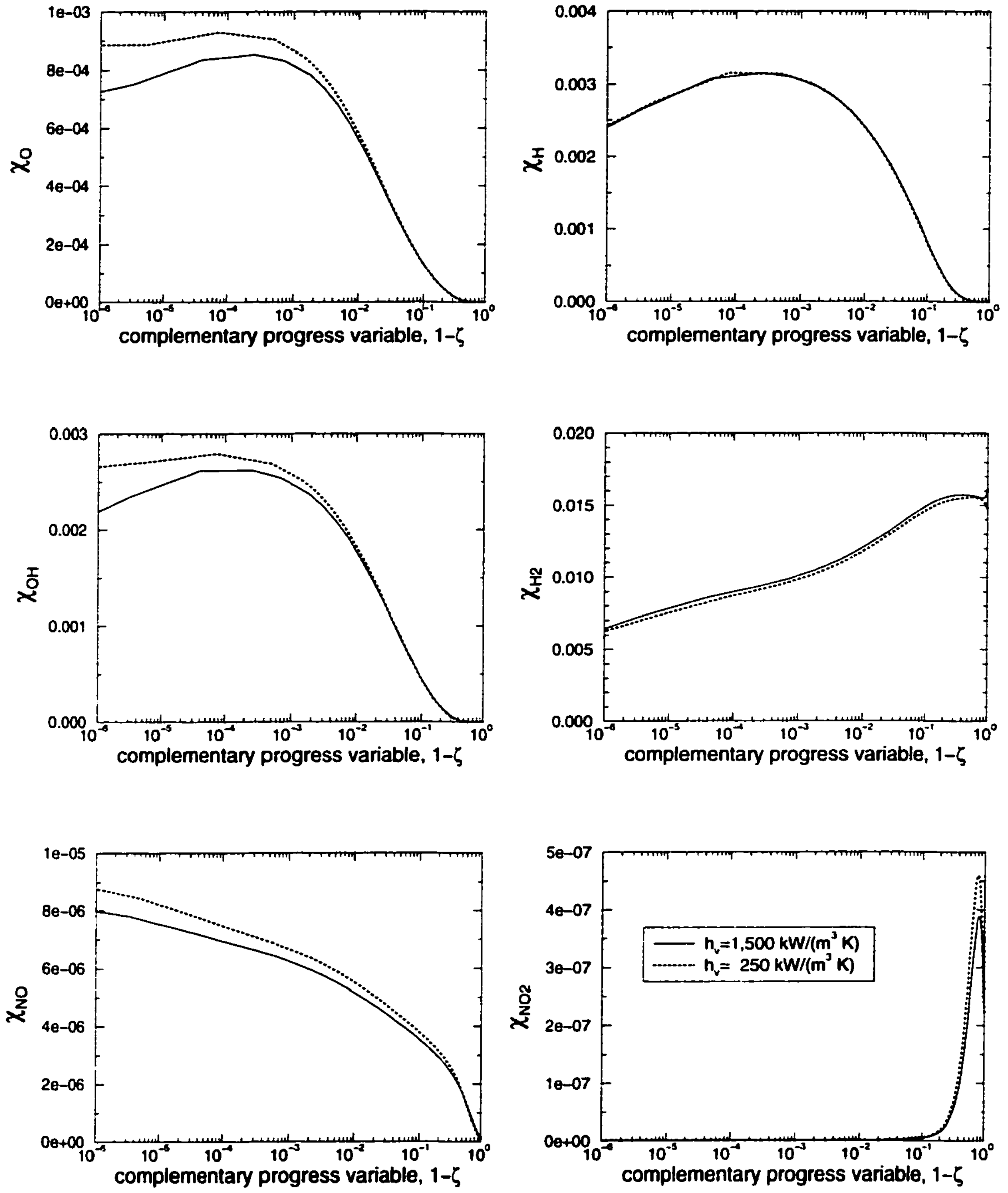

Figure 5.17. Minor species distribution inside the model burner in terms of the complementary progress variable, $1-\zeta$, for two different values of the volumetric heat transfer coefficient, h_v.

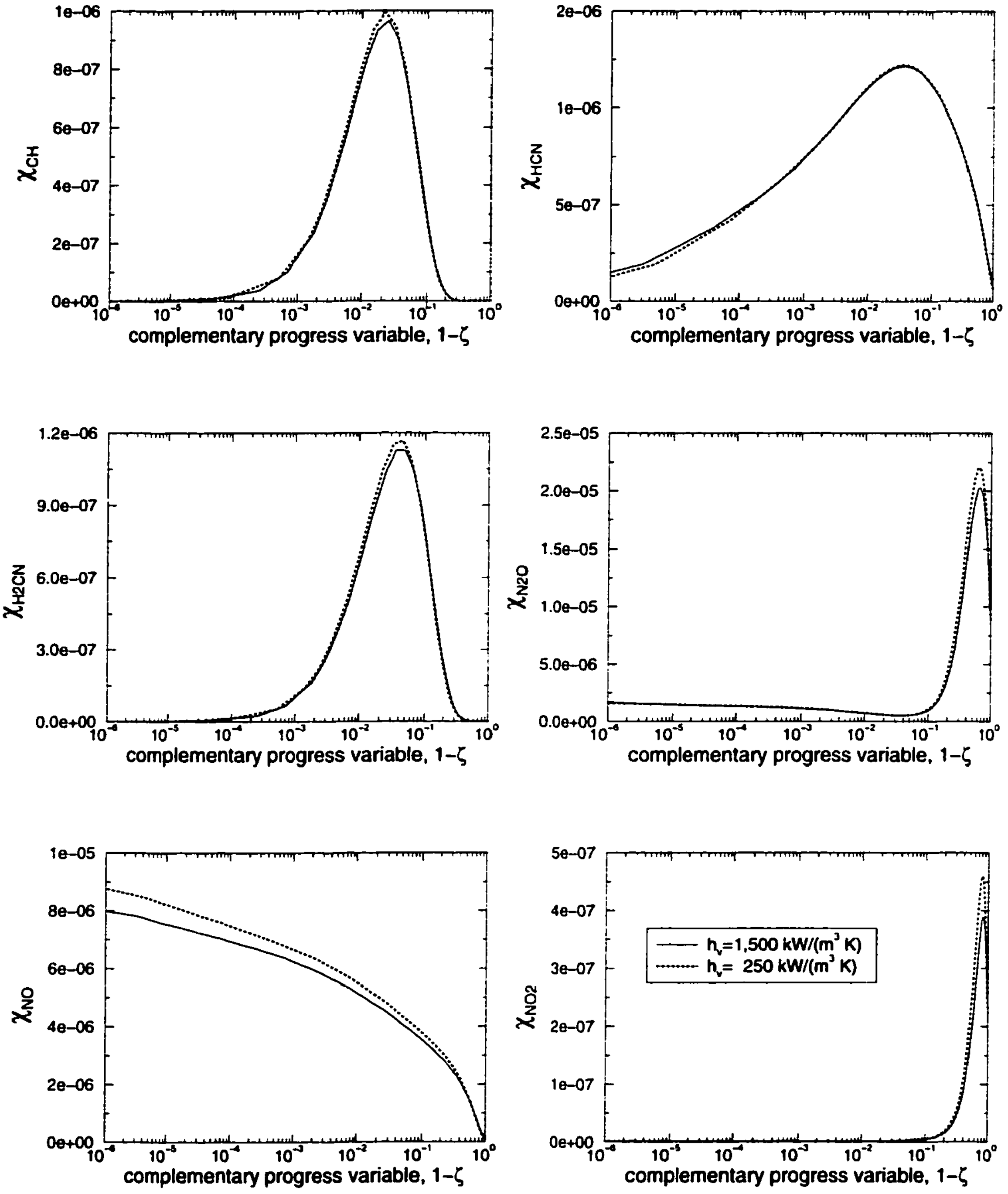

Figure 5.18. Selected species (relevant to NO mechanisms) distribution inside the model burner in terms of the complementary progress variable, $1-\zeta$, for two different values of the volumetric heat transfer coefficient, h_v.

system in the form of thermal radiation. Typical results are summarized in Table 5.2. The solid matrix surface temperature is also included to aid in the comparison. In this case, higher radiation efficiency is associated with higher surface temperature. However, it is important to realize that these two values do not necessarily always follow the same trend; it is shown later in Table 5.5 (Section 5.4) that an increase in the radiation efficiency is possible with a reduction in the surface temperature. Furthermore, different radiation efficiency values can be obtained, even though the matrix surface temperature remains constant (Table 5.6 in Section 5.5) or changes only a few degrees. It is shown below in Table 5.8 (Section 5.7) that drastic changes in radiation efficiency (up to 100%) are possible without similar changes in surface temperature. The radiation efficiency of a porous (i.e., semitransparent) burner is strongly dependent on the conditions inside the bulk of the solid matrix.

Table 5.2. Model burner radiation efficiency, η_{rad}, for different values of the volumetric heat transfer coefficient, h_v. The firing rate is 200 $\frac{kW}{m^2}$ and the equivalence ratio is $\Phi = 1.1$.

Volumetric Heat Transfer Coefficient $[\frac{kW}{m^3K}]$	Radiation Efficiency [%]	Surface Temperature $[K]$
1.500	23.2	842
1.000	22.4	826
750	19.4	808
500	15.1	767
400	13.2	759
300	10.4	729
250	9.1	709

5.3. Influence of the Equivalence Ratio

The effect of the inlet mixture equivalence ratio on the temperature distribution in the burner is shown in Figure 5.19. The back-diffusion of air is considered, i.e., some oxidizer is provided with the inlet mixture, but there is also O_2 diffusing from the downstream boundary toward the reaction zone[8]. The species boundary conditions downstream for O_2 and N_2 are not the zero-gradient type, as used for the rest species. Note that the firing rate used for the comparison in this section is 225 $\frac{kW}{m^2}$, about 10% larger than the one for the baseline case described in Section 5.1. This was done in order to obtain a submerged premixed flame for the fuel lean condition ($\Phi = 0.9$), since the code results predict a surface flame at 200 $\frac{kW}{m^2}$ (as discussed in Section 4.3).

The temperature of the premixed flame increases with the equivalence ratio in the range of this study, because of the decrease in the specific heat of the mixture. The flame location moves upstream, since a hotter flame accelerates the preheating process. The temperature of the diffusion flame is also increased when augmenting the equivalence ratio, due to two factors: the larger amount of fuel available (mostly H_2 and CO) in the richer cases, and the higher temperature of the premixed flame products leaving the porous matrix. These situations where both a premixed and a diffusion flame are present are usually referred to as "double flames" (see Section 1.3.4; e.g., Yamaoka and Tsuji, 1975). The second flame becomes stronger for the richer conditions. The effects of the O_2 concentration at the boundary, as well as relevant species distributions, are studied in Section 5.5.

Table 5.3 summarizes the dependence of the radiation efficiency with the equivalence ratio near stoichiometric conditions. Two firing rates (the baseline value and another about 10% larger) are included, to compare only those situations where the flame stabilizes within the burner matrix[9]. In the studied range, the radiation effi-

---

[8] This situation is more realistic (than when no diffusion is allowed) for most applications, since air is usually readily available at the burner exit.

[9] It was noted in Section 4.3 that a surface-flame-type solution was obtained for $\Phi = 0.9$ and $FR = 200 \frac{kW}{m^2}$. By choosing a larger firing rate in this section, the effect of the surface flame is eliminated and only the differences due to the equivalence ratio change are compared.

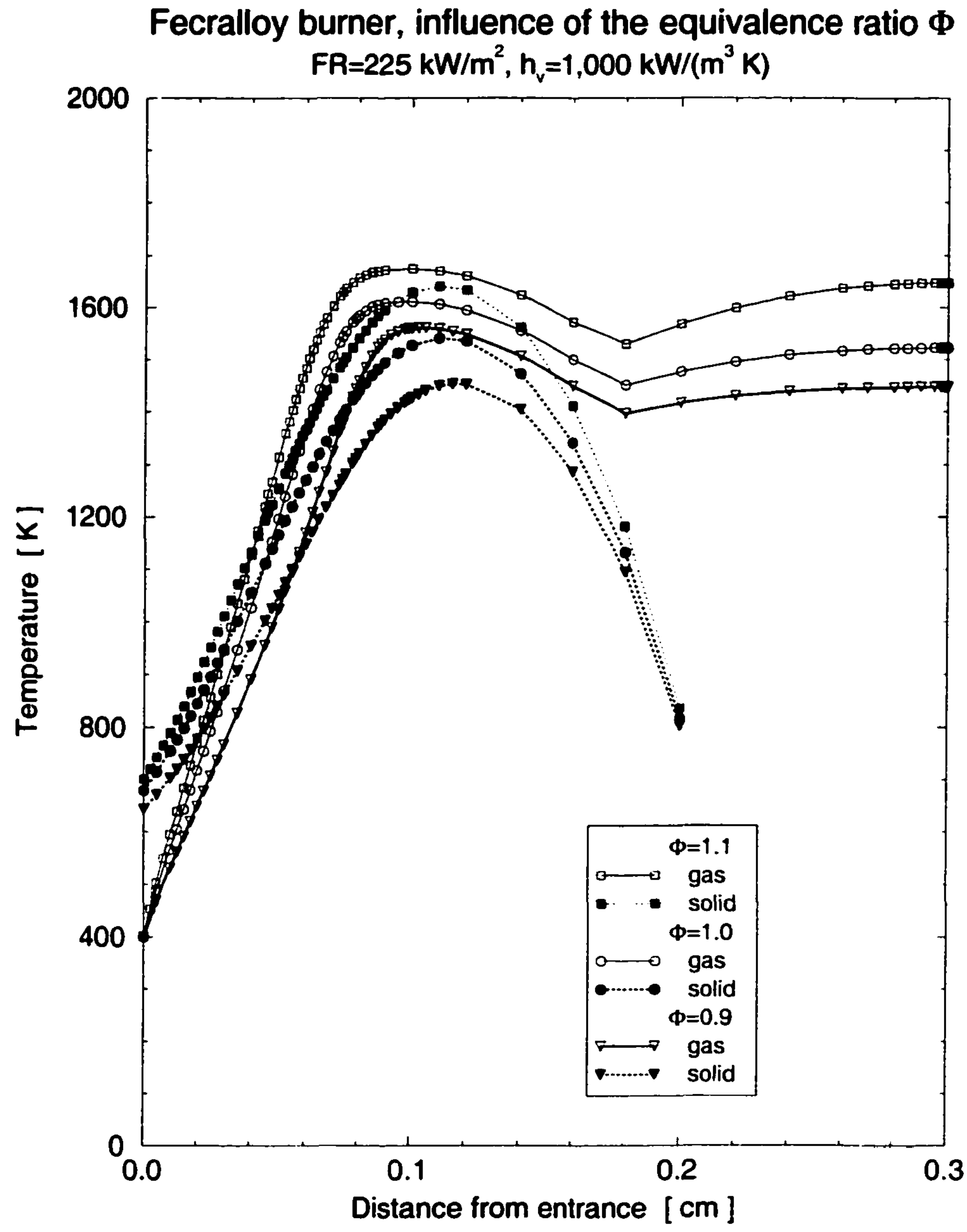

Figure 5.19. Temperature distribution inside the model burner for different values of the equivalence ratio, Φ. Note that the strength of the diffusion flame increases with the equivalence ratio.

ciency increases when increasing the equivalence ratio. This trend follows the behavior of the burner temperature (Figure 5.19), as expected.

Table 5.3. Model burner radiation efficiency, η_{rad}, for different equivalence ratios, Φ. Two firing rates (200 and 225 $\frac{kW}{m^2}$) are included. Note that the drastic radiation efficiency reduction for the lean mixture at the low firing rate is due to the flame not being embedded in the porous matrix.

Equivalence Ratio	Radiation Efficiency [%] (Surface Temperature [K]) $FR = 200 \frac{kW}{m^2}$		Radiation Efficiency [%] (Surface Temperature [K]) $FR = 225 \frac{kW}{m^2}$	
0.9	1.4	(640)	15.1	(802)
1.0	18.6	(811)	19.1	(817)
1.1	22.4	(826)	24.2	(835)

The rich inlet mixture considered so far ($\Phi = 1.1$) is close to stoichiometric conditions, corresponding to a defect of only 10% of stoichiometric air in the supply. Therefore, it produces only a relatively weak diffusion flame with temperature below that of the premixed flame (see Figure 5.19). Figure 5.20 illustrates the temperature profiles when richer inlet mixtures are used. It must be noted that the firing rate selected for this comparison is 340 $\frac{kW}{m^2}$, which is about 50% larger than before[10]. The temperature of the gas increases initially with an increase in Φ, but the trend is reversed beyond $\Phi = 1.3$. The reaction zone moves downstream and the temperatures decrease for $\Phi > 1.3$, when the effect of the insufficient primary O_2 becomes apparent and the flame "reaches out" for the secondary oxidizer supplied by the back-diffusion process. The diffusion flame follows the behavior of the premixed flame; an initial increase in Φ makes it stronger (due to a larger supply of CO and H_2), but a further

---

[10] In order to maintain the firing rate constant, a richer inlet mixture corresponds to a lower flow rate. It was not possible to increase Φ significantly beyond 1.2 at $FR = 225 \frac{kW}{m^2}$ without obtaining a surface stabilized flame (not embedded in the solid matrix).

increase causes a marked decrease due to the lower temperature of this secondary fuel, i.e., the mixture of CO and H_2.

Species distributions for selected major and minor species are shown in Figures 5.21 and 5.22, respectively. The most significant changes due to the higher concentration of fuel at the inlet are a delay in the methane and primary O_2 consumption, as well as the in the generation of CO_2. As expected, the increase in the CO and H_2 produced by the rich premixed flame is considerable; peak CO and H_2 are increased by more than 50% and 100%, respectively, when increasing Φ from 1.1 to 1.4. It is interesting to note that the concentrations of the radicals O and OH are comparable for both premixed and diffusion flames when $\Phi = 1.1$. However, a large increase in the concentration of these radicals at the diffusion flame front occurs when the equivalence ratio is increased, in detriment of the premixed flame. Additionally, the emissions of the pollutants CO and NO is doubled when Φ increases from 1.1 to 1.4. Similar increase was obtained for the unburned hydrocarbon emissions.

Table 5.4 summarizes the dependence of the radiation efficiency with the equivalence ratio for rich inlet mixtures. It is somewhat surprising that the radiation efficiency of the model burner increases considerably when increasing the equivalence ratio beyond $\Phi > 1.1$, but then drops for $\Phi > 1.3$. This trend closely matches the behavior of the burner temperature (Figure 5.20). However, it is necessary to point out that the gain in the radiation efficiency is associated with a significant increase in the pollutant emissions.

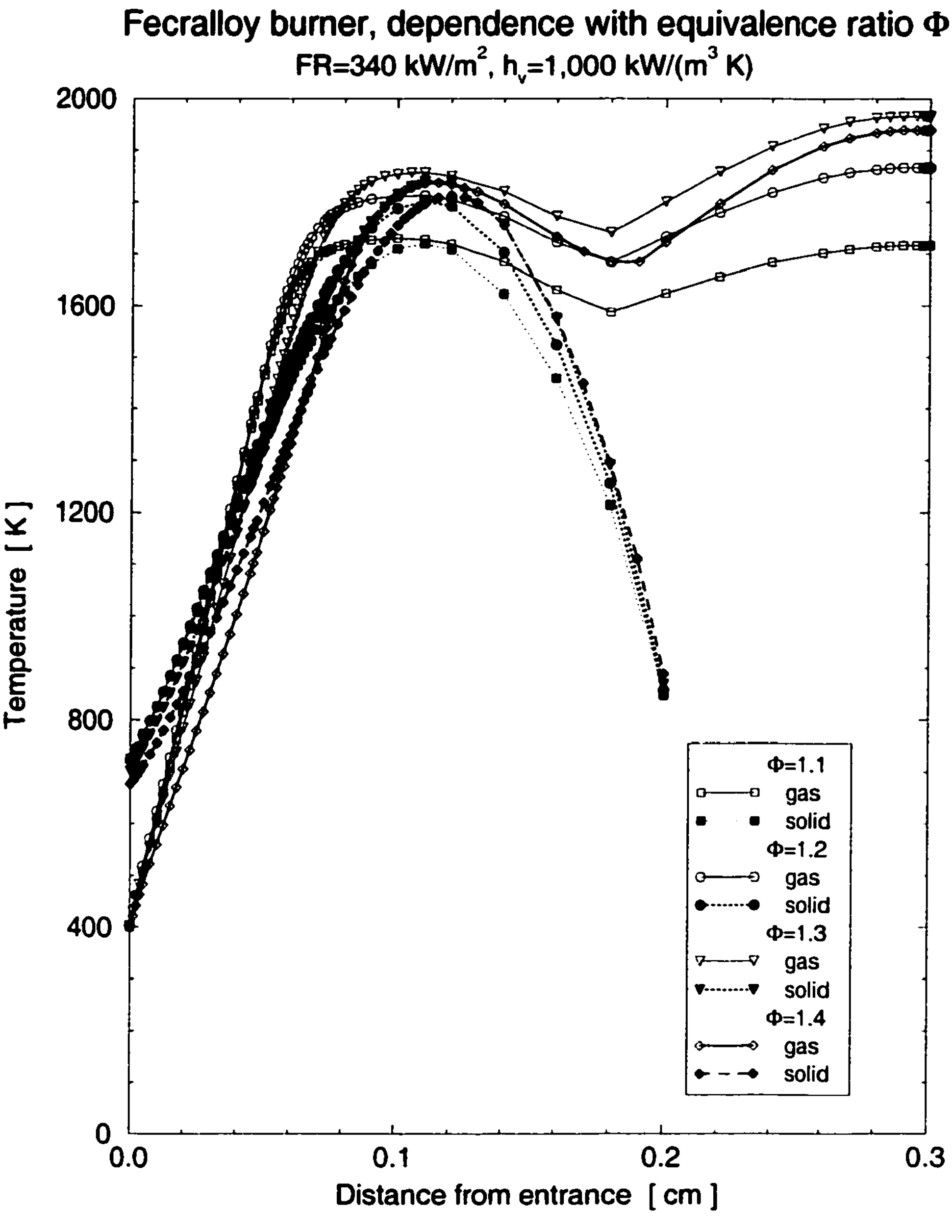

Figure 5.20. Temperature distribution inside the model burner for different values of the equivalence ratio, Φ, when using fuel rich inlet mixtures. Note that the strength of both the premixed and diffusion flames initially increase with the equivalence ratio (up to Φ = 1.3) and subsequently decrease.

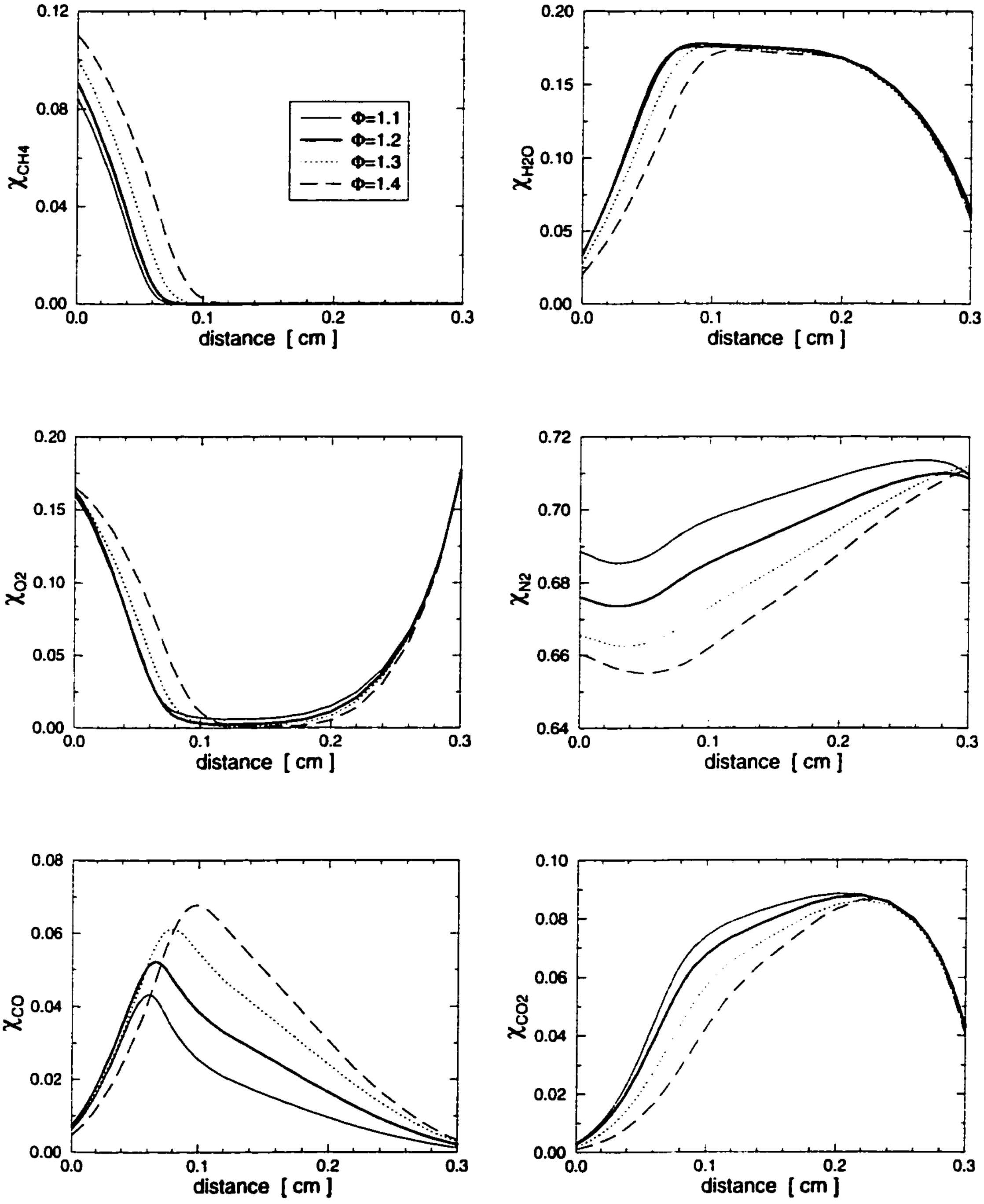

Figure 5.21. Major species distribution inside the model burner for four different values of the equivalence ratio, Φ, for fuel rich flames.

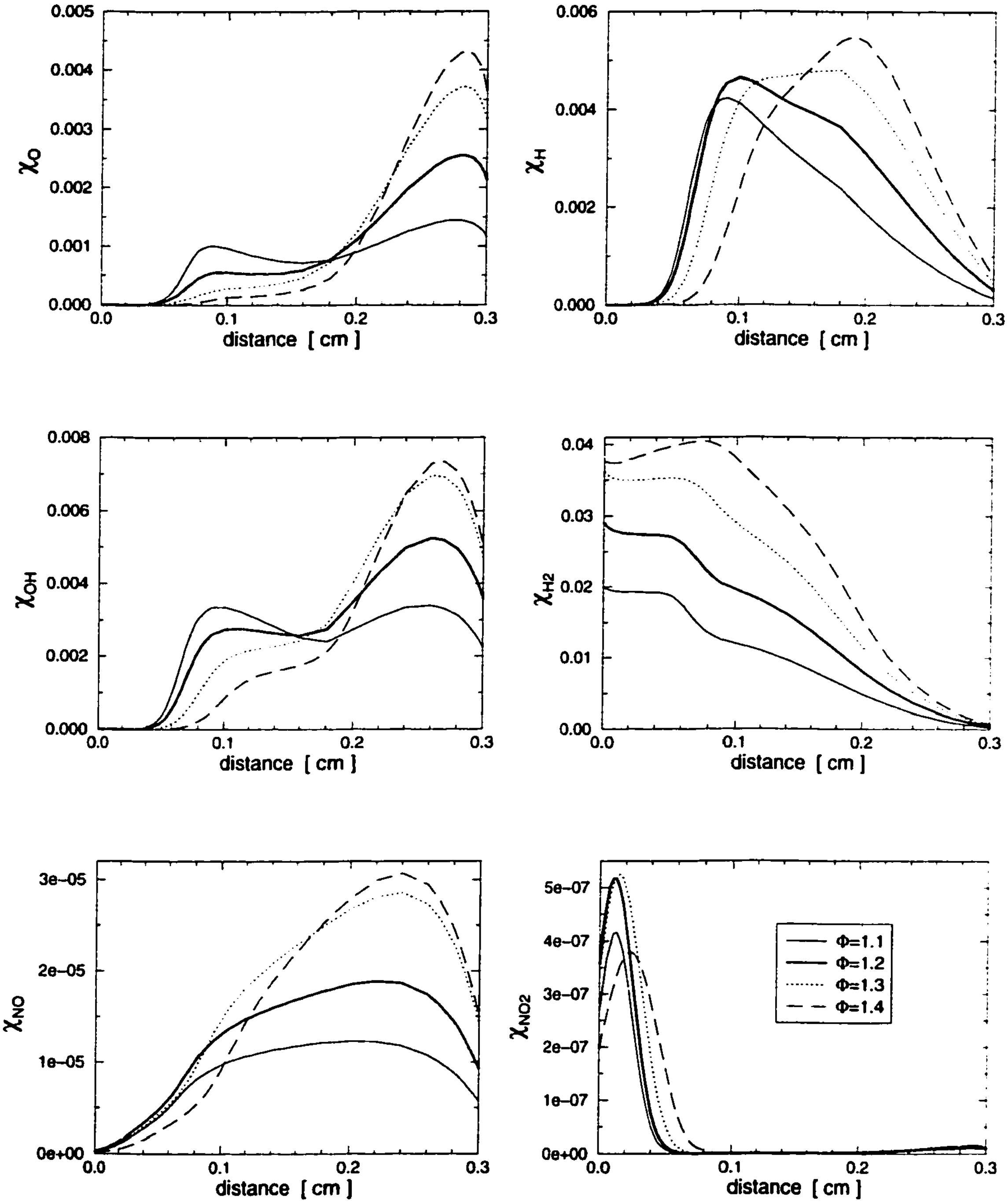

Figure 5.22. Minor species distribution inside the model burner for $\Phi = 1.1$ for four different values of the equivalence ratio, Φ, for fuel rich flames.

Table 5.4. Model burner radiation efficiency, η_{rad}, for different equivalence ratios, Φ, for fuel rich flames. The firing rate was 340 $\frac{kW}{m^2}$ in this case.

Equivalence Ratio	Radiation Efficiency [%]	Surface Temperature [K]
1.1	23.1	847
1.2	29.9	866
1.3	33.5	877
1.4	32.4	889

5.4. Influence of the Firing Rate

Changing the firing rate (i.e., the inlet gas flow rate) has proven to be difficult, since it is the single parameter that affects to the greatest extent the governing equations. Effectively, the firing rate enters directly into the continuity equation (Equation 3.2), the K species equations (Equation 3.3) and the gas phase energy balance (Equation 3.4), and indirectly into the solid phase energy balance (Equation 3.5). As a result, very small steps in this variable can be used with the restart feature described in Section 3.6.

Starting with the baseline case with a firing rate of 200 $\frac{kW}{m^2}$, the maximum change that permits obtaining converged solutions is only 0.2 $\frac{kW}{m^2}$ (i.e., a change of 0.1%). A significant computational expense was necessary to obtain converged solutions at different firing rates.

Figure 5.23 depicts the temperature profiles inside the burner for the gas and solid phases, with a fuel rich inlet mixture ($\Phi = 1.1$) and three different firing rates: 170, 200 and 340 $\frac{kW}{m^2}$. As expected, the temperatures increase with an increase in the firing rate.

It is interesting to compare the behavior of the flame location in this porous burner with an embedded flame against a surface, burner stabilized flame. The submerged flame moves upstream when the firing rate is increased due to the effect of preheating, in agreement with the experimental observations (and also in agreement with the data reported by Mital, 1996). However, a burner stabilized flame moves further downstream for larger firing rates, as shown recently by Rumminger (1996).

A very different set of results for the same three firing rate conditions is observed in Figure 5.24, when the inlet mixture is fuel lean ($\Phi = 0.9$). In this case, the flame cannot stabilized inside the burner for the low firing rate of 200 $\frac{kW}{m^2}$, since this relatively low temperature flame cannot sustain the convective heat losses to the porous material[11]. A different equilibrium, where gas-phase conduction balances the

---

[11] A submerged-flame-type solution can be obtained in this case for a smaller value of the volumetric heat transfer coefficient.

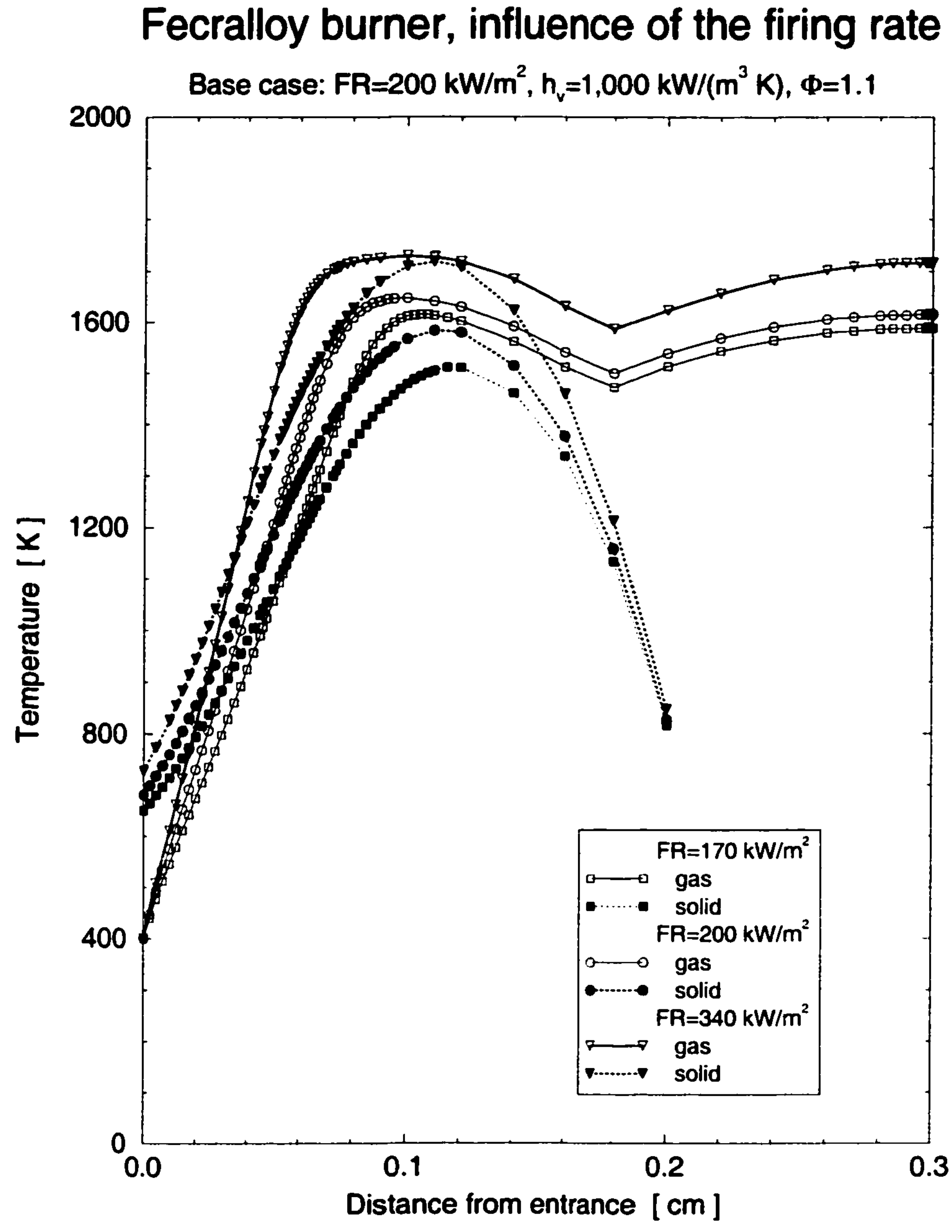

Figure 5.23. Temperature distribution inside the model burner for different values of the firing rate (fuel rich inlet mixture with $\Phi = 1.1$).

chemical release is achieved, as opposed to the submerged flame situation, where the chemical release is balanced by several heat transfer modes (gas and solid conduction, convection and radiation).

The effect of the firing rate on the radiation efficiency was described in detail in Section 4.3.3. A few additional values are presented in Table 5.5, to stress here that the model predicts an initial increase and subsequent decrease of the radiation efficiency when increasing the firing rate in the range covered by this investigation.

Table 5.5. Model burner radiation efficiency, η_{rad}, for different firing rates, *FR*. The equivalence ratio is $\Phi = 1.1$ for the baseline case, but also the results using $\Phi = 0.9$ are included to show the drastic decrease in radiation efficiency ($\eta_{rad} = 1.4\%$) when the premixed flame anchors at the surface of the porous pad. It is interesting to notice that the results indicate that it is possible to increase the radiation efficiency with a decrease in the surface temperature.

Firing Rate $[\frac{kW}{m^2}]$	Radiation Efficiency [%] (Surface Temperature [K]) $\Phi = 1.1$	$\Phi = 0.9$
200	22.4 (826)	1.4 (640)
280	27.5 (853)	16.9 (815)
310	26.6 (855)	17.9 (823)
340	23.1 (847)	17.6 (843)

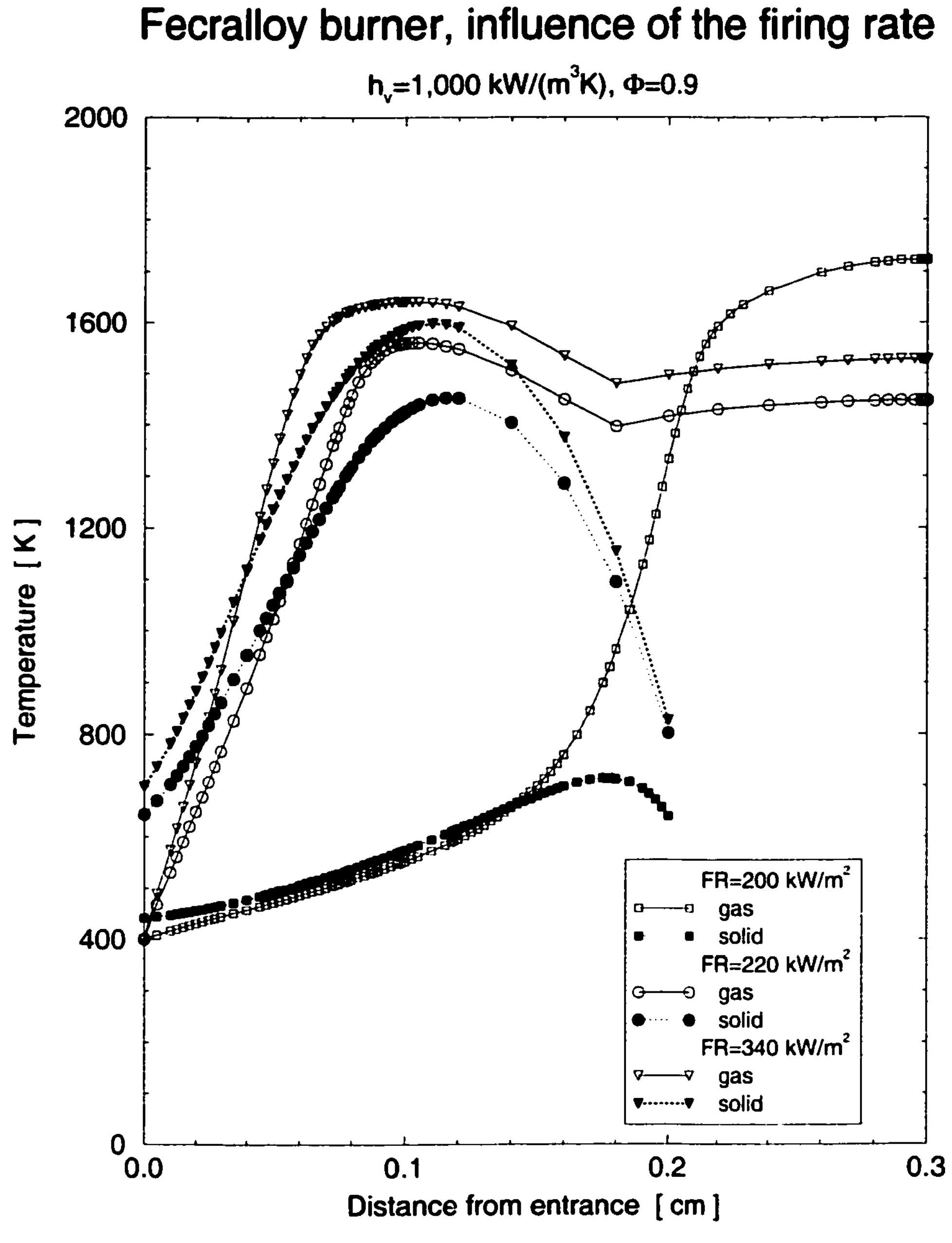

Figure 5.24. Temperature distribution inside the model burner for different values of the firing rate (fuel lean inlet mixture with $\Phi = 0.9$).

5.5. Influence of the Downstream O_2 Concentration

Partially-premixed flames are characterized by the dual source of oxidizer, i.e., part is initially premixed with the injected fuel mixture, and the rest diffuses back from the downstream boundary. In this section, the effects of the O_2 concentration downstream from the burner on the flame characteristics and species concentrations are investigated.

Temperature profiles are shown in Figure 5.25 for different downstream conditions, $\chi_{O2} = 0.30$, 0.20, 0.10, and 0.00. When the back-diffusion is not permitted (i.e., the O_2 concentration at the exit is zero), the diffusion flame outside the porous layer is not present, and the temperature of the premixed flame is reduced. Increasing the amount of O_2 available and, therefore, allowing for this species diffusion from the boundary, a second flame is observed, as previously noted in Section 5.3.

The intensity of the diffusion flame is strongly dependent on the amount of oxygen available. When there is more oxidizer available to the products, the overall chemical reaction is more complete, resulting in higher temperatures. This agrees with the intuitive fact that the temperature follows the reaction completion rate. For the slightly rich mixture of this example ($\Phi = 1,1$), most of the change occurs when increasing χ_{O2} from zero to 0.10, since relatively low concentration of CO, H_2 and unburned hydrocarbons are left over after the premixed flame. Little improvement is obtained by increasing χ_{O2} from 0.10 to 0.20, and hardly any occurs beyond the latter value. Numerical experiments showed that a further increase in the downstream oxygen concentration does not produce any more changes.

A comparison between the species profiles for the four different boundary conditions described above is given in Figures 5.26 and 5.27. The CH_4 mole fraction distribution follows a similar trend for all $\chi_{O2,out}$ (Figure 5.26). However, the different curves are shifted, being further from the inlet when there is less oxygen available downstream. This effect shows that the diffusion of air from the right boundary affects the species distributions throughout the computational domain, even though the N_2 plot seems to indicate that the influence is confined to the last 0.2 *cm*. The difference

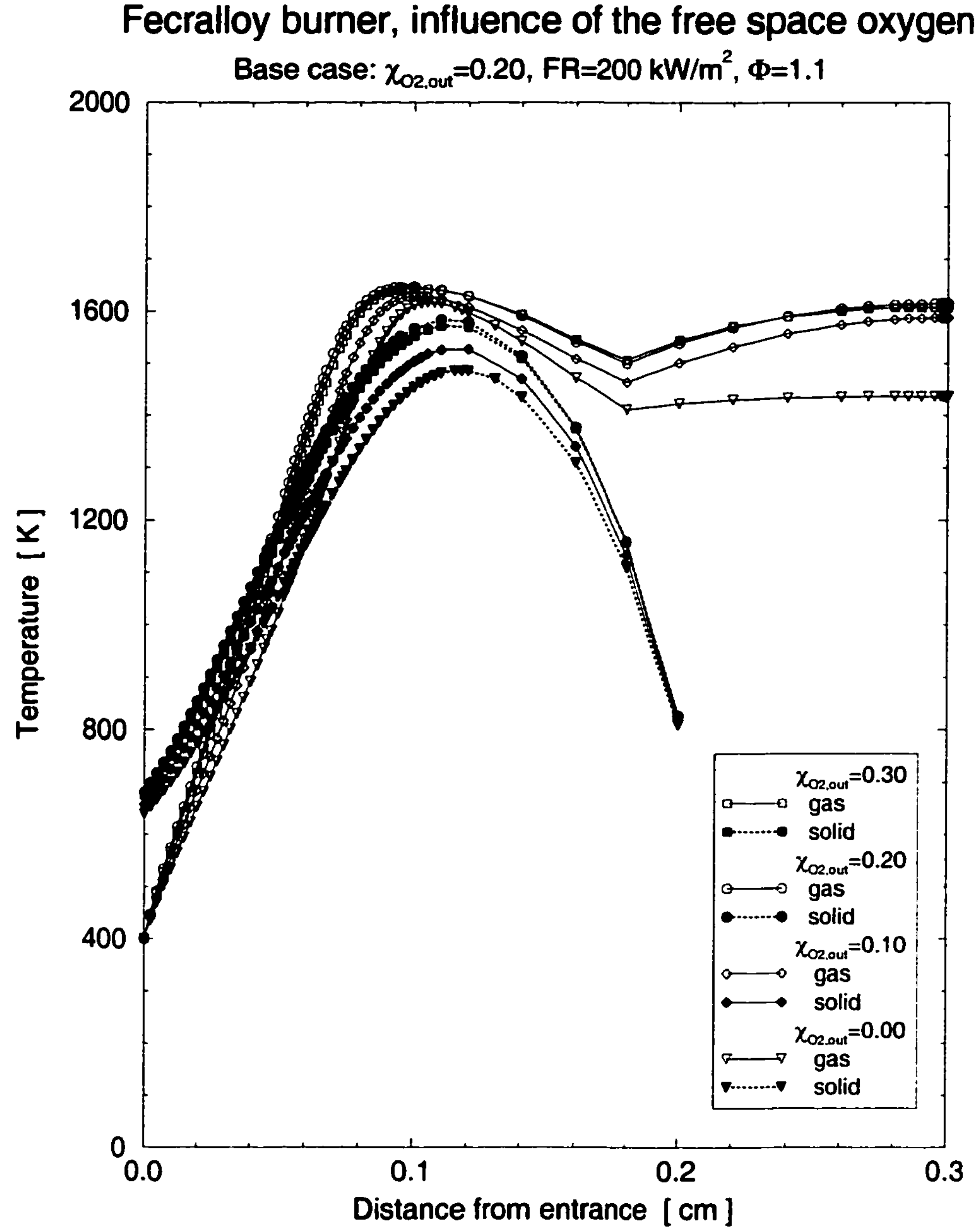

Figure 5.25. Temperature distribution inside the model burner for four different values of the downstream oxygen mole fraction, $\chi_{O2,out}$. The value of the volumetric heat transfer coefficient was $h_v = 1,000 \frac{kW}{m^3K}$ for these simulations.

in the O_2 profiles is quite marked, especially between $\chi_{O2,out} = 0$ and $\chi_{O2,out} \neq 0$. More CO is produced after the premixed flame when less air is diffusing toward it. This also results in a lower mole fraction of CO_2.

Minor species are plotted in Figure 5.27. As expected, the difference in O_2 concentration is also reflected in the oxygenated radicals O and OH. After the first peak that corresponds to the premixed flame, a second maximum of those species correlates to the diffusion flame. The height of the second peak and its position are both functions of the amount of O_2 available, moving upstream when $\chi_{O2,out}$ is increased. The generation of H_2 (and, consequently, radical H) at the premixed flame is increased and displaced downstream when the levels of O_2 are decreased. The NO distributions are quite similar in shape, but the levels are proportional to the temperature of the exhaust gases: they increase with the amount of diffusing oxygen up to when $\chi_{O2,out} = 0.20$, then decrease slightly for $\chi_{O2,out} = 0.30$. The NO_2 peaks out in the colder region upstream of the premixed flame. Its maximum displays an analogous trend to that of the NO. A small second NO_2 peak is present, coinciding with the diffusion flame, probably due to recombination of NO during the temperature dip between the two reaction zones; the magnitude of this peak is proportional to the extent of the aforementioned dip (i.e., non-existent for $\chi_{O2,out} = 0$ and most pronounced for $\chi_{O2,out} = 0.30$).

The species profiles show that if no air is supplied at the downstream boundary to allow for back-diffusion[12], the numerical solution predicts a significant, unrealistic increase in the CO and H_2 emissions.

Table 5.6 summarizes the dependence of the radiation efficiency on the back-diffusion of air. Note that initially, when increasing the mole fraction of O_2 from $\chi_{O2,out} = 0.00$ to $\chi_{O2,out} = 0.20$, the radiation efficiency increases, driven by a moderate increase in the solid matrix temperature. However, a further increase up to

---

[12] This was the boundary condition of the original version of PREMIX. It was not adequate for modeling radiant burners.

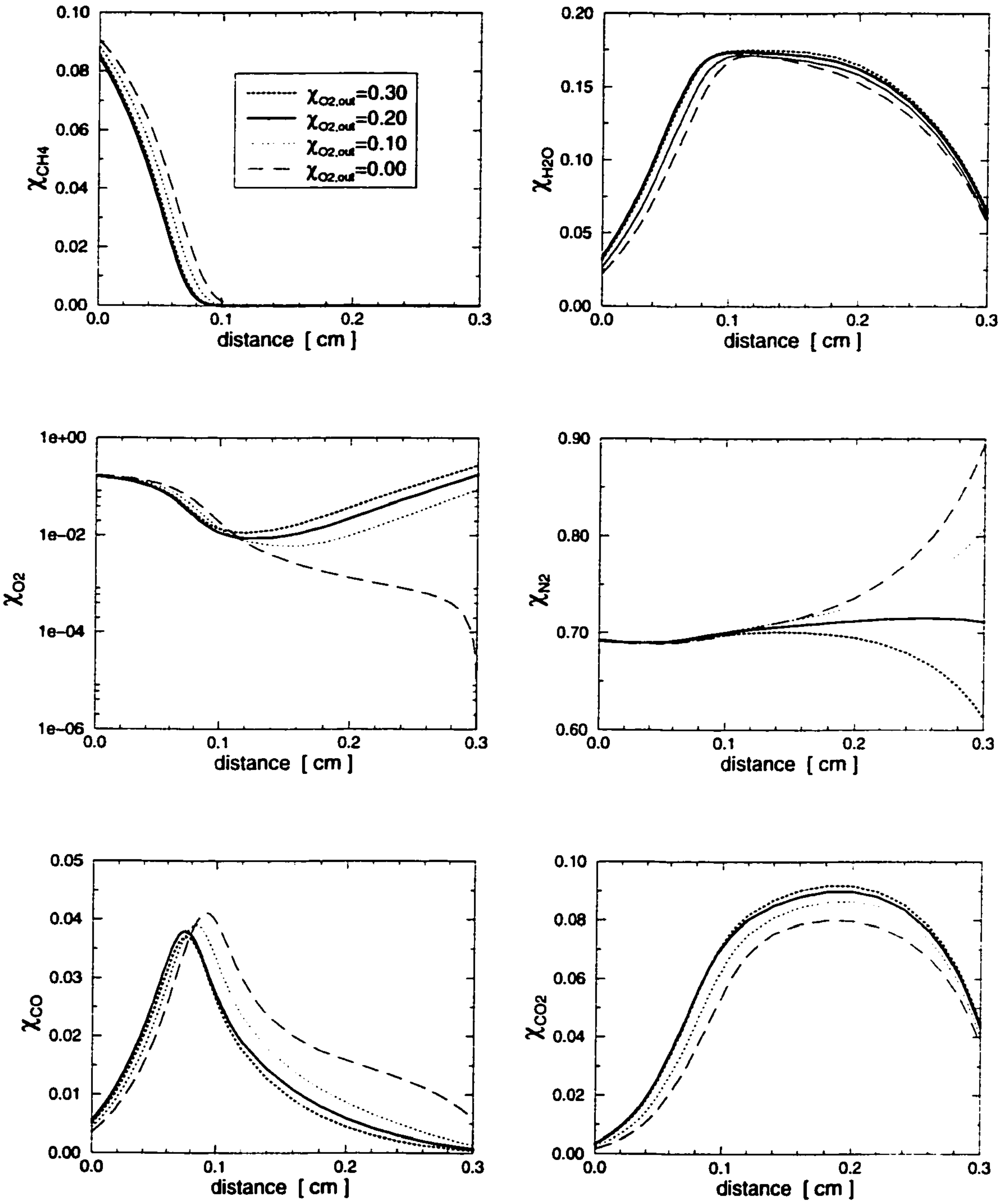

Figure 5.26. Major species distribution inside the model burner for $\Phi = 1.1$ for four different values of the downstream oxygen mole fraction, $\chi_{O2,out}$.

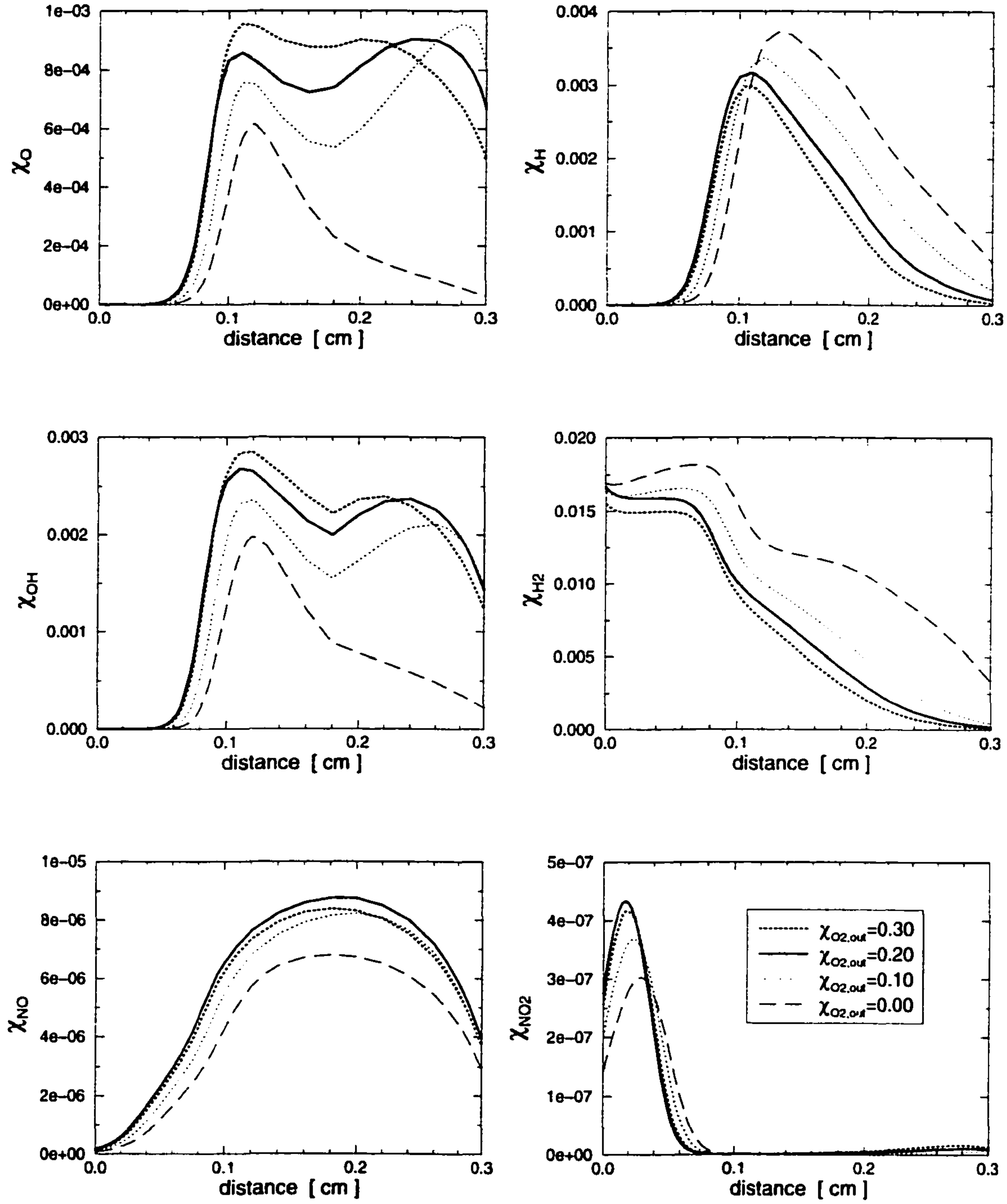

Figure 5.27. Minor species distribution inside the model burner for $\Phi = 1.1$ for four different values of the downstream oxygen mole fraction, $\chi_{O2,out}$.

$\chi_{O2,out} = 0.30$ causes a minor decrease in the radiation efficiency, mirroring the temperature behavior.

Table 5.6. Model burner radiation efficiency, η_{rad}, for four different values of the downstream oxygen mole fraction, $\chi_{O2,out}$. The firing rate is 200 $\frac{kW}{m^2}$ and the equivalence ratio is $\Phi = 1.1$.

$\chi_{O2,out}$	Radiation Efficiency [%]	Surface Temperature [K]
0.00	17.4	809
0.10	19.3	817
0.20	22.4	826
0.30	21.8	826

5.6. Influence of the Surface Emittance

The increase in the effective solid emittance, ε, increases the radiative heat loss from the burner matrix, as expected, resulting in lower overall temperatures for both solid and gas phases; the converse is also true.

Figure 5.28 illustrates the temperature profiles inside the model burner for three values of ε, the baseline case ($\varepsilon = 0.65$) and two other values, in increments of ±30% ($\varepsilon = 0.85$ and $\varepsilon = 0.45$, respectively.) Note that, even though the change in emittance is large between the three situations, almost doubling the value between the limit cases (i.e., from 0.45 to 0.85), the temperature difference among them is not too significant: about $50K$ (3%) for the peak gas temperature and about $150K$ (10%) for the solid. This is because the heat loss from the porous matrix (emitted thermal radiation) is a volumetric rather than surface phenomenon. Additionally, when the emittance is increased, the embedded flame moves downstream, trying to reduce its heat loss from the volume of the solid matrix, and the equilibrium is reached with the reaction zone closer to the burner face.

In what seems to be a counterintuitive result, a reduction in the surface emittance of the flame support material increases the radiation efficiency of the model burner. The smaller surface losses contribute to an increase of the temperature of the porous matrix and, for the problem parameters (see Table 5.1), actually significantly increase radiation efficiency. Table 5.7 attests that, by lowering the surface emittance from $\varepsilon = 0.65$ to $\varepsilon = 0.45$, a 3% (absolute, or 13% in relative terms) radiation efficiency gain is possible.

Table 5.7. Model burner radiation efficiency, η_{rad}, for different values of the matrix surface emittance, ε. The firing rate is 200 $\frac{kW}{m^2}$ and the equivalence ratio is $\Phi = 1.1$.

Emittance	Radiation Efficiency [%]	Surface Temperature [K]
0.45	25.4	895
0.65	22.4	826
0.85	18.3	776

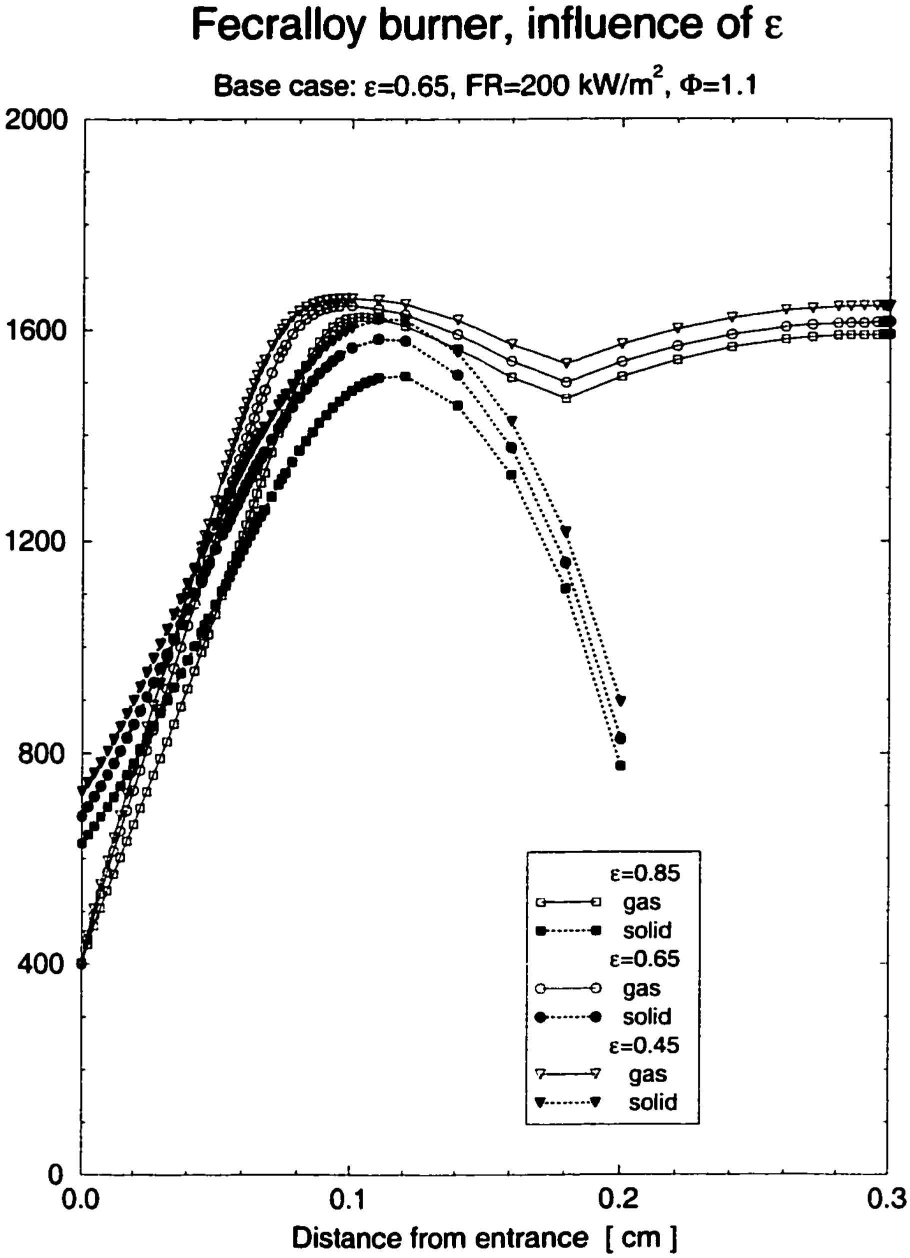

Figure 5.28. Influence of the emittance of the solid, ε, on the temperature distributions of the model burner.

5.7. Influence of the Solid Thermal Conductivity

The effective thermal conductivity of the solid[13] was found to have a strong impact on the solution of the model equations. Figure 5.29 illustrates the temperature profiles for the gas and solid phases for the baseline problem ($k_s = 0.13\ \frac{W}{m\ K}$) and two other values, in increments of ±15% ($k_s = 0.15\ \frac{W}{m\ K}$ and $k_s = 0.11\ \frac{W}{m\ K}$, respectively.) Peak gas temperature varies about $100K$ (only 6%) between the extreme values of k_s; peak solid temperature is significantly more affected, varying more than $250K$ (over 15%).

Larger thermal conductivity results in lower overall burner temperatures, since the energy released at the embedded flame front is conducted away more readily and, therefore, total losses from the flame are larger (resulting in less complete combustion and increased pollutant emissions also.) The premixed flame location stabilizes further downstream within the solid matrix for larger values of k_s.

It is interesting to note that the temperature of the burner face ($x = 0.2\ cm$) is only a weak function of any single problem parameter. Even though the temperatures at that point seem to be identical for the three values of k_s used in this section (see Figure 5.29), there is actually a small difference (only $10K$). Similar situations are predicted when varying the volumetric heat transfer coefficient (Figure 5.9), equivalence ratio (Figure 5.19), firing rate (Figure 5.23), oxygen concentration downstream (Figure 5.25), etc. This weak dependence can be explained by closely examining the boundary condition for the burner face, Equation 3.13. Changes in the terms on the left-hand-side that model convection (due to changes in the temperature difference between the gas and solid phases) and conduction (due to changes in the solid temperature gradient) are compensated by a relatively small adjustment in the temperature of the solid matrix, which enters the radiation term raised to the fourth power.

Table 5.8 summarizes the dependence of the radiation efficiency on the thermal conductivity of the solid matrix. It is evident that a significant performance improvement can be obtained by selecting porous materials with low thermal conductivity, doubling η_{rad} when reducing k_s less than 30%, from 0.15 to 0.11 $\frac{W}{m\ K}$). This is in

---

[13] It is implicit in the rest of this section that k_s is an *effective* property.

agreement with the results reported by Golombok et al. (1991) for a sintered metal fiber material, but opposite to the conclusions of Zhou and Pereira (1997) for bilayered ceramic blocks.

Table 5.8. Model burner radiation efficiency, η_{rad}, for different thermal conductivities of the solid matrix, k_s. The firing rate is 200 $\frac{kW}{m^2}$ and the equivalence ratio is $\Phi = 1.1$. Note that drastic changes in the radiation efficiency are possible even though the surface temperature remains virtually unchanged.

Thermal Conductivity $[\frac{W}{m\,K}]$	Radiation Efficiency [%]	Surface Temperature $[K]$
0.15	14.7	822
0.13	22.4	826
0.11	28.0	824

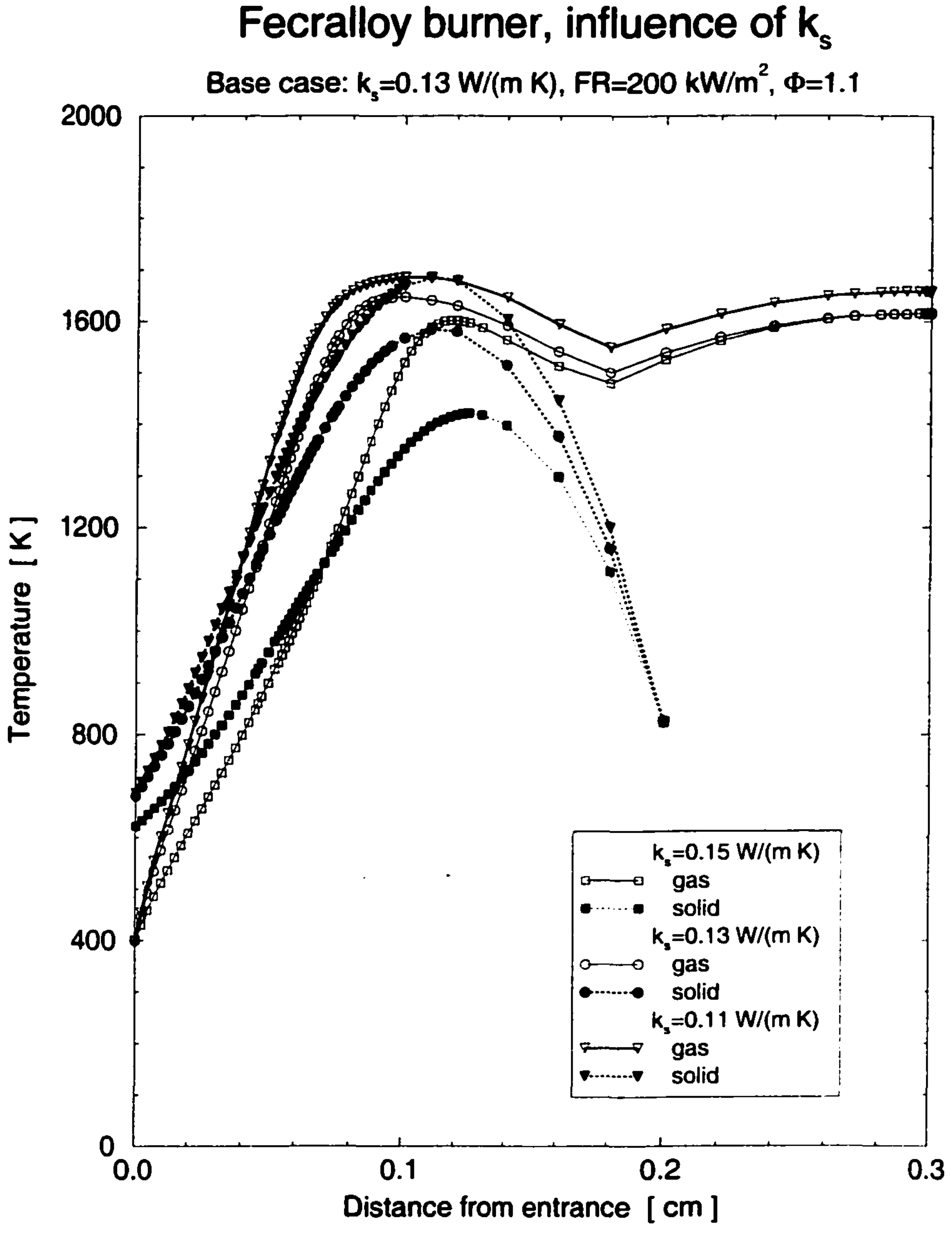

Figure 5.29. Influence of the thermal conductivity of the solid, k_s, on the temperature distributions of the model burner.

5.8. Influence of the Extinction Coefficient

The magnitude of the extinction coefficient, β, affects significantly the temperature profiles inside the burner. The value of the scattering coefficient was constant for the calculations of this section; therefore, changes in the extinction coefficient only affect the absorption coefficient. Figure 5.30 depicts the gas and solid temperatures for the base value ($\beta = 200\ m^{-1}$), a reduction of 25% ($\beta = 150\ m^{-1}$) and an increase of 25% ($\beta = 250\ m^{-1}$). Table 5.9 presents the radiation efficiency data for those three values of this parameter.

Increasing the extinction coefficient (i.e., increasing the opacity of the pad) corresponds to an effective decrease of the radiation mean free path. The thermal energy emitted by the high temperature region of the solid matrix which is near the premixed flame is absorbed strongly, actually "locking in" energy. Conversely, when the extinction coefficient is smaller, radiant energy can leave the hot matrix region more readily, reducing the peak. Since the embedded premixed flame loses less energy when β is large, its temperature increases in that case. Additionally, there is chemical kinetics feedback, which favors a more complete combustion at higher flame temperatures.

The aforementioned factors interact to determine the burner performance. For the selected model parameters, this interaction results in a significant increase of the radiation efficiency with increasing extinction coefficient, almost a three-fold increase when varying β from 150 to 250 m^{-1}.

In a similar situation to that observed for the solid thermal conductivity (Section 5.7), the solid temperature is more sensitive than the gas temperature to the magnitude of the extinction coefficient, differing by more than $250K$ between these three cases. Also, the gas temperature peak broadens with increasing β, and the temperature difference between the gas and the solid becomes smaller. It is important to realize that the surface temperatures increase slightly with increasing β, which also contributes to the subsequent improvement in radiant efficiency of the burner.

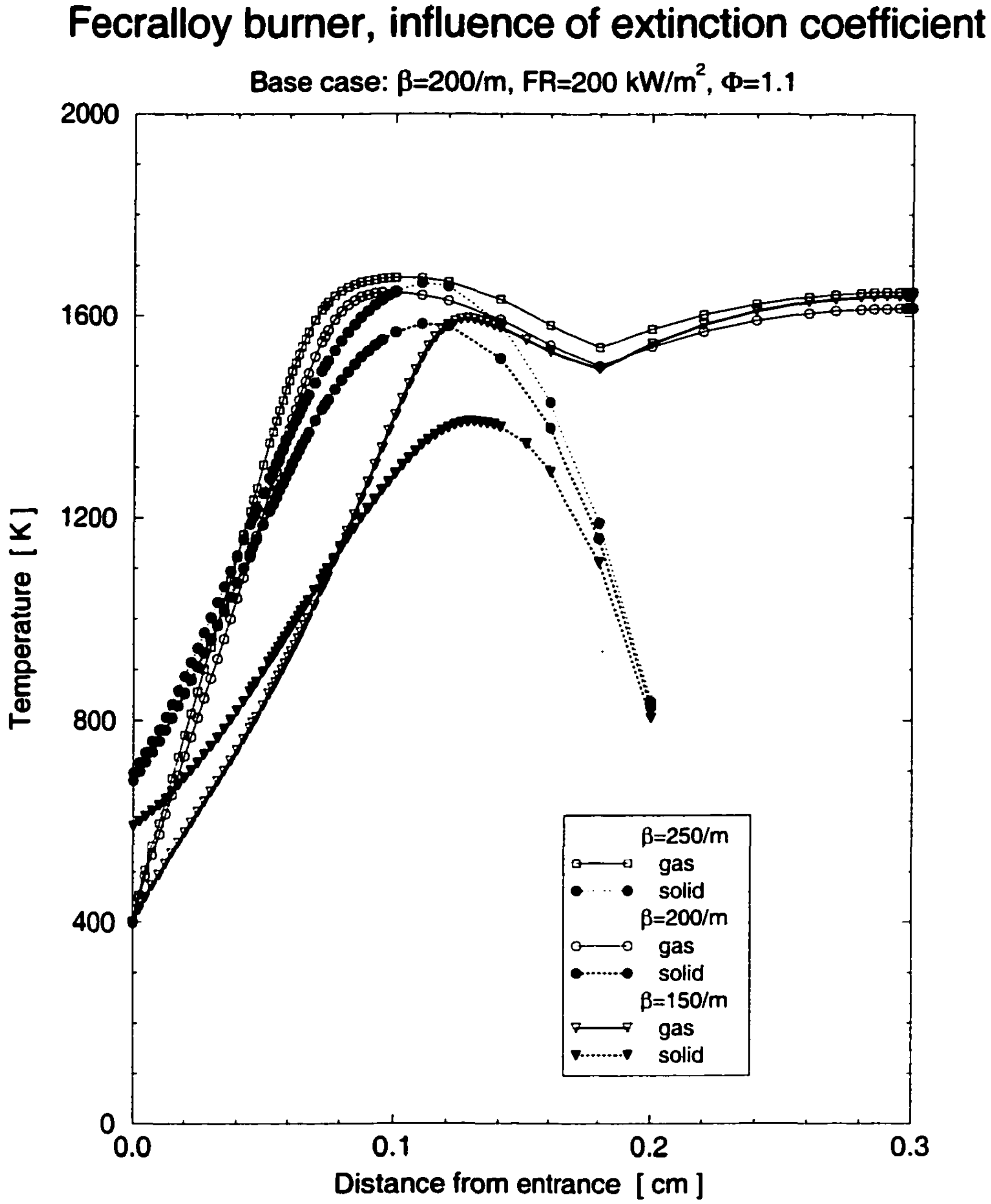

Figure 5.30. Influence of the extinction coefficient, β, on the temperature distributions of the model burner.

Table 5.9. Model burner radiation efficiency, η_{rad}, for different values of the extinction coefficient, β. The firing rate is 200 $\frac{kW}{m^2}$ and the equivalence ratio is $\Phi = 1.1$. The scattering coefficient is fixed at $\sigma_s = 20\ m^{-1}$.

Extinction Coefficient [m^{-1}]	Radiation Efficiency [%]	Surface Temperature [K]
150	11.1	806
200	22.4	826
250	30.0	838

5.9. Influence of the Scattering Coefficient (Albedo)

The effect of the scattering coefficient[14], σ_s, on the temperature distributions inside the model burner are shown in Figure 5.31. The extinction coefficient is fixed at $\beta = 200\ m^{-1}$. When the scattering coefficient (albedo) is small ($\sigma_s < 20\ m^{-1}$, or $\omega < 0.10$), gas and solid matrix temperatures reach their maxima, and the premixed flame is located at about the center of the porous material. When the scattering effects are more significant ($\sigma_s = 45\ m^{-1}$, or $\omega = 0.22$), temperatures of both gas and solid phases decrease, since the energy from the hot flame front is more readily transported to colder regions. Larger scattering coefficients ($\sigma_s > 60\ m^{-1}$, or $\omega > 0.35$) cause the flame to stabilize outside the porous layer.

Table 5.10 shows the behavior exhibited by the radiation efficiency when varying the scattering coefficient (or albedo, since they are proportional for a fixed β). Increasing this parameter leads to a decrease of the temperature of the solid, which results in a reduced radiation efficiency.

Table 5.10. Model burner radiation efficiency, η_{rad}, for different values of the scattering coefficient, σ_s. The firing rate is 200 $\frac{kW}{m^2}$ and the equivalence ratio is $\Phi = 1.1$. The extinction coefficient is fixed at $\beta = 200\ m^{-1}$.

Scattering Coefficient $[m^{-1}]$	(Albedo, ω)	Radiation Efficiency [%]	Surface Temperature $[K]$
10	(0.05)	22.7	826
20	(0.10)	22.4	826
45	(0.22)	16.4	815
70	(0.35)	1.6	688

---

[14] This discussion is given in terms of the scattering coefficient. However, note that the single scattering albedo is $\omega = \frac{\sigma_s}{\beta}$ (i.e., proportional to σ_s) and, therefore, this section covers also the variation of ω.

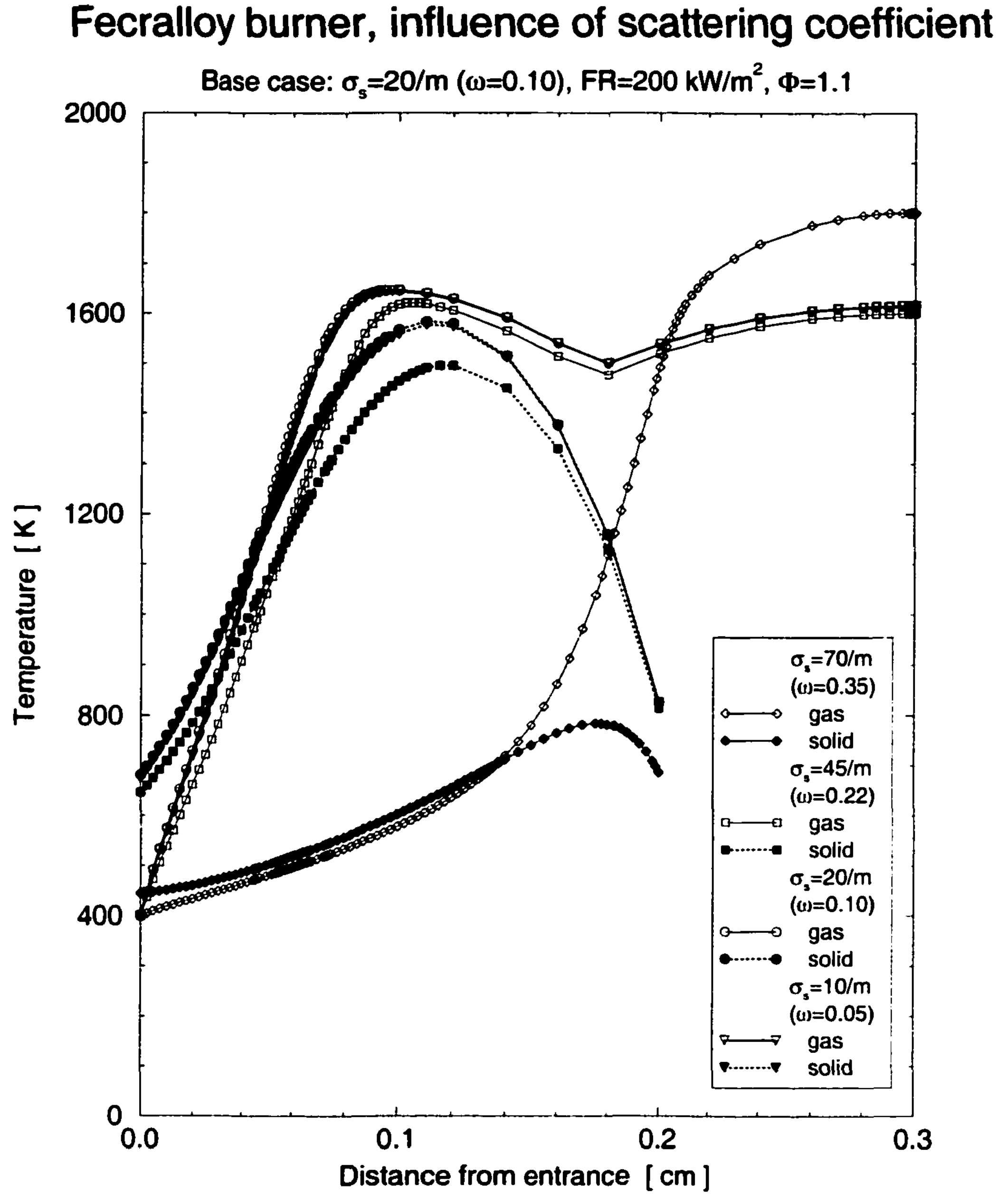

Figure 5.31. Influence of the scattering coefficient, σ_s, on the temperature distributions of the model burner.

5.10. Influence of the Fuel Composition

It was suggested in Section 4.3.6 that one possible cause for the large unburned hydrocarbon concentration (much larger than the numerically predicted emissions) was that, in the numerical simulation, the fuel was considered to be a mixture of pure methane and air, when natural gas was actually used in the experiments. It is important to mention here that, to the knowledge of the author, all researchers use this simplification for radiant burner modeling.

Figure 5.32 depicts the temperature profiles inside the model burner, which indicates that there is hardly any difference with regard to the heat release. The temperatures are slightly higher when using pure methane, since the heating value for CH_4 is larger than for C_2H_4[15].

The major species distributions for the two different fuel compositions are shown in Figure 5.33. As with the temperature, these major species do not exhibit large differences with the fuel type. Figure 5.34 illustrates the profiles of selected minor species, where the differences between fuels start to become apparent, especially in the mole fractions of the radicals (O, H, OH) at both premixed and diffusion flames, and also in the amount of H_2. Unburned hydrocarbon emissions are extremely (unrealistically) low in both cases, as discussed in Section 4.3.6. However, in spite of the actual low values (a limitation of the chemical mechanism), the ratios for selected hydrocarbon species at the exit of the burner can still provide some useful insights. Table 5.11 shows the significant percentage increase in stable[16] C_xH_y species when switching from pure methane to natural gas as the fuel[17].

Finally, it is interesting to remark that there is a small difference in the radiation efficiency when using the different fuels, as evident from Table 5.12. Pure methane results in a 0.9% efficiency gain, which is the consequence of slightly higher temperature and a more complete combustion (i.e., less pollutant emissions).

---

[15] The lower heating value for methane is 6% larger than for ethene (Turns, 1996).

[16] Short-lived radicals CH_2, CH_3, C_2H_3, etc. are not considered.

[17] GRI-Mech 2.11 is a "C2" mechanism; therefore, C_xH_y species with more than two carbon atoms (i.e., $x > 2$) are not included (but might be present in the experiment.

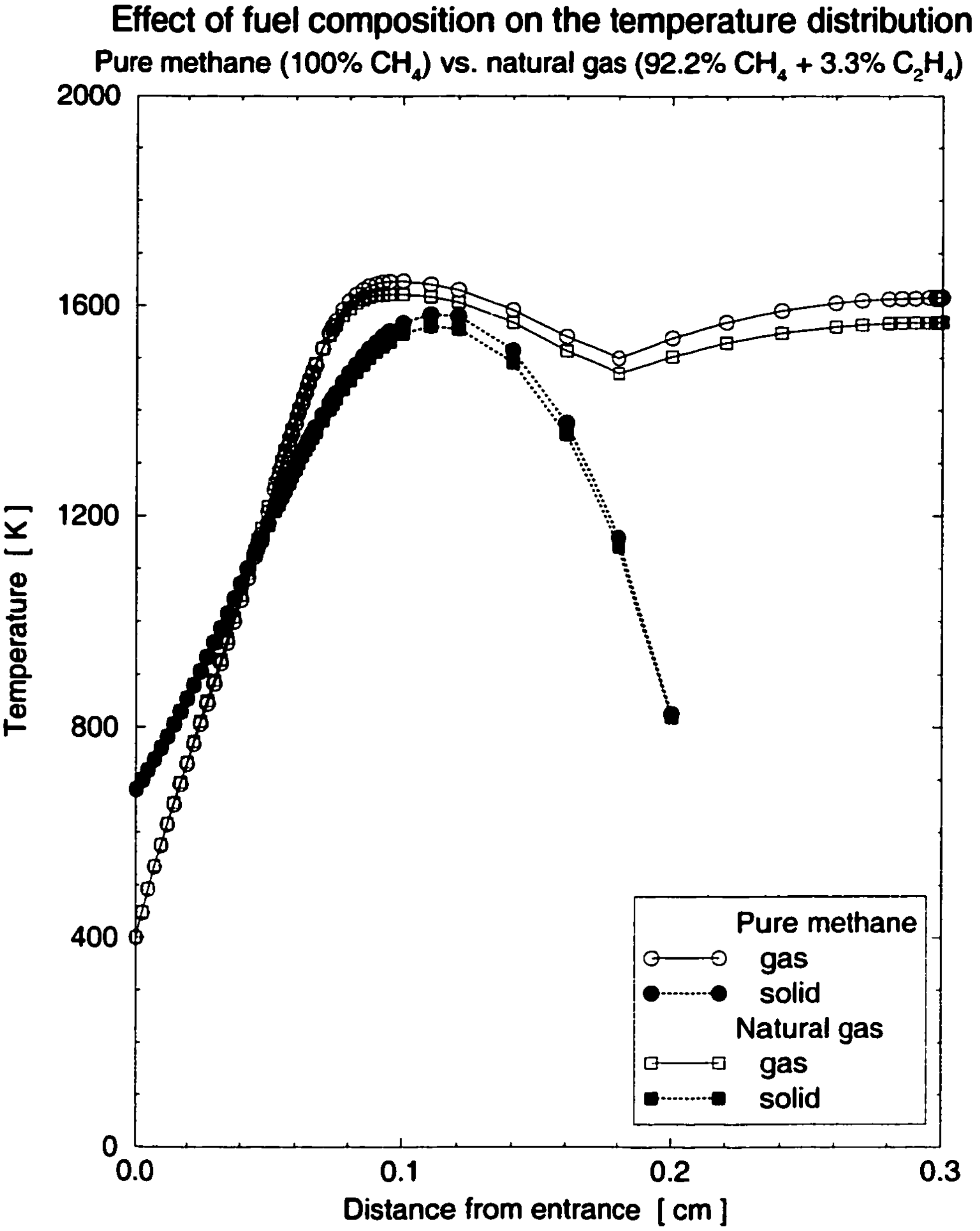

Figure 5.32. Temperature distribution inside the model burner for two different fuels: pure methane and natural gas.

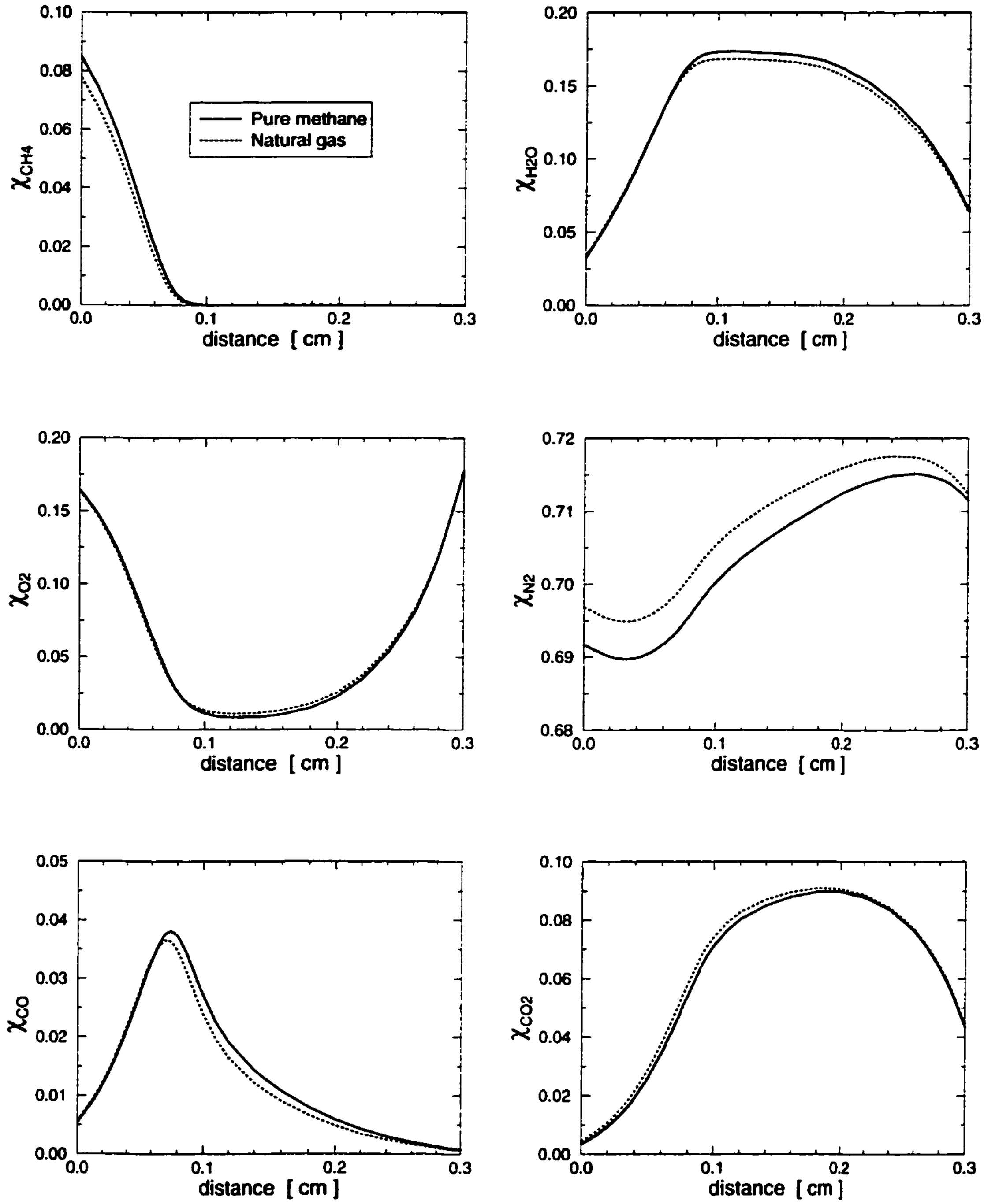

Figure 5.33. Major species distribution inside the model burner for two different fuels: pure methane and natural gas.

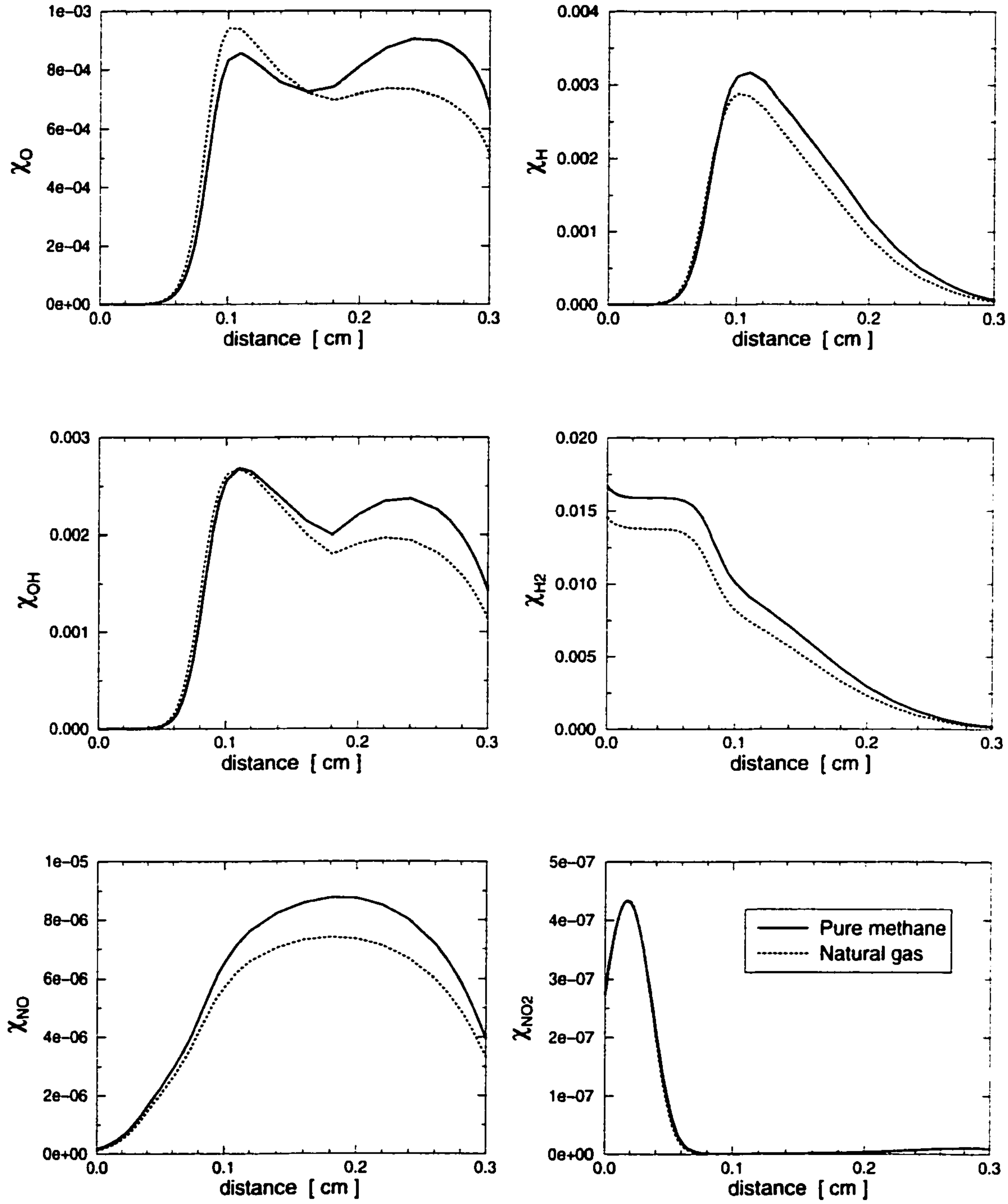

Figure 5.34. Minor species distribution inside the model burner for two different fuels: pure methane and natural gas.

Table 5.11. Unburned hydrocarbon emissions increase for the model burner using natural gas as fuel, instead of pure methane. The predictions for C_2H_6 are very low, virtually zero in both cases; therefore, a ratio cannot be computed for this species.

Relevant Hydrocarbons	Increase when using Natural Gas (Relative to Methane) [%]
CH_4	195
C_2H_2	96
C_2H_4	86
C_2H_6	n/a

Table 5.12. Model burner radiation efficiency, η_{rad}, for different fuel compositions. The firing rate is 200 $\frac{kW}{m^2}$ and the equivalence ratio is $\Phi = 1.1$.

Fuel	Radiation Efficiency [%]	Surface Temperature [K]
Pure methane	22.4	826
Natural gas	21.3	820

5.11. Summary

An extensive parametric study was carried out to investigate the effects of the several model input parameters on the porous radiant burner performance: volumetric heat transfer coefficient, equivalence ratio, firing rate, downstream oxygen concentration, surface emittance, thermal conductivity of the solid matrix, extinction coefficient, scattering coefficient, and fuel composition. The physical properties whose values influence the characteristics or behavior of the radiant burner and their influence on its main indicators (i.e., temperatures, flame location, radiation efficiency) are summarized in Table 5.13, which condenses the effects of each parameter investigated. It is interesting to note the behavior of the flame location: when a given parameter enhances the preheating, the premixed flame ignites closer to the entrance; however, when that flame cannot sustain the heat losses to the solid matrix, it becomes a surface flame (and not submerged in the porous pad.)

Table 5.13. Summary of the effects of the different problem parameters on burner performance characteristics. The arrows indicate the direction of the change for the given quantity when the parameter is increased; two arrows pointing in the same direction indicate a strong effect, and opposing arrows indicate a change in the trend.

Increase of:	h_v	Φ	FR	$\chi_{O2,out}$	ε	k_s	β	σ_s	%CH_4
Baseline value:	10^6	1.1	200	0.2	0.65	0.13	200	20	100
	$\frac{W}{m^3 K}$		$\frac{kW}{m^2}$			$\frac{W}{m\ K}$	$\frac{1}{m}$	$\frac{1}{m}$	%
Range:	$2.5 \cdot 10^5$	0.9	170	0.0	0.45	0.11	150	0	92.
	$1.5 \cdot 10^6$	1.4	340	0.3	0.85	0.15	250	70	100
Causes:									
Gas temperature	↓	↑	↑	↑	↓	↑	↑	↓	↑
Solid temperature	↑↑	↑	↑	↑	↓	↑	↑	↓	↑
Flame location	←	←	←	←	→	→	←	→	=
Diffusion flame temperature	↓	↑	↑	↑	↓	↑	=	=	↑
Radiation efficiency	↑	↓	↑,↓	↑	↓	↓	↑	↓	↑

6. CONCLUSIONS AND RECOMMENDATIONS

6.1. Conclusions

A theoretical and experimental investigation of the performance characteristics of inert, direct-fired, woven-metal-fiber (Fecralloy) porous burners was presented. Three inlet equivalence ratios, in the neighborhood of stoichiometric conditions ($\Phi = 0.9$, 1.0, 1.1), as well as typical firing rates utilized in industrial applications (from 170 to 340 $\frac{kW}{m^2}$) were studied. Special emphasis was placed on the partially-premixed (fuel rich) conditions, which produced a typical dual-flame, as a result of the combination of premixed and diffusion flames[1].

A one-dimensional, steady-state model for solving the heat transfer and combustion problem for a submerged flame radiant burner, including the detailed chemical kinetics for methane-air mixtures, was developed. The interaction of the reacting flow with a porous material, i.e., coupled combustion, conduction, convection and radiation, all occurring simultaneously, was considered in the numerical model. An existing computer program that solved a burner-stabilized flame, PREMIX, was tailored to the new porous radiant burner application. An energy equation for the solid matrix was added to the original system, and the thermal coupling between the gas and solid phases was modeled by means of a volumetric heat transfer coefficient.

The chemical reactions were modeled using the GRI-Mech 2.11 mechanism for methane combustion. This combination of elementary reactions and rates was among the most detailed mechanisms available at the time. As mentioned in Chapter 3,

---

[1] Even stoichiometric mixtures ($\Phi = 1.0$) produce double flames in the presence of heat loss. The combustion inside the solid matrix is not complete; CO and H_2 are generated and they fuel a diffusion flame.

GRI-Mech 3.0 became recently available; however, it was still not clear at the time of this investigation if it represented an actual improvement for a radiant burner.

The radiation heat transfer within the semitransparent system was modeled using the discrete ordinates method, which was considered to be more accurate than the enhanced conductivity (as in Golombok et al., 1991) or the two-flux approximation used by other researchers (Andersen, 1992; Rumminger, 1996). Some of the material properties needed for the calculations were not available; therefore, reasonable estimates were used (Section 4.2) and then sensitivity calculations were performed (Chapter 5).

A novel design for a burner housing was developed, which consists of using several small diffusers in parallel to assure uniform gas flow distribution at any flow rate, while keeping the burner housing dimensions relatively small[2]. This arrangement proved especially convenient when using high-porosity materials at low firing rates, since the pads do not induce significant pressure drop and result in poor flow uniformity.

The selected flame support pad was a woven-metal fiber layer, Fecralloy. This material presents considerable advantages when compared to ceramic fiber pads (like Nextel) or reticulated ceramics, since it is virtually unaffected by prolonged high temperature operation and frequent thermal cycling. Fecralloy became a clear choice from the durability point of view, and the fact that no degradation was observed under any conditions helped in the characterization process. Nextel fibers, though promising from the combustion perspective, are delicate and susceptible to breakup under burner operating conditions.

The experimental burner consisted then of a specially-designed, multi-diffuser stainless steel housing capable of supplying uniform gas flow (for a wide range of firing rates) to the flame support layer, a single Fecralloy pad. Commercial-grade methane was used to simulate the natural gas. Radiation efficiency, gas and solid temperatures, and pollutant emissions data (CO, NO, unburned hydrocarbons) were

---

[2] A disclosure of invention was filed with Purdue University Office of Technology Commercialization: "Porous radiant burner with uniform gas flow at a very wide range of firing rates", P-99074, September 10, 1999.

obtained at atmospheric pressure for inlet mixture equivalence ratios, using single- and double-layer burner configurations.

A unique set of experimental data that included radiation and total efficiencies, gas and solid temperatures, and pollutant (NO, CO, unburned hydrocarbons) was obtained for the Fecralloy burner. It was determined that the radiation efficiency of this prototype burner initially increased with the firing rate, and then remained approximately constant. Temperatures increased with the firing rate. Pollutant emissions were observed to rise with the firing rate, except for the unburned hydrocarbons that remained approximately constant. Double-layer burners showed generally higher temperatures and radiation efficiencies, increased CO and NO, and reduced unburned hydrocarbon emissions, when compared to the single-layer counterparts.

The model predictions were compared against the experimental measurements obtained with the single-layer Fecralloy burner (Chapter 4). Good agreement was observed for radiation efficiency and temperature predictions, as well as for the nitrous oxide emissions. More limited success was obtained for carbon monoxide, since only the trends were correct. The magnitudes were overestimated. Unburned hydrocarbons were severely underpredicted under all conditions. Possible experimental sources of error were discussed in Chapter 4. However, the most likely culprit is the detailed kinetics mechanism itself, which has not been validated completely for non-adiabatic conditions.

A surface flame (i.e., not submerged) was predicted by the code for certain conditions, like using a fuel lean mixture at low firing rates. Even though the actual magnitude of the firing rate at which this transition occurred was not adequately reproduced (the needed firing rate to cause that change in the laboratory was significantly lower), it is encouraging that the model captures the behavior. Additionally, the drastic radiation efficiency drop predicted when the premixed flame moves outside the pad was in agreement with the experimental observations.

An extensive parametric study (Chapter 5) was carried out to investigate the effects on the burner performance of several of the code input parameters: volumetric heat transfer coefficient, equivalence ratio, firing rate, downstream oxygen concentration, surface emittance, thermal conductivity of the solid matrix, extinction coefficient, scattering coefficient, and fuel composition. All of them play an important role in determining the thermal characteristics of the system. According to the presented results, the most desirable situation would include a solid matrix with large volumetric heat transfer coefficient, small surface emittance, low effective thermal conductivity, large extinction coefficient and small scattering albedo, operating at the greatest equivalence ratio ($\Phi \leq 1.3$) that the pollutant emission limits permit, and with a downstream oxygen mole fraction of about 0.20.

Finally, this work provided some additional experimental information (the double-layer burner data) for further comparison with modeling.

6.2. Recommendations for Future Work

A multitude of modeling challenges must still be resolved before a full understanding of the porous radiant behavior is reached. Inclusion of gas radiation, though not a critical element, will improve the pollutant emission predictions. A two-dimensional extension might also prove useful if a more adequate representation of the pad geometry is desired, especially for porous materials with a definite structure, like woven fiber pads. Moreover, highly two-dimensional flames were reported by Min and Shin (1991), adding merit to the need of a two-dimensional formulation (as recently shown by Hackert et al., 1999). Adding spectral effects, as well as anisotropic scattering within the porous matrix will also contribute to a more truthful description.

The inclusion of catalytic reactions must be considered. Even an "inert" porous matrix can be affected by the presence of chemical reactions induced or affected by the walls of the pores or fibers (Bogdanov et al., 1995). Some modeling has been performed (Kendall et al., 1992; Rumminger et al., 1999), but much research remains to be done, especially in the area of detailed surface chemistry, mass transfer to the solid surfaces in the porous medium, and catalyst durability (Rumminger, 1996).

The necessity of using detailed kinetics in models for premixed combustion within porous media has been determined some time ago by Hsu and Matthews (1993). They demonstrated that global chemistry is not adequate. and concluded that it is essential to use multistep kinetics if accurate predictions of the temperature distributions. composition profiles and emissions, energy release rates. and total energy release are sought. It has not been possible so far to obtain accurate predictions of emissions and, in most cases, the discrepancies can only be partially attributed to experimental uncertainties and imprecise knowledge of the properties of the solid matrix. Some important aspects of the physical processes are still not well simulated. The fact that a given chemical mechanism produces much better predictions for a free flame than for an embedded flame in a porous media suggests the possibility of the problem being rooted in the kinetics description itself. So far, the same set of elementary reactions and rates have been used for all types of simulations. It is imperative then to investigate the applicability of GRI-Mech (and similar mechanisms) to non-adiabatic conditions such as combustion in porous media

The physical properties whose values influence the characteristics or behavior of the radiant burner and their impact on its main indicators (i.e., temperatures, flame location, radiation efficiency) were summarized in Table 5.13 (Section 5.11), which condensed the effects of each of the parameters investigated in this thesis. In view of the large number of factors involved. it would be useful to develop a methodology to aid in creating a hierarchy, a way of identifying which are the parameters that affect the most a certain aspect of the burner performance (radiation efficiency, temperatures, pollutant emissions, etc.) Two possible procedures are the construction of a neural network or the determination of a set of sensitivity coefficients. However. it is necessary to point out here that the system behavior is strongly dependent on the operating conditions (especially the firing rate); therefore, several different neural networks or sets of sensitivity coefficients would be required.

Species profiles were found to collapse when presented in terms of the fuel-based progress variable, ζ. However, in order to investigate the similarity in greater depth.

reaction rates for individual chemical reactions must be computed and compared for different volumetric heat transfer coefficients. In this manner, the effect of heat loss on chemistry could be assessed. Quantitative reaction path diagrams (QRPD)[3] were used by Lim (1998) to identify key reactions in laminar counterflow flames, and they could also be used in the case of a porous burner to analyze which reactions contribute the most to pollutant formation.

Even though the aforementioned recommendations are all oriented toward enhancement of the model itself, there are also several experimental aspects that need to be addressed in the future. First and foremost, a focussed experimental study of emissions is necessary to provide the most complete and accurate set of data for model validation. In this study, only a handful of species concentrations (CO, NO, CH_4) were available for comparison with the myriad of information of the program output (49 species); a greater number of measured concentrations would be useful to assess future modeling efforts. The gas analyzers used in this investigation were adequate for this purpose, but more sophisticated techniques (such as gas chromatography or spectroscopy) will be needed for a pollutant emissions study.

Additionally, a more appropriate calibration of the pollutants emission detection equipment would involve the use of a calibration flame, instead of (cold) bottled gases. In this manner, possible probe-dependent effects, such as quenching, would be more readily identified.

A detailed characterization of the porous matrix used as the flame support material is also recommended. Thermophysical (especially effective thermal conductivity) and radiation (extinction and scattering) properties should be experimentally determined, since the information provided by the manufacturers is usually limited and incomplete. Their dependence with the temperature would be needed as well, so a model can include and evaluate those effects.

---

[3] These diagrams consist of a set of arrows linking the different species that contribute to the formation of a given species; the direction of the arrow denotes the reaction direction, and the thickness of the arrow is proportional to the net reaction rate; each arrow is numbered according to the corresponding elementary reaction of the detailed mechanism.

Furthermore, a deeper understanding of the thermal coupling between the reactive gas and the solid would be desired. For example, a study of the volumetric heat transfer coefficient of porous materials in terms of the local (rather than entrance) variables, including not only gas-phase but also solid-phase details, would allow an additional level of model sophistication and better simulations.

Finally, some experimental information of temperatures and species concentrations within the porous pad would permit further validation of the numerical results. Due to the difficulties imposed by the nature of the Fecralloy structure (Section 2.4), it has not been possible to obtain local data in this work; all model validation was performed against global (i.e., at the burner exit) measurements. New techniques need to be developed, suitable for procuring the necessary experimental measurements in the small inter-fiber geometry, but without disrupting the flow or distorting/quenching the flame front.

LIST OF REFERENCES

LIST OF REFERENCES

Alder, B. L. 1996, *Nitric Oxide Formation in Laminar Partially Premixed Ethane-Air Flames*, Master's thesis, School of Mechanical Engineering, Purdue University, West Lafayette, IN.

Alifanov, O. M., Tryanin, A. P. and Lozhkin, A. L. 1987, Experimental investigation of the method of determining the internal heat-transfer coefficient in a porous material from the solution of the inverse problem, *Journal of Engineering Physics* **52**, 340–346.

Andersen, F. 1992, Heat-transport model for fiber burners, *Progress in Energy and Combustion Science* **18**(1), 1–12.

Anderson, R. B., Stein, K. C., Freenan, J. J. and Hofer, L. J. E. 1961, Catalytic oxidation of methane, *Industrial & Engineering Chemistry* **53**(10), 809–812.

Arai, H., Yamada, T., Eguchi, K. and Seiyama, T. 1986, Catalytic combustion of methane over various perovskite-type oxides, *Applied Catalysis* **26**, 265–276.

Araki, N., Makino, A. and Nitta, Y. 1990, The structure of partially-premixed diffusion flames (Measurement of temperature and concentration profiles with CARS), *Nippon Kikai Gakkai Ronbunshu, B* **56**(526), 1770–1774 (*in Japanese*).

Arcoya, A., Cortes, A., Fierro, J. L. G. and Soane, X. L. 1991, Comparative study of the deactivation of group viii metal catalysts by thiophene poisoning in ethylbenzene hydrogenation, *Catalyst Deactivation (C. H. Bartholomew and J. B. Butt, editors), Proceedings of the Fifth International Symposium, Evanston IL, June 24-26*, Vol. 68 of *Studies in Surface Science and Catalysis*, Elsevier, Amsterdam, pp. 557–564.

Artizzu, P., Garbowski, E., Primet, M., Brulle, Y. and Saint-Just, J. 1999, Catalytic combustion of methane on aluminate-supported copper oxide, *Catalysis Today* **47**(1–4), 83–93.

Baclic, B. S., Heggs, P. J. and Ziyan, H. A. 1986, The differential fluid enthalpy method, *Proceedings of the Eighth International Heat Transfer Conference, San Francisco, CA*, Vol. V, Hemisphere Publishing Corporation, Washington, D. C., pp. 2616–2622.

Barlow, J. B., (Jr.), W. H. R. and Pope, A. 1999, *Low-Speed Wind Tunnel Testing*, 3rd. edn, John Wiley & Sons, New York.

Bird, R. B., Stewart, W. E. and Lightfoot, E. N. 1960, *Transport Phenomena*, John Wiley & Sons, New York.

Blevins, L. G. and Gore, J. P. 1996, CH radicals in partially premixed methane/air flames, *Proceedings of the 1996 Technical Meeting*, Central States Section of the Combustion Institute, pp. 239–244.

Blevins, L. G. and Gore, J. P. 1999, Computed structure of low strain rate partially premixed CH4/air counterflow flames: implications for NO formation, *Combustion and Flame* **116**(4), 546–566.

Bogdanov, A. V., Dubrovskiy, G. V., Krutikov, M. P., Kulginov, D. V. and Strelchenya, V. M. 1995, *Interaction of Gases with Surfaces. Detailed Description of Elementary Processes and Kinetics*, Springer-Verlag, Berlin.

Bouma, P. H., de Goey, L. P. H., Nieuwenhuizen, J. K. and van der Drift, A. 1993, Modeling of twofold flame behavior of ceramic foam radiant gas burners, *Proceedings of the Second International Conference on Combustion Technologies for a Clean Environment*, Lisbon, Portugal, pp. 15–19.

Bouma, P. H., Eggels, R. L. G. M., de Goey, L. P. H., Nieuwenhuizen, J. K. and van der Drift, A. 1995, A numerical and experimental study of the NO emission of ceramic foam surface burners, *Combustion Science and Technology* **108**, 193–203.

Bowman, C., Hanson, R., Davidson, D., (Jr.), W. G., Lissianski, V., Smith, G., Golden, D., Frenklach, M. and Goldenberg, M. 1996, *GRI-Mech 2.11, http://euler.me.berkeley.edu/gri_mech/.*

Bradshaw, A. V., Johnson, A., McLachlan, N. H. and Yin, Y. T. 1970, Heat transfer between air and nitrogen and packed beds of non-reacting solids, *Transactions of the Institution of Chemical Engineers* **48**, 77–84.

Bui-Pham, M., Seshadri, K. and Williams, F. A. 1992, The asymptotic structure of premixed methane-air flames with slow CO oxidation, *Combustion and Flame* **89**, 343–362.

Cai, Z. H., Li, M. L., Wu, Y. W. and Ren, H. S. 1984, A modified selected point matching technique for testing compact heat exchanger surfaces, *International Journal of Heat and Mass Transfer* **27**(3), 971–978.

Cain, J. B. and McKay, N. 1991, Thermal radiative properties of metallized films, *Journal of Thermal Insulation* **14**, 221–240.

Cant, R. S., Bray, K. N. C., Kostiuk, L. W. and Rogg, B. 1994, Flow divergence effects in strained laminar flamelets for premixed turbulent combustion, *Combustion Science and Technology* **95**(1–6), 261–276.

Carlson, B. G. and Lathrop, K. D. 1968, *Transport Theory-The Method of Discrete Ordinates*, Computing Methods in Reactor Physics, Gordon and Breach, New York.

Catalytic Industrial Systems 1996, Company information brochure. P.O. Box 827, Independence, KS 67301.

Chambrion, P., Jander, H., Petereit, N. and Wagner, H. G. 1996, Soot growth in atmospheric C_2H_4/air/O_2-flames. Influence of the fuel carbon density, *Zeitschrift für Physikalische Chemie* **194**(1), 1–19.

Chandrasekhar, S. 1960, *Radiative Transfer*, Dover Publications, New York.

Cis-Can Industries Ltd. 1998, Company information brochure. 5918 Roper Road, Edmonton, Alberta T6B 3E1, Canada.

Coltrin, M. E., Kee, R. J. and Rupley, F. M. 1990, SURFACE CHEMKIN: a Fortran package for analizing heterogeneous chemical kinetics at a solid-surface–gas-phase interface, *Technical Report SAND90-8003B*, Sandia National Laboratory.

Cooper, C. F. 1976, Burners, *United States Patent Office*. Patent number 3,954,387; 2 claims.

Correa, S. M. 1992, A review of NO_x formation under gas-turbine combustion conditions, *Combustion Science and Technology* **87**, 329–362.

Coulaud, O., Morel, P. and Caltagirone, J. P. 1988, Numerical modelling of nonlinear effects in laminar flow through a porous medium, *Journal of Fluid Mechanics* **190**, 393–407.

Curtiss, C. and Hirschfelder, J. 1949, Transport properties of multicomponent gas mixtures, *The Journal of Chemical Physics* **17**, 550–551.

Dogwiler, U., Benz, P. and Mantzaras, J. 1999, Two-dimensional modelling for catalytically stabilized combustion of a lean methane-air mixture with elementary homogeneous and heterogeneous chemical reactions, *Combustion and Flame* **116**, 243–258.

Dongworth, M. R. and Melvin, A. 1976, Diffusive catalytic combustion, *Proceedings of the Sixteenth International Symposium on Combustion*, The Combustion Institute, Pittsburgh, PA, pp. 255–264.

Echigo, R. 1982, Effective energy conversion method between gas enthalpy and thermal radiation and application to industrial furnaces, *Proceedings of the Seventh International Heat Transfer Conference, Munich, Germany*, Vol. IV, Hemisphere Publishing Corporation, Washington. D. C., pp. 361–366.

Echigo, R., Yoshizawa, Y., Hanamura, K. and Tomimura, T. 1986, Analytical and experimental studies on radiative propagation in porous media with internal heat generation, *Proceedings of the Eighth International Heat Transfer Conference, San Francisco, CA*, Vol. II, Hemisphere Publishing Corporation, Washington, D. C., pp. 827–832.

Eclipse Combustion 1992, *Bulletin 405*. 1665 Elmwood Rd., Rockford, IL 61103.

Eliseev, B. V., Ufatov, I. V. and Chikov, V. P. 1983, Transient conditions of temperature establishment in a porous heater, *High Temperature* **21**(4), 587–591.

Fedorov, A. G., Lee, K. H. and Viskanta, R. 1998, Inverse optimal design of the radiant heating in materials processing and manufacturing, *Journal of Materials Engineering and Performance* **7**(6), 729–726.

Fiveland, W. A. 1987, Discrete ordinate methods for radiative heat transfer in isotropically and anisotropically scattering media, *Journal of Heat Transfer, Transactions of the ASME* **109**(3), 809–812.

Forzatti, P. and Groppi, G. 1998, Combustion catalysis for the production of heat and energy, *Second World Congress on Environmental Catalysis*, American Institute of Chemical Engineers, Miami Beach, FL.

Fox, J. S. 1976, Comments on burners producing large excess enthalpies. *Combustion Science and Technology* **12**, 147–151.

Fu, X. 1997, *Modeling of a Submerged Flame in a Porous Burner/Radiant Heater*. PhD thesis, School of Mechanical Engineering, Purdue University, West Lafayette, IN.

Fu, X., Viskanta, R. and Gore, J. P. 1998a, Combustion and heat transfer interaction in a pore-scale refractory tube burner, *Journal of Thermophysics and Heat Transfer* **12**(2), 164–171.

Fu, X., Viskanta, R. and Gore, J. P. 1998b, Measurement and correlation of volumetric heat transfer coefficients of cellular ceramics, *Experimental Thermal and Fluid Science* **17**(4), 285–293.

Fu, X., Viskanta, R. and Gore, J. P. 1999, Idealized radiation efficiency model for a porous radiant burner, *ASHRAE Transactions (Paper 4298)* **105**(Part 2), 267–273.

Furnas, C. C. 1930, Heat transfer from a gas stream to a bed of broken solids - I, *Industrial and Engineering Chemistry* **22**, 26–31.

Gardon, R. 1956, The emissivity of transparent materials, *Journal of the American Ceramic Society* **39**(8), 278–287.

Gollahalli, S. R. and Subba, S. 1997, Partially premixed laminar gas flames from triangular burners, *Journal of Propulsion and Power* **13**(2), 226–232.

Golodets, G. I. 1983, *Heterogeneous Catalytic Reactions Involving Molecular Oxygen*, Vol. 15 of *Studies in Surface Science and Catalysis*, Elsevier, New York.

Golombok, M. and Shirvill, L. C. 1990, Radiation characteristics of surface combustion burners, *Proceedings of EUROTHERM Seminar N° 17*, pp. 7–13.

Golombok, M., Prothero. A., Shirvill, L. C. and Small, L. M. 1991, Surface combustion in metal fibre burners, *Combustion Science and Technology* **77**, 203–223.

Goralski, C. 1998, University of Minessota, Minneapolis, MN, *personal communication*.

Gore, J. P. 1999, Purdue University, West Lafayette, IN, *personal communication*.

Gore, J. P. and Zhan, N. J. 1996, NO_x emission and major species concentrations in partially premixed laminar methane/air co-flow jet flames, *Combustion and Flame* **105**(3), 414–427.

Goss, L. P., Vilimpoc, V., Sarka, B. and Lynn, W. F. 1988, Thin-filament pyrometry: a novel thermometric technique for combusting flows, *American Society of Mechanical Engineers (Paper). Presented at the Gas Turbine and Aeroengine Congress (Amsterdan, Netherlands)*, Vol. 88-GT-28, ASME, New York.

Gouldin, F. C. 1996, Combustion intensity and burning rate integral of premixed flames, *Twenty-Sixth International Symposium on Combustion*, Vol. 1, The Combustion Institute, Pittsburgh, PA, pp. 381–388.

Grcar, J. F. 1992, The TWOPNT program for boundary value problems, *Technical Report SAND91-8230*, Sandia National Laboratory.

Groppi, G., Bellotto, M., Cristiani, C., Forzatti, P. and Villa, P. C. 1993, Preparation and characterization of hexaaluminate-based materials for catalytic combustion, *Applied Catalysis A* **104**(2), 101–108.

Grosshandler, W. L. 1993, Radcal, *Technical Report NIST-1402*, National Institute of Standards and Technology, Gaithersburg, MD.

Hackert, C. L., Ellzey, J. L. and Ezekoye, O. A. 1999, Combustion and heat transfer in model two-dimensional porous burners, *Combustion and Flame* **116**(1–2), 177–191.

Hamins, A., Theridandam, H. and Seshadri, K. 1985, Structure and extinction of a counterflow partially premixed diffusion flame, *Chemical Engineering Science* **40**(11), 2027–2038.

Hardesty, D. R. and Weinberg, F. J. 1974, Burners producing large excess enthalpies, *Combustion Science and Technology* **8**, 201–214.

Hardesty, D. R. and Weinberg, F. J. 1976, Converter efficiency in burner systems producing large excess enthalpies, *Combustion Science and Technology* **12**, 153–157.

Hardison, L. 1967, Catalytic infra-red heater, *United States Patent Office*. Patent number 3,310,098; 5 claims.

Hausen, H. 1983, *Heat Transfer in Counterflow, Parallel-flow, and Cross-flow*, (translated from German by M. S. Sayer, editted by A. J. Willmott), McGraw-Hill, New York.

Heberle, N. H., Smith, P. S., Crosley, D. R., Jeffries, J. B., Muss, J. A. and Dibble, R. W. 1995, Laser-induced fluorescence measurements in atmospheric pressure partially premixed methane/air flames, *Proceedings of the 1995 Joint Technical Meeting*, Central States Section of the Combustion Institute, pp. 134–138.

Heggs, P. J. and Burns, D. 1988, Single-blow experimental prediction of heat transfer coefficients – A comparison of four commonly used techniques, *Experimental Thermal and Fluid Science* **1**, 243–251.

Holman, J. P. 1971, *Experimental Methods for Engineers*, McGraw-Hill, New York.

Hougen, O. A. and Watson, K. M. 1947, *Chemical Process Principles*, John Wiley & Sons, New York.

Howell, J. R., Hall, M. J. and Ellzey, J. L. 1996, Combustion of hydrocarbon fuels within porous inert media, *Progress in Energy and Combustion Science* **22**, 121–145.

Hoyle, N. D., Kumarasamy, P., Self, V. A., Sermon, P. A. and Vong, M. S. W. 1999, Catalysis of H_2, CO and alkane oxidation over Pt/Silica catalysts: evidence of coupling and promotion, *Catalysis Today* **47**(1–4), 45–49.

Hoyos, L. J., Praliaud, H. and Primet, M. 1993, Catalytic combustion of methane over palladium supported on alumina and silica in presence of hydrogen sulfide, *Applied Catalysis A* **98**(2), 125–138.

Hsu, P.-F. and Matthews, R. D. 1993, The necessity of using detailed kinetics in models for premixed combustion within porous media, *Combustion and Flame* **93**(4), 457–466.

Hsu, P.-F., Evans, W. D. and Howell, J. R. 1993a, Experimental and numerical study of premixed combustion within nonhomogeneous porous ceramics, *Combustion Science and Technology* **90**(1–4), 149–172.

Hsu, P.-F., Howell, J. R. and Matthews, R. D. 1993b, A numerical investigation of premixed combustion within porous inert media, *Journal of Heat Transfer, Transactions of the ASME* **115**(3), 744–750.

Hulgaard, T. and Damjohansen, K. 1992, Nitrous oxide sampling, analysis, and emission measurements from various combustion systems, *Environmental Progress* **11**(4), 302–309.

Jakob, M. and Hawkins, G. A. 1957, *Elements of Heat Transfer*, John Wiley & Sons, New York.

Jang, B. W.-L., Nelson, R. M., Spivey, J. J., Ocal, M., Oukaci, R. and Marcelin, G. 1999, Catalytic oxidation of methane over hexaaluminates and hexaaluminate-supported Pd catalysts, *Catalysis Today* **47**(1–4), 101–113.

Ji, J., Gore, J. P., Sivathanu, Y. R. and Lim, J. 2000a, Fast infrared array spectrometer used for radiation measurements of lean premixed flames, *Proceedings of the 34th. National Heat Transfer Conference, Pittsburgh, PA, August 20-22.* Submitted for publication.

Ji, J., Sivathanu, Y. R. and Gore, J. P. 2000b, Thermal radiation properties of turbulent lean premixed methane air flames, *Twenty-Eighth International Symposium on Combustion*, The Combustion Institute, Pittsburgh, PA. Submitted for publication.

Kang, S. K., Moon, S. M., Ryu, I. S. and Ha, Y. O. 1994, The study of the characteristics of low temperature catalytic combustion and sulfur, *Proceedings of the Second International Workshop on Catalytic Combustion*, Tokyo, Japan.

Kazakov, A. and Frenklach, M. 1998, DRM-19, *http://euler.me.berkeley.edu/drm*.

Kee, R., Grcar, J. F., Smooke, M. and Miller, J. 1988, A Fortran program for modeling steady laminar one-dimensional premixed flames, *Technical Report SAND85-8240*, Sandia National Laboratory.

Kee, R. J., Miller, J. and Jefferson, T. 1980, CHEMKIN: a general purpose, problem-independent, transportable, Fortran, chemical kinetic program package, *Technical Report SAND80-8003*, Sandia National Laboratory.

Kee, R., Warnatz, J. and Miller, J. 1983, A Fortran computer program package for the evaluation of gas-phase viscosities, conductivities and diffusion coefficients, *Technical Report SAND83-8209*, Sandia National Laboratory.

Kendall, R. M., DesJardin, S. and Sullivan, J. D. 1992, Basic research on radiant burners (for Gas Research Institute, Report 92/0181), *Technical Report 92-7027-171*, Alzeta Corporation.

Kerker, M. 1969, *The Scattering of Light, and Other Electromagnetic Radiation*, Physical Chemistry, A Series of Monographs, Academic Press, New York.

Kilham, J. K. and Lanigan, E. P. 1970, A study of the mechanism of radiant burners, *I. G. E. Journal* pp. 700–719.

Kim, T. K., Alder, B. J., Laurendeau, N. M. and Gore, J. P. 1995, Exhaust and in-situ measurements of nitric oxide for laminar partially premixed C_2H_6-air flames: effect of premixing level at constant fuel flowrate, *Combustion Science and Technology* **111**, 361–378.

Kline, S. J., Abbot, D. E. and Fow, R. W. 1959, Optimum design for straight-walled diffusers, *Journal of Basic Engineering, Transactions of the ASME* **81**(9), 321–331.

Klvana, D., Kirchnerova, J., Chaouki, J., Delval, J. and Yaïci, W. 1999, Fiber supported perovskites for catalytic combustion of natural gas, *Catalysis Today* **47**(1–4), 115–121.

Kohlmayr, G. F. 1966, Exact maximum slopes for transient matrix heat-transfer testing, *International Journal of Heat and Mass Transfer* **9**, 671–680.

Kohlmayr, G. F. 1968a, An indirect curve matching method for transient matrix heat-transfer testing in the low NTU-range, *International Journal of Heat and Mass Transfer* **11**, 567–581.

Kohlmayr, G. F. 1968b, Extension of the maximum slope method to arbitrary upstream fluid temperature changes, *Journal of Heat Transfer, Transactions of the ASME* **90**, 130–134.

Komori, T. and Makishima, K. 1978, Estimation of fiber orientation and length in fiber assemblies, *Textile Research Journal* **48**(6), 309–314.

Kopal, Z. 1961, *Numerical Analysis, with Emphasis on the Application of Numerical Techniques to Problems of Infinitesimal Calculus in Single Variable*, 2nd. edn, John Wiley & Sons, New York.

Kumar, S., Majumdar, A. and Tien, C. L. 1990, The differential-discrete-ordinate method for solutions of the equation of radiative transfer, *Journal of Heat Transfer, Transactions of the ASME* **112**(2), 424–429.

Kuo, K. 1986, *Principles of Combustion*, John Wiley & Sons, New York.

Kurosaki, Y. and Yamada, J. 1991, Radiation transport in porous fibrous media, *in* S. Kakaç, B. Kilkiş, F. Kulnacki and F. Arinç (eds), *Convective Heat and Mass Transfer in Porous Media*, Kluwer Academic Publishers, Dordrecht, pp. 347–390.

Lathrop, K. D. 1966, Use of discrete-ordinate methods for solution of photon transport problems, *Nuclear Science and Engineering* **24**, 381–388.

Lathrop, K. D. and Carlson, B. G. 1965, Discrete-ordinates angular quadrature of the neutron transport equation, *Technical Report LASL-3186*, Los Alamos Scientific Laboratory.

Law, C. K., Li, T. X., Chung, S. H., Kim, J. S. and Zhu, D. L. 1989, On the structure and extinction dynamics of partially-premixed flames - Theory and experiment, *Combustion Science and Technology* **64**(4-6), 199–232.

Lee, C. E. 1962, The discrete S_N approximation to transport theory, *Technical Report LA2595*, Lawrence Livermore Laboratory.

Lee, J. H. and Trimm, D. L. 1995, Catalytic combustion of methane, *Fuel Processing Technology* **42**(2-3), 339–359.

Lee, S. C. 1986, Radiative transfer through a fibrous medium: allowance for fiber orientation, *Journal of Quantum Spestroscopic Radiation Transfer* **36**(3), 253–263.

Lee, Y. I., Shin, H. D. and Baek, S. W. 1996, Experimental and numerical study on the laminar premixed flame stabilized inside a honeycomb ceramic, *Combustion Science and Technology* **112**, 75.

Leonardi, S. A., Gore, J. P. and Viskanta, R. 2000, Surface temperature and radiation efficiency measurements with a uniform flow porous radiant gas burner, *Proceedings of the 2000 Technical Meeting of the Central States Section of the Combustion Institute.* Indianapolis, IN, April 17 - 18.

Leonardi, S. A., Viskanta, R. and Gore, J. P. 1998, Comparison of several types of gas-fired burners/radiant heaters (submitted to S.S. Energy Environmental International, Inc., Rockford, IL 61108), *Technical report*, Mechanical Engineering, Purdue University.

Liang, C. Y. and Yang, W.-J. 1975, Modified single-blow technique for performance evaluation on heat transfer surfaces, *Journal of Heat Transfer, Transactions of the ASME* **97**(1), 16–21.

Libby, P. A. 1998, Laminar triple flames in partially premixed opposed flows, *Combustion Science and Technology* **138**(1-6), 179–212.

Libby, P. A. and Economos, C. 1963, A flame zone model for chemical reaction in a laminar boundary layer with application to the injection of hydrogen-oxygen mixtures, *International Journal of Heat and Mass Transfer* **6**, 113–128.

Lim, J. 1998, *A Study of the Effects of Preheat and Steam Addition on the Flame Structure and NO Formation in Laminar Counterflow Flames*, PhD thesis, School of Mechanical Engineering, Purdue University, West Lafayette, IN.

Locke, G. L. 1950, Heat transfer and flow friction characteristics of porous solids, *Technical Report 10*, Mechanical Engineering, Stanford University.

Loehrke, R. I. 1990, Evaluating the results of the single-blow transient heat exchanger, *Experimental Thermal and Fluid Science* **3**, 574–580.

Lyle, K. H. 1997, *An Experimental Study of NO_x Emissions in Turbulent and Laminar Partially Premixed Flames*, Master's thesis, School of Mechanical Engineering, Purdue University, West Lafayette, IN.

Lyons, J. W. 1987, *Fire*, Scientific American Library, W. H. Freeman and Company, New York.

Lyubovsky, M. and Pfefferle, L. 1999, Complete methane oxidation over Pd catalyst supported on α-alumina. Influence of temperature and oxygen pressure on the catalyst activity, *Catalysis Today* **47**(1-4), 29–44.

Machida, M., Eguchi, K. and Arai, H. 1989, Catalytic properties of $BaMAl_{11}O_{19-\alpha}$ (M=Cr, Mn, Fe, Co, and Ni) for high temperature catalytic combustion, *Journal of Catalysis* **120**, 377–386.

Machida, M., Eguchi, K. and Arai, H. 1990, Effect of structural modification on the catalytic property of Mn-substituted hexaaluminates, *Journal of Catalysis* **123**, 477–485.

Makino, A., Araki, N. and Nitta, Y. 1991, The structure of partially-premixed diffusion flames (Investigation of the flame structure near the blow-off limit with CARS), *JSME Journal, B* **57**(533), 333-338.

Mathur, S., Tondon, P. K. and Saxena, S. C. 1967, Thermal conductivity of binary, ternary and quaternary mixtures of rare gases, *Molecular Physics* **12**(6), 569–579.

McCarty, J. G. and Wise, H. 1990, Perovskite catalysts for methane combustion, *Catalysis Today* **8**(2), 231-248.

Miller, J. A. and Bowman, C. T. 1989, Mechanism and modeling of nitrogen chemistry in combustion, *Progress in Energy and Combustion Science* **15**, 287–338.

Min, D. K. and Shin, H. D. 1991, Laminar premixed flame stabilized inside a honeycomb ceramic, *International Journal of Heat and Mass Transfer* **34**(2), 341–356.

Mital, R. 1996, *An Experimental and a Theoretical Investigation of Combustion and Heat Transfer Characteristics of Reticulated Ceramic Burners*, PhD thesis, School of Mechanical Engineering, Purdue University, West Lafayette, IN.

Mital, R., Gore, J. P. and Viskanta, R. 1996, Measurements of radiative properties of cellular ceramics at high temperatures, *Journal of Thermophysics and Heat Transfer* **10**(1), 33–38.

Mitrovic, A. and Lee, T. W. 1998, Soot formation characteristics of laminar partially premixed flames, *Combustion and Flame* **115**(3), 437–442.

Modest, M. F. 1993, *Radiative Heat Transfer*, McGraw-Hill Series in Mechanical Engineering, McGraw-Hill, New York.

Mohamad, A., Ramadhyani, S. and Viskanta, R. 1994, Modeling of combustion and heat transfer in a packed bed with embedded coolant tubes, *International Journal of Heat and Mass Transfer* **37**(8), 1181-1191.

Muller, C. A., Maciejewski, M., Koeppel, R. A. and Baiker, A. 1999, Combustion of methane over palladium/zirconia: effect of Pd-particle size and role of lattice oxygen, *Catalysis Today* **47**(1-4), 245–252.

Mullisen, R. S. and Loehrke, R. I. 1986, A transient heat exchanger evaluation test for arbitrary fluid inlet temperature variation and longitudinal heat conduction, *Journal of Heat Transfer, Transactions of the ASME* **108**, 370–376.

Neuber, A., Krieger, G., Tacke, M., Hassel, E. and Janicka, J. 1998. Finite rate chemistry and NO molefraction in non-premixed turbulent flames, *Combustion and Flame* **113**(1-2), 198-211.

Nguyen, Q. V., Dibble, R. W., Carter, C. D., Fiechtner, G. J. and Barlow, R. S. 1996, Raman-LIF measurements of temperature, major species, OH, and NO in a methane-air Bunsen flame, *Combustion and Flame* **105**(4), 499-510.

Nishioka, M., Kondoh, Y. and Takeno, T. 1996, Behavior of key reactions on NO formation in methane-air flames, *Twenty-Sixth International Symposium on Combustion*, The Combustion Institute, Pittsburgh, PA, pp. 2139-2145.

Nishioka, M., Nakagawa, S., Ishikawa, Y. and Takeno, T. 1994, NO emission characteristics of methane air double flame, *Combustion and Flame* **98**(1-2), 127-138.

Peters, N. 1976, Analysis of a laminar flat plate boundary-layer diffusion flame, *International Journal of Heat and Mass Transfer* **19**, 385.

Peters, N. 1979, Premixed burning in diffusion flames - the flame zone model of Libby and Economos, *International Journal of Heat and Mass Transfer* **22**, 691-703.

Peters, N. 1984, Partially premixed diffusion flamelets in non-premixed turbulent combustion, *Twentieth International Symposium on Combustion*, The Combustion Institute, Pittsburgh, PA, pp. 353-360.

Pitts, W. M. 1996, Thin-filament pyrometry in flickering laminar diffusion flames, *Twenty-Sixth International Symposium on Combustion*, Vol. 1, The Combustion Institute, Pittsburgh, PA, pp. 1171-1179.

Pitts, W. M., Smyth, K. C. and Everest, D. A. 1998, Effects of finite time response and soot deposition on thin filament pyrometry measurements in time-varying diffusion flames, *Twenty-Seventh International Symposium on Combustion*, The Combustion Institute, Pittsburgh, PA, pp. 563-569.

Plesniak, M. 1999, Purdue University, West Lafayette, IN, *personal communication*.

Prasad, B., Tawkek, A. A. and Mohanty, A. K. 1991, Heat transfer from a circular cylinder rotating about an orthogonal axis in quiescent air. *Experiments in Fluids* **10**(5), 267-272.

Prasad, R. O. S., Paul, R. N., Sivathanu, Y. R. and Gore, J. P. 1999, Evaluation of combined flame surface density and mixture fraction models for nonisenthalpic premixed turbulent flames, *Combustion and Flame* **117**(3), 514-528.

Proceedings of the Ninth International Symposium on Combustion, Ithaca, NY 1963, Academic Press.

Proceedings of the Twenty-Third International Symposium on Combustion, Orleans, France 1991, The Combustion Institute, Pittsburgh, PA.

Pucci, P. F., Howard, C. P. and (Jr.), C. H. P. 1967, The single-blow transient testing technique for compact heat exchanger surfaces, *Journal of Engineering for Power, Transactions of the ASME* **89**(1), 29-40.

Radcliffe, S. W. and Hickman, R. G. 1975, Diffusive Catalitic Combustors, *Journal of the Institute of Fuel* **208**, 48-54.

Ramakrishna, C., Zhan, N. J., Kelkar, A. S. and Gore, J. P. 1996. A study of structure of partially premixed laminar coflow jet flames, *Proceedings of the 1996 Technical Meeting*, Central States Section of the Combustion Institute. pp. 442–447. St. Louis, MO, May 5 - 7.

Rawson, H. 1993, Radiative heat transfer in glass manufacture: one-dimensional and 2-dimensional problems, *Glastechnische Berichte (Glass Science and Technology)* **66**(4), 77–84.

Redenius, J. 1999, University of Minessota, Minneapolis, MN, *personal communication.*

Robertson, J. M. and Fraser, H. E. 1960, Separation prediction for conical diffusers, *Journal of Basic Engineering, Transactions of the ASME* **82**(3), 201–209.

Rudham, R. and Sanders, M. K. 1972, The catalytic properties of zeolite X containing transition metal ions, Part 2–Methane oxidation, *Journal of Catalysis* **27**, 287–292.

Ruff, R. J. 1964, Catalytic radiant heat treating apparatus, *United States Patent Office.* Patent number 3,147,960; 9 claims.

Rumminger, M. D. 1996, *Numerical and Experimental Investigation of Heat Transfer and Pollutant Formation in Porous Direct-Fired Radiant Burners*, PhD thesis, Department of Mechanical Engineering, University of California, Berkeley.

Rumminger, M. D., Hamlin, R. D. and Dibble, R. W. 1999, Numerical analysis of a catalytic radiant burner: effect of catalyst on radiant efficiency and operability, *Catalysis Today* **47**(1–4), 253–262.

Ryu, C. K., Ryoo, M. W., Ryu, I. S. and Kang, S. K. 1999, Catalytic combustion of methane over supported bimetallic Pd catalysts: effects of Ru or Rh addition, *Catalysis Today* **47**(1–4), 141–147.

Sadamori, H. 1999, Application concepts and evaluation of small scale catalytic combustors for natural gas, *Catalysis Today* **47**(1–4), 325–338.

Samaddar, S. N. 1970, Scattering of plane electromagnetic waves by radially inhomogeneous infinite cylinders, *Nuovo Cimento della Societa Italiana de Fisica B* **66**(1), 33–50.

Sathe, S. B., Peck, R. E. and Tong, T. W. 1990a, A numerical analysis of heat transfer and combustion in porous radiant burners, *International Journal of Heat and Mass Transfer* **33**(6), 1331–1338.

Sathe, S. B., Peck, R. E. and Tong, T. W. 1990b, Flame stabilization and multimode heat transfer in inert porous media: a numerical study, *Combustion Science and Technology* **70**, 93–109.

Seiyama, T. 1992, *Properties and applications of perovskite-type oxides*, Vol. 50 of *Chemical Industries Series (L. G. Tejuca and J. L. G. Fierro, editors)*, Marcel Dekker, New York.

Seo, Y.-S., Kang, S.-K., Han, M.-H. and Baek, Y.-S. 1999, Development of a catalytic burner with Pd/NiO catalysts, *Catalysis Today* **47**(1–4), 421–427.

Seshadri, K., Puri, I. and Peters, N. 1985, Experimental and theoretical investigationof partially-premixed diffusion flames at extinction, *Combustion and Flame* **61**, 237–249.

Siegel, R. and Howell, J. R. 1992, *Thermal Radiation Heat Transfer*, 3rd. edn. Hemisphere Publishing Corporation, Washington, D. C.

Singh, P. 1999, Purdue University, West Lafayette, IN, *personal communication.*

Singh, S., Ziolkowswski, M., Sultzbaugh, J. and Viskanta, R. 1991, Mathematical model of a ceramic burner radiant heater, *Fossil Fuel Combustion* **33**, 111–116.

Soufiani, A. and Taine, J. 1997, High temperature gas radiative property parameters of statistical narrow-band model for H_2O, CO_2 and CO, and correlated-K model for H_2O and CO_2, *International Journal of Heat and Mass Transfer* **40**(4), 987–991.

Speyer, R. F., Lin, W.-Y. and Agarwal, G. 1996, Radiant efficiencies and performance considerations of commercially manufactured gas radiant burners, *Experimental Heat Transfer* **9**(3), 213–245.

Sun, K. 1997, *Numerical Modeling of Premixed and Partially-Premixed Flames.* Master's thesis, School of Mechanical Engineering, Purdue University, West Lafayette, IN.

Takeno, T. and Moriyama, M. 1986, One-dimensional flame with extended reaction zone, *in* J. R. Bowen, J. C. Leyer and R. I. Soloukhin (eds), *Dynamics of reactive systems*, Vol. 105 of *Progress in Astronautics and Aeronautics*, American Institute of Aeronautics and Astronautics, pp. 246–262.

Takeno, T. and Sato, K. 1979, Excess enthalpy flame theory, *Combustion Science and Technology* **20**, 73–84.

Tanoff, M. A., Smooke, M. D., Osborne, R. J., Brown, T. M. and Pitz, R. W. 1996, Sensitive structure of partially premixed methane-air vs. air counterflow flames, *International Symposium on Combustion*, Vol. 1, The Combustion Institute, Pittsburgh, PA, pp. 1121-1128.

Tong, T. W. and Li, W. 1995, Enhancement of thermal emission from porous radiant burners, *Journal of Quantitative Spectroscopy and Radiative Heat Transfer* **53**, 235–248.

Tong, T. W. and Sathe, S. B. 1991, Heat transfer characteristics of porous radiant burners, *Journal of Heat Transfer, Transactions of the ASME* **113**(2), 423–428.

Tong, T. W. and Tien, C. L. 1980, Analytical models for thermal radiation in fibrous insulations, *Journal of Thermal Insulation* **4**, 27–44.

Tong, T. W. and Tien, C. L. 1983, Radiative heat transfer in fibrous insulations–Part I: Analytical study, *Journal of Heat Transfer, Transactions of the ASME* **105**, 70–85.

Tong, T. W., Yang, Q. S. and Tien, C. L. 1983, Radiative heat transfer in fibrous insulations–Part II: Experimental study, *Journal of Heat Transfer, Transactions of the ASME* **105**, 76–81.

Trimm, D. L. and Lam, C.-W. 1980a, The combustion of methane on platinum-alumina fibre catalysis-I. Kinetics and mechanism. *Chemical Engineering Science* **35**, 1405–1413.

Trimm, D. L. and Lam, C.-W. 1980b, The combustion of methane on platinum-alumina fibre catalysis-II. Design and testing of a convective-diffusive type catalytic combustor, *Chemical Engineering Science* **35**, 1731–1739.

Truelove, J. S. 1987, Discrete-ordinate solutions of the radiation transport equation, *Journal of Heat Transfer, Transactions of the ASME* **109**(4), 1048–1051.

Turns, S. E. 1996, *An Introduction to Combustion*, McGraw-Hill Series in Mechanical Engineering, McGraw-Hill, New York.

van Giezen, J. C., van den Berg, F. R., Kleinin, J. L., van Dillen, A. J. and Geus, J. W. 1999, The effect of water on the activity of supported palladium catalysts in the catalytic combustion of methane, *Catalysis Today* **47**(1–4), 287–293.

Vanoostendorp, D. L., Borghols, W. T. A. and Levinsky, H. B. 1991, The influence of ambient air entrainment on partially premixed burner flames – LIF imaging of CO and OH, *Combustion Science and Technology* **79**(4–6), 195–206.

Veser, G., Ziaudin, M. and Schmidt, L. D. 1999, Ignition in alkane oxidation on noble-metal catalysts, *Catalysis Today* **47**(1–4), 219–228.

Vilimpoc, V. and Goss, L. P. 1988, , *Twenty-Second International Symposium on Combustion*, The Combustion Institute, Pittsburgh, PA, pp. 1907–1914.

Viskanta, R. 1995, Interaction of combustion and heat transfer in porous inert media, *Transport Phenomena in Combustion: Proceedings of the Eighth International Symposium on Transport Phenomena in Combustion (ISTP-8)*, Vol. 1, Pacific Center of Thermal-Fluids Engineering, Hawaii, pp. 64–87. San Francisco, CA, July 16 - 20.

Viskanta, R. 1998, Overview of convection and radiation in high temperature gas flows, *International Journal of Engineering Science* **130**(12–14), 1677–1699.

Viskanta, R. and Mengüç, M. P. 1987, Radiation heat transfer in combustion systems, *Progress in Energy and Combustion Science* **13**, 97–160.

Viskanta, R. and Mengüç, M. P. 1989, Radiative transfer in dispersed media, *Applied Mechanics Reviews* **42**(9), 241–259.

Vortmeyer, D. 1975, Axial heat dispersion in packed beds, *Chemical Engineering Science* **30**, 999–1001.

Vortmeyer, D. and Schaefer 1974, Equivalence of one- and two-phase models for heat transfer processes in packed beds: one dimensional theory, *Chemical Engineering Science* **29**, 485–491.

Wang, K. Y., Kumar, S. and Tien, C. L. 1987, Radiative transfer in thermal insulations of hollow and coated fibers, *Journal of Thermophysics and Heat Transfer* **1**(4), 289–295.

Weinberg, F. J. 1971, Combustion temperatures: the future?, *Nature* **233**, 239–241.

Weinberg, F. J. 1975, The first half-million years of combustion research and today's burning problems, *Fifteenth International Symposium on Combustion*, The Combustion Institute, Pittsburgh, PA, pp. 1–17.

Westbrook, C. and Dryer, F. 1981, Simplified reaction mechanisms for the oxidation of hydrocarbon fuels in flames, *Combustion Science and Technology* **27**, 31–43.

Westbrook, C. K. and Dryer, F. L. 1984, Chemical kinetic modeling of hydrocarbon combustion, *Progress in Energy and Combustion Science* **10**(1), 1–57.

Widjaja, H., Sekizawa, K., Eguchi, K. and Arai, H. 1999, Oxidation of methane over Pd/mixed oxides for catalytic combustion, *Catalysis Today* **47**(1-4), 95–101.

Yamaoka, I. and Tsuji, H. 1975, The structure of rich fuel-air flames in the forward stagnation point of a porous cylinder, *Fifteenth International Symposium on Combustion*, The Combustion Institute, Pittsburgh, PA, pp. 637–644.

Yamaoka, I. and Tsuji, H. 1976, Structure analysis of rich fuel-air flames in the forward stagnation point of a porous cylinder, *Sixteenth International Symposium on Combustion*, The Combustion Institute, Pittsburgh, PA, pp. 1145–1154.

Yamaoka, I. and Tsuji, H. 1977, An experimental study of flammability limits using counterflow flames, *Seventeenth International Symposium on Combustion*, The Combustion Institute, Pittsburgh, PA, pp. 843–855.

Yoshizawa, Y., Sasaki, K. and Echigo, R. 1988, Analytical study of the structure of radiation controlled flame, *International Journal of Heat and Mass Transfer* **31**(2), 311–319.

Younis, L. 1991, *Experimental of the Volumetric Heat Transfer Coefficient Between a Stream of Air and a Ceramic Foam*, Master's thesis, School of Mechanical Engineering, Purdue University, West Lafayette, IN.

Zhan, J. 1994, *An Investigation of Partially Premixed Flames in a Coflow Jet Configuration*, Master's thesis, School of Mechanical Engineering, Purdue University, West Lafayette, IN.

Zhou, X. 1999, *An Experimental and Theoretical Investigation of the Flows Induced by Buoyant Diffusion Flames*, PhD thesis, School of Mechanical Engineering, Purdue University, West Lafayette, IN.

Zhou, X. Y. and Pereira, J. C. F. 1997, Numerical study of combustion and pollutants formation in inert nonhomogeneous porous media, *Combustion Science and Technology* **130**(1-6), 335–364.

Žukauskas A. 1972, *Heat transfer from tubes in crossflow*, Vol. 8 of *Advances in Heat Transfer*, Academic Press, New York, pp. 93–160.

Zwinkels, M. F. M., Haussner, O., Menon, P. G. and Järas, S. G. 1999, Preparation and characterization of $LaCrO_3$ and Cr_2O_3 methane combustion catalysts supported on $LaAl_{11}O_{18}$ and Al_2O_3-coated monoliths, *Catalysis Today* **47**(1), 73–82.

APPENDICES

Appendix A: Experimental Uncertainty Estimation

The radiation efficiency was defined in Equation (2.2) in terms of the radiant flux (RF) and the firing rate (FR), as follows:

$$\eta_{rad} = \frac{RF}{FR} .$$

According to the usual formulation for error propagation (Holman, 1971), the experimental uncertainty can be estimated as:

$$\Delta\eta_{rad} = \sqrt{\left(\frac{\partial\eta_{rad}}{\partial FR}\right)^2 (\Delta FR)^2 + \left(\frac{\partial\eta_{rad}}{\partial RF}\right)^2 (\Delta RF)^2} . \qquad \text{(A.1)}$$

The firing rate uncertainty, ΔFR, is directly proportional to the methane flow rate uncertainty, which has been estimated to be less than 10% of the minimum flow rate used (or, equivalently, 5% of the maximum firing rate, i.e., 17.4 $\frac{kW}{m^2}$). The radiant flux uncertainty, ΔRF, has several error sources, mainly the radiation detector accuracy and the alignment between the detector and the burner[1]. The latter was deemed negligible for the present experimental arrangement, since the detector separation distance and position were carefully determined. The Gardon-type heat transfer gauge accuracy was 3% (Table 2.4).

Substituting the definition of the radiation efficiency into Equation (A.1) yields:

$$\Delta\eta_{rad} = \sqrt{\left(-\frac{RF}{FR^2}\right)^2 (\Delta FR)^2 + \left(\frac{1}{FR}\right)^2 (\Delta RF)^2} , \qquad \text{(A.2)}$$

or, after simplification,

$$\Delta\eta_{rad} = \sqrt{\frac{(RF\,\Delta FR)^2}{(FR)^4} + \frac{(\Delta RF)^2}{FR^2}} . \qquad \text{(A.3)}$$

The estimated experimental uncertainties for the single-layer Fecralloy burner using a stoichiometric ($\Phi = 1.0$) fuel mixture (see Figure 4.9) are shown in Table A.1. In all cases, the uncertainty is below 2%.

---

[1] The detector position determines the view factor.

Table A.1. Error propagation for radiation efficiency for different firing rates.

$FR\ [\frac{kW}{m^2}]$	$\Delta FR\ [\frac{kW}{m^2}]$	$RF\ [\frac{kW}{m^2}]$	$\Delta RF\ [\frac{kW}{m^2}]$	η_{rad} %	$\Delta\eta_{rad}$ %
174	17.4	33.2	1.0	19.1	2.0
196	17.4	41.2	1.2	21.0	2.0
223	17.4	49.3	1.5	22.1	1.8
255	17.4	54.8	1.6	21.5	1.6
281	17.4	60.1	1.8	21.4	1.5
309	17.4	66.4	2.0	21.5	1.4
340	17.4	73.8	2.2	21.7	1.3

Appendix B: Volumetric Heat Transfer Coefficient of Fiber Mats

B.1. Introduction

In recent years an increasing number of applications have involved heat transfer in porous media. However, theoretical predictions of the value of the volumetric heat transfer coefficient, h_v, cannot presently overcome the difficulty imposed by the complex irregular geometry of fiber mats. This coefficient is an important parameter required in modeling, since it determines the thermal coupling between the flowing fluid and the solid matrix. Therefore, several semi-empirical methods have been used to obtain the value of h_v for materials under several different conditions.

Volumetric heat transfer coefficient of porous materials have been determined for sintered steel heated to about $750K$ by radiative flux incident on the outer surface of the specimens, and then the heating was terminated before forcing air through the porous matrix (Alifanov et al., 1987). Another technique that was employed consisted of inserting a heating device inside the porous medium until it reached a specified temperature; then the heater was discontinued and coolant was forced through the medium (Eliseev et al., 1983). But these techniques present problems when applied to fibrous materials, especially the second one because of the structural disturbance and the difficulty of heating the specimen uniformly.

A single-blow method (Heggs and Burns, 1988; Loehrke, 1990; Younis, 1991) is then selected here to determine h_v. Hot air is suddenly blown through the porous material, and the temperature history of air in front of the sample is measured. Since the outlet fluid temperature variation (the breakthrough curve) is a function of h_v, the solution of an inverse problem can be found. The problem becomes now to match this measured response with some mathematical description of the process.

B.2. Mathematical Description and Theory for Data Reduction

The mathematical description of the heat transfer from a hot gas to porous material can be formulated in terms of the individual energy balance equations for each phase (Pucci et al., 1967; Vortmeyer, 1975). The assumptions made in constructing the mathematical model are (Fu, 1997):

1. The material is homogeneous and the porosity is uniform.
2. The gas stream velocity is uniform, i.e., plug flow.
3. Heat conduction is one-dimensional for both phases.
4. Thermophysical properties are independent of temperature.
5. There is no heat generation or heat dissipation in the solid matrix.
6. Radiation within the solid is considered to be negligible in comparison to heat convection.
7. The gas and the solid are not in thermal equilibrium, which means that separate energy balance equations are needed.

The resulting conservation of energy equations for the gas and solid phases are as follows:

Energy for gas:

$$\rho_g c_{pg}\left(\frac{\partial T_g}{\partial t} + u\frac{\partial T_g}{\partial x}\right) = k_g\frac{\partial^2 T_g}{\partial x^2} + h_v(T_s - T_g)\ . \tag{B.1}$$

Energy for solid:

$$(1-\phi)\rho_s c_{ps}\frac{\partial T_s}{\partial t} = k_s\frac{\partial^2 T_s}{\partial x^2} + h_v(T_g - T_s)\ . \tag{B.2}$$

where the volumetric heat transfer coefficient, h_v, constitutes the coupling between the two equations. The effective thermal conductivities, k_g and k_s, are approximated using a parallel model, i.e., multiplying by a factor ϕ for the gas phase, and a factor $(1-\phi)$ for the solid phase.

The boundary and initial conditions are:

$$(1-\phi)h_0(T_s - T_g) = \rho_g c_{pg} u(T_g - T_{g,in}) \quad \text{at} \quad x = 0 \; . \tag{B.3}$$

$$\frac{dT_g}{dx} = 0 \quad \text{at} \quad x = L \; . \tag{B.4}$$

$$-k_s \frac{dT_s}{dx} = h_0(T_g - T_s) - \varepsilon_0(T_s^4 - T_{surr,in}^4) \quad \text{at} \quad x = 0 \; . \tag{B.5}$$

$$-k_s \frac{dT_s}{dx} = h_L(T_s - T_{g,out}) - \varepsilon_L(T_s^4 - T_{surr,out}^4) \quad \text{at} \quad x = L \; . \tag{B.6}$$

$$T_g = T_{g,in} \quad \text{at} \quad x = 0,\ t = 0 \; . \tag{B.7}$$

Ideally, the system of equations is solved for several values of h_v and the predicted gas temperature history is compared to the experimental data. The closest (in some sense) solution is assumed to give the "real" magnitude of the volumetric heat transfer coefficient. But experimental uncertainties and non-ideal conditions usually prevent researchers from using this simple approach.

Early studies were restricted to direct curve matching of experiment with theory. Furnas (1930) first used this technique employing a graphical procedure. Later investigators, with the aid of computers, used this trial-and-error approach to minimize some functional relationship (i.e., an ad hoc definition of the error) between the experimental and theoretical curves. The most common choice of that functional relationship was the root-mean-square deviation, but Bradshaw et al. (1970) arbitrarily chose to minimize the following expression:

$$\sum_{i=1}^{i=N} \left[\ln \left(\frac{T_{theory,i}}{T_{experiment,i}} \right) \right]^2 ,$$

where T_{theory} and $T_{experiment}$ are the predicted and measured fluid outlet temperatures, respectively, i represents each data point, and N is the total number of intervals on the experimental breakthrough curve.

Liang and Yang (1975) suggested matching at five selected equally spaced points on the breakthrough curve. An average value of the heat transfer coefficient is obtained at each point, and the arithmetic average is used to represent the complete curve. Cai et al. (1984) proposed an improvement to this method that involved optimizing the points selected. Mullisen and Loehrke (1986) recommend matching points on the breakthrough curve and minimizing the area between them. These last three groups of workers allowed for non-ideal step inputs to the experimental test section, whereas previous investigators assumed ideal step inputs into the system.

The accommodation of the experimental form of the inlet forcing function in the data reduction scheme is extremely important (Heggs and Burns, 1988). It is physically impossible to produce an ideal step in the fluid temperature at the entrance of the test section, and Baclic et al. (1986) have shown that the error in the data analysis is dependent on the time constant of the inlet forcing function, varying between 2% and 40% over the range of time constants used by previous researchers.

A different approach is based in determining a unique relationship between the breakthrough curve and so-called the number of transfer units ($NTU = \frac{h_v L}{\dot{m} c_{pg}}$). Locke (1950) pioneered the use of the unique maximum slope criterion. This method is unsuitable for use in systems in which NTU is less than 3 (Kohlmayr, 1966; Pucci et al., 1967). The method has been extended for the case of non-ideal step inputs (Kohlmayr, 1968a), but again the range of NTU values is restricted.

To allow experimentation in the low NTU range, Kohlmayr (1968b) proposed another indirect matching technique. This involved the evaluation of the centroid of the area between the inlet and outlet fluid temperatures, but there is no evidence that it has been used to analyze experimental data (Heggs and Burns, 1988).

Although all techniques would ideally produce the same result for the coefficient h_v, the experimental uncertainties particular to each set-up and the range of the dimensionless group NTU usually render one of them more suitable than others.

B.3. Measurements and Data Reduction

The same technique and the same apparatus used by Younis (1991) was employed here to obtain the volumetric heat transfer coefficient data. Younis designed a low-speed wind tunnel and a test section that includes two samples (a dummy and the actual sample, of size 0.1×0.1 m^2), mounted on two slide rails. A variable-speed air blower and a heater are used to control the air flow conditions, as shown in Figure B.1.

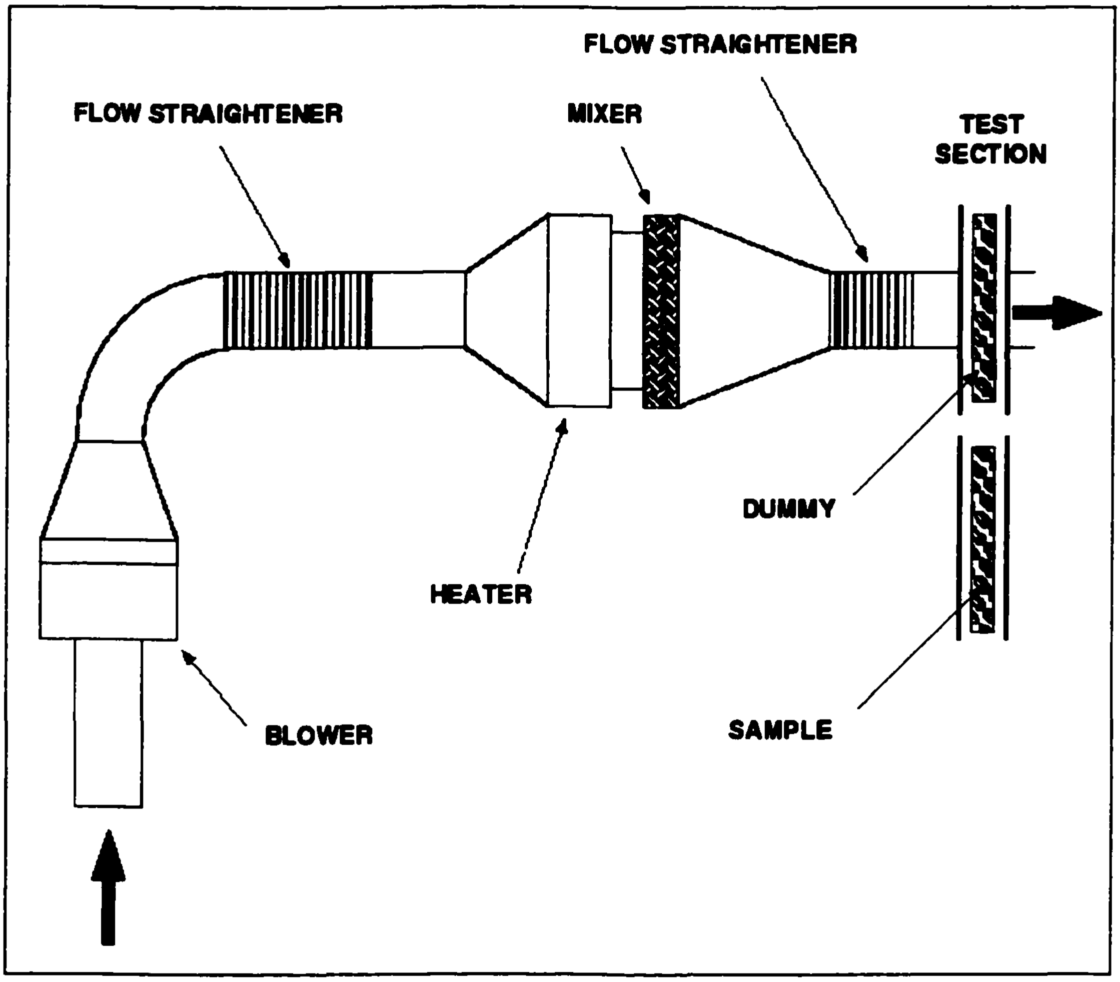

Figure B.1. Schematic of the single-blow apparatus used to measure the volumetric heat transfer coefficient of a porous sample.

The instrumentation consists of two T-type (Copper-Constantan) thermocouples (0.0762 *mm* in diameter) located before and after the dummy, and two microthermocouples (25 μm diameter, the thinnest available wire) before and after the sample. An optical sensor is used to synchronize the starting point for the temperature recording with the sliding of the sample. A Hewlett-Packard 3852A Data Acquisition/Control Unit system collects the temperature transient after the sample is inserted in the hot air stream, and the data are logged into a Hewlett-Packard 85 computer. Air velocity is measured with a hand-held hot wire anemometer probe (TSI[1] VELOCICALC Model 8350). More details regarding the experimental apparatus can be found elsewhere (Younis, 1991; Fu, 1997) and are not repeated here.

Some changes in the data acquisition system were implemented with respect to the methodology of Younis (1991). The sampling rate was increased to 16 Hz by measuring voltages instead of temperatures, and converting afterwards. A three-step sequence initiated when the sample was pushed into the wind tunnel:

1. Open the heater power relay to eliminate the 60 Hz electronic noise originating in the transformer.
2. Read the cold-junction compensation voltages into a vector.
3. Start a fast loop measuring the thermocouple voltages.

Once the thermocouple data were recorded, the vector with the cold-junction voltages was used cyclically to convert the readings into temperature. This new procedure had a longer overhead because some time was needed to open the power relay and measure the cold-junction voltages, which resulted in the first two points being separated by about 0.7 s. However, most of this time corresponded to the sliding time of the test specimen into the duct, when the air flow was perturbed.

In this particular case, the temperature uncertainties resulting from the initial delay deemed inappropriate the direct matching technique, because a small misadjustment at the starting time yielded large root-mean-square errors, preventing the convergence of the numerical scheme for the data reduction. On the other hand, the breakthrough curves obtained in the experiments were smooth and easy to differen-

---

[1] TSI, Inc., Environmental Measurements and Controls, P. O. Box 64394, St. Paul, MN 55164

tiate accurately: for typical test conditions $NTU \approx 6$ (i.e., quite large). Therefore, a maximum slope method was chosen: the maximum slope of the experimental data was matched to the maximum derivative of the model for a given h_v; in this way, the errors induced by the initial time mismatch were minimized.

The numerical solution of the model equations (Equations (B.1) and (B.2)), with the boundary and initial conditions (Equations (B.3) to (B.7)) was implemented using a tri-diagonal matrix solver (TDMA). The code allowed the use of several convergence criteria:

1. Total error, i.e., minimum least-square deviation of the numerical solution from the temperature history.
2. A secant-method-based maximum first derivative, that stopped after a solution within a specified error tolerance was found.
3. An alternative secant-method-based minimum second derivative, which was similar to the previous one, but required very good experimental data suitable for double differentiation.
4. A so-called *infinite search* that computed all solutions in a given range of h_v and then selected the one which gave the closest match. This method was computationally very expensive, and it was used when the sensitivity of the least-square deviation with h_v was low.

Most of the results were obtained using the first derivative criterion. Additionally, the program had a feature that allowed to calculate the temperature transient for a given value of the volumetric heat transfer coefficient.

Figure B.2 shows the comparison between experimental and predicted temperature variation, together with the first derivatives. Note that the numerical predictions were shifted (compensating for the initial delay introduced by the acquisition system) so that the maximum slope location was correctly identified. The agreement is excellent, and the result for the volumetric heat transfer coefficient ($h_v = 715,000\ \frac{W}{m^3K}$ for inlet velocity of $1.44\ \frac{m}{s}$) is considered quite accurate.

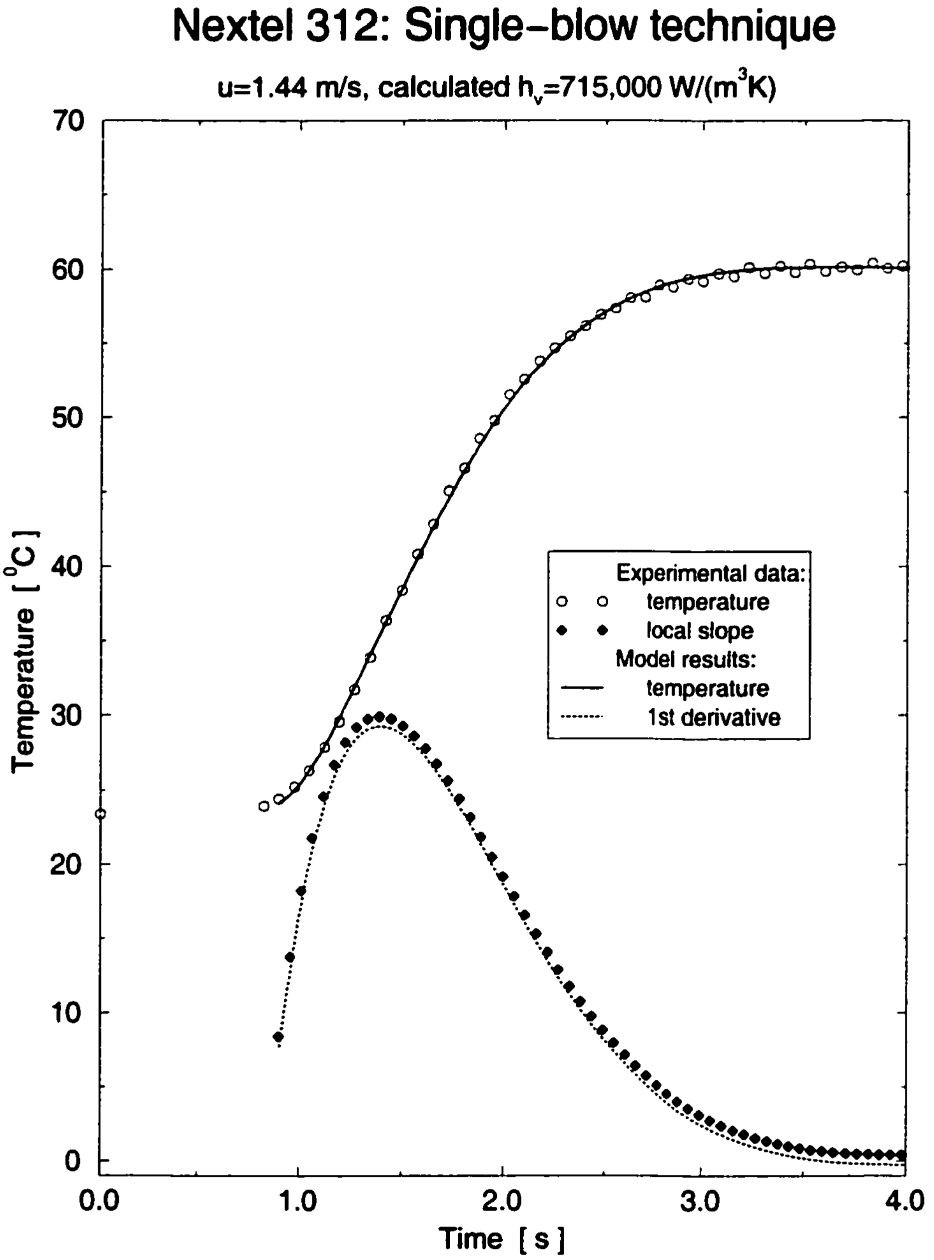

Figure B.2. Measured and predicted temperature transients for the single-blow technique. Numerical results are obtained for several values of h_v and the one that gives the best match is considered to be the correct value of that parameter.

B.4. Correlations

The volumetric heat transfer coefficient results for the Nextel 312 fiber mat (sample thickness of 10 *mm*) as a function of the inlet air stream velocity are presented in Figure B.3. The same data are shown in terms of non-dimensional parameters in Figure B.4. A smooth variation is observed in the center of the range, with more significant data scattering at low and high velocities.

The reduced data were correlated by the following equation,

$$Nu_v = 0.0043 Re^{1.13} \tag{B.8}$$

obtained using a least-squares fit.

The minimum Reynolds number attained corresponded to an air velocity of 0.17 $\frac{m}{s}$. The experimental uncertainties with lower air flows made impossible to obtain data at even lower air velocities. At the other end, the maximum Reynolds number corresponded to an air velocity of 2.13 $\frac{m}{s}$. In this range, the temperature transient of the single-blow technique became too short; the data acquisition system could not record useful data at a faster rate, therefore, preventing from increasing the air velocity. However, the measured range was broad enough to cover the velocities needed for the numerical modeling of a typical radiant burner.

B.5. Shortcomings for Some Materials

The methodology described in Section B.3 was successful in determining the volumetric heat transfer coefficient for Nextel 312. However, satisfactory results would not be obtained for the case of Fecralloy NIT100S and NIT200S.

These Fecralloy-based materials are more dense than Nextel and have a larger heat capacity, but the samples are too thin (about 2 *mm*) and the resulting single-blow transients are too rapid, and the data are difficult to reduce. Furthermore, due to their woven nature, the Fecralloy mats are inherently non-homogeneous, presenting an arrangement of holes (of several characteristic sizes) given by the spacing in between the strands of the fibers.

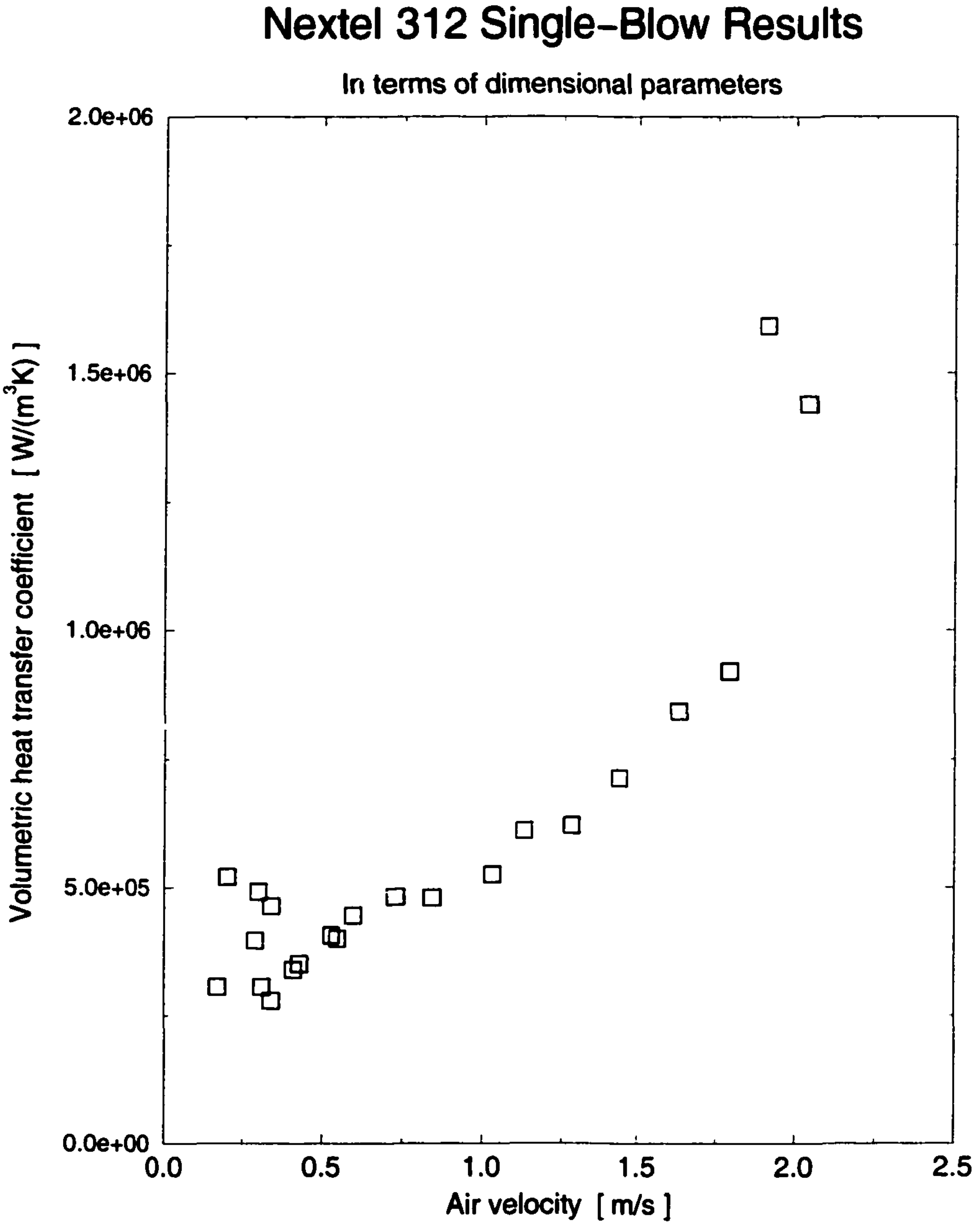

Figure B.3. Volumetric heat transfer coefficient of a Nextel 312 fiber mat. The thickness of the sample was 10 *mm*.

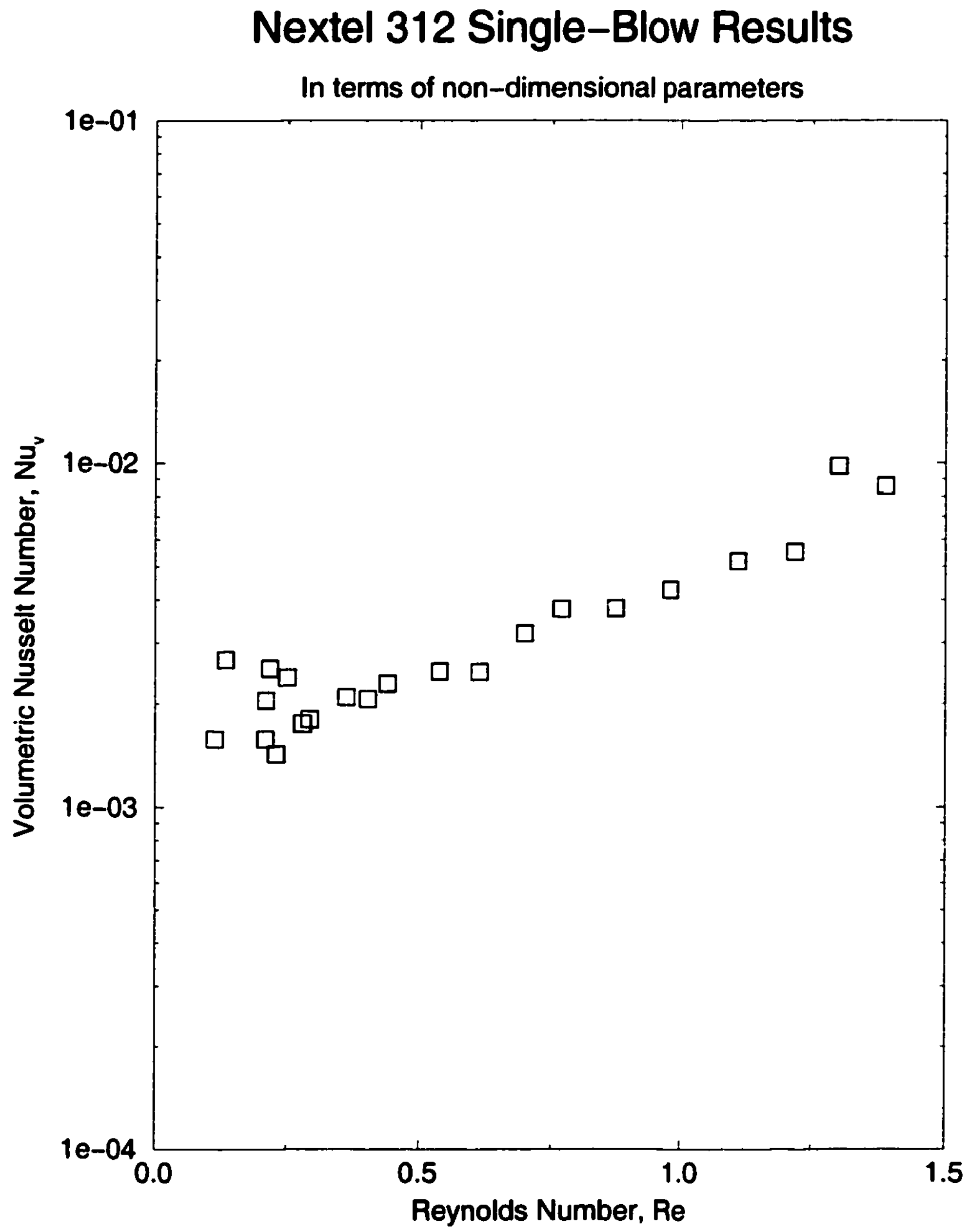

Figure B.4. Volumetric heat transfer coefficient of a Nextel 312 fiber mat in terms on non-dimensional parameters. The thickness of the sample was 10 *mm*.

Some useful data were obtained after placing together several layers of Fecralloy and repeating the single-blow experiments. By doing this, the resulting sample was "homogenized", since the large pores of each layer were not aligned. However, it was unclear if the results obtained would be applicable at all for the case of a single layer. In any case, the temperature transients measured with the single-blow technique for Fecralloy were different from those observed for a Nextel sample. There was no curvature change, rendering the maximum slope criterion as inapplicable.

Appendix C: Specific Heat Determination

C.1. Nextel 312 Specific Heat Results

A sample of Nextel 312 was submitted to the Thermophysical Properties Research Laboratory[1] for specific heat determinations. The Nextel sample was chopped into small pieces and encapsulated in an aluminum pan. Specific heat was measured using a standard Perkin-Elmer (Model DSC-2) differential scanning calorimeter with sapphire as the reference material. The standard and the sample were subjected to an identical heat flux as a blank. Then, the differential powers required to heat at the same rate both the specimens were determined using a digital acquisition system. Using the masses of the sapphire standard and the sample, the measured differential powers, and the known specific heat of sapphire, the specific heat of the Nextel 312 sample was computed. Two runs were made, and the results were within a 1% band (Figure C.1.) The lower values obtained for the second run were attributed to the moisture loss during the first run (Report TPRL 1932, October 1997.)

All measured quantities were directly traceable to NIST[2] standards. The procedures outlined in ASTM E1269 were followed.

C.2. Fecralloy Specific Heat Results

Three Fecralloy samples were submitted to the Thermophysical Properties Research Laboratory for specific heat determination (Figure C.2). The same methodology described in Section C.1 was followed (Report TPRL 1972, December 1997.)

---

[1] TPRL, Purdue University Research Park, 2595 Yeager Road, West Lafayette, IN 47906. Phone 765-463-1581.

[2] NIST: United States National Institute of Standards and Technology

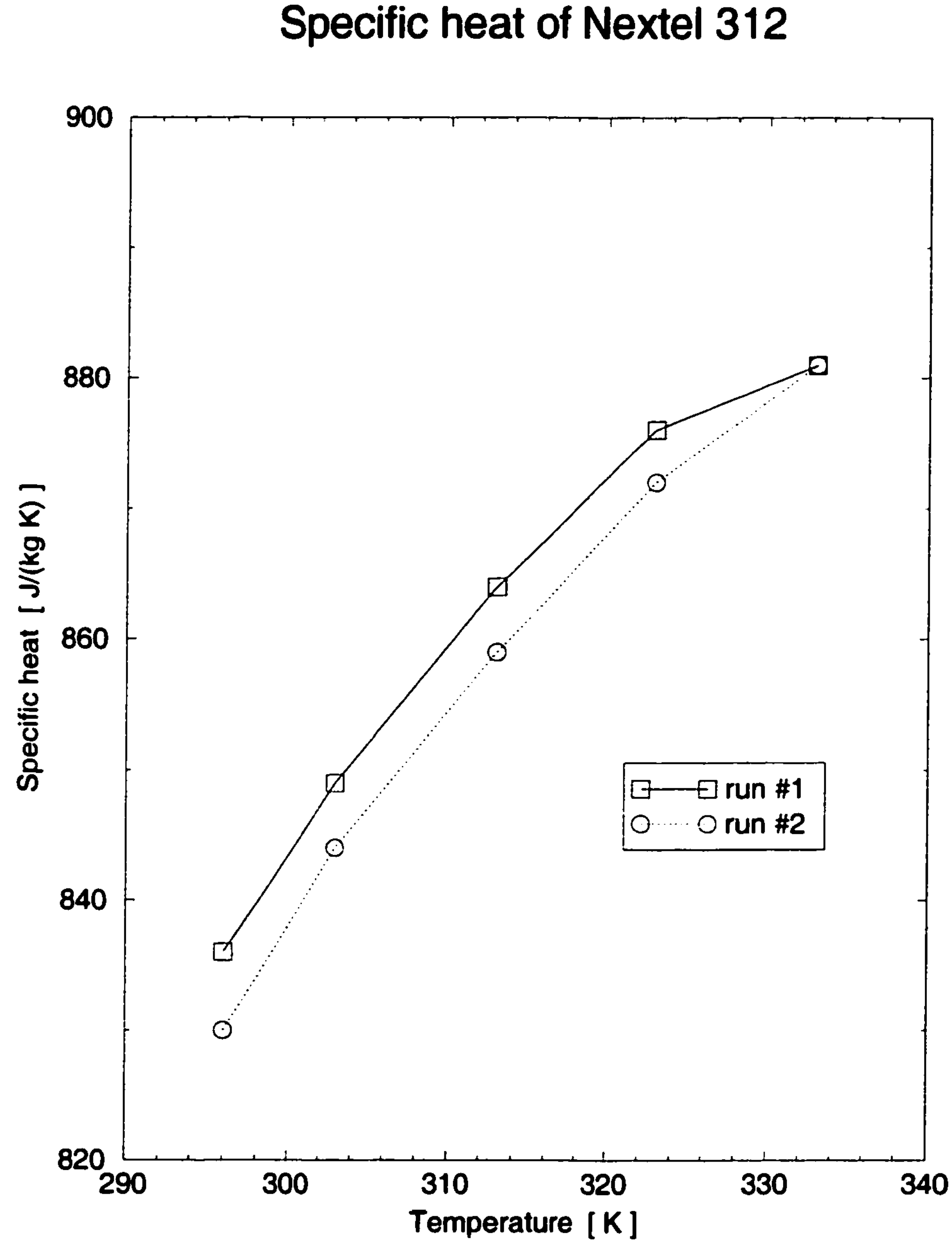

Figure C.1. Specific heat of Nextel 312 fiber mat (according to TPRL 1932, October 1997).

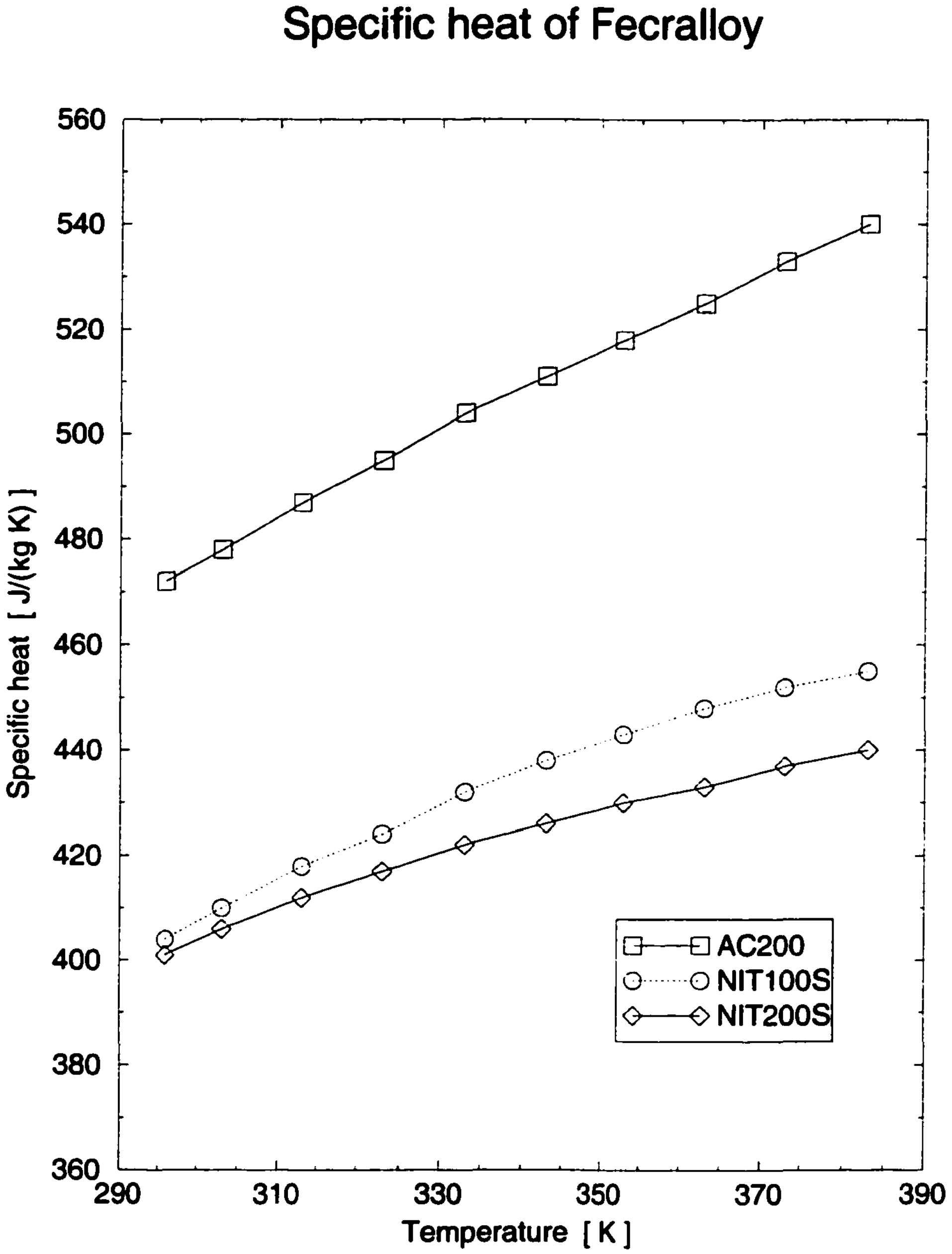

Figure C.2. Specific heat of Fecralloy AC200, NIT100S and NIT200S fiber mats (according to TPRL 1972, December 1997).

Appendix D: Radiation Thermometer Calibrations

The handheld radiation thermometers used to obtain the solid matrix surface temperature (Raytek Raynger ST8, in the range 0–540°C; Irtec Ultimax UX-81, in the range 500–2800°C) were calibrated against a blackbody.

The ST8 shows excellent agreement with the blackbody; the UX-81 needs a small correction due to underprediction of the temperature. The experimental data are shown in Figure D.1.

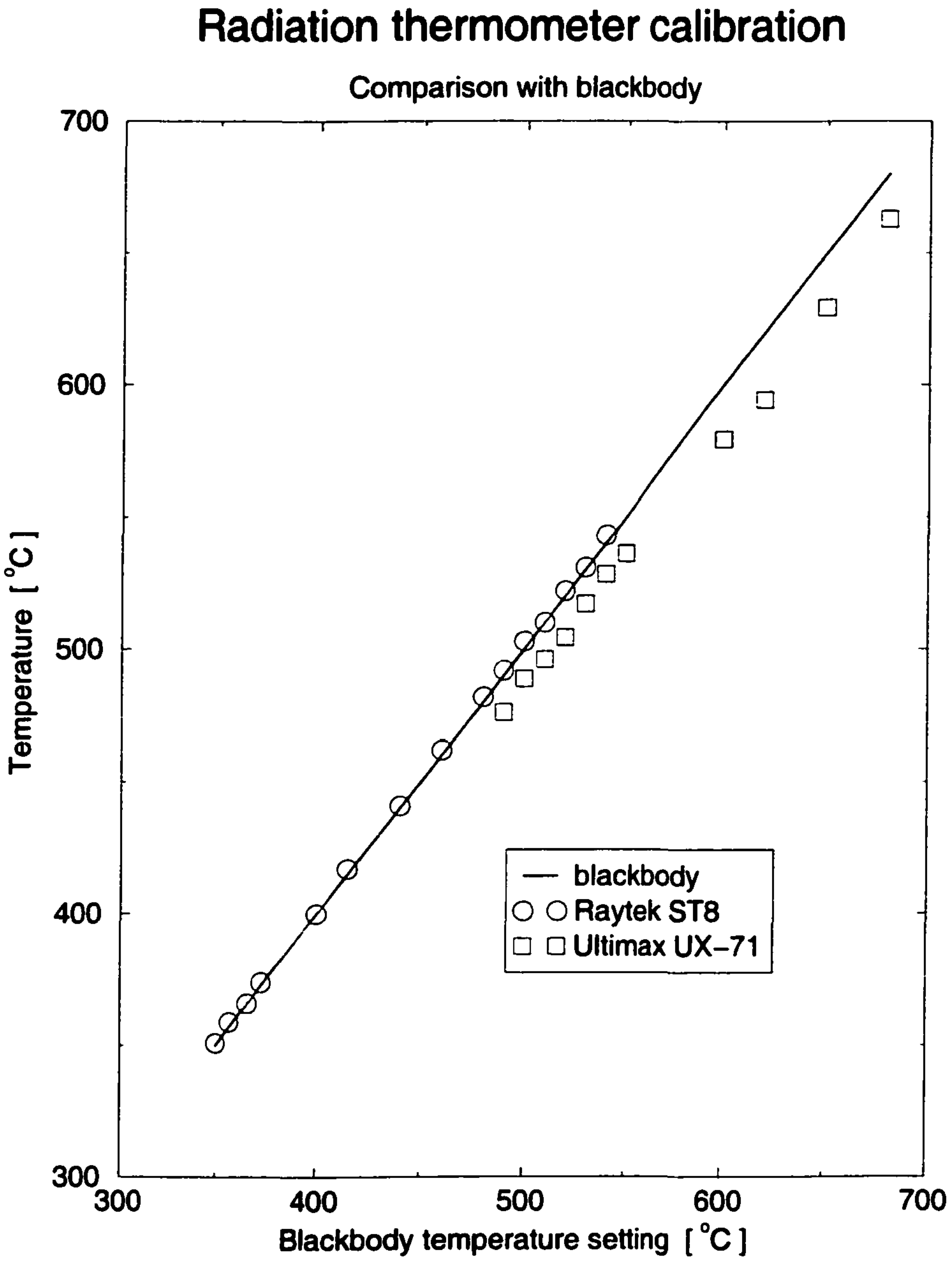

Figure D.1. Radiation thermometer calibration against a blackbody.

Appendix E: GRI-Mech 2.11 Chemical Mechanism for CH_4 Combustion

E.1. Involved Elements and Species

GRI-Mech 2.11 is a chemical mechanism that consists in 277 reactions involving 49 species formed as the combination of five elements (O, H, C, N, Ar). The species are: H_2, H, O, O_2, OH, H_2O, HO_2, H_2O_2, C, CH, CH_2, $CH_2(S)$, CH_3, CH_4, CO, CO_2, HCO, CH_2O, CH_2OH, CH_3O, CH_3OH, C_2H, C_2H_2, C_2H_3, C_2H_4, C_2H_5, C_2H_6, HCCO, CH_2CO, HCCOH, N, NH, NH_2, NH_3, NNH, NO, NO_2, N_2O, HNO, CN, HCN, H_2CN, HCNN, HCNO, HOCN, HNCO, NCO, N_2, and Ar.

E.2. Chemical Reactions

The chemical kinetics is simulated assuming that each reaction proceeded according to the law of mass action and that the forward rate coefficients, k_f, were in the modified Arrhenius form:

$$k_f = a_1 T^{a_2} \exp\left(-\frac{\mathcal{E}}{\mathcal{R}T}\right) . \tag{E.1}$$

The reaction rates are computed from the reaction data presented below; the units of a_1 are given in the system *mol-cm-s-K* (i.e., $[\frac{cm^3}{mol\ s\ K}]$ for a bimolecular reaction, and $[\frac{cm^6}{mol^2\ s\ K}]$ for a termolecular recombination), a_2 is dimensionless, and $\mathcal{E}$ is in $[\frac{cal}{mol\ K}]$. Some reactions contain "M" as a reactant or product to specify third body efficiencies of certain species; "(+M)" (e.g., reactions 50, 52, 54, 56, 57...) indicates that those reactions are also pressure dependent. Keyword "LOW" is used to specify low-pressure limit Arrhenius parameters, and "TROE" is used to specify Troe fall-off reaction parameters. The theory underlying the use of these fall-off coefficients in the combustion chemistry, which are applicable near the pressure limits, is described by W.C. Gardiner and J. Troe in Chapter 4 of *Combustion Chemistry*, Springer-Verlag, New York, 1984.

```
  1. 2O+M<=>O2+M                                  1.20E+17   -1.0       0.0
       H2                 Enhanced by   2.400E+00
       H2O                Enhanced by   1.540E+01
       CH4                Enhanced by   2.000E+00
       CO                 Enhanced by   1.750E+00
       CO2                Enhanced by   3.600E+00
       C2H6               Enhanced by   3.000E+00
       AR                 Enhanced by   8.300E-01
  2. O+H+M<=>OH+M                                 5.00E+17   -1.0       0.0
       H2                 Enhanced by   2.000E+00
       H2O                Enhanced by   6.000E+00
       CH4                Enhanced by   2.000E+00
       CO                 Enhanced by   1.500E+00
       CO2                Enhanced by   2.000E+00
       C2H6               Enhanced by   3.000E+00
       AR                 Enhanced by   7.000E-01
  3. O+H2<=>H+OH                                  5.00E+04    2.7    6290.0
  4. O+HO2<=>OH+O2                                2.00E+13    0.0       0.0
  5. O+H2O2<=>OH+HO2                              9.63E+06    2.0    4000.0
  6. O+CH<=>H+CO                                  5.70E+13    0.0       0.0
  7. O+CH2<=>H+HCO                                8.00E+13    0.0       0.0
  8. O+CH2(S)<=>H2+CO                             1.50E+13    0.0       0.0
  9. O+CH2(S)<=>H+HCO                             1.50E+13    0.0       0.0
 10. O+CH3<=>H+CH2O                               8.43E+13    0.0       0.0
 11. O+CH4<=>OH+CH3                               1.02E+09    1.5    8600.0
 12. O+CO+M<=>CO2+M                               6.02E+14    0.0    3000.0
       H2                 Enhanced by   2.000E+00
       O2                 Enhanced by   6.000E+00
       H2O                Enhanced by   6.000E+00
       CH4                Enhanced by   2.000E+00
       CO                 Enhanced by   1.500E+00
       CO2                Enhanced by   3.500E+00
       C2H6               Enhanced by   3.000E+00
       AR                 Enhanced by   5.000E-01
 13. O+HCO<=>OH+CO                                3.00E+13    0.0       0.0
 14. O+HCO<=>H+CO2                                3.00E+13    0.0       0.0
 15. O+CH2O<=>OH+HCO                              3.90E+13    0.0    3540.0
 16. O+CH2OH<=>OH+CH2O                            1.00E+13    0.0       0.0
 17. O+CH3O<=>OH+CH2O                             1.00E+13    0.0       0.0
 18. O+CH3OH<=>OH+CH2OH                           3.88E+05    2.5    3100.0
 19. O+CH3OH<=>OH+CH3O                            1.30E+05    2.5    5000.0
 20. O+C2H<=>CH+CO                                5.00E+13    0.0       0.0
 21. O+C2H2<=>H+HCCO                              1.02E+07    2.0    1900.0
 22. O+C2H2<=>OH+C2H                              4.60E+19   -1.4   28950.0
 23. O+C2H2<=>CO+CH2                              1.02E+07    2.0    1900.0
 24. O+C2H3<=>H+CH2CO                             3.00E+13    0.0       0.0
 25. O+C2H4<=>CH3+HCO                             1.92E+07    1.8     220.0
 26. O+C2H5<=>CH3+CH2O                            1.32E+14    0.0       0.0
 27. O+C2H6<=>OH+C2H5                             8.98E+07    1.9    5690.0
 28. O+HCCO<=>H+2CO                               1.00E+14    0.0       0.0
 29. O+CH2CO<=>OH+HCCO                            1.00E+13    0.0    8000.0
 30. O+CH2CO<=>CH2+CO2                            1.75E+12    0.0    1350.0
 31. O2+CO<=>O+CO2                                2.50E+12    0.0   47800.0
 32. O2+CH2O<=>HO2+HCO                            1.00E+14    0.0   40000.0
 33. H+O2+M<=>HO2+M                               2.80E+18   -0.9       0.0
       O2                 Enhanced by   0.000E+00
       H2O                Enhanced by   0.000E+00
       CO                 Enhanced by   7.500E-01
       CO2                Enhanced by   1.500E+00
       C2H6               Enhanced by   1.500E+00
       N2                 Enhanced by   0.000E+00
       AR                 Enhanced by   0.000E+00
 34. H+2O2<=>HO2+O2                               3.00E+20   -1.7       0.0
 35. H+O2+H2O<=>HO2+H2O                           9.38E+18   -0.8       0.0
```

```
 36. H+O2+N2<=>HO2+N2                                     3.75E+20   -1.7        0.0
 37. H+O2+AR<=>HO2+AR                                     7.00E+17   -0.8        0.0
 38. H+O2<=>O+OH                                          8.30E+13    0.0    14413.0
 39. 2H+M<=>H2+M                                          1.00E+18   -1.0        0.0
        H2                 Enhanced by    0.000E+00
        H2O                Enhanced by    0.000E+00
        CH4                Enhanced by    2.000E+00
        CO2                Enhanced by    0.000E+00
        C2H6               Enhanced by    3.000E+00
        AR                 Enhanced by    6.300E-01
 40. 2H+H2<=>2H2                                          9.00E+16   -0.6        0.0
 41. 2H+H2O<=>H2+H2O                                      6.00E+19   -1.2        0.0
 42. 2H+CO2<=>H2+CO2                                      5.50E+20   -2.0        0.0
 43. H+OH+M<=>H2O+M                                       2.20E+22   -2.0        0.0
        H2                 Enhanced by    7.300E-01
        H2O                Enhanced by    3.650E+00
        CH4                Enhanced by    2.000E+00
        C2H6               Enhanced by    3.000E+00
        AR                 Enhanced by    3.800E-01
 44. H+HO2<=>O+H2O                                        3.97E+12    0.0      671.0
 45. H+HO2<=>O2+H2                                        2.80E+13    0.0     1068.0
 46. H+HO2<=>2OH                                          1.34E+14    0.0      635.0
 47. H+H2O2<=>HO2+H2                                      1.21E+07    2.0     5200.0
 48. H+H2O2<=>OH+H2O                                      1.00E+13    0.0     3600.0
 49. H+CH<=>C+H2                                          1.10E+14    0.0        0.0
 50. H+CH2(+M)<=>CH3(+M)                                  2.50E+16   -0.8        0.0
     Low pressure limit:  0.32000E+28 -0.31400E+01  0.12300E+04
     TROE centering:      0.68000E+00  0.78000E+02  0.19950E+04  0.55900E+04
        H2                 Enhanced by    2.000E+00
        H2O                Enhanced by    6.000E+00
        CH4                Enhanced by    2.000E+00
        CO                 Enhanced by    1.500E+00
        CO2                Enhanced by    2.000E+00
        C2H6               Enhanced by    3.000E+00
        AR                 Enhanced by    7.000E-01
 51. H+CH2(S)<=>CH+H2                                     3.00E+13    0.0        0.0
 52. H+CH3(+M)<=>CH4(+M)                                  1.27E+16   -0.6      383.0
     Low pressure limit:  0.24770E+34 -0.47600E+01  0.24400E+04
     TROE centering:      0.78300E+00  0.74000E+02  0.29410E+04  0.69640E+04
        H2                 Enhanced by    2.000E+00
        H2O                Enhanced by    6.000E+00
        CH4                Enhanced by    2.000E+00
        CO                 Enhanced by    1.500E+00
        CO2                Enhanced by    2.000E+00
        C2H6               Enhanced by    3.000E+00
        AR                 Enhanced by    7.000E-01
 53. H+CH4<=>CH3+H2                                       6.60E+08    1.6    10840.0
 54. H+HCO(+M)<=>CH2O(+M)                                 1.09E+12    0.5     -260.0
     Low pressure limit:  0.13500E+25 -0.25700E+01  0.14250E+04
     TROE centering:      0.78240E+00  0.27100E+03  0.27550E+04  0.65700E+04
        H2                 Enhanced by    2.000E+00
        H2O                Enhanced by    6.000E+00
        CH4                Enhanced by    2.000E+00
        CO                 Enhanced by    1.500E+00
        CO2                Enhanced by    2.000E+00
        C2H6               Enhanced by    3.000E+00
        AR                 Enhanced by    7.000E-01
 55. H+HCO<=>H2+CO                                        7.34E+13    0.0        0.0
 56. H+CH2O(+M)<=>CH2OH(+M)                               5.40E+11    0.5     3600.0
     Low pressure limit:  0.12700E+33 -0.48200E+01  0.65300E+04
     TROE centering:      0.71870E+00  0.10300E+03  0.12910E+04  0.41600E+04
        H2                 Enhanced by    2.000E+00
        H2O                Enhanced by    6.000E+00
        CH4                Enhanced by    2.000E+00
        CO                 Enhanced by    1.500E+00
```

```
        CO2               Enhanced by     2.000E+00
        C2H6              Enhanced by     3.000E+00
 57. H+CH2O(+M)<=>CH3O(+M)                               5.40E+11    0.5      2600.0
     Low pressure limit:  0.22000E+31 -0.48000E+01  0.55600E+04
     TROE centering:      0.75800E+00  0.94000E+02  0.15550E+04  0.42000E+04
        H2                Enhanced by     2.000E+00
        H2O               Enhanced by     6.000E+00
        CH4               Enhanced by     2.000E+00
        CO                Enhanced by     1.500E+00
        CO2               Enhanced by     2.000E+00
        C2H6              Enhanced by     3.000E+00
 58. H+CH2O<=>HCO+H2                                     2.30E+10    1.1      3275.0
 59. H+CH2OH(+M)<=>CH3OH(+M)                             1.80E+13    0.0         0.0
     Low pressure limit:  0.30000E+32 -0.48000E+01  0.33000E+04
     TROE centering:      0.76790E+00  0.33800E+03  0.18120E+04  0.50810E+04
        H2                Enhanced by     2.000E+00
        H2O               Enhanced by     6.000E+00
        CH4               Enhanced by     2.000E+00
        CO                Enhanced by     1.500E+00
        CO2               Enhanced by     2.000E+00
        C2H6              Enhanced by     3.000E+00
 60. H+CH2OH<=>H2+CH2O                                   2.00E+13    0.0         0.0
 61. H+CH2OH<=>OH+CH3                                    1.20E+13    0.0         0.0
 62. H+CH2OH<=>CH2(S)+H2O                                6.00E+12    0.0         0.0
 63. H+CH3O(+M)<=>CH3OH(+M)                              5.00E+13    0.0         0.0
     Low pressure limit:  0.86000E+29 -0.40000E+01  0.30250E+04
     TROE centering:      0.89020E+00  0.14400E+03  0.28380E+04  0.45569E+05
        H2                Enhanced by     2.000E+00
        H2O               Enhanced by     6.000E+00
        CH4               Enhanced by     2.000E+00
        CO                Enhanced by     1.500E+00
        CO2               Enhanced by     2.000E+00
        C2H6              Enhanced by     3.000E+00
 64. H+CH3O<=>H+CH2OH                                    3.40E+06    1.6         0.0
 65. H+CH3O<=>H2+CH2O                                    2.00E+13    0.0         0.0
 66. H+CH3O<=>OH+CH3                                     3.20E+13    0.0         0.0
 67. H+CH3O<=>CH2(S)+H2O                                 1.60E+13    0.0         0.0
 68. H+CH3OH<=>CH2OH+H2                                  1.70E+07    2.1      4870.0
 69. H+CH3OH<=>CH3O+H2                                   4.20E+06    2.1      4870.0
 70. H+C2H(+M)<=>C2H2(+M)                                1.00E+17   -1.0         0.0
     Low pressure limit:  0.37500E+34 -0.48000E+01  0.19000E+04
     TROE centering:      0.64640E+00  0.13200E+03  0.13150E+04  0.55660E+04
        H2                Enhanced by     2.000E+00
        H2O               Enhanced by     6.000E+00
        CH4               Enhanced by     2.000E+00
        CO                Enhanced by     1.500E+00
        CO2               Enhanced by     2.000E+00
        C2H6              Enhanced by     3.000E+00
        AR                Enhanced by     7.000E-01
 71. H+C2H2(+M)<=>C2H3(+M)                               5.60E+12    0.0      2400.0
     Low pressure limit:  0.38000E+41 -0.72700E+01  0.72200E+04
     TROE centering:      0.75070E+00  0.98500E+02  0.13020E+04  0.41670E+04
        H2                Enhanced by     2.000E+00
        H2O               Enhanced by     6.000E+00
        CH4               Enhanced by     2.000E+00
        CO                Enhanced by     1.500E+00
        CO2               Enhanced by     2.000E+00
        C2H6              Enhanced by     3.000E+00
        AR                Enhanced by     7.000E-01
 72. H+C2H3(+M)<=>C2H4(+M)                               6.08E+12    0.3       280.0
     Low pressure limit:  0.14000E+31 -0.38600E+01  0.33200E+04
     TROE centering:      0.78200E+00  0.20750E+03  0.26630E+04  0.60950E+04
        H2                Enhanced by     2.000E+00
        H2O               Enhanced by     6.000E+00
        CH4               Enhanced by     2.000E+00
```

```
       CO               Enhanced by   1.500E+00
       CO2              Enhanced by   2.000E+00
       C2H6             Enhanced by   3.000E+00
       AR               Enhanced by   7.000E-01
73. H+C2H3<=>H2+C2H2                             3.00E+13    0.0        0.0
74. H+C2H4(+M)<=>C2H5(+M)                        1.08E+12    0.5     1820.0
    Low pressure limit:  0.12000E+43 -0.76200E+01  0.69700E+04
    TROE centering:      0.97530E+00  0.21000E+03  0.98400E+03  0.43740E+04
       H2               Enhanced by   2.000E+00
       H2O              Enhanced by   6.000E+00
       CH4              Enhanced by   2.000E+00
       CO               Enhanced by   1.500E+00
       CO2              Enhanced by   2.000E+00
       C2H6             Enhanced by   3.000E+00
       AR               Enhanced by   7.000E-01
75. H+C2H4<=>C2H3+H2                             1.32E+06    2.5    12240.0
76. H+C2H5(+M)<=>C2H6(+M)                        5.21E+17   -1.0     1580.0
    Low pressure limit:  0.19900E+42 -0.70800E+01  0.66850E+04
    TROE centering:      0.84220E+00  0.12500E+03  0.22190E+04  0.68820E+04
       H2               Enhanced by   2.000E+00
       H2O              Enhanced by   6.000E+00
       CH4              Enhanced by   2.000E+00
       CO               Enhanced by   1.500E+00
       CO2              Enhanced by   2.000E+00
       C2H6             Enhanced by   3.000E+00
       AR               Enhanced by   7.000E-01
77. H+C2H5<=>H2+C2H4                             2.00E+12    0.0        0.0
78. H+C2H6<=>C2H5+H2                             1.15E+08    1.9     7530.0
79. H+HCCO<=>CH2(S)+CO                           1.00E+14    0.0        0.0
80. H+CH2CO<=>HCCO+H2                            5.00E+13    0.0     8000.0
81. H+CH2CO<=>CH3+CO                             1.13E+13    0.0     3428.0
82. H+HCCOH<=>H+CH2CO                            1.00E+13    0.0        0.0
83. H2+CO(+M)<=>CH2O(+M)                         4.30E+07    1.5    79600.0
    Low pressure limit:  0.50700E+28 -0.34200E+01  0.84350E+05
    TROE centering:      0.93200E+00  0.19700E+03  0.15400E+04  0.10300E+05
       H2               Enhanced by   2.000E+00
       H2O              Enhanced by   6.000E+00
       CH4              Enhanced by   2.000E+00
       CO               Enhanced by   1.500E+00
       CO2              Enhanced by   2.000E+00
       C2H6             Enhanced by   3.000E+00
       AR               Enhanced by   7.000E-01
84. OH+H2<=>H+H2O                                2.16E+08    1.5     3430.0
85. 2OH(+M)<=>H2O2(+M)                           7.40E+13   -0.4        0.0
    Low pressure limit:  0.23000E+19 -0.90000E+00 -0.17000E+04
    TROE centering:      0.73460E+00  0.94000E+02  0.17560E+04  0.51820E+04
       H2               Enhanced by   2.000E+00
       H2O              Enhanced by   6.000E+00
       CH4              Enhanced by   2.000E+00
       CO               Enhanced by   1.500E+00
       CO2              Enhanced by   2.000E+00
       C2H6             Enhanced by   3.000E+00
       AR               Enhanced by   7.000E-01
86. 2OH<=>O+H2O                                  3.57E+04    2.4    -2110.0
87. OH+HO2<=>O2+H2O                              2.90E+13    0.0     -500.0
88. OH+H2O2<=>HO2+H2O                            1.75E+12    0.0      320.0
    Declared duplicate reaction...
89. OH+H2O2<=>HO2+H2O                            5.80E+14    0.0     9560.0
    Declared duplicate reaction...
90. OH+C<=>H+CO                                  5.00E+13    0.0        0.0
91. OH+CH<=>H+HCO                                3.00E+13    0.0        0.0
92. OH+CH2<=>H+CH2O                              2.00E+13    0.0        0.0
93. OH+CH2<=>CH+H2O                              1.13E+07    2.0     3000.0
94. OH+CH2(S)<=>H+CH2O                           3.00E+13    0.0        0.0
95. OH+CH3(+M)<=>CH3OH(+M)                       6.30E+13    0.0        0.0
```

```
        Low pressure limit:  0.27000E+39 -0.63000E+01  0.31000E+04
        TROE centering:      0.21050E+00  0.83500E+02  0.53980E+04  0.83700E+04
           H2                Enhanced by    2.000E+00
           H2O               Enhanced by    6.000E+00
           CH4               Enhanced by    2.000E+00
           CO                Enhanced by    1.500E+00
           CO2               Enhanced by    2.000E+00
           C2H6              Enhanced by    3.000E+00
  96. OH+CH3<=>CH2+H2O                                  5.60E+07    1.6      5420.0
  97. OH+CH3<=>CH2(S)+H2O                               2.50E+13    0.0         0.0
  98. OH+CH4<=>CH3+H2O                                  1.00E+08    1.6      3120.0
  99. OH+CO<=>H+CO2                                     4.76E+07    1.2        70.0
 100. OH+HCO<=>H2O+CO                                   5.00E+13    0.0         0.0
 101. OH+CH2O<=>HCO+H2O                                 3.43E+09    1.2      -447.0
 102. OH+CH2OH<=>H2O+CH2O                               5.00E+12    0.0         0.0
 103. OH+CH3O<=>H2O+CH2O                                5.00E+12    0.0         0.0
 104. OH+CH3OH<=>CH2OH+H2O                              1.44E+06    2.0      -840.0
 105. OH+CH3OH<=>CH3O+H2O                               6.30E+06    2.0      1500.0
 106. OH+C2H<=>H+HCCO                                   2.00E+13    0.0         0.0
 107. OH+C2H2<=>H+CH2CO                                 2.18E-04    4.5     -1000.0
 108. OH+C2H2<=>H+HCCOH                                 5.04E+05    2.3     13500.0
 109. OH+C2H2<=>C2H+H2O                                 3.37E+07    2.0     14000.0
 110. OH+C2H2<=>CH3+CO                                  4.83E-04    4.0     -2000.0
 111. OH+C2H3<=>H2O+C2H2                                5.00E+12    0.0         0.0
 112. OH+C2H4<=>C2H3+H2O                                3.60E+06    2.0      2500.0
 113. OH+C2H6<=>C2H5+H2O                                3.54E+06    2.1       870.0
 114. OH+CH2CO<=>HCCO+H2O                               7.50E+12    0.0      2000.0
 115. 2HO2<=>O2+H2O2                                    1.30E+11    0.0     -1630.0
      Declared duplicate reaction...
 116. 2HO2<=>O2+H2O2                                    4.20E+14    0.0     12000.0
      Declared duplicate reaction...
 117. HO2+CH2<=>OH+CH2O                                 2.00E+13    0.0         0.0
 118. HO2+CH3<=>O2+CH4                                  1.00E+12    0.0         0.0
 119. HO2+CH3<=>OH+CH3O                                 2.00E+13    0.0         0.0
 120. HO2+CO<=>OH+CO2                                   1.50E+14    0.0     23600.0
 121. HO2+CH2O<=>HCO+H2O2                               1.00E+12    0.0      8000.0
 122. C+O2<=>O+CO                                       5.80E+13    0.0       576.0
 123. C+CH2<=>H+C2H                                     5.00E+13    0.0         0.0
 124. C+CH3<=>H+C2H2                                    5.00E+13    0.0         0.0
 125. CH+O2<=>O+HCO                                     3.30E+13    0.0         0.0
 126. CH+H2<=>H+CH2                                     1.11E+08    1.8      1670.0
 127. CH+H2O<=>H+CH2O                                   1.71E+13    0.0      -755.0
 128. CH+CH2<=>H+C2H2                                   4.00E+13    0.0         0.0
 129. CH+CH3<=>H+C2H3                                   3.00E+13    0.0         0.0
 130. CH+CH4<=>H+C2H4                                   6.00E+13    0.0         0.0
 131. CH+CO(+M)<=>HCCO(+M)                              5.00E+13    0.0         0.0
      Low pressure limit:  0.26900E+29 -0.37400E+01  0.19360E+04
      TROE centering:      0.57570E+00  0.23700E+03  0.16520E+04  0.50690E+04
         H2                Enhanced by    2.000E+00
         H2O               Enhanced by    6.000E+00
         CH4               Enhanced by    2.000E+00
         CO                Enhanced by    1.500E+00
         CO2               Enhanced by    2.000E+00
         C2H6              Enhanced by    3.000E+00
         AR                Enhanced by    7.000E-01
 132. CH+CO2<=>HCO+CO                                   3.40E+12    0.0       690.0
 133. CH+CH2O<=>H+CH2CO                                 9.46E+13    0.0      -515.0
 134. CH+HCCO<=>CO+C2H2                                 5.00E+13    0.0         0.0
 135. CH2+O2<=>OH+HCO                                   1.32E+13    0.0      1500.0
 136. CH2+H2<=>H+CH3                                    5.00E+05    2.0      7230.0
 137. 2CH2<=>H2+C2H2                                    3.20E+13    0.0         0.0
 138. CH2+CH3<=>H+C2H4                                  4.00E+13    0.0         0.0
 139. CH2+CH4<=>2CH3                                    2.46E+06    2.0      8270.0
 140. CH2+CO(+M)<=>CH2CO(+M)                            8.10E+11    0.5      4510.0
      Low pressure limit:  0.26900E+34 -0.51100E+01  0.70950E+04
```

```
     TROE centering:      0.59070E+00  0.27500E+03  0.12260E+04  0.51850E+04
        H2                Enhanced by   2.000E+00
        H2O               Enhanced by   6.000E+00
        CH4               Enhanced by   2.000E+00
        CO                Enhanced by   1.500E+00
        CO2               Enhanced by   2.000E+00
        C2H6              Enhanced by   3.000E+00
        AR                Enhanced by   7.000E-01
141. CH2+HCCO<=>C2H3+CO                             3.00E+13   0.0         0.0
142. CH2(S)+N2<=>CH2+N2                             1.50E+13   0.0       600.0
143. CH2(S)+AR<=>CH2+AR                             9.00E+12   0.0       600.0
144. CH2(S)+O2<=>H+OH+CO                            2.80E+13   0.0         0.0
145. CH2(S)+O2<=>CO+H2O                             1.20E+13   0.0         0.0
146. CH2(S)+H2<=>CH3+H                              7.00E+13   0.0         0.0
147. CH2(S)+H2O(+M)<=>CH3OH(+M)                     2.00E+13   0.0         0.0
     Low pressure limit:  0.27000E+39 -0.63000E+01  0.31000E+04
     TROE centering:      0.15070E+00  0.13400E+03  0.23830E+04  0.72650E+04
        H2                Enhanced by   2.000E+00
        H2O               Enhanced by   6.000E+00
        CH4               Enhanced by   2.000E+00
        CO                Enhanced by   1.500E+00
        CO2               Enhanced by   2.000E+00
        C2H6              Enhanced by   3.000E+00
148. CH2(S)+H2O<=>CH2+H2O                           3.00E+13   0.0         0.0
149. CH2(S)+CH3<=>H+C2H4                            1.20E+13   0.0      -570.0
150. CH2(S)+CH4<=>2CH3                              1.60E+13   0.0      -570.0
151. CH2(S)+CO<=>CH2+CO                             9.00E+12   0.0         0.0
152. CH2(S)+CO2<=>CH2+CO2                           7.00E+12   0.0         0.0
153. CH2(S)+CO2<=>CO+CH2O                           1.40E+13   0.0         0.0
154. CH2(S)+C2H6<=>CH3+C2H5                         4.00E+13   0.0      -550.0
155. CH3+O2<=>O+CH3O                                2.68E+13   0.0     28800.0
156. CH3+O2<=>OH+CH2O                               3.60E+10   0.0      8940.0
157. CH3+H2O2<=>HO2+CH4                             2.45E+04   2.5      5180.0
158. 2CH3(+M)<=>C2H6(+M)                            2.12E+16  -1.0       620.0
     Low pressure limit:  0.17700E+51 -0.96700E+01  0.62200E+04
     TROE centering:      0.53250E+00  0.15100E+03  0.10380E+04  0.49700E+04
        H2                Enhanced by   2.000E+00
        H2O               Enhanced by   6.000E+00
        CH4               Enhanced by   2.000E+00
        CO                Enhanced by   1.500E+00
        CO2               Enhanced by   2.000E+00
        C2H6              Enhanced by   3.000E+00
        AR                Enhanced by   7.000E-01
159. 2CH3<=>H+C2H5                                  4.99E+12   0.1     10600.0
160. CH3+HCO<=>CH4+CO                               2.65E+13   0.0         0.0
161. CH3+CH2O<=>HCO+CH4                             3.32E+03   2.8      5860.0
162. CH3+CH3OH<=>CH2OH+CH4                          3.00E+07   1.5      9940.0
163. CH3+CH3OH<=>CH3O+CH4                           1.00E+07   1.5      9940.0
164. CH3+C2H4<=>C2H3+CH4                            2.27E+05   2.0      9200.0
165. CH3+C2H6<=>C2H5+CH4                            6.14E+06   1.7     10450.0
166. HCO+H2O<=>H+CO+H2O                             2.24E+18  -1.0     17000.0
167. HCO+M<=>H+CO+M                                 1.87E+17  -1.0     17000.0
        H2                Enhanced by   2.000E+00
        H2O               Enhanced by   0.000E+00
        CH4               Enhanced by   2.000E+00
        CO                Enhanced by   1.500E+00
        CO2               Enhanced by   2.000E+00
        C2H6              Enhanced by   3.000E+00
168. HCO+O2<=>HO2+CO                                7.60E+12   0.0       400.0
169. CH2OH+O2<=>HO2+CH2O                            1.80E+13   0.0       900.0
170. CH3O+O2<=>HO2+CH2O                             4.28E-13   7.6     -3530.0
171. C2H+O2<=>HCO+CO                                5.00E+13   0.0      1500.0
172. C2H+H2<=>H+C2H2                                4.07E+05   2.4       200.0
173. C2H3+O2<=>HCO+CH2O                             3.98E+12   0.0      -240.0
174. C2H4(+M)<=>H2+C2H2(+M)                         8.00E+12   0.4     88770.0
```

```
          Low pressure limit:  0.70000E+51 -0.93100E+01  0.99860E+05
          TROE centering:      0.73450E+00  0.18000E+03  0.10350E+04  0.54170E+04
             H2                Enhanced by    2.000E+00
             H2O               Enhanced by    6.000E+00
             CH4               Enhanced by    2.000E+00
             CO                Enhanced by    1.500E+00
             CO2               Enhanced by    2.000E+00
             C2H6              Enhanced by    3.000E+00
             AR                Enhanced by    7.000E-01
    175. C2H5+O2<=>HO2+C2H4                                8.40E+11     0.0      3875.0
    176. HCCO+O2<=>OH+2CO                                  1.60E+12     0.0       854.0
    177. 2HCCO<=>2CO+C2H2                                  1.00E+13     0.0         0.0
    178. N+NO<=>N2+O                                       3.50E+13     0.0       330.0
    179. N+O2<=>NO+O                                       2.65E+12     0.0      6400.0
    180. N+OH<=>NO+H                                       7.33E+13     0.0      1120.0
    181. N2O+O<=>N2+O2                                     1.40E+12     0.0     10810.0
    182. N2O+O<=>2NO                                       2.90E+13     0.0     23150.0
    183. N2O+H<=>N2+OH                                     4.40E+14     0.0     18880.0
    184. N2O+OH<=>N2+HO2                                   2.00E+12     0.0     21060.0
    185. N2O(+M)<=>N2+O(+M)                                1.30E+11     0.0     59620.0
          Low pressure limit:  0.62000E+15  0.00000E+00  0.56100E+05
             H2                Enhanced by    2.000E+00
             H2O               Enhanced by    6.000E+00
             CH4               Enhanced by    2.000E+00
             CO                Enhanced by    1.500E+00
             CO2               Enhanced by    2.000E+00
             C2H6              Enhanced by    3.000E+00
             AR                Enhanced by    7.000E-01
    186. HO2+NO<=>NO2+OH                                   2.11E+12     0.0      -480.0
    187. NO+O+M<=>NO2+M                                    1.06E+20    -1.4         0.0
             H2                Enhanced by    2.000E+00
             H2O               Enhanced by    6.000E+00
             CH4               Enhanced by    2.000E+00
             CO                Enhanced by    1.500E+00
             CO2               Enhanced by    2.000E+00
             C2H6              Enhanced by    3.000E+00
             AR                Enhanced by    7.000E-01
    188. NO2+O<=>NO+O2                                     3.90E+12     0.0      -240.0
    189. NO2+H<=>NO+OH                                     1.32E+14     0.0       360.0
    190. NH+O<=>NO+H                                       5.00E+13     0.0         0.0
    191. NH+H<=>N+H2                                       3.20E+13     0.0       330.0
    192. NH+OH<=>HNO+H                                     2.00E+13     0.0         0.0
    193. NH+OH<=>N+H2O                                     2.00E+09     1.2         0.0
    194. NH+O2<=>HNO+O                                     4.61E+05     2.0      6500.0
    195. NH+O2<=>NO+OH                                     1.28E+06     1.5       100.0
    196. NH+N<=>N2+H                                       1.50E+13     0.0         0.0
    197. NH+H2O<=>HNO+H2                                   2.00E+13     0.0     13850.0
    198. NH+NO<=>N2+OH                                     2.16E+13    -0.2         0.0
    199. NH+NO<=>N2O+H                                     4.16E+14    -0.5         0.0
    200. NH2+O<=>OH+NH                                     7.00E+12     0.0         0.0
    201. NH2+O<=>H+HNO                                     4.60E+13     0.0         0.0
    202. NH2+H<=>NH+H2                                     4.00E+13     0.0      3650.0
    203. NH2+OH<=>NH+H2O                                   9.00E+07     1.5      -460.0
    204. NNH<=>N2+H                                        3.30E+08     0.0         0.0
    205. NNH+M<=>N2+H+M                                    1.30E+14    -0.1      4980.0
             H2                Enhanced by    2.000E+00
             H2O               Enhanced by    6.000E+00
             CH4               Enhanced by    2.000E+00
             CO                Enhanced by    1.500E+00
             CO2               Enhanced by    2.000E+00
             C2H6              Enhanced by    3.000E+00
             AR                Enhanced by    7.000E-01
    206. NNH+O2<=>HO2+N2                                   5.00E+12     0.0         0.0
    207. NNH+O<=>OH+N2                                     2.50E+13     0.0         0.0
    208. NNH+O<=>NH+NO                                     7.00E+13     0.0         0.0
```

```
209. NNH+H<=>H2+N2                                      5.00E+13   0.0        0.0
210. NNH+OH<=>H2O+N2                                    2.00E+13   0.0        0.0
211. NNH+CH3<=>CH4+N2                                   2.50E+13   0.0        0.0
212. H+NO+M<=>HNO+M                                     8.95E+19  -1.3      740.0
       H2                  Enhanced by   2.000E+00
       H2O                 Enhanced by   6.000E+00
       CH4                 Enhanced by   2.000E+00
       CO                  Enhanced by   1.500E+00
       CO2                 Enhanced by   2.000E+00
       C2H6                Enhanced by   3.000E+00
       AR                  Enhanced by   7.000E-01
213. HNO+O<=>NO+OH                                      2.50E+13   0.0        0.0
214. HNO+H<=>H2+NO                                      4.50E+11   0.7      660.0
215. HNO+OH<=>NO+H2O                                    1.30E+07   1.9     -950.0
216. HNO+O2<=>HO2+NO                                    1.00E+13   0.0    13000.0
217. CN+O<=>CO+N                                        7.70E+13   0.0        0.0
218. CN+OH<=>NCO+H                                      4.00E+13   0.0        0.0
219. CN+H2O<=>HCN+OH                                    8.00E+12   0.0     7460.0
220. CN+O2<=>NCO+O                                      6.14E+12   0.0     -440.0
221. CN+H2<=>HCN+H                                      2.10E+13   0.0     4710.0
222. NCO+O<=>NO+CO                                      2.35E+13   0.0        0.0
223. NCO+H<=>NH+CO                                      5.40E+13   0.0        0.0
224. NCO+OH<=>NO+H+CO                                   2.50E+12   0.0        0.0
225. NCO+N<=>N2+CO                                      2.00E+13   0.0        0.0
226. NCO+O2<=>NO+CO2                                    2.00E+12   0.0    20000.0
227. NCO+M<=>N+CO+M                                     8.80E+16  -0.5    48000.0
       H2                  Enhanced by   2.000E+00
       H2O                 Enhanced by   6.000E+00
       CH4                 Enhanced by   2.000E+00
       CO                  Enhanced by   1.500E+00
       CO2                 Enhanced by   2.000E+00
       C2H6                Enhanced by   3.000E+00
       AR                  Enhanced by   7.000E-01
228. NCO+NO<=>N2O+CO                                    2.85E+17  -1.5      740.0
229. NCO+NO<=>N2+CO2                                    5.70E+18  -2.0      800.0
230. HCN+M<=>H+CN+M                                     1.04E+29  -3.3   126600.0
       H2                  Enhanced by   2.000E+00
       H2O                 Enhanced by   6.000E+00
       CH4                 Enhanced by   2.000E+00
       CO                  Enhanced by   1.500E+00
       CO2                 Enhanced by   2.000E+00
       C2H6                Enhanced by   3.000E+00
       AR                  Enhanced by   7.000E-01
231. HCN+O<=>NCO+H                                      1.11E+04   2.6     4980.0
232. HCN+O<=>NH+CO                                      2.77E+03   2.6     4980.0
233. HCN+O<=>CN+OH                                      2.13E+09   1.6    26600.0
234. HCN+OH<=>HOCN+H                                    1.10E+06   2.0    13370.0
235. HCN+OH<=>HNCO+H                                    4.40E+03   2.3     6400.0
236. HCN+OH<=>NH2+CO                                    1.60E+02   2.6     9000.0
237. H+HCN+M<=>H2CN+M                                   1.40E+26  -3.4     1900.0
       H2                  Enhanced by   2.000E+00
       H2O                 Enhanced by   6.000E+00
       CH4                 Enhanced by   2.000E+00
       CO                  Enhanced by   1.500E+00
       CO2                 Enhanced by   2.000E+00
       C2H6                Enhanced by   3.000E+00
       AR                  Enhanced by   7.000E-01
238. H2CN+N<=>N2+CH2                                    6.00E+13   0.0      400.0
239. C+N2<=>CN+N                                        6.30E+13   0.0    46020.0
240. CH+N2<=>HCN+N                                      2.86E+08   1.1    20400.0
241. CH+N2(+M)<=>HCNN(+M)                               3.10E+12   0.1        0.0
     Low pressure limit:   0.13000E+26 -0.31600E+01  0.74000E+03
     TROE centering:       0.66700E+00  0.23500E+03  0.21170E+04  0.45360E+04
       H2                  Enhanced by   2.000E+00
       H2O                 Enhanced by   6.000E+00
```

```
          CH4                 Enhanced by    2.000E+00
          CO                  Enhanced by    1.500E+00
          CO2                 Enhanced by    2.000E+00
          C2H6                Enhanced by    3.000E+00
          AR                  Enhanced by    7.000E-01
 242. CH2+N2<=>HCN+NH                                      1.00E+13    0.0   74000.0
 243. CH2(S)+N2<=>NH+HCN                                   1.00E+11    0.0   65000.0
 244. C+NO<=>CN+O                                          1.90E+13    0.0       0.0
 245. C+NO<=>CO+N                                          2.90E+13    0.0       0.0
 246. CH+NO<=>HCN+O                                        5.00E+13    0.0       0.0
 247. CH+NO<=>H+NCO                                        2.00E+13    0.0       0.0
 248. CH+NO<=>N+HCO                                        3.00E+13    0.0       0.0
 249. CH2+NO<=>H+HNCO                                      3.10E+17   -1.4    1270.0
 250. CH2+NO<=>OH+HCN                                      2.90E+14   -0.7     760.0
 251. CH2+NO<=>H+HCNO                                      3.80E+13   -0.4     580.0
 252. CH2(S)+NO<=>H+HNCO                                   3.10E+17   -1.4    1270.0
 253. CH2(S)+NO<=>OH+HCN                                   2.90E+14   -0.7     760.0
 254. CH2(S)+NO<=>H+HCNO                                   3.80E+13   -0.4     580.0
 255. CH3+NO<=>HCN+H2O                                     9.60E+13    0.0   28800.0
 256. CH3+NO<=>H2CN+OH                                     1.00E+12    0.0   21750.0
 257. HCNN+O<=>CO+H+N2                                     2.20E+13    0.0       0.0
 258. HCNN+O<=>HCN+NO                                      2.00E+12    0.0       0.0
 259. HCNN+O2<=>O+HCO+N2                                   1.20E+13    0.0       0.0
 260. HCNN+OH<=>H+HCO+N2                                   1.20E+13    0.0       0.0
 261. HCNN+H<=>CH2+N2                                      1.00E+14    0.0       0.0
 262. HNCO+O<=>NH+CO2                                      9.80E+07    1.4    8500.0
 263. HNCO+O<=>HNO+CO                                      1.50E+08    1.6   44000.0
 264. HNCO+O<=>NCO+OH                                      2.20E+06    2.1   11400.0
 265. HNCO+H<=>NH2+CO                                      2.25E+07    1.7    3800.0
 266. HNCO+H<=>H2+NCO                                      1.05E+05    2.5   13300.0
 267. HNCO+OH<=>NCO+H2O                                    4.65E+12    0.0    6850.0
 268. HNCO+OH<=>NH2+CO2                                    1.55E+12    0.0    6850.0
 269. HNCO+M<=>NH+CO+M                                     1.18E+16    0.0   84720.0
          H2                  Enhanced by    2.000E+00
          H2O                 Enhanced by    6.000E+00
          CH4                 Enhanced by    2.000E+00
          CO                  Enhanced by    1.500E+00
          CO2                 Enhanced by    2.000E+00
          C2H6                Enhanced by    3.000E+00
          AR                  Enhanced by    7.000E-01
 270. HCNO+H<=>H+HNCO                                      2.10E+15   -0.7    2850.0
 271. HCNO+H<=>OH+HCN                                      2.70E+11    0.2    2120.0
 272. HCNO+H<=>NH2+CO                                      1.70E+14   -0.8    2890.0
 273. HOCN+H<=>H+HNCO                                      2.00E+07    2.0    2000.0
 274. HCCO+NO<=>HCNO+CO                                    2.35E+13    0.0       0.0
 275. CH3+N<=>H2CN+H                                       6.10E+14   -0.3     290.0
 276. CH3+N<=>HCN+H2                                       3.70E+12    0.1     -90.0
 277. NH3+H<=>NH2+H2                                       5.40E+05    2.4    9915.0
 278. NH3+OH<=>NH2+H2O                                     5.00E+07    1.6     955.0
 279. NH3+O<=>NH2+OH                                       9.40E+06    1.9    6460.0
```

Appendix F: Modified PREMIX Input File

The PREMIX input file is organized in the sequential manner, containing comment lines (which begin with "/") and actual data lines. Each data line consists of a a four-letter keyword that can have a meaning by itself or need additional parameters. A fully-commented sample input file for Fecralloy follows, in which extra spaces were included for the sake of clarity:

```
/ Type of problem: burner stabilized flame or one in which the
/ temperature profile is given
BURN
/ TGIV

/ To solve the energy equation
/ If keyword is removed, the isothermal problem is solved
ENRG

/ Indicates a restart from a previous solution
RSTR

/ Determines boundary condition downstream: default is zero gradient
/ If this keyword is present, back-diffusion of air is allowed
DIFF

/ Pressure in atmospheres
PRES  1.00


/ Order of the discrete ordinates method
ORSN   4


/ Mass flow rate in g/(cm^2 s)
FLRT 0.015

/ Time steps for isothermal problem (initial solution) and
/ the energy equation iterations, respectively
TIME   300  5.00E-6
TIM2   500  6.00E-6

/ Initial number of grid points.  A low number is reccommended,
/ and it should be chosen carefully to have nodes at the solid faces
NPTS    8

/ Volumetric heat transfer coefficient in SI units
HVOL 1000000
```

```
/ Heat transfer coefficients at the solid faces in SI units
CHTO    50.
CHT1    50.

/ Emittance at the solid faces
EPSO 0.65
EPS1 0.65


/ Temperaure of the surroundings downstream, upstream (in K)
SURO    400.
SUR1    400.

/ Porosity of the solid
PORO   0.91

/ Effective thermal conductivity of the solid in SI units
CONS 0.13


/ Specific heat of the solid in SI units
CPSS   430.


/ Apparent density of the solid in SI units
DENS   600.


/ Diameter of the fibers in m
DIAM  22.E-06


/ Extinction coefficient in 1/m
BETA  200.


/Scattering coefficient in 1/m
SGMA  20.


/ Definition of the computational interval: coordinate of the first node,
/ guessed flame location, coordinate of the last node, guessed flame
/ thickness, in cm
XSTR   0.00
XCEN   0.28
XEND   1.40
WMIX   0.05

/ Beginning and end of solid phase in cm
XSRT   0.20
XSND   0.40

/ Adaptive mesh criteria: maximum gradient and curvature allowed between
/ adjacent data points, for ALL variables
GRAD   0.4

CURV   0.4
```

```
/ Composition given in mole units (other option is mass units)
MOLE

/ Reactants and their unreacted mole fractions
REAC   O2   0.19194
REAC   N2   0.72169
REAC   CH4  0.08637


/ Estimated products, also downstream boundary condition for N2 and O2
/ if the DIFF option is active (partially premixed flames)
PROD   N2   0.7
PROD   O2   0.2
PROD   CO2  0.010
PROD   H2O  0.090

/ Estimated intermediate mole fractions
INTM   CO    .08
INTM   HCO   .00001
INTM   HO2   .001
INTM   O     .0001
INTM   H2O2  .0001
INTM   H     .02
INTM   H2    .01
INTM   OH    .001
INTM   CH2   .0001
INTM   CH    .00001
INTM   CH2O  .0001
INTM   CH3   .0005

/ Include thermal diffusion (default is no thermal diffusion)
TDIF

/ Tolerances for the Newton iteration: absolute and relative
ATOL  1.E-9
RTOL  1.E-4

/ Tolerances for the time step Newton iteration: absolute and relative
ATIM  1.E-5
RTIM  1.E-5

/ Print control: 0,1,2 (gives different amount of information
/ regarding the numerical convergence process)
PRNT    1

/ Given temperature profile as initial guess
TEMP    .0000  4.000E+02
TEMP    .1000  5.437E+02
TEMP    .2000  6.875E+02
TEMP    .4000  1.535E+03
TEMP    .6000  1.500E+03
TEMP    .8000  1.488E+03
TEMP   1.0000  1.485E+03
TEMP   1.2000  1.484E+03
TEMP   1.4000  1.484E+03
END
```

Appendix G: Description of PREMIX Solution Algorithm (TWPNT)

The TWOPNT subroutine (Grcar, 1992) included in the PREMIX code (Kee et al., 1988) to solve the burner-stabilized flame problem uses a "Modified Damped Newton's Method". The procedure can be described as follows:

1. Discretize on a given mesh and obtain a system of nonlinear algebraic equations.
2. Determine a sequence of approximate solutions (vector ϕ) that approach the "true" solution.
3. Any arbitrary ϕ is not a solution of the finite difference equations. They are not satisfied, they equal a residual vector $\mathcal{F}(\phi) \neq 0$. The purpose is to find ϕ such as $\mathcal{F}(\phi) = 0$.
4. A good initial estimate $\phi^{(0)}$ is needed, otherwise is difficult for the flame problem to converge. Usually an old solution of a similar/simplified problem is used.
5. The purest form of algorithm is $\phi^{(n+1)} = \phi^{(n)} - \left(\frac{\partial \mathcal{F}}{\partial \phi}\right)^{-1}_{\phi^{(n)}} \mathcal{F}(\phi^{(n)})$. But this is too expensive and delicate to use in practice.
6. The Jacobian $\left(\frac{\partial \mathcal{F}}{\partial \phi}\right)$ is expensive to compute; therefore, an old $J^{(n)}$ inherited from previous step is used. Since this approximate method might not give a good solution when using a full "step", a damping parameter, $0 < \lambda^{(n)} \leq 1$, is used to obtain $\phi^{(n+1)}$.
7. The iteration becomes then: $\phi^{(n+1)} = \phi^{(n)} - \lambda^{(n)}[J^{(n)}]^{-1}\mathcal{F}(\phi^{(n)})$.
8. The inverse of $J^{(n)}$ is not computed; a system of linear equations is solved instead, $J^{(n)}\Delta\phi^{(n)} = \mathcal{F}(\phi^{(n)})$, for the undampened correction vector $\Delta\phi^{(n)}$.
9. The selection process for $J^{(n)}$ and $\lambda^{(n)}$ is governed by a look ahead procedure; having tentatively chosen $\phi^{(n+1)}$, $\phi^{(n+2)}$ is calculated. The solution for the new step, $\phi^{(n+1)}$, is accepted if:

$$\left|[J^{(n)}]^{-1}\mathcal{F}(\phi^{(n+1)})\right| < \left|[J^{(n)}]^{-1}\mathcal{F}(\phi^{(n)})\right| ,$$

i.e., the undampened step decreases in magnitude.

10. The damping parameter is initially chosen to be as large as possible so that $\phi^{(n+1)}$ does not violate the bounds upon the solution variables. If $\phi^{(n+1)}$ fails the criterion given above, repeat the algorithm with a halved damping parameter.
11. If that fails, compute a new Jacobian.
12. If that fails, take time steps. This is a way of moving from one trial solution that is not within the domain of Newton convergence to one that is.

In this case, the Jacobian is a large banded matrix, block tridiagonal, which provides information on how a perturbation of any variable affects the residual of any equation.

VITA

VITA

Sergio Adrián Leonardi was born in Buenos Aires, Argentina, on December 24, 1968. His early schooling was in Instituto Sarmiento in Buenos Aires. He moved to Funes, Santa Fe, in 1982 when he entered the Liceo Aeronáutico Militar (Air Force High School). He graduated with honors in 1986. Back in his home town, in January 1987 he enrolled at Buenos Aires Institute of Technology.

In August of 1989 he moved to Bariloche, Río Negro, with a scholarship to study Nuclear Engineering. He graduated first-in-the-class in 1993 with a degree equivalent to a Masters of Science in Nuclear Engineering. After four months as a "Praktikum" at the Hahn-Meitner-Institut (Berlin, Germany), he enrolled in the Ph.D. program in Nuclear Engineering at Purdue University (January 1994).

On September 17, 1996 he married Tauna Lea Wilmarth.

In December of 1996 he finished his second MSNE and transferred to the School of Mechanical Engineering to complete a Ph.D. in the area of heat transfer and combustion. On February 1, 1999 his first son, Paul Antonio, was born in Lafayette.

After graduation, he will leave West Lafayette to join Exxon Mobil's Upstream Research Company in Houston, Texas.